

Field assisted sintering technology/spark plasma sintering in the direct recycling of hot-deformed Nd-Fe-B scrap and PM T15 steel swarf

Monica Theresa Maria Keszler

Energie & Umwelt / Energy & Environment
Band / Volume 682
ISBN 978-3-95806-866-7

Forschungszentrum Jülich GmbH
Institute of Fusion Energy and Nuclear Waste Management (IFN)
Plasma Physics (IFN-1)

Field assisted sintering technology/spark plasma sintering in the direct recycling of hot-deformed Nd-Fe-B scrap and PM T15 steel swarf

Monica Theresa Maria Keszler

Schriften des Forschungszentrums Jülich
Reihe Energie & Umwelt / Energy & Environment

Band / Volume 682

ISSN 1866-1793

ISBN 978-3-95806-866-7

Bibliografische Information der Deutschen Nationalbibliothek.
Die Deutsche Nationalbibliothek verzeichnet diese Publikation in der
Deutschen Nationalbibliografie; detaillierte Bibliografische Daten
sind im Internet über <http://dnb.d-nb.de> abrufbar.

Herausgeber
und Vertrieb: Forschungszentrum Jülich GmbH
Zentralbibliothek, Verlag
52425 Jülich
Tel.: +49 2461 61-5368
Fax: +49 2461 61-6103
zb-publikation@fz-juelich.de
www.fz-juelich.de/zb

Umschlaggestaltung: Grafische Medien, Forschungszentrum Jülich GmbH

Druck: Grafische Medien, Forschungszentrum Jülich GmbH

Copyright: Forschungszentrum Jülich 2025

Schriften des Forschungszentrums Jülich
Reihe Energie & Umwelt / Energy & Environment, Band / Volume 682

D 294 (Diss. Bochum, Univ., 2025)

ISSN 1866-1793

ISBN 978-3-95806-866-7

Vollständig frei verfügbar über das Publikationsportal des Forschungszentrums Jülich (JuSER)
unter www.fz-juelich.de/zb/openaccess.



This is an Open Access publication distributed under the terms of the [Creative Commons Attribution License 4.0](#), which permits unrestricted use, distribution, and reproduction in any medium, provided the original work is properly cited.

Abstract

The push for a more circular economy worldwide has necessitated further research into direct recycling. There are many waste streams that currently do not have a possible direct recycling route developed. While many indirect recycling techniques may exist, they often come with the use of hazardous chemicals or a large consumption of energy. The aim of this work has been to investigate the use of field assisted sintering technology/spark plasma sintering (FAST/SPS) in the direct recycling of two waste streams that currently have no direct recycling route.

The first stream of interest was scrap, out-of-spec hot deformed Nd-Fe-B magnets. These magnets, provided by an industry partner, WILO SE, have a desirable microstructure that would be destroyed by consolidation techniques like hot-deformation or sintering. A benefit of FAST/SPS is its capability to maintain and fine-tune microstructures due to its high heating rates and quick sinter times. Firstly, these scrap powders were partially densified into pre-forms via FAST/SPS. Afterwards, this work employed two different electric current assisted sintering (ECAS) techniques in the formation of new magnets from this scrap. The first was flash SPS (FSPS), a technique that uses a single power pulse and uniaxial pressure to deform a pre-form. The second was spark plasma texturing (SPT), a modified FAST/SPS technique that deforms a pre-form to a wider diameter. As the FAST/SPS and flash SPS devices allow for fine-tuned parameter control, different aspects such as deformation speed, applied pressure, pressure dwell time, and maximum temperature were adjusted across experiments. The ultimate goal was to generate magnets made from 100 wt% recycled hot-deformed Nd-Fe-B scrap for use in a demonstrator motor. The spark plasma texturing technique generated 100 wt% scrap magnets with a maximum energy product, $(BH)_{\max}$, of over 200 kJ/m³, which were successfully tested in a pump motor of the industrial partner, WILO.

The second stream of interest was PM T15 high-speed steel swarf, provided by a second industry partner, Berghaus GmbH. This swarf was contaminated with lubricant oil and grinding medium, such as Al₂O₃. Because of the contamination, this sort of swarf is typically disposed of in landfill rather than recycled. After being cleaned of the lubricant oil, the swarf was sintered under various FAST/SPS conditions to optimize densification. Modifications to both the swarf and the FAST/SPS procedure were necessary to generate dense samples that would not break tools upon extraction. Samples were scaled up from Ø 20 mm to Ø 120 mm, leading to a demonstrator part of Ø 120 mm made from 100 wt% PM T15 swarf that could be tested in a mock tunneling rig.

Despite the two very different waste streams, FAST/SPS showed its strengths in microstructural control, densification, deformation, and utilization of unconventional powder morphology. Alongside this, energy measurements of the ECAS processes were taken for the discussion of practical industrial applications.

Kurzfassung

Der weltweite Vorstoß in Richtung einer Kreislaufwirtschaft hat zur Etablierung ein erneuen Forschungsrichtung, dem direkten Recycling, gefuehrt. Es gibt viele Abfallströme, für die es derzeit keine direkte Recyclingmöglichkeit gibt. Zwar gibt es viele indirekte Recyclingtechniken, doch sind diese oft mit dem Einsatz gefährlicher Chemikalien oder einem hohen Energieverbrauch verbunden. Ziel dieser Arbeit war es, den Einsatz der feldunterstützten Sintertechnologie/Spark-Plasma-Sintern (FAST/SPS) für das direkte Recycling von zwei Abfallströmen zu untersuchen, für die es derzeit keinen direkten Recyclingweg gibt.

Der erste Abfallstrom waren schrottreife, nicht spezifikationsgerechte heiß umgeformte Nd-Fe-B-Magnete. Diese Magnete, die von einem Industriepartner, WILO SE, zur Verfügung gestellt wurden, haben eine fuer die Magneteigenschaften spezifische Mikrostruktur, die durch die etablierten Herstellungsverfahren Umformung oder Sintern zerstört würde. Ein Vorteil von FAST/SPS ist die Fähigkeit, diese Mikrostruktur aufgrund der hohen Heizraten und schnellen Sinterzeiten zu erhalten und nach zu justieren. Zunächst wurden die Abfallpulver mittels FAST/SPS zu Halbzeugen vorverdichtet. Anschließend wurden im Rahmen dieser Arbeit zwei verschiedene stromunterstützte Sintertechniken, „electric current assisted sintering (ECAS)“, für die Herstellung neuer Magnete aus diesem Abfall eingesetzt. Das erste war Flash-SPS, ein Verfahren, bei dem ein kurzer Stromimpuls und einachsiger Druck zur Verformung des Halbzeugs verwendet werden. Das zweite Verfahren war die Funkenplasma-Texturierung, eine modifizierte FAST/SPS-Technik, bei der das Halbzeug in einer FAST/SPS-Form auf einen größeren Durchmesser verformt wird. Da die FAST/SPS- und Flash-SPS-Technologie eine fein abgestimmte Einstellung der Parameter ermöglichen, wurden wesentliche Parameter wie Verformungsgeschwindigkeit, Druck, Druckverweildauer und maximale Temperatur in systematischen Versuchsreihen angepasst. Das ultimative Ziel war die Herstellung von Magneten aus 100 Gew.-% recyceltem, heiß verformtem Nd-Fe-B-Schrott zur Anwendung in einem Demonstrationsmotor. Mit der Funkenplasma-Texturierungstechnik wurden Magnete aus 100 Gew.-% Schrott mit einem maximalen Energieprodukt, $(BH)_{\max}$, von über 200 kJ/m³ hergestellt, die erfolgreich in einem Pumpenmotor des Industriepartners WILO getestet wurden.

Der zweite Abfallstrom von Interesse waren Spaene aus PM T15 Schellarbeitsstahl, die von einem zweiten Industriepartner, der Berghaus GmbH, bereitgestellt wurden. Diese Späne waren mit Schmieröl und Schleifmittel, wie z. B. Al₂O₃, verunreinigt. Aufgrund der Verunreinigungen werden diese Späne in der Regel nicht recycelt, sondern auf einer Deponie entsorgt. Nachdem die Späne vom Schmieröl gereinigt worden waren, wurden sie durch eine gezielte Variation der FAST/SPS Parameter gesintert, um die Verdichtung zu optimieren. Sowohl die Morphologie der Stahlspaenen als auch der Versuchsaufbau des FAST/SPS-Verfahrens mussten gezielt veraendert werden, um dichte Proben zu

erzeugen, die die FAST/SPS-Formen bei der Entnahme der Bauteile nicht zerbrechen lassen. In Rahmen der Arbeit wurde der Probendurchmesser von \varnothing 20 mm auf \varnothing 120 mm vergrößert. Diese Sklaierung ermöglichte die Herstellung einer 120 mm Scheidscheibe als Demonstratorbauteil, die zu 100 Gew.% aus PM T15 Spaen bestand und erfolgreich in einem Tuennelvortriebsteststand getestet wurde.

Am Beispiel der beiden sehr unterschiedlichen Abfallströme konnte nachgewiesen werden, dass FAST/SPS Vorteile gegenüber anderen Recyclingrouten in Bezug auf die Kontrolle der Mikrostruktur, die Verdichtung, die Verformung und die Nutzung von Pulver mit unkonventioneller Pulvermorphologie besitzt. Parallel dazu wurden Energiemessungen der ECAS-Prozesse durchgeführt, um das praktische industrielle Anwendungspotential zu diskutieren.

Table of Contents

Abbreviations	vii
Variables	viii
1 Introduction	1
1.1 Project Motivation	1
1.2 Organization of the Thesis	3
1.3 Motivation for Recycling	3
1.3.1 Circular Economy	3
1.3.2 Direct Recycling	4
2 State of the Art	6
2.1 Fundamentals of Sintering	6
2.2 Sintering Techniques Used in this Work	9
2.2.1 Pressure Assisted Sintering	9
2.2.2 Liquid Phase Sintering	11
2.2.3 Field Assisted Sintering Technology/Spark Plasma Sintering (FAST/SPS)	12
2.2.4 Flash SPS	14
2.3 Introduction to Nd-Fe-B Magnets	16
2.3.1 Basics of Magnetism	16
2.3.2 Permanent Magnet Materials	18
2.3.3 Nd-Fe-B – Material Properties and Applications	23
2.3.4 Production of Nd-Fe-B Magnets	24
2.3.5 Review of FAST/SPS Usage in Nd-Fe-B Recycling	28
2.4 Introduction to PM T15 Steel	29
2.4.1 PM T15 Applications	29
2.4.2 Production and Material Properties	29
2.4.3 Steel Swarf and Contaminants	31
2.4.4 Processing – Casting vs. Powder Metallurgy	31
2.4.5 Review of FAST/SPS Usage in Metal Swarf Recycling	32
3 Experimental	33
3.1 Powder Characterization	33
3.1.1 Particle Size Distribution	33
3.1.1 Compositional Analysis	35
3.2 Nd-Fe-B Recycling	36
3.2.1 Jaw-Crushing	36
3.2.2 Powder Designation and Mixing	37
3.2.3 FAST/SPS Pre-Sintering and Hot Compaction	39
3.2.4 Flash SPS Experiments	41

3.2.5 Flash SPS in a Boron Nitride Ring.....	43
3.2.6 Spark Plasma Texturing	44
3.2.7 Demonstrator Magnets	50
3.3 PM T15 Steel Swarf Recycling	52
3.3.1 Thermodynamic Equilibrium Calculations	52
3.3.2 Cleaning and Milling.....	53
3.3.3 FAST/SPS Sintering of PM T15	54
3.3.4 FAST/SPS of Milled PM T15 and Scale-Up.....	56
3.3.5 Heat treatment and Shaping	59
3.3.6 Demonstrator Part	60
3.4 Sample Characterization Methods and Process Evaluation.....	62
3.4.1 Microstructure and Compositional Analysis Post-Sinter	62
3.4.2 Nd-Fe-B: Magnetic Characterization	64
3.4.3 PM T15: Hardness.....	66
3.4.4 Other Physical Properties	67
3.4.5 Energy Consumption Measurements.....	68
4 Results and Discussion: Nd-Fe-B	69
4.1 Analysis of the Powders	69
4.2 Magnetic Performance and Microstructure of Flash SPS (FSPS) Samples.....	71
4.2.1 Magnetic Performance of FSPS Samples from Mixed Recyclate and Commercial Powders	72
4.2.2 Microstructure of Samples Made from Mixed Recyclate and Commercial Powders	74
4.2.3 Analysis of MQU-F Samples Deformed with Boron Nitride Dies (25-30 mm)	79
4.2.4 Analysis of Samples made from Recyclate or Commercial Powders Deformed with Boron Nitride Dies (31-33 mm).....	82
4.3 Magnetic Performance and Microstructure of Spark Plasma Texturing (SPT) Samples	85
4.3.1 SPT Comparison Between Hot-Compacted and Pre-Sintered Pellets from Commercial Powder.....	85
4.3.2 Quick Deformation SPT.....	87
4.3.3 Gradual Pressure Application SPT and Scale-Up	90
4.3.4 SPT of Recyclate Hot Compacts	92
4.3.5 Modifications for a Demonstrator Magnet.....	97
4.3.6 Operation of the Demonstrator Magnets in a Water Pump Motor	99
4.4 Process Energy Consumption	102
4.5 Summary.....	105
5 Results and Discussion: PM T15 High-Speed Steel	107
5.1 Analysis of the Swarf	107
5.2 Analysis of Samples from Un-Milled Swarf.....	110

5.2.1 Single-Stage FAST/SPS	110
5.2.2 FAST/SPS Pre-sintering and Deformation.....	113
5.3 FAST/SPS Scale-Up to a Demonstrator Part.....	118
5.3.1 Process Design and Troubleshooting	118
5.3.2 Heat Treatment and Demonstrator Part.....	124
5.3.3 Operation of the Demonstrator Part	126
5.4 Energy Consumption and Life Cycle Analysis	129
5.5 Summary.....	130
6 Conclusion and Relevance to Industrial Application.....	132
6.1 ECAS in Hot-Deformed Nd-Fe-B Recycling	132
6.2 PM T15 Steel Swarf Recycling via FAST/SPS	137
7 Outlook	139
Acknowledgements.....	141
List of Figures.....	143
List of Tables	149
Bibliography	151
Appendix A Nd-Fe-B recyclate powder data.....	162
Appendix B Comprehensive magnetic performance data (Flash SPS).....	163
Appendix C Comprehensive magnetic performance data (SPT)	165
Appendix D FAST/SPS and FSPS machine data.....	168
List of Publications	170
Curriculum Vitae	172

Abbreviations

BN	boron nitride
BSE	back-scattered electrons
cBN	cubic boron nitride
CCT	continuous cooling transformation
CE	circular economy
CGHE	carrier gas hot extraction
DIA	dynamic image analysis
ECAS	electric current assisted sintering
EDS	electro-discharge sintering
EDX	energy dispersive X-ray analysis
EMF	electromotive force
EQPC	diameter of a circle of equal projection area
FAST/SPS	field assisted sintering technology/spark plasma sintering
FSPS	flash spark plasma sintering
GD-OES	glow discharge optical emission spectrometry
HDDR	hydrogenation-disproportionation-desorption-recombination
HIP	hot isostatic pressing
HREE	heavy rare earth element
HSS	high speed steel
ICP-OES	inductively coupled plasma optical emission spectroscopy
IR	infrared
IT	isothermal transformation
LPS	liquid phase sintering
LREE	light rare earth element
PM	powder metallurgy
PSD	particle size distribution
REE	rare earth element
SE	secondary electrons
SEM	scanning electron microscopy
SiC	silicon carbide
SLPS	supersolidus liquid phase sintering
SPT	spark plasma texturing
TTT	time-temperature-transformation
TZM	titanium-zirconium-molybdenum
VSM	vibrating sample magnetometer
XRF	X-ray fluorescence analysis

Variables

θ	angle
A	area
Ω	atom volume
μ_B	Bohr magneton
k_B	Boltzmann constant
b	Burgers vector
H_{cJ}	coercivity
T_c	Curie temperature
φ	deformation degree
$\dot{\epsilon}$	densification rate
ρ	density, sintering neck surface radius
F	force
G	grain size
I_0	incident intensity
I	intensity
M	internal magnetization
H	magnetic field strength
B	magnetic flux density
J	magnetic polarization
χ_m	magnetic susceptibility
$(BH)_{max}$	maximum energy product
a	neck radius
R	particle radius
D	particle size, diffusion coefficient
μ	permeability
P	pressure
μ_r	relative magnetic permeability
B_r	remanence
M_s	saturation magnetization
σ	stress
γ	surface energy, interfacial energy
T	temperature
μ_0	vacuum permeability
HV	Vickers hardness
λ	wavelength

1 Introduction

1.1 Project Motivation

The research into innovative recycling strategies is vital for the transition into a more energy-efficient circular economy for critical raw materials. One branch of exploration of material recycling is via powder metallurgy. Powder metallurgy techniques have the potential to feed waste from the machining of metallic materials or the scrap made from out-of-spec magnets directly back into the materials cycle. This technique could save a large amount of energy that would have been spent synthesizing material from primary raw materials, could prevent many tons of material from entering landfills, and could reinsert a variety of critical elements, such as Co, Nd, or W, directly back into production and use.

In this work, the two main materials of interest are neodymium-iron-boron (Nd-Fe-B) based magnets and high-speed steel PM T15. Nd-Fe-B magnets have the best magnetic properties of all permanent magnets and are necessary components in the fields of electromobility, energy generation through wind power, and circulatory pumps [1]–[3]. There is an urgent need for a recycling route for Nd-Fe-B. This is especially the case due to the presence of the rare earth elements, REE, including the light rare earth element, LREE, Nd and heavy rare earth elements, HREE, of Dy and Pr, which are often added to Nd-Fe-B magnets [4]. Addition of these elements leads to a variety of improvements in magnetic performance [5]. Primary raw material deposits of these elements are dwindling, and reliance on these deposits simultaneously lead to undesired geopolitical dependencies [6]. A variety of techniques are being researched for the extraction of REEs, such as pyrometallurgical, hydrometallurgical, solvent-based, and kinetics-based techniques [4], [7]–[12]; however, this work focuses on direct recycling of hot-deformed Nd-Fe-B, which avoids the use of harsh chemicals or heating to the point of fully melting the material.

The second material of interest is high-speed steel, HSS - more specifically PM T15 (DIN EN 1.3202 / AISI T15) grinding swarf produced during the machining of HSS tools. During machining, the excess material sheared off during grinding or polishing, known as swarf, still contains all the same valuable elements as the tool itself. As this swarf tends to be contaminated with grinding medium and lubricant, as well as having too small of a size for convenient reuse, it tends to be disposed of [13]–[17]. This could mean significant amounts of critical elements, such as Co, W, or Mo, being dumped and not considered for reuse. PM T15 steel is a steel with high wear resistance and a large W content, making it of great interest for recycling.

The powder metallurgical route of choice for recycling these powders is performed using electric current assisted sintering (ECAS) techniques. The specific ECAS method used here is known as field assisted sintering technology/spark plasma sintering, commonly referred to as FAST/SPS [18]. In the

case of the Nd-Fe-B recycling, two secondary techniques known as Flash SPS (FSPS) and spark plasma texturing (SPT) are also implemented.

FAST/SPS uses direct pulsed current to achieve high heating rates through a conductive tool, which holds the sample, while pressure is added by a hydraulic piston. Flash SPS has the sample in contact with the electrode via graphite spacers, and a powerful pulse of current is forced through the sample, with or without a surrounding die [19]. SPT deforms a pre-sintered compact in the FAST/SPS setup using a die with a diameter larger than the pre-compact [20]. All of these techniques can produce sintered material in a short amount of time (the scale of seconds or minutes) at moderate temperatures (below 1200 °C). In the case of the grinding swarf, these techniques also have the potential to create a matrix of the HSS while suspending grinding medium or other additives like solid lubricants to make new materials with unique properties. Iron and steel alloys, along with multi-component material composites, have been successfully sintered via FAST/SPS in various studies [21]. Net-shaping of some metallic alloys has also been performed via FAST/SPS, such as with TiAl [22]. Therefore, FAST/SPS became an attractive candidate to utilize for the consolidation of HSS swarf for new tools, such as cutting disks. In the case of the Nd-Fe-B magnets, sintering of a new magnet can be done potentially without encouraging further grain growth, opening up the possibility of the direct recycling of particles with anisotropic grains [23]. Evaluation of FAST/SPS as a waste consolidation technique helps to determine the industrial potential of the technology beyond research scale.

This research is a part of the EnerGieffziENtE Kreislaufwirtschaft kritischer Rohstoffe (GENESIS) project funded by the Bundesministerium für Wirtschaft und Energie (BMWE). GENESIS operates between the Ruhr-Universität Bochum, the Bergische Universität Wuppertal, the Lehrstuhl für Anthropogene Stoffkreisläufe (ANTS) at RWTH Aachen and the Forschungszentrum Jülich as scientific institutions, the German companies WILO SE, Klaus Kuhn Edelstahl, Berghaus, Berger Gruppe as users and Glamatronic, OWL and Dr. Fritsch Sondermaschinen GmbH as equipment manufacturers. The division of tasks within this project is illustrated in Figure 1.1. Outside of the GENESIS consortium, assistance was provided by the Functional Materials group at TU Darmstadt and from Fraunhofer IWKS. The aim of this project is to preserve the value of these materials for as long as possible, reduce waste and greenhouse gas emissions, develop strategies for upcycling recyclates with improved material properties, demonstrate the viability of these strategies for integration into the energy transition, and evaluate the developed material cycles.

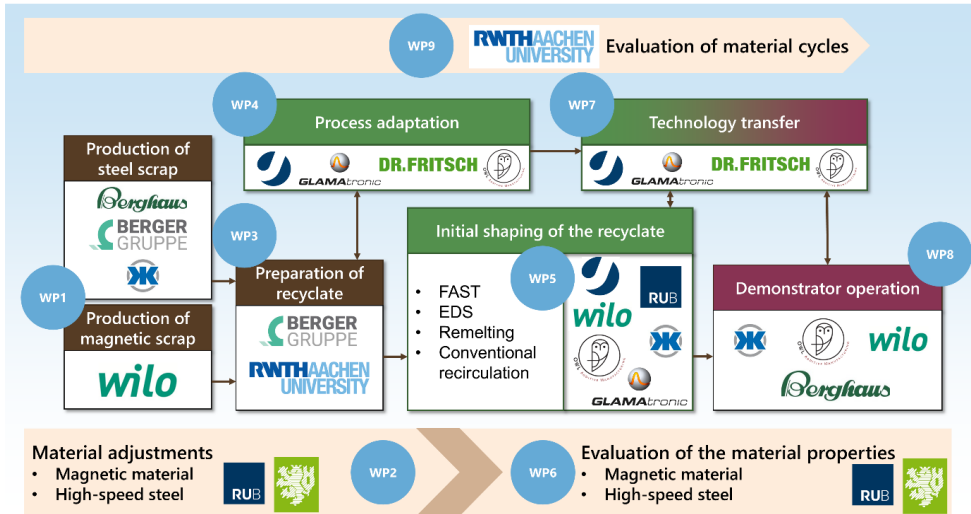


Figure 1.1 - Organization and distribution of tasks within the GENESIS Project

1.2 Organization of the Thesis

The continuation of Chapter 1 emphasizes the motivation of recycling, with a brief overview of what materials have been chosen for this work and why. Chapter 2 discusses state-of-the-art, giving a general introduction to sintering and the sintering techniques used in this work. It also introduces the two materials of interest in this study – Nd-Fe-B and PM T15 high speed steel. It briefly describes their production, function, and relevance. All subsequent chapters are divided based on their specific material. Chapter 3 describes the experimental method chosen for processing these materials, including analysis of the starting material, equipment, and characterization techniques for the final samples. Chapter 4 contains the results and discussions of the experiments regarding Nd-Fe-B magnets. Chapter 5 details the results and discussions of experiments regarding PM T15 high-speed steel. Chapter 6 gives a brief perspective on the industrial relevance of the results. Chapter 7 concludes this thesis with an outlook as to what can be done beyond this work. The thesis is closed with acknowledgements to all who have contributed to the completion of the work.

1.3 Motivation for Recycling

1.3.1 Circular Economy

Ongoing pressure is continuing to develop for more sustainable systems of material production and living, as resources on Earth are limited and infinite growth cannot last forever [24], [25]. Current means of industrial production and consumption lead to a variety of issues, such as environmental problems

[26], social and equity issues [27], and supply risk [28]. A proposed method to handle these problems is through the concept of circular economy. While sustainability is a broad concept with many individual definitions [29], it encompasses a change to human lifestyle that emphasizes ongoing support of future security and health for future generations by maintaining the supply of non-replaceable resources while simultaneously supporting the survival of all other lifeforms on earth [30], [31]. Circular economy (CE) is a sustainable focus on industrial economics. CE would introduce an economy in the shape of a theoretical closed loop – in terms of material input and output, with special emphasis on preventing waste production and increasing resource efficiency. The need for raw material input would be limited, as, ideally, resources could be extracted and regenerated from end-of-life products for re-use in the production loop; simultaneously, waste, emissions, and energy leakage would be minimized [27], [32], [33]. Though CE involves a variety of different elements to be fully implemented, such as product design for long lifespans, freedom of maintenance and repair, reuse, refurbishment and remanufacturing, the element of focus in this work is on the idea of recycling [27].

1.3.2 Direct Recycling

Recycling is a method of using materials in a continuous cycle. This cycle begins with the extraction of resources, to their formation into a product, to the product's disposal – or, in the framework of recycling, its recovery – finally to be re-formed into a new product or reduced back to a usable resource [34]. With the growing world population comes the growing demand and use of products that eventually turn to waste streams, such as plastics [35], metals [36], and e-waste [37], each with their own unique challenges in recovery and resource extraction. In this work, the primary focus is on direct recycling of materials with a specific focus to their relevance for technical applications. Direct recycling is a method of recycling a material as-is, without destroying the material's chemical structure [38]. Direct recycling is a popular field of research, especially in regards to the field of Li-ion batteries, as it avoids the use of hydrometallurgical extraction, which can use environmentally harmful leaching reagents, and is modeled to be a low-cost method of regaining material from electric vehicles [39]. Direct recycling is not limited to batteries, however. The methodology can be applied to other materials, such as Nd-Fe-B magnets or HSS swarf.

Hot-deformed Nd-Fe-B magnets

Much of primary REE mining is localized in just a few countries, such as China, the USA, Australia, and India. The growing demand for REEs in burgeoning technological fields is becoming more and more difficult to meet. However, as electronic devices reach their end-of-life stage, e-waste rich in REEs – which include Nd-Fe-B magnets doped with REEs – becomes more and more abundant. This e-waste has the potential to be harnessed, have its resources extracted, and have those resources recycled, which could mitigate REE supply risk to an extent, in the mid-term [6], [37]. Hot-deformed

Nd-Fe-B magnets, which are fully dense, have a higher Nd-Fe-B content than other forms of Nd-Fe-B magnets, specifically polymer bonded Nd-Fe-B magnets. This high Nd-Fe-B content leads to better magnetic performance [40]. Due to the high REE content of Nd-Fe-B magnets, which can be more than 30 wt%, fully dense Nd-Fe-B magnets have become attractive as recycling candidates [41]. This candidature extends to sintered Nd-Fe-B magnets, as well as hot-deformed ones – regardless, this work focuses entirely on hot-deformed magnets. Currently, the recycling techniques of sintered magnets include re-sintering into a new magnet, melt-spinning, hydrogenation-disproportionation-desorption-recombination (HDDR), or recasting into a new master alloy [42]–[45]. Few direct recycling techniques have been explored for reimplementing hot-deformed magnet scrap back into new hot-deformed magnets [46], [47].

High Speed Steel grinding swarf

The steel industry is of great interest for more sustainable development, as steel production is responsible for nearly one-quarter of all industrial greenhouse gas emissions and 6% of global CO₂ emissions [48], [49]. Though steel recycling is already industrially implemented, and secondary steel production emits three times fewer emissions than primary steel production, limits to steel recycling exist [50]. These include potential quality loss due to contamination and increased demand outpacing the rate of recycling [51]–[53]. Simultaneously, nearly 400 kg of by-products is produced per ton of steel, which includes sludge from grinding [54]. Shaping processes in the steel industry include turning, milling, grinding, and drilling produce waste streams with metal chips and grinding sludge, with the German metal-working industry producing nearly 280 kt of grinding sludge per year [55]. There is no waste treatment option currently available for grinding sludge to extract high-value elements, such as W or Co, and often the sludge is landfilled. Landfilling of the sludge is costly and burdensome to the environment [15], [17]. The sludge can be cleaned of its lubricant using techniques including combustion or supercritical CO₂, but these processes could be cost-intensive and possibly uneconomical. Recycling costs, specifically energy costs, would greatly increase when the cleaning processes are combined with the energy input required to re-melt the swarf [56]–[58]. The swarf within the sludge can also trap abrasives from grinding wheels. The HSS of interest in this work is PM T15, a high-tungsten alloyed steel. Tungsten, along with other elements in PM T15 like cobalt, is a critical material [59]. Landfilling of the grinding sludge would therefore cause these elements to be lost from the supply chain. Therefore, it is of interest to clean the PM T15 sludge of its lubricant by more economical methods, separate it as much as possible from its non-metallic grinding contamination, and attempt to directly recycle it into a new tool.

2 State of the Art

2.1 Fundamentals of Sintering

When a powder is sintered, it is due to the driving force of reducing the total interfacial, or surface, energy of the powder particles. It is represented through Equation (2.1), where the total surface energy of the powder is expressed as γA . In this case, γ is the surface energy, and A is the total surface area within the powder. The reduction of this total energy is given by:

$$\Delta(\gamma A) = \Delta\gamma A + \gamma\Delta A \quad (2.1)$$

The two changes, the change in surface energy ($\Delta\gamma$) and the change in surface area (ΔA) are primarily responsible for two phenomena, respectively – $\Delta\gamma$ typically results in densification, while ΔA leads to grain growth of the powder compact. In conventional sintering, these processes occur simultaneously, represented by $\Delta(\gamma A)$ [60]. A visual representation of sintering is shown in Figure 2.1.

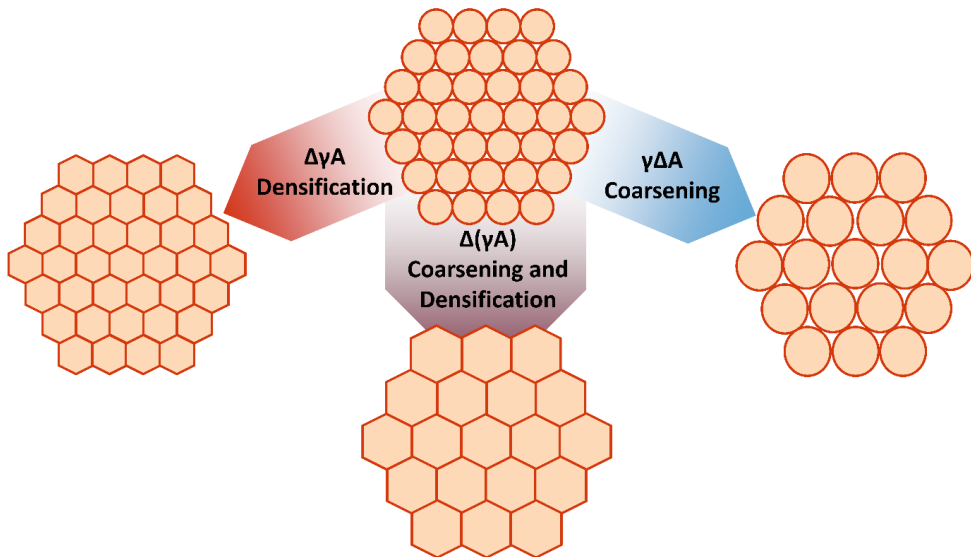


Figure 2.1 – Visual representation of the sintering process via coarsening and densification. Adapted from [60]

Besides the lowering of surface energy, solid-state sintering also occurs through defects. Defects are the imperfections of the crystalline arrangement of atoms. They can happen for a number of chemical reasons. Polycrystalline materials are, in the real world, imperfect in structure. If they were in a perfect,

three-dimensional crystalline order, the lowering of energy through the resolution of defects would be impossible. However, as these defects exist, they allow diffusional matter transfer to take place during sintering and grain growth. Defects are classified in three groups with respect to their dimensional order:

1. Point defects, which could refer to vacancies of atoms, atoms occupying interstices between two atoms, impurity atoms, and atoms that are substituted by the parent atom.
2. Line defects, which represent a defect that are multiple atoms in length. These are referred to as dislocations.
3. Planar defects, which represent the discontinuity of a perfect crystal structure across an entire plane. This is referred to as a grain boundary when it separates two distinctly oriented crystals. This category also includes the segregation of impurity atoms to grain interfaces [61].

The process of sintering occurs via three overlapping stages. These are (I) the initial stage, (II) the intermediate stage, and (III) the final stage. During stage I, the sintering process occurs primarily through the formation of inter-particle necks. Stage II contributes to the most densification of all stages and is characterized by an interconnected porosity. Stage III is marked by pore removal at grain boundaries [60].

The sintering process combines both the densification and grain growth of the initial powder. This densification can be defined as the ratio between the change of porosity of the compact after sintering versus its starting porosity prior to sintering. During sintering, a number of material transport mechanisms occur within the network of powder particles. The dominating mechanism can vary based on a variety of factors, such as particle size, neck radius, temperature, and time. These mechanisms are defined in several different paths of diffusional matter transport. All six of these mechanisms lead to particle bonding and neck growth between particles. However, only three of the mechanisms contribute to densification [60], [62]. The summary of which mechanisms do and do not contribute to densification is listed in Table 2.1. A visualization of how they occur is given in Figure 2.2.

Table 2.1 - Material transport mechanisms during sintering, specifically in polycrystalline solids, with numbers corresponding to the illustrated mechanisms in Figure 2.2 [62].

Sintering Mechanism	Matter Source	Matter Sink	Contributes to densification
1- Surface diffusion	Surface	Neck	No
2- Lattice diffusion	Surface	Neck	No
3 - Vapor transport	Surface	Neck	No
4 - Grain Boundary Diffusion	Grain Boundary	Neck	Yes
5 - Lattice Diffusion	Grain Boundary	Neck	Yes
6 - Plastic Flow	Dislocation	Neck	Yes

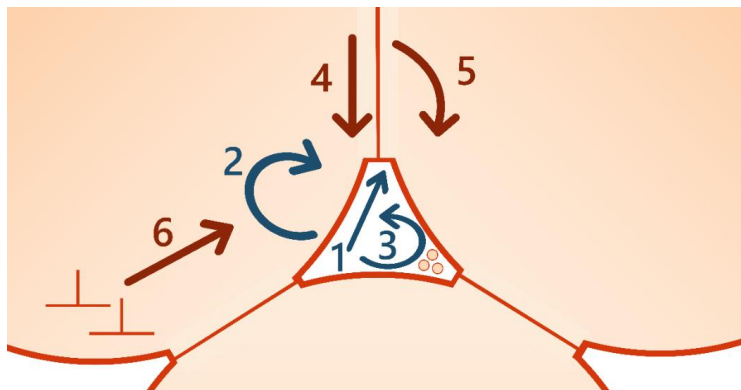


Figure 2.2 – Schematic displaying the types of sintering mechanisms that lead to neck formation and grain coarsening (1-3) and shrinkage (4-6) using the three-particle model. The mechanisms are as follows: 1. Surface diffusion, 2. Lattice diffusion from the surface, 3. Evaporation and re-condensation, 4. Grain boundary diffusion, 5. Lattice diffusion from the grain boundary, and 6. Plastic flow through dislocations. Adapted from [62]

In polycrystalline materials, the sintering process tends to be complex. This is due to the presence of planar defects, which are crystalline interfaces previously introduced as grain boundaries. These grain boundaries participate in several types of mass transport mechanisms as matter sources, specifically in grain boundary diffusion and lattice diffusion. As a powder is sintered, multiple mechanisms can be active simultaneously, contributing to the growth of necks and densification of the compact in parallel. Generally, though, despite the complicated nature of multiple transport mechanisms happening all at once, the diffusion processes tend to be dictated by the microstructure and particle size of the powder. Some pathways will be more thermodynamically favorable and therefore more dominating.

The non-densification mechanisms only contribute to the growth of necks between particles. These mechanisms lead to a reduction in a particle's curvature. When a particle's curvature is reduced, the main driving force of sintering is also reduced – as growing necks contribute to lower surface area. This decreases the rate of densification. Therefore, it is optimal to design sintering parameters that can favor densifying mechanisms to generate a fully dense sample [60], [62], [63]. In particular, high heating rates have the advantage of activating the mechanisms contributing to densification directly [64].

2.2 Sintering Techniques Used in this Work

Traditional sintering relies on the thermal activation of its transport mechanisms through prolonged exposure to increased temperature. With technological advances, newer properties are demanded of sintered materials which can only be accomplished through more efficient sintering techniques [19], [65]. In this section, sintering methods that extend beyond just the application of high temperatures are described, along with the ways in which they improve the sintering process. As the majority of experiments performed on this work relied on field assisted sintering, such as Field Assisted Sintering Technology/Spark Plasma Sintering (FAST/SPS) and Flash SPS (FSPS), these techniques are explained in more detail relative to others.

2.2.1 Pressure Assisted Sintering

Improved densification can occur during sintering with the application of pressure upon a compact. When pressure is not applied, the driving force for sintering comes from the powder compacts' reduction in total interfacial energy. Vacancies diffuse from the surface of particles to the necks between sintered particles and finally to the contact grain boundary between particles, where they are eliminated [60], [66]. The curvature of the neck is responsible for the increased vacancy concentration, causing tensile stress, considered capillary stress. In a two-particle model, the description of capillary stress as the driving force is given in Equation (2.2):

$$\sigma_{CS} = \gamma \left(\frac{1}{a} - \frac{1}{\rho} \right) \quad (2.2)$$

In this equation, γ represents surface tension, a represents the neck radius between two particles, and ρ is the surface radius of the neck. With the application of pressure, compressive force is generated between powder particles. This compressive force leads to the reduction in vacancy concentration at the regions where particles contact one another. The additional driving force given by the application of external pressure is represented in Equation (2.3).

$$\sigma_{PS} = \frac{3PR^2}{2a^2} \quad (2.3)$$

In this case, R , the radius of the particle, and P , the external pressure, are considered.

The influence of both of these stresses is combined in the calculation of densification rate, $\dot{\epsilon}$. In pressure-assisted sintering, the primary methods of densification are through diffusion along the grain boundary (Equation (2.4)) and lattice diffusion adjacent to grain boundaries (Equation (2.5)) [66], [67].

$$\dot{\epsilon}_{PS,GB} = D_{GB} \frac{4b\Omega}{k_B T} \frac{1}{a^2 R} \left(\frac{3PR^2}{2a^2} + 2\gamma \left[\frac{1}{a} - \frac{1}{\rho} \right] \right) \quad (2.4)$$

$$\dot{\epsilon}_{PS,L} = D_L \frac{4\rho\Omega}{k_B T} \frac{1}{a^2 R} \left(\frac{3PR^2}{2a^2} + 2\gamma \left[\frac{1}{a} - \frac{1}{\rho} \right] \right) \quad (2.5)$$

These equations are a simplification with the assumption that every atom moves in a way that leads to densification. Other factors are included, such as the volume of an atom (Ω), temperature (T), Boltzmann constant (k_B), diffusion coefficient (D_{GB} or D_L), and, in the case of grain boundary densification, Burgers vector (b), which is a representation of atomic displacement as a dislocation moves along the slip plane [68]. Due to the positive linear nature of the combination of capillary stress and stress from external pressure, the application of an external pressure will always increase the densification rate.

The addition of pressure in the sintering process greatly increases the contact stress, thus enhancing powder densification at a lower sintering temperature than without external pressure [62], [69]. Pressure can also accelerate the sintering process by forming dislocations, especially at particle contact points. Sintering techniques that utilize the application of external pressure alongside an increase in temperature are known as pressure-assisted sintering techniques. A variety of pressure-assisted sintering techniques exist, which are classified by the ways that pressure is applied to a sample during sintering.

Hot Pressing

In hot pressing, the external pressure is applied uniaxially to the green compact as the temperature is increased. For the production of hot-deformed and backwards-extruded Nd-Fe-B magnets, hot pressing is performed at a temperature of 800 °C to achieve semi-finished compacts with full density, which will be deformed in a subsequent processing step [70]. Hot-pressing of Nd-Fe-B often occurs experimentally in a pressure range of 100-200 MPa in vacuum [71]. This differs greatly from the hot-pressing of

ceramics, which is often done at operating temperatures between 1400-2000 °C and lower pressures of 10 to 75 MPa [62]. Hot-pressing Nd-Fe-B at such low temperatures assists in mitigating excess grain growth prior to deformation, though it can occur, especially with significantly higher pressures than what is used for ceramics [72]. While the uniaxial configuration may induce texture in the microstructure of hot-pressed materials, the goal for Nd-Fe-B is to generate an isotropic and dense compact. Ideally texture is not introduced until the hot-deformation stage [71]–[73]. For lower pressures (<50 MPa), graphite tools may be used in hot pressing. For higher pressures, other tool materials such as tungsten carbide or titanium-zirconium-molybdenum (TZM) are used.

Sinter Forging

Sinter forging, or hot forging, is similar in nature to hot-pressing. For metals, a hot preform is transferred to a forging die and forged to the same density of wrought materials by a single stroke. When compared to other powder metallurgical processes and wrought processing, sinter-forging shows a number of advantages, such as eliminating the need for a large amount of machining after forging [74]. A modified version of sinter forging, referred to as electro-sinter-forging, involves the injection of a high-intensity electric pulse through the plungers pressing on the powder [75]. This is a form of electro-discharge-sintering (EDS), which shares similarities FAST/SPS, as it is also a form of electric current assisted sintering.

Hot-Isostatic Pressing

Hot isostatic pressing (HIP) is performed through the application of high temperature (over 1000 °C, in most cases) and high external pressure (typically gas pressure, generally over 98 MPa) across all faces of a component. HIP can be used to directly consolidate a powder or further densify an already sintered or cast part. Porous compacts must be sealed in a gas-impermeable container that is plastic under the applied temperature and pressure [76]. Components with isolated pores may be HIPped with a capsule-free method, but open pores will not be eliminated. For metals, HIP is typically used to remove the remaining pores from a sintered metal body, as HIP is considered a very effective means of eliminating defects from metals [77].

2.2.2 Liquid Phase Sintering

Liquid phase sintering (LPS) is a sintering technique in which certain components of an alloy or composite melt during the sintering processes. The liquid formed wets the remaining solid, which creates a capillary force that pulls the solid grains together. Simultaneously, the high temperature of the sintering process softens the solid grains, which assists in densification. The primary advantage of LPS

is that it results in faster sintering, as the liquid phase allows for faster atomic diffusion than within solid-state sintering through a solution/precipitation process. LPS also assists in controlling grain size and allowing for more efficient particle packing through the dissolution of sharp particle edges. However, the formation of too much liquid can cause shape distortion in a compact [78], [79]. In Nd-Fe-B magnets, a Nd-rich liquid phase begins to form at 655 °C, causing a densification burst during sintering. Maximum density is vital to achieve good magnetic performance, which makes LPS a key step in the sintering of Nd-Fe-B [80]. Excess oxygen within Nd-Fe-B inhibits the formation of the liquid Nd-rich phase, which mitigates material transport and in turn slowing grain growth. A small amount of oxygen helps in the control of excess grain growth [81].

Supersolidus Liquid Phase Sintering

Supersolidus liquid phase sintering (SLPS) is similar to liquid phase sintering but occurs with prealloyed powders rather than mixed powders. The sintering temperature is chosen to be between the liquidus and solidus temperatures for the alloy composition. At the sintering temperature, a liquid phase forms within each particle, and the particles individually undergo fragmentation and repacking. This leads to a homogeneous distribution of the liquid. The presence of the liquid phase leads to a rapid sintering rate through capillary forces, which ensure a rapid compaction of the semi-liquid material [79]. Steels, such as X155CrVMo12-1/DIN EN 1.2379/AISI D2 (referred to as D2), are able to fully densify under SLPS, when the steel is in the starting form of a gas atomized powder. However, unconventionally shaped D2 powders, such as that from grinding swarf, were only able to densify to 76% under the same sintering parameters used for the gas atomized powder [82]. Milling the swarf prior to SLPS leads to better compaction during sintering [83].

2.2.3 Field Assisted Sintering Technology/Spark Plasma Sintering (FAST/SPS)

Field assisted sintering technology/spark plasma sintering (FAST/SPS) belongs to the sintering category of ECAS [84]. FAST/SPS is a sintering method that combines the application of heat and pressure with the introduction of electric current as additional sintering parameters. It is categorized as a consolidation method that uses low-voltage, DC electric pulses and is seen as comparable to hot-pressing. In FAST/SPS, powder is placed within a conductive die with punches above and below the powder. The die is then placed between two electrodes, from which the electrical current flows. These electrodes clamp the die setup through the application of hydraulic pressure. Through exposure to the electric current, inter-particle contacts within a conductive powder compact are heated, and the die surrounding the powder is likewise heated by electrical resistance, known as Joule heating. This method significantly increases the heating rate and shortens processing time. Due to the short cycle times and moderate temperatures, FAST/SPS has the potential of maintaining nano- and sub-micrometer structures within a powder after densification [18], [65].

A diagram of a standard FAST/SPS set-up can be seen in Figure 2.3. Here, a graphite die is lined with protective graphite foil before powder is placed inside. Once filled with powder, the graphite die is secured between two coni, also made from graphite, which act as a spacer between the electrodes and punches. The graphite set-up is situated between copper electrodes, which within them contain a cooling system for temperature control. From these electrodes, force is applied via a hydraulic system. Holes are present on the top and on the side of the graphite tool, allowing for temperature measurement by means of either pyrometer or thermocouple. The electrodes are housed in a chamber, which is closed and secured for the entirety of the FAST/SPS cycle. This chamber can be reduced to a light vacuum in the mbar range or filled with an inert gas, such as argon. Besides graphite, other materials can be used as a punch and die, including tungsten carbide (WC), hard metal (WC-Co), and titanium-zirconium-molybdenum (TZM). These are choice materials when the applied uniaxial pressure of a FAST/SPS cycle is planned to exceed 80 MPa. Application of high pressure can allow for the activation of new densification mechanisms such as plastic deformation and grain boundary sliding [18]. The graphite foil, which is used to protect the tools during sintering, can also be replaced by other materials, such as copper, or coated with a protective coating, such as boron nitride (BN). During FAST/SPS sintering, the die is surrounded by a carbon felt to increase insulation. Process parameters and sintering cycles are programmed and monitored with a control unit, with multiple aspects being measured through the cycle, including applied force, movement of the punches, temperature, chamber pressure, and current.

Through the FAST/SPS cycle, thermal effects influence the powder densification. A key advantage of FAST/SPS sintering is its ability to achieve high heating rates. High heating rates favor densification mechanisms with higher activation energy, such as grain boundary diffusion [85]. Simultaneously, coarsening mechanisms are mitigated, as the final sintering temperature is quickly achieved. This ideally allows for increased densification and decreased grain coarsening [18].

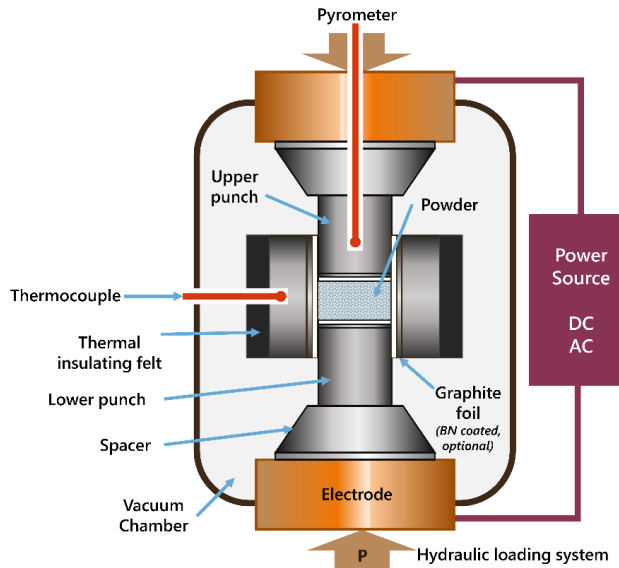


Figure 2.3 –Schematic of an example of a FAST/SPS setup

Spark Plasma Texturing

FAST/SPS has been used as a die-upsetting technique with the goal of generating a desired microstructural texture within a material. This form of FAST/SPS is commonly referred to in literature as spark plasma texturing (SPT), where a self-supporting pellet is placed within a die with a larger diameter than its own. With the application of heat, which is generated through the electrical current of FAST/SPS, and pressure, the pellet deforms. The intention is to induce a platelet morphology of the material's grains through free deformation of the pellet. The grains would ideally grow in a layered brick-like geometry and formation with their c-axes parallel to the applied uniaxial force [20]. This type of deformation is especially attractive in the deformation of Nd-Fe-B magnets, as the texturing would produce the necessary grain anisotropy for optimal magnetic performance, as is described in more detail in Section 2.3.4.

2.2.4 Flash SPS

Flash SPS (FSPS) is a novel sintering method developed by Grasso *et al.* for the densification of ceramic materials [86]. FSPS can be performed with or without a die and involves compressing a sample between two punches while a high-power pulse is forced through it for a specific amount of time. A diagram of a FSPS setup can be seen in Figure 2.4. FSPS can be performed in a conventional FAST/SPS device. The benefit of FSPS is that it results in simultaneous densification and hot deformation with a large height reduction in the chosen compact. FSPS has the capability of tuning the crystallographic

texture of Nd-Fe-B while maintaining grain size on the nanoscale, which is key for high Nd-Fe-B performance [23], [87]. While FSPS is traditionally done without a die to restrain the sample, specially made rings can be utilized to constrict the edges of a sample being deformed.

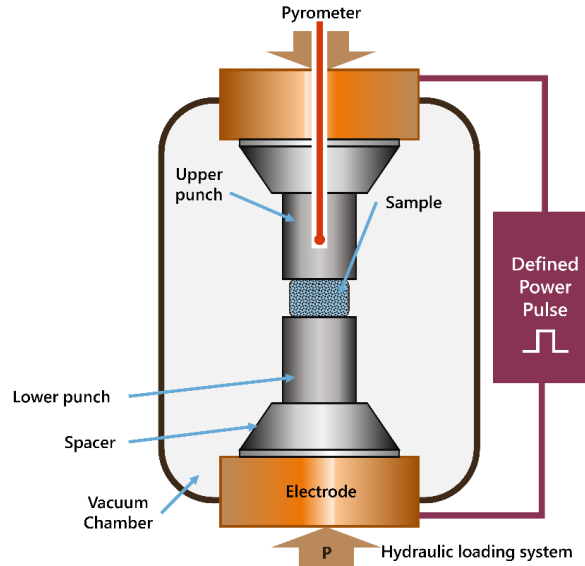


Figure 2.4 - Schematic of an example of a Flash SPS setup

2.3 Introduction to Nd-Fe-B Magnets

2.3.1 Basics of Magnetism

Magnetic forces are generated through the movement of electrically charged particles [88]. The most elementary quantity in magnetism is the magnetic moment, m , which is expressed by the Bohr magneton, μ_B . The generation of this magnetic moment comes from the spin of each of an atom's electrons combined with the orbital motion of the electron around the atom's nucleus [89]. Magnetic force is often thought of and illustrated in terms of fields, with lines of force to indicate the direction of the force at different points relative to the field source. These lines of force loop, originating from and returning to the source of the magnetic field. This leads to a magnetic dipole.

Most elements on the periodic table do not have a magnetic moment, due to the magnetic moments of each individual electrons cancelling out other electrons' moments. Electrons in pairs have spins anti-parallel to one another, and these anti-parallel spins lead to a cancelled magnetic moment. When an atom has an incomplete electron shell, however, not all magnetic moments of the electrons are nullified, leading to magnetic behavior [88].

There are a number of vectors that govern magnetic behavior and relationships. An important tool in determining the magnetic behavior of a material is through exposing it to an external magnetic field. The force of this field, referred to as magnetic field strength, is designated H . The units of H are amperes per meter (A/m).

A magnetic substance contains an internal field strength when exposed to a magnetic field. This is referred to as magnetic flux density, designated B . The unit of B is often in Teslas (T). B and H are related by the following equation:

$$B = \mu H \quad (2.6)$$

The parameter μ is what is known as permeability. This value is related to the susceptibility of the material, through which the H field passes and B is measured [88], [89]. Permeability has dimensions of webers per ampere-meter (Wb/A*m) or henries per meter (H/m). The permeability of a vacuum, μ_0 , is a universal constant with a value of 1.257×10^{-7} H/m. This value is used when determining the magnetization of the solid, M . This is defined by the equation

$$B = \mu_0 H + \mu_0 M \quad (2.7)$$

The term μ_0M represents how magnetic moments within a material will tend to become aligned to the external magnetic field and reinforce it. Often, this relationship is rewritten using polarization, J , in place of μ_0M . Polarization is measured in Teslas (T) and is a representation of the contribution of magnetization to the magnetic induction. Therefore, Equation (2.7) is occasionally rewritten as

$$B = \mu_0H + J \quad (2.8)$$

The magnetization of the solid is related to the applied field through magnetic susceptibility, χ_m . Magnetic susceptibility is unitless and generates the proportional relationship between M and H as follows:

$$M = \chi_mH \quad (2.9)$$

Depending on the magnetic susceptibility of a material, the material can be classified in five different categories. These categories are diamagnetic, paramagnetic, ferromagnetic, antiferromagnetic and ferrimagnetic. An overview of these behaviors is seen in Figure 2.5.

Diamagnetism is a weak, nonpermanent form of magnetism that only occurs under the application of an external field. When there is no field applied, the magnitude of the B field within a diamagnetic solid is less than that of a vacuum [88].

Paramagnetism occurs when a material contains randomly oriented moments and possesses no net magnetization on its own, but the free rotation of dipoles allows them to orient to an external field. Both diamagnetic and paramagnetic materials are considered nonmagnetic as they only exhibit magnetization in an external field.

A ferromagnet has a spontaneous magnetic moment, meaning that, even when the magnet is outside of an applied magnetic field, the material still retains magnetization. The electron spins and magnetic moments are arranged all in the same direction to achieve this [90].

In antiferromagnets, magnetic moments are coupled in an antiparallel alignment, with spin moments of neighboring atoms or ions in exact opposite directions and same magnitudes as one another. This leads to the material having no net magnetic moment.

In ferrimagnets, there is an uneven mix between antiparallel atomic and ionic moments. This leads to a net magnetization, but one that is less strong than a ferromagnet.

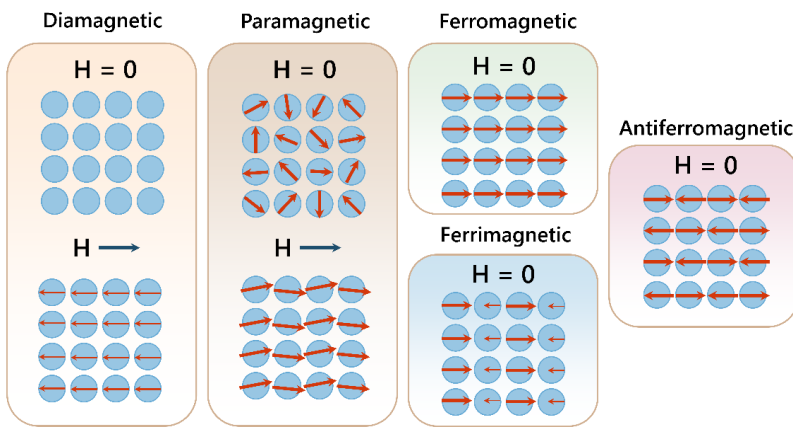


Figure 2.5 – Diagram showing visualizations of the categories of magnetic susceptibility with arrows representing magnetic polarization

2.3.2 Permanent Magnet Materials

Permanent magnets are either ferro- or ferrimagnetic, with Nd-Fe-B falling into the category of ferromagnetic. For ferromagnetic materials, the relative magnetic permeability is more often used to describe the magnetic response. This is represented by

$$\mu_r = \frac{\mu}{\mu_0} = 1 + \chi_m \quad (2.10)$$

This form is more utilized as ferromagnetic materials are often associated with use in electromagnetic devices, where B is present to generate a voltage [91].

Intrinsic Properties

Magnetic behavior is dictated by a number of intrinsic properties, which are characteristic features of the magnetic material, and extrinsic properties. The microstructure of the magnet material determines how the intrinsic properties are expressed within the extrinsic properties. Intrinsic properties exist regardless of the microstructure of the magnet. Intrinsic properties, such as exchange interaction and exchange stiffness, are related to interactions of electrons that are not studied extensively in this work.

Curie Temperature

The Curie temperature, referred to as T_c , is the temperature where, above which, spontaneous magnetization disappears [90]. The Curie temperature represents the point at which thermal energy is high enough to disrupt the regular alignment of magnetic moments. This leads to a transition from a ferromagnetic to a paramagnetic state [92].

Magnetocrystalline anisotropy

Prior to exposure to an external magnetic field, an energy exists within the ferromagnetic crystal that directs the magnetization along a certain axis or multiple axes. This energy is referred to as magnetocrystalline anisotropy energy and generates what is known as the easy axis of magnetization. It is a characterization of crystal-field interaction and spin-orbit coupling, and it specifies the energetically-preferred orientations of the crystal [90], [93], [94]. Strong easy axis anisotropy is required for hard magnetism [94].

Magnetic domains

Within a ferromagnet exists small regions called domains, inside of which the local magnetization is saturated and all magnetic moments are parallel. Different domains do not necessarily exhibit magnetic moments that are parallel to one another, however. When an external magnetic field is applied upon a ferromagnetic specimen, domains that are favorably oriented – that is, parallel or close to parallel to the applied field direction – will grow at the expense of unfavorably oriented domains. After they have grown, the magnetic moment will rotate to become parallel to the applied field, if it was not parallel already [90].

When a magnetic material is in equilibrium, it prefers to adopt the lowest possible magnetostatic energy configuration. This minimization leads to the formation of magnetic domains. A minimum system energy can be achieved by a certain number of domains. A single domain specimen has a high magnetostatic energy. As long as the energy needed to produce a domain wall is smaller than that of maintaining the current magnetostatic energy, 180-degree domain walls will form. However, the

division into further domains is not indefinite – other forces exist inside the magnet to control the number of domains formed within the specimen, depending on its size, shape, and intrinsic properties. Depending on the anisotropy of a material, closure domains may form as well at end surfaces. This causes the magnetic flux to be fully contained within the specimen [91].

As domains can differ in their magnetic orientation, magnetic transitions are formed known as domain walls or Bloch walls. The transition from one magnetic orientation to another does not happen in a discrete manner but rather takes place in a gradual way over many atomic planes [90].

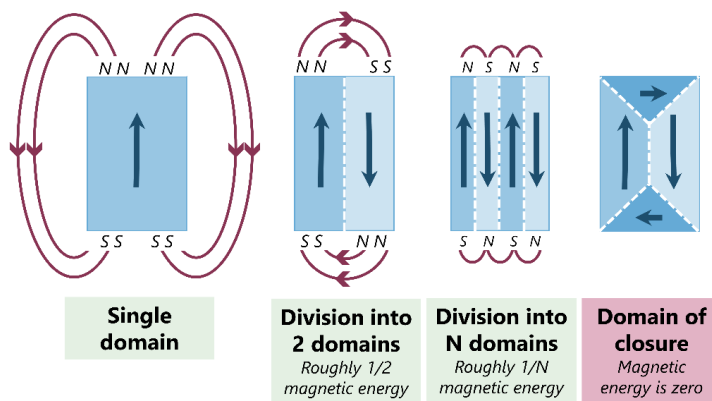


Figure 2.6 - The origin of domains, with explanations on their effect on magnetic energy. Adapted from [90]

The presence of magnetocrystalline anisotropy energy forces the Bloch wall to remain a certain thickness. This leads to what is known as the characteristic length. This length is specific to each magnetic material and is determined by the competition between exchange energy – which is the difference in energy among the relative orientation of electron spins – and the magnetic anisotropy energy [90]. Magnetic anisotropy energy prefers a thinner domain wall, while exchange energy prefers a thicker wall. The characteristic length, once derived from the relationship between these energies, is key to determine the magnetic coupling between grains that constitute a magnet – therefore, it is a vital parameter in dense-packed nanocrystalline materials, such as Nd-Fe-B [93]. Bloch walls are not rigid and can be moved as one domain can increase its volume at the expense of another. This phenomenon is further explained when discussing the extrinsic properties and the hysteretic response of a magnet.

Single domain

Within a magnetic material, it is possible to have grain sizes small enough as to only contain a single domain. This is due to the existence of a critical diameter at which it is not energetically practical for a grain to generate a domain wall [92]. Single domain grains are efficient carriers of magnetization, but they only occur in a narrow grain size range [95], [96].

Extrinsic Properties

Extrinsic parameters are dependent upon the microstructure of the magnet. As a ferromagnet is exposed to an external magnetic field, it will respond through a hysteresis curve that reflect these extrinsic properties.

Hysteresis

Permanent magnets are defined by their magnetic hysteresis – that is, the M (or J) of the material as a function of the H . For a permanent magnet, the relationship between M (or J) and H is a non-linear hysteretic loop that is, ideally, broad and square. From the M - H (or J - H) curve, the relationship between magnetic induction (B) and the applied field can also be calculated. From the calculation of B , the B - H curve can be plotted, which is done to determine both the remanence, B_r , and the maximum energy product, $(BH)_{\max}$, of the material. Though both the B - H and M/J - H curves give specific information about magnetic performance, it is more common to display M - H or J - H curves in literature. From the M - H (or J - H) curve, the suitability of ferromagnetic materials for different applications can be determined, as the hysteresis provides information on the coercivity, H_{cJ} , and saturation magnetization, M_s [97].

The hysteresis curve is a direct visualization of the domain behaviors within the magnetic material. When an external magnetic field is applied, first, the domains that are oriented most parallel to the applied field will grow. The domain walls will move to allow the favorable orientation to expand. Once it has expanded fully, the domains will rotate to be parallel to the applied field. Domain wall motion is irreversible, which causes different curves for both increasing and decreasing external fields [92]. B - H and J - H / M - H hysteresis curves can be seen in Figure 2.7.

Saturation Magnetization

In the first quadrant of the hysteresis curve, M_s , becomes known. This is the point at which the magnetic material can be magnetized no further. If a magnet reaches this point with a small applied field, it is considered magnetically soft. If it reaches this point with a large field, it is considered magnetically hard [92]. Permanent magnets are magnetically hard.

Coercivity

Coercivity, which in this case is intrinsic coercivity, is labeled as H_{cJ} and given in units of kA/m. It is the magnet material's resistance to demagnetization. Coercivity originates from the magnetocrystalline anisotropy field, H_A , which sets an upper limit to what coercive field value can be realized in a particular material [93]. Coercivity is sensitive to the structure of the ferromagnet. H_{cJ} can be determined from the second quadrant of the J - H hysteretic curve, where $M = 0$. This is the reverse field necessary to revert, or "coerce," the material back to zero induction [92].

Remanence

From the B - H hysteretic curve, the magnetic remanence, labeled as B_r , can be determined. This value is given in units of T. B_r is the amount of magnetic flux within the material, even at zero external field applied. In an ideal permanent magnet, a large residual magnetic flux will remain at zero field [93]. B_r is found in the second quadrant of the B - H hysteretic curve and is indicated by the intercept with the x-axis, where $H = 0$.

Energy Product

The figure of merit for permanent magnet materials is what is known as the maximum energy product $(BH)_{\max}$, given in kJ/m³, from which the magnet is graded on its suitability for certain applications. From the B-H hysteretic curve, $(BH)_{\max}$ is represented by the area of the largest rectangle that can be drawn within the curve's second quadrant. $(BH)_{\max}$ is directly influenced by B_r and H_{cJ} , with an increase in both leading to a broader, squarer magnetization loop, and thus a larger $(BH)_{\max}$ [93].

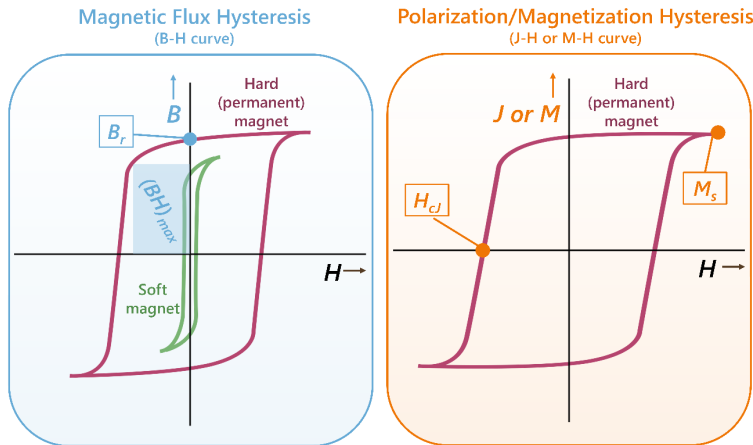


Figure 2.7 – B - H and J - H / M - H curves showing their key points of extrinsic data and the difference between soft and hard magnetic behavior

2.3.3 Nd-Fe-B – Material Properties and Applications

Nd-Fe-B is a permanent magnet material. Its hard magnetic phase, which is responsible for its magnetic performance, is $\text{Nd}_2\text{Fe}_{14}\text{B}$. Its space group is $\text{P}4_2/\text{mn}m$, with a ferromagnetic magnetic moment with all Nd and Fe moments parallel to the c-axis of the tetragonal cell [98]. Figure 2.8 shows the structure of $\text{Nd}_2\text{Fe}_{14}\text{B}$. The space occupied by the Nd atoms can also be occupied by other elements, such as Ce and Sm. However, Nd and Pr are the only two elements that allow $\text{R}_2\text{Fe}_{14}\text{B}$ to achieve high energy products [99]. In Nd-Fe-B, $H_{c,J}$ peaks in grain sizes of around roughly 200 nm in width, as this is the largest grain size that can contain a single domain before transition into multi-domain grains [100]. Nd-Fe-B magnets are used in a wide variety of applications, such as in e-mobility, wind turbines, and consumer electronics [1]–[3], [101]. It has the highest known energy product of all magnetic materials, capable of achieving values of over 470 kJ/m^3 and having a theoretical limit of $\sim 509 \text{ kJ/m}^3$. However, Nd-Fe-B alone is not suitable for high-temperature applications as the magnetic behavior becomes unstable. For higher-temperature applications, a slight substitution of Dy for Nd has been developed. This increases the coercivity of the Nd-Fe-B magnet at the expense of reducing $(BH)_{\text{max}}$ [1], [98]. Doping with other elements also influences the magnetic behavior, especially the coercivity. Ga has been shown to enhance the intrinsic coercivity in die-upset Nd-Fe-B magnets [102]–[104].

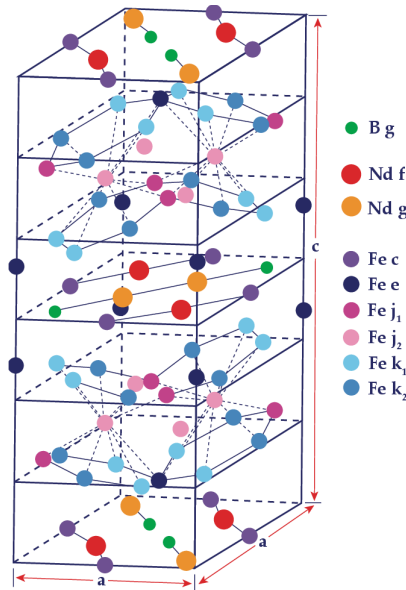


Figure 2.8 – Crystallographic Nd-Fe-B unit cell [98]

2.3.4 Production of Nd-Fe-B Magnets

Nd-Fe-B magnets are produced through three primary production routes: polymer bonding, sintering, and hot deformation. As this work focuses on the recycling of hot-deformed Nd-Fe-B, the other production methods will only be mentioned in brief.

Bonded Nd-Fe-B

Bonded Nd-Fe-B magnets were once made from melt-spun nanocrystalline Nd-Fe-B ribbons that had been crushed and polymer bonded [101]. Modern bonded Nd-Fe-B magnets are made from anisotropic powders generated from the hydrogenation-decomposition-desorption-recombination (HDDR) method [105]–[109]. While it is expected that remanence and energy product of a bonded magnet are linked to the amount of binder used, other influences, such as pore volume and internal magnetic shear loss, lead to lower B_r values [101], [110]. In the case of anisotropic-bonded magnets, a large aligning field (~2.4 T) is necessary in order to fully align all the particles within the matrix for optimal magnetic performance [111].

Sintered Nd-Fe-B

Sintered Nd-Fe-B magnets were invented in the 1980s with production starting in 1985 [112]. They are fully dense and consist primarily of three phases: $\text{Nd}_2\text{Fe}_{14}\text{B}$, $\text{Nd}_{1+\epsilon}\text{Fe}_4\text{B}_4$, and an Nd-rich phase.

Improvement in B_r comes from an increase in $\text{Nd}_2\text{Fe}_{14}\text{B}$ and the avoidance of impurities such as oxygen or nitrogen. To form sintered Nd-Fe-B magnets, material produced by induction furnace is crushed into nearly single-crystal grains of 3-5 μm in diameter. The powder is subsequently aligned in a magnetic field prior to pressing [2]. A variety of shaping techniques have been implemented in order to improve the degree of grain orientation, such as rubber isostatic pressing [113]. Afterwards, the green body is sintered, with densification beginning to occur at temperatures close to 655 °C [81]. Sintered Nd-Fe-B magnets have several advantages, including superior magnetic performance and the ability to be sintered in a variety of shapes and sizes, though without additives, they tend to be quite brittle [114].

Hot-deformed Nd-Fe-B

For a plane magnet of Nd-Fe-B, a starting material is produced using a rapid quenching machine, followed by pulverization to form a flake powder. This starting powder contains nanocrystalline $\text{Nd}_2\text{Fe}_{14}\text{B}$ grains of roughly 10-30 nm in size with random orientation. This powder is cold pressed at room temperature before being hot-pressed at roughly 800 °C. At this point, the hot-pressed magnet is isotropic in nature. When the hot-pressed body is hot-deformed, typically done at 800 °C, thermomechanical alignment of the grains occurs. The c-axis of the grains aligns perpendicular to the pressing direction, and the grains widen laterally, ideally to a width of 200-500 nm and thickness of 20-50 nm [70]. According to Croat [115], this deformation stage is done at a rate of 0.1 mm/s in a period of 30-45 seconds. The temperature is kept high enough to melt the grain boundary phase, as the wetting-phase transition temperature of the grain boundary is roughly 690 °C, with the eutectic phase temperature being 665 °C [116], [117]. In die-upsetting of Nd-Fe-B, a form of hot-deformation, the magnetic behavior is dependent on a variety of process parameters, such as strain rate, working temperature, and extent of deformation. The greatest magnetic alignment has been found to occur if the sample height is reduced by at least a factor of four during the die-upsetting process [102], [104]. A measurement often used to correlate successful deformation is the degree of deformation, or strain, calculated in Equation (2.11), where h_0 is the sample's initial height before deformation and h is the sample's height after deformation [118]. In literature, the degree of deformation is either discussed as strain or as a percentage difference between the initial and final heights of the sample. Ideally the deformation degree would be approximately $\varphi = 1$, or roughly a 50-65% reduction in height. Greater degrees of deformation have not shown to be favorable for magnetic behavior [119].

$$\varphi = \ln \frac{h_0}{h} \quad (2.11)$$

Neodymium magnet grades

Based on the final coercivity and remanence of the Nd-Fe-B magnet, and in tandem, the energy product, the magnet is assigned a grade. This grading scale originates from the Chinese standard GB/T 13560-2017 but is used globally [120], [121]. The nomenclature of the grading scale starts with the letter “N” (for neodymium, sometimes referred to in industry as simply “neo”), followed by a pair of numbers, and possibly a set of letters to indicate the temperature limit of the magnet. Magnet grades of Nxx, with “x” representing the maximum energy product in units of Gauss Oersted (MGoe), have the lowest suggested maximum operating temperature of 80 °C, while magnet grades of NxxVH / NxxAH can operate at a maximum of 230 °C. In this work specifically, the magnet grade requested by the industrial partner, WILO SE, requires a remanence of roughly 1.2-1.3 T and a coercivity of 1300-1400 kA/m. According to tabular data on magnet grades, this refers to the grades listed in Table 2.2. These magnets are listed as NxxH magnets, which have a suggested upper operating temperature of 120 °C. It is important to note that the temperature resistance of a neodymium magnet is due to its additional alloying elements, and the temperature resistance is not influenced by the magnetic performance. As neodymium magnet grades cover a wide range of values, if magnets produced fall outside of the desired range, there is still a possibility to utilize them in applications that correspond a lower respective grade.

Table 2.2 – Performance of neodymium magnets in the industry specified range. Data from [121]

Magnet Grade	B_r (T)	H_{cJ} (kA/m)	$(BH)_{max}$ (kJ/m ³)
N38H	1.22	1355	286
N40H	1.25	1355	302
N42H	1.28	1355	318

Grain growth and microstructure control in hot deformation

A key issue with regards to Nd-Fe-B magnets is their integration of HREEs used to increase coercivity. A potential way of developing Nd-Fe-B magnets with reduced use of HREEs is through the grain boundary diffusion process. HREE oxides have been shown to preferentially diffuse into the grain boundary of sintered Nd-Fe-B, creating a shell around Nd₂Fe₁₄B grains and enhancing the coercivity [122]. Using HREE oxides, rather than HREE metals, avoids the reduction step necessary to obtain and use just the metal. However, manipulating the Nd-Fe-B microstructure without the use of HREEs is more appealing from a cost and resource consumption standpoint. This involves the fine-tuning of the Nd-Fe-B microstructure through grain size reduction and magnetic grain isolation [123]. Magnetic grain isolation is achieved through the formation of an Nd-rich phase grain boundary between Nd₂Fe₁₄B grains, which can be enhanced through grain boundary diffusion [124]. Grain size reduction comes with a different set of challenges, as the final grain size should ideally fit into an ideal aspect ratio, along

with a preferred grain orientation. Starting from the nanocrystalline grains of melt-spun Nd-Fe-B, the grains should grow laterally to roughly 200-500 nm in width with a thickness of 20-50 nm. The grains also need to align with their *c*-axes perpendicular to the pressing direction [70]. This all happens within several tens of seconds, with no clear consensus on the contributing mechanisms. As stated previously, the melting of the Nd-rich grain boundary phase at temperatures above 665 °C assists in the mass diffusion between grains. Higher temperatures likely lead to higher mass diffusion, causing excessive grain growth. This is associated with a mechanism known as solution-precipitation creep, which occurs when portions of the material become liquid and, through varied stresses and diffusional transport, precipitate at other crystal interfaces [118], [125]. This liquid phase acts as a lubricant between the grains, which allows the grains to slide over one another. It is theorized that, in this case, texturing then occurs from a preferred orientation of the crystal that comes forth from the crystallization occurring under stress [126]. A visualization of rotation and grain boundary sliding is given in Figure 2.9.

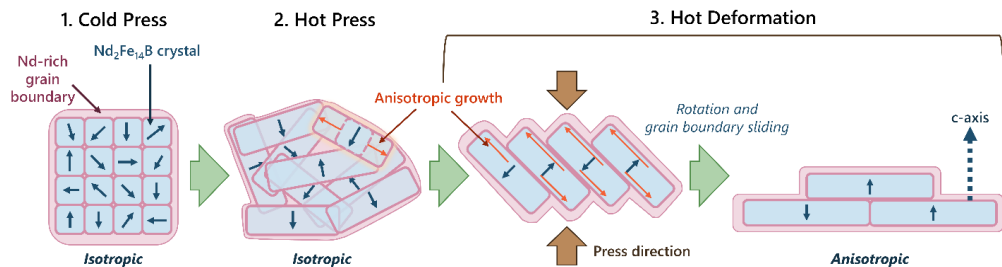


Figure 2.9 - Proposed mechanism for anisotropic grain development in hot-deformed Nd-Fe-B magnets. Adapted from [70]

Growth experiments on single-crystal Nd₂Fe₁₄B have shown that, when under pressure, crystal growth occurs primarily in the *a*-axis of the tetragonal crystal structure, with the *a*-axis being perpendicular to the applied force [127]. It is also proposed that the Nd₂Fe₁₄B grains rotate during hot deformation to have their *c*-axes parallel to the stress axis, which is dictated by diffusion slip. Afterwards, unfavorably oriented grains are consumed by selective grain boundary migration [72]. Deformation is not thought to be caused by dislocations, as dislocations in Nd₂Fe₁₄B grains were observed to be activated by temperatures above 1000 °C, which is considerably above the standard hot deformation temperatures used [128]. In recent work, it has been shown that the *c*-axis of micrometer sized matrix grains will rotate in the direction of compression in temperatures >1000 °C. Experimental data was not collected for magnets deformed closer to 800 °C. Flow stresses were found to be highly dependent on the initial orientation of the grains prior to compression, with more lower angle grain boundaries leading to higher flow stress. The predominant mechanism of grain rotation, which was noted to be either grain boundary

sliding or dislocation movement, was observed to be highly dependent on the initial orientation of the grains. Grains with an orientation closer to 90° than to 45° relative to the compression direction were seen to rotate based on grain boundary sliding. The rate of solution and precipitation is also dependent on the starting grain size, with fine-grained materials experiencing interface-reaction creep and coarse-grained materials experiencing diffusion-controlled creep [129]. With the use of recycled Nd-Fe-B in this work, variations in starting grain size and orientation must be considered when developing deformation parameters. The possibility also exists that regions of the Nd-Fe-B material can achieve temperatures over 1000 °C during Flash SPS, or even during FAST/SPS, as particle interface hotspots can occur.

2.3.5 Review of FAST/SPS Usage in Nd-Fe-B Recycling

The use of field assisted sintering techniques for the recycling of Nd-Fe-B was first implemented via EDS. EDS, like FAST/SPS, is a pressure-assisted sintering technique, but rather than a constant electrical current input, it uses electrical energy discharged from capacitors. This was first developed by Leich *et al.*, leading to sintered magnets that could not achieve the same properties as hot-deformed magnets due to the lack of a texturing step. EDS also led to inhomogeneous densification and grain coarsening, which decreased H_{cJ} [47], [130]. Nevertheless, this work was a great introductory step into the usage of FAST for Nd-Fe-B recycling. Ikram *et al.* have similarly used a combination of FAST/SPS for hot-compacting and hot-deformation of an HDDR Nd-Fe-B powder from scrap magnets. The FAST/SPS hot-deformed magnet with the highest achieved performance had values of $B_r = 1.01$ T and $H_{cJ} = 1060$ kA/m [46]. This work is similar in nature but focuses only on crushed hot-deformed Nd-Fe-B scrap, whereas whether their scrap material is sintered or hot-deformed in nature is unknown. The starting point of the FAST Nd-Fe-B deformation in this work came from developments by Mishra *et al.* and Maccari *et al.*, who developed FAST/SPS pre-sintering parameters and Flash SPS deformation parameters of melt-spun MQU-F that could then be applied to recycled anisotropic Nd-Fe-B powder [23], [87].

2.4 Introduction to PM T15 Steel

2.4.1 PM T15 Applications

PM T15 belongs to the class of steels known as high-speed steels (HSS). HSS have the common ability to maintain high hardness when exposed to elevated temperatures. The term “high-speed” refers to their primary use as cutting tools that generate heat during their usage in high-speed machining. PM T15 is also used for broaches, form tools, milling cutters, taps, and reamers [131]. The “PM” in the name refers to “powder metallurgy,” designating how the steel was processed. When cast, the steel is referred to as T15.

2.4.2 Production and Material Properties

HSS are tool steels that contain the largest amount of alloying elements and consist of a dispersion of M_6C , $M_{23}C_6$, and MC carbides within a martensitic matrix. Within T15, and other HSS, W and Mo are responsible for the formation of the M_6C carbides and Cr for the formation of $M_{23}C_6$. V, along with other strong carbide forming elements, combine with carbon to form MC [132]. The compositional limits of T15, according to AISI, are given in Table 2.3. The amount of carbon within HSS must be balanced with the amount of strong carbide forming elements, as this controls the amount of retained austenite and forgeability. T15 refers to the substantial increase level of vanadium, slight decrease in tungsten, and high carbon, relative to T1 steel – the base of the tungsten group of high-speed steels [131]. The addition of Co adds to the hot strength of the steel. Oil-quenched W-based HSS can achieve hardness values of HRc 65. Because of the high C-content of the steel, it can become decarburized during hot working and form oxide scales at its surface [133]

Table 2.3 – Compositional limits of T15 steel (wt%) [131]

AISI	C	Mn	Si	Cr	Ni	Mo	W	V	Co
T15	1.5-1.6	0.15-0.40	0.15-0.40	3.75-5.00	max 0.3	max 1.00	11.75-13.00	4.50-5.25	4.75-5.25

The determination of the stable phases within steel is often done with phase diagrams, primarily Fe-C diagrams, which indicate what phase or phases are thermodynamically stable. Continuous cooling transformation (CCT) and isothermal transformation (IT), alternatively referred to as time-temperature-transformation (TTT), diagrams are the basis for visualization of the steel heat treatment process. The first step in the heat treatment of T15 is the formation of a ferrite matrix through annealing. Ferrite is a phase of steel with a crystallographic body-centered cubic (bcc) structure, and it is nearly carbon-free. Austenite in contrast has a face-centered cubic (fcc) structure, with a larger unit cell volume than ferrite. Austenite is the solid solution microstructure of steel that forms before the hardening of the steel. Within

steel phase diagrams, steels are designated as austenite when gamma (γ) iron is the solvent and as ferrite when alpha (α) iron is the solvent. Adding alloying elements shifts the critical temperature ranges for phase formation and the eutectoid composition in the Fe-C diagram. Besides ferrite and austenite, another key phase is martensite, a phase with bcc tetragonal structure with lattice parameters related to the steel's carbon content. Martensite is typically hard and brittle, with hardness also varying with respect to the steel's carbon content. Transformation from austenite to martensite is diffusionless and occurs through the lattice shearing of austenite [134]. As T15 contains a carbon content >0.6 mass%, martensite in plate formation forms upon quenching. The amount of retained austenite (RA) increases as C-content increases, and higher RA leads to lower as-quenched hardness. RA does improve steel toughness, however. The high-alloy nature of T15 allows for better hardenability, which means martensite transformation can occur with a slower cooling rate. The cooling rate required to form martensite is dependent on the alloy's composition [135].

A typical heat treatment of tungsten-based HSS is shown in Figure 2.10. In the production of HSS, annealing is necessary to produce a low-hardness microstructure made of carbide spheres dispersed within a ferrite matrix. Tungsten-based HSS, like PM T15, are annealed between 870-900 °C. Because annealing leads to a low hardness, machining is performed afterwards. After machining, austenitizing for hardening is performed to establish the volume fraction of primary carbides and control the chemical composition of the matrix. In HSS, the dissolution of carbides is difficult, and some percentage of carbides is always present in the steel. Austenitizing is performed at temperatures between 1290-1330 °C, and it includes a pre-heating step from 750-850 °C to avoid thermal shock. Austenitizing determines the balance of the carbon content between the austenite, which will later be transformed into martensite, and the undissolved carbides. This balance determines the final hardness and strength properties of the steel. It also establishes the austenitic grain size of the HSS, with properly hardened steels having fine grain sizes. HSS is typically quenched in an oil or salt bath after austenitization. The final heat treatment step is tempering, which is performed between 500-600 °C and can be repeated multiple times. It causes a secondary hardening due to transitory carbides forming in the matrix, including M_2C carbides rich in tungsten. Vacuum heat treatment has become preferential for HSS, as it reduces or avoids the formation of an oxide layer that forms during salt bath quenching. Having an oxide layer affects the hardness of the steel, and the thicker the oxide layer, the lower the hardness [131], [133].

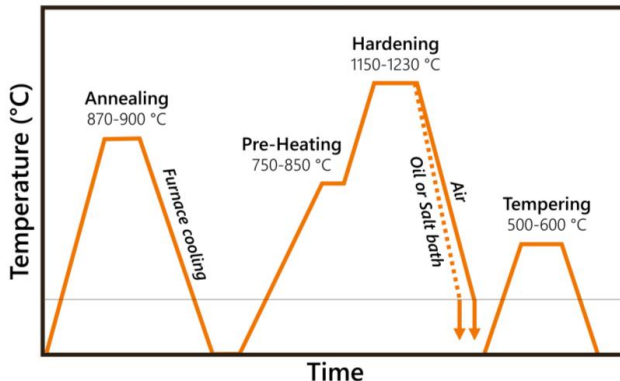


Figure 2.10 - Typical heat treatment cycle of W-based high-speed steels. Adapted from [133]

2.4.3 Steel Swarf and Contaminants

The machining of PM T15 tools into their final shape creates what is known as swarf. When the swarf is on the micrometer scale, it can be extremely thin and curled, interlocking with other steel swarf particles. When steel is ground or polished by grinding or polishing wheels, small particles of the wheels can break off and become interspersed with the steel swarf. The tangled spheres of steel swarf can often trap grinding lubricant and grinding medium within, making it difficult to remove through physical separation processes. The type of grinding wheel used, e.g. Al_2O_3 (corundum), can also influence the size of the steel swarf [13]. The lubricant, grinding medium, and steel swarf, along with water and additives, intermix into what is referred to as grinding sludge. Grinding sludge, when dried, can contain 10-50% oil, 45-80% metal, and 1-5% of other materials, such as grinding wheel particles. These other materials can cause an undesired slag if the swarf were to be remelted, and oil above 3 wt% may burn within the melt [136]. Some grinding medium can react with the steel during reprocessing, such as cubic boron nitride (cBN) or SiC , and can dissolve into the steel matrix if not removed. This will change the alloy composition and properties [137]. While grinding sludge is, at present, primarily landfilled, studies are ongoing on the recovery of different components of grinding sludge, such as the lubricant oil and the valuable metal, for direct recycling [17], [136].

2.4.4 Processing – Casting vs. Powder Metallurgy

As mentioned previously, “PM” in PM T15 refers to powder metallurgy, which is a technique of consolidating metal powders into a densified component. Powder metallurgical techniques help to improve uniformity and reduce segregation within HSS, when compared to casting ingots. Cast T15 requires substantial amounts of hot work at high temperatures to achieve uniformity, as coarse carbides are formed in a matrix of ferrite [138]. The hot work of cast T15 ideally leads to a uniform dispersion

of alloy carbides in an austenitic matrix and eliminates the alignment of carbides in bands [131]. Inhomogeneity in the steel causes distortions during austenitization and anisotropy in strength and toughness after full heat treatment. Control over size and distribution of carbides is necessary for the optimization of mechanical properties and performance. In the use of powder metallurgy for the production of T15, powder is pre-alloyed via gas atomization and then consolidated via techniques such as hot-isostatic pressing. The benefit to the PM of T15 is that each pre-alloyed powder particle behaves as its own “mini-ingot”, which limits the segregation of carbides. After consolidation, such as through HIP, a fine microstructure is achieved, which leads to improvements in strength, toughness, grindability, and tool life, when directly compared to cast T15 [138]. Carbide size in consolidated PM tool steels can range from 0 to 3 μm , while ingot tool steels can have carbide sizes from 0 to 35 μm [139].

2.4.5 Review of FAST/SPS Usage in Metal Swarf Recycling

Almost no literature exists on the direct recycling of steel swarf, especially in regard to HSS. Sintering through traditional techniques, such as hydraulic compaction and furnace sintering, has been attempted with mild steel swarf produced at the laboratory scale. It must be noted that this swarf primarily consisted of a favorable spherical morphology rather than the tendril-like shape typical of HSS grinding swarf [140]. EDS of D2 cold work tool steel swarf has also been performed, with some success in dissolving contaminants like SiC into the metal matrix [141]. A primary influence in the use of FAST/SPS for HSS recycling came from work by the University of Sheffield, who developed a combination of FAST consolidation and subsequent forging, referred to as FAST-forging, to recycle titanium waste [142], [143].

3 Experimental

3.1 Powder Characterization

3.1.1 Particle Size Distribution

Nd-Fe-B powders were analyzed for particle size distribution via laser granulometry using a Horiba LA-950V2 (Horiba Ltd., Japan) laser particle size analyzer with a wavelength of 405 nm. Particle size distribution (PSD) was determined as well as cumulative values of d_{10} , d_{50} , and d_{90} . With this device, light scattering is used to determine particle size. PSD is calculated based on the relationship between the scattering angle of the light and the individual particle sizes of the investigated powder.

The PSD analyzer emits a laser that interacts with the powder particles. When this laser strikes a particle, a fraction of the beam is scattered. The correlation between the variations in the scattered beam intensity and the particle's size can be used to determine the PSD. This is calculated via diffraction theory, and two different theories are typically used for the characterization of ceramic powders – Fraunhofer and Mie theories. Mie theory is a more complex theory applied for nano-sized particles. Fraunhofer theory is utilized for large particles, where the particle size D is larger than the wavelength of the laser source λ . For a monodisperse particle system, in which all of the particles are spherical and larger than the wavelength of the light used, the diffraction pattern is described in Equation (3.1) [144]:

$$I(\theta) = I_0 \int_0^{\infty} \frac{\pi^2 D^4}{16\lambda^2} \left[\frac{2J_1(\frac{\pi D \theta}{\lambda})}{\frac{\pi D \theta}{\lambda}} \right]^2 n(D) dD \quad (3.1)$$

where $I(\theta)$ is the scattered intensity at any angle θ , I_0 is the incident intensity, λ is the wavelength of the incident light, D is the diameter of the particles, and $n(D)$ is the numerical particle size distribution. In Fraunhofer particle size analysis, a sample, typically a liquid or gas suspension of particles, is irradiated with the laser. A portion of the scattered laser pattern is focused onto a lens of known focal length onto a detector. The detector response is recorded, averaged, and numerically inverted to determine the particle size distribution [145]. Due to the particles in this work primarily being larger than nano-sized, only Fraunhofer theory was used for PSD analysis.

The PSD analysis of the PM T15 steel swarf had to be adaptable to the unusual, tendril-like shape of the particles. As the steel swarf was not at all spherical, laser granulometry would not give an accurate overview of the swarf PSD. An alternative technique was utilized that specialized in unconventionally shaped powder analysis called dynamic image analysis (DIA). In this work, PSD of PM T15 was

performed with QicPic (Sympatec GmbH, Germany) using a RODOS/L dry dispersing unit, QICPIC/L sensor, and PAQXOS software. QicPic DIA was performed by project partners at RUB.

DIA uses a high-speed digital camera and automated image analysis instrumentation to measure the PSD of particles in motion [146]. The particles are distributed in a finite depth that is instrument defined, with several approaches in place to avoid images being taken out of focus. DIA systems primarily use wet analysis, where the particles are suspended in a liquid medium for easy control of the particle flow rate. However, Sympatec Inc. developed QicPic, a DIA system that can capture images of dry powder particles in a quick moving airstream [147]. Dry powder is placed on a vibratory chute and accelerated to high speed through the means of a Venturi tube. Then, images of the particles are captured via high-speed digital camera with a synchronized light source. To reduce motion blur, the light source is pulsed with an exposure time of roughly 1 ns [148]. From the images taken, analysis software is able to algorithmically determine the PSD through image contrast.

Besides PSD, DIA is also able to provide data on individual particles that are unusually shaped or sized relative to the rest of the powder. This includes the following:

- Diameter of a circle of equal projection area (EQPC), which is the diameter of a circle that has the same area as the projection area of the particle [149]
- Minimum and maximum Feret diameters, which are the distances between two parallel tangents on opposite sides of the particle. Maximum Feret is the largest distance, while minimum Feret is the smallest distance [150].
- Sphericity, which is a numerical value that represents how close the particle is to being a perfect sphere [151].
- Aspect ratio, which is the ratio of the maximum to minimum Feret diameter [150]

An example measurement of a PM T15 particle analyzed by QicPic is shown in Figure 3.1.

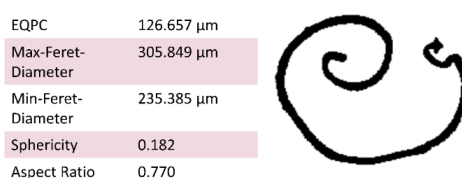


Figure 3.1 - Example QicPic analysis of a single PM T15 particle

For Nd-Fe-B, sieving was occasionally used to determine fractions of different particle sizes or separate out specific particle size fractions. Later experiments with Nd-Fe-B powder involved the sieving out of material smaller than 180 μm . This was done with a sieve shaker, which was set to vibrate the recyclate powder through a 180 μm gap mesh sieve for 10 minutes. Other sieved fractions were separated by ANTS and sent for analysis.

3.1.1 Compositional Analysis

Carrier gas hot extraction (CGHE) was utilized to determine the amounts of elements C, N, and O within both the Nd-Fe-B and PM T15 powders. For the measurement of N and O, CGHE is performed in an inert atmosphere. The sample is melted, and helium is used as the carrier gas to transport gases emitted from the sample, such as CO_2 , to an infrared (IR) detector. N₂ determination is performed by thermal conductivity cells. C and S measurements require CGHE to be performed in a reactive atmosphere. The sample is oxidized through an oxygen gas feed in induction or tube furnaces to form CO_2 and SO_2 , and the amount of each is detected by IR spectroscopy [152]. CGHE in this work was performed using a type CS-800 by Eltra (Germany) for C analysis, while measurement of N and O contents was performed a type TCH 600 by Leco (USA).

For heavier elements, inductively coupled plasma optical emission spectroscopy (ICP-OES) was utilized for the determination of the powder composition using an iCAP 6500 ICP-OES CID Spectrometer (Thermo Fisher Scientific, USA). The inductively coupled plasma is a partially ionized gas, typically Ar, produced in a quartz torch. Samples are then introduced into the center of the plasma as aerosols to be analyzed. Light emitted from the plasma is focused on a sensor to monitor spectral emission from different elements. The detected signal depends on the number of atoms in the plasma and the fraction of the atoms that are excited. The collection of photons in ICP-OES is nonintrusive [153].

With larger samples, X-ray fluorescence analysis (XRF) is performed using a type Niton XL2 air by Thermo Scientific (USA). This device is a hand-held XRF gun. In X-ray fluorescence spectroscopy, materials are exposed to short-wavelength X-rays, which lead to an electron from an inner shell being excited. Electrons with higher energies then drop down to fill this gap, emitting energy in the form of a fluorescent photon. Each element exhibits characteristic X-ray fluorescence, with the intensity of the fluorescence being proportional to the amount of each element in the material. Detectors within the hand-held XRF device sort the energies of the photons in order to determine the type and amount of each element [154].

3.2 Nd-Fe-B Recycling

The Nd-Fe-B recycling portion of this project focused specifically on anisotropic hot-deformed Nd-Fe-B scrap. Currently, a direct recycling route for this type of scrap has not yet been established. Investigations focused on the influence of a variety of parameters, including deformation type (FSPS vs. SPT), deformation temperature, pressure, time, speed, and die constriction. Tests were performed with pristine MQU-F powder, 100 wt% recyclate, or mixtures between recyclate and MQU-F powder. A flow chart showing a general overview of the experiments performed can be seen in Figure 3.2.

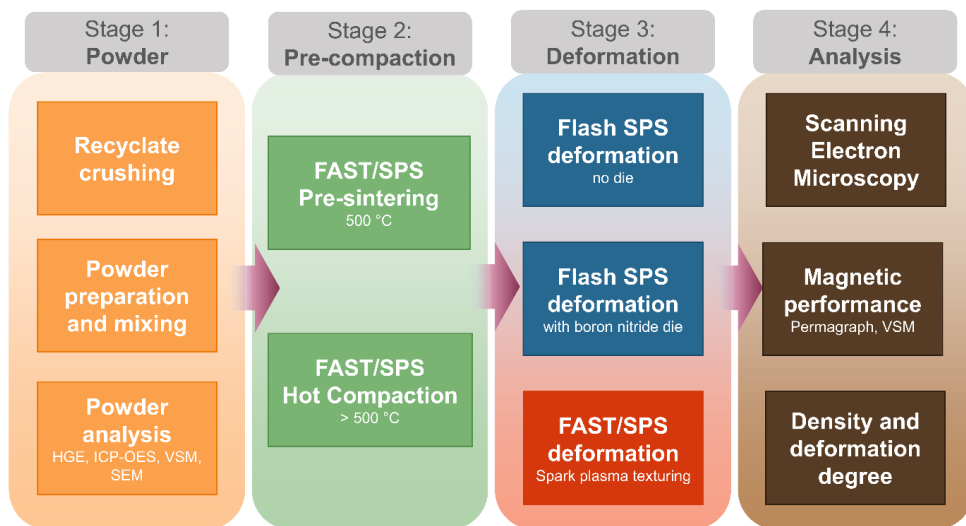


Figure 3.2 – Steps in the processing of hot-deformed Nd-Fe-B recycled scrap in this work

3.2.1 Jaw-Crushing

Prior to use in sintering experiments, out-of-spec hot-deformed Nd-Fe-B magnets provided by WILO SE were jaw-crushed. Crushing was done in a glove box using a type BB 50 benchtop jaw crusher (Retsch GmbH, Haan, Germany) by project partners at ANTS. The resulting powder was sieved to varied particle size ranges to be used together or separately. The volume of oxygen in the glove box was controlled via the pumping in of nitrogen throughout the crushing process. In earlier powder batches, due to imperfect sealing, a small amount of oxygen entered the chamber from the air resulting in a residual oxygen content of 3 vol.%. Better sealing in later crushing experiments led to a clearly reduced oxygen content of 0.3 vol% within the glove box. In jaw crushing, material is fed into a feed hopper and then falls in between two breaking jaws set apart at a chosen distance, known as the gap

width. One jaw is fixed, while one moves at a set speed input by the user. The material is crushed repeatedly by the jaws until it passes downwards to the collection chamber at the bottom of the device.

3.2.2 Powder Designation and Mixing

The body of powders used for this work included not only jaw crushed recyclate from ANTS RWTH Aachen, but also commercial material known as MQU-F, Batch #55557 (Magnequench International LLC, China). MQU-F is a melt-spun isotropic Nd-Fe-B powder, formed by the casting of alloy onto a rapidly rotating metallic wheel to generate a nanosized microstructure of grains roughly 50 nm in size. This powder, and powders of similar kinds, have previously been used as the starting material for demonstrating the capabilities of alternative Nd-Fe-B sintering technologies like FAST/SPS, FSPS, and EDS [23], [47], [87], [130], [155]. Use of this material in the same FAST/SPS and FSPS experiments as the recyclate allows for the direct comparison of microstructural and magnetic differences between isotropic commercial powder and anisotropic recycled powder after processing. This powder was also used in mixes with recyclate powder.

Another Nd-Fe-B recyclate powder, also made from out-of-spec WILO SE magnets, was utilized in experiments. This powder was provided by Less Common Metals (LCM Batch J9348/FP33302 delivered by WILO SE). The crushing conditions for this magnetic material were not stated. This powder is considered to be reflective of a large-scale industrial Nd-Fe-B crushing process. The powder was labeled to be beneath 200 μm by LCM, and this was confirmed by both sieve analysis and PSD measurement.

All unmixed powders, including jaw-crushed batches provided by ANTS, are listed in Table 2.1, along with information about their particle size and origin.

Table 3.1 - Overview of unmixed Nd-Fe-B powders used in this work, with different particle sizes achieved by sieving

Powder	Origin	Abbreviation	Particle Size (μm)
MQU-F Batch 55557	Melt-spun commercial powder from Magnequench	MQU-F	<400
LCM Batch J9348	WILO out-of-spec magnets, crushed by Less Common Metals	LCM1	<200
LCM Batch J9348, sieved	WILO out-of-spec magnets, crushed by Less Common Metals. <180 μm sieved out	LCM2	180-200
RC1	WILO out-of-spec magnets, crushed by ANTS	RC1	<200

RC2	WILO out-of-spec magnets, crushed by ANTS	RC2	200-125
RC3	WILO out-of-spec magnets, crushed by ANTS	RC3	500-1000
MRV1	WILO out-of-spec magnets, crushed by ANTS	MRV1	180-500
MRV2	WILO out-of-spec magnets, crushed by ANTS	MRV2	500-1000

Powder mixes of commercial MQU-F and recyclate material were generated in batches of 5, 10, 15, 20, and 50 wt% of recycled material. These powder batches were made specifically for the experimental work described in Section 3.2.4. Dry mixing was performed in a tumble mixer for 10 minutes at 42 RPM. Sample codes and general data about these mixes are listed in Table 3.2.

Table 3.2 - Overview of mixed commercial and recyclate Nd-Fe-B powders used in this work

Powder Code	Commercial material	Scrap material	Particle size range, recyclate (μm)	wt% of recyclate
MQU-F	MQU-F	none	N/A	0
LCM1-9505	MQU-F	LCM1	<200	5
LCM1-9010	MQU-F	LCM1	<200	10
LCM1-8515	MQU-F	LCM1	<200	15
LCM1-8020	MQU-F	LCM1	<200	20
LCM1-5050	MQU-F	LCM1	<200	50
LCM1-0100	MQU-F	LCM1	<200	100
RC1-9505	MQU-F	RC1	<200	5
RC1-9010	MQU-F	RC1	<200	10
RC1-8515	MQU-F	RC1	<200	15
RC1-8020	MQU-F	RC1	<200	20
RC1-5050	MQU-F	RC1	<200	50
RC1-0100	MQU-F	RC1	<200	100

RC2-9505	MQU-F	RC2	125-200	5
RC2-9010	MQU-F	RC2	125-200	10
RC2-8515	MQU-F	RC2	125-200	15
RC2-8020	MQU-F	RC2	125-200	20
RC2-5050	MQU-F	RC2	125-200	50
RC2-0100	MQU-F	RC2	125-200	100
RC3-9505	MQU-F	RC3	500-1000	5
RC3-9010	MQU-F	RC3	500-1000	10
RC3-8515	MQU-F	RC3	500-1000	15
RC3-8020	MQU-F	RC3	500-1000	20
RC3-5050	MQU-F	RC3	500-1000	50
RC3-0100	MQU-F	RC3	500-1000	100

3.2.3 FAST/SPS Pre-Sintering and Hot Compaction

All samples made with Nd-Fe-B powder, regardless of their secondary deformation step, began with a pre-sintering step or hot compaction step. This step helped to generate a pellet that could resist an applied force during deformation and maintain electrical contact to the upper and lower punches, which was especially vital for FSPS processing. In the early stages of this work, 15 g of magnet powder was pre-compacted into a graphite die (SGL Carbon, SIGRAFINE R7710) with an inner diameter of 20 mm. For experiments requiring larger deformed samples, 30 g of Nd-Fe-B powder was used while keeping the tool diameter constant. For tool preservation and improvement of sample contact, a graphite foil with thickness 0.38 mm (SGL Carbon, SIGRAFLEX) was inserted. For the 30 g samples, to accommodate for the extra height, one graphite punch was swapped for a specialized graphite punch of half the height. FAST/SPS was performed in an HP-D5 device (FCT Systeme GmbH, Rauenstein, Germany), and all experiments were performed under vacuum. The pellets were heated to maximum temperatures of 500, 600, 700, or 725 °C with a heating rate of 100 K min⁻¹. Temperature measurements were performed via thermocouple. A constant pressure of 50 MPa (16 kN) was applied throughout the procedure. The FCT HP-D5 device and a diagram of the experimental set-up can be seen in Figure 3.3.

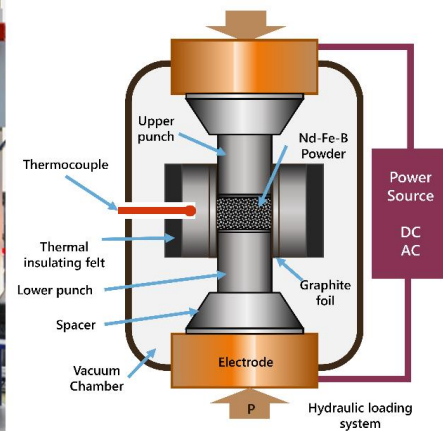


Figure 3.3 – FCT HP-D5 FAST/SPS device and diagram of set-up for pre-sintering of Nd-Fe-B powder

Different dwell times were used in the 500 °C pre-sintering of the pellets. In the first experiments, the dwell time at maximum temperature was 30 seconds. Later experiments extended this dwell period to 120 seconds. This was in accordance with findings by Maccari et al. [87] that stated that an extended dwell time in the pre-sintering stage led to benefits in microstructural development via inhibiting grain growth during the FSPS stage. Samples labeled as sintered with set “PRE1” were held for 30 seconds, while samples sintered with “PRE2” were held for 120 seconds. “PRE3” involved 30 g samples held for 120 seconds.

Hot compaction was also explored as a pre-forming step, in order to generate denser forms that could withstand a greater applied force. In this work, hot compaction is differentiated from pre-sintering through having a maximum temperature above 500 °C with the intention of total or near densification. All hot compaction cycles had a dwell time of 60 seconds to mitigate excessive grain growth. “HC1” was an experimental series utilizing a higher temperature of 725 °C, performed to generate magnets that are totally dense prior to SPT deformation. “HC2” and “HC3” were performed at 600 and 700 °C respectively. These two series were pre-formed with the intention of generating a near-dense particle network capable of withstanding increased SPT pressure. Table 3.3 gives a summary of the pre-sintering and hot compaction parameters for reference later in the work.

Table 3.3 – Table of parameters used for Nd-Fe-B sample pre-sintering and hot compaction

FAST/SPS Pre-sintering/hot compaction

Parameter set name	Powder Mass (g)	Dwell time (sec.)	Temperature (°C)	Force (kN)/Pressure (MPa)	Diameter (mm)	Heating rate (K/min)
PRE1	15	30	500	16/50	20	100
PRE2	15	120	500	16/50	20	100
PRE3	30	120	500	16/50	20	100
HC1	15	60	725	14/45	20	100
HC2	30	60	600	16/50	20	100
HC3	30	60	700	16/50	20	100

3.2.4 Flash SPS Experiments

FSPS was carried out on FAST/SPS pellets made from the powders listed in Table 3.2. The primary goal of this experimental series was to see the influence of particle size and recyclate percentage on magnetic performance of a FSPS deformed magnet.

FSPS experiments were performed in a hybrid FAST/SPS device (H-HP-D 25 SD/FL/MoSi from FCT Systeme GmbH, Rauenstein, Germany). All Flash SPS experiments were done with pre-sintered FAST/SPS pellets, described previously in Section 3.2.3. An image of the FCT H-HP-D 25 device and a diagram of the FSPS set-up can be seen in Figure 3.4

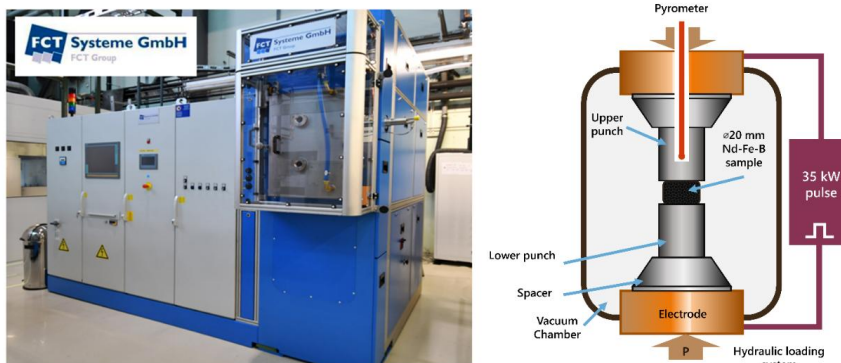


Figure 3.4 – FCT H-HP-D 25 hybrid FAST/SPS device and diagram of FSPS set-up for Nd-Fe-B deformation

The FSPS parameters were chosen based on the favorable results provided by Mishra *et al.* and meant to compare directly to work by Maccari *et al.* [23], [87]. Mishra *et al.* had successfully demonstrated that FSPS could deform recycle powder into a fully dense magnet, and that FSPS deformation on isotropic Nd-Fe-B powder, MQU-F, could lead to well-aligned, anisotropic hot-deformed magnets. It was hypothesized for this work that FSPS could potentially mechanically realign anisotropic Nd-Fe-B powder to the uniaxial pressing direction, leading to a direct recycling use case for hot-deformed Nd-Fe-B scrap.

All FSPS deformation was performed under a vacuum of roughly 0.4 mbar. The pre-sintered pellets were placed between two graphite punches (\varnothing 60 mm) with plane parallel surfaces. A load of 10 kN (roughly 32 MPa for a \varnothing 20 mm sample) was applied to the samples.

Deviation in the two FSPS parameters occurred in the maximum pre-heating temperature. In FSPS1, the samples were then pre-heated to 300 °C via direct Joule heating with a maximum heating power of 10 kW. Temperature measurements were performed via pyrometer. In FSPS2, the preheating temperature was set to 600 °C. This transition was due to findings by Maccari *et al.* showing improvements in the magnetic performance with increased FSPS pre-heating temperature [87]. The samples then dwelled at their respective temperatures for 120 s. After dwell, the samples were subjected to a pulse of continuous direct current at a maximum power of 35 kW for a duration of 30 s. At the end of the power pulse, current was switched off to allow the sample to cool for 10 minutes before the vacuum was released and the chamber opened for sample extraction. Table 3.4 summarizes the parameters used in FSPS deformation experiments across the body of this work. Table 3.5 specifically describes the series of samples involving mixed recycle and commercial powders, naming the series “RC” for future reference.

Table 3.4 – Flash SPS processing parameters used in this work

Flash SPS Processing

Parameter set name	Pre-heat T (°C)	Pre-heat dwell (sec.)	Force (kN)	Flash power pulse (kW)	Flash dwell (sec.)
FSPS1	300	120	10	35	30
FSPS2	600	120	10	35	30

Table 3.5 – Summary of parameters for the FSPS series “RC”

Mixed Recyclate and Commercial Nd-Fe-B FSPS

	Pre-sintering		Flash SPS processing
Series Name	Powders used	Pre-sintering (see Table 3.3)	Parameters (see Table 3.4)
RC	All from Table 3.2	PRE1	FSPS1

3.2.5 Flash SPS in a Boron Nitride Ring

To improve the dimensional accuracy of the FSPS deformed Nd-Fe-B magnets, experimental series were run using a boron nitride (BN) adapter and BN ring nestled inside the adapter. The goal of these experiments was to utilize resistance from a wall to generate smooth edges to the Nd-Fe-B samples and ideally more homogeneous magnetic behavior across the sample. Constriction from a BN ring would hypothetically improve density of the deformed magnet and increase reproducibility, as a standard ring size would consistently produce magnets of the same diameter every FSPS experiment. A photo of the ring and adapter installed in the H-HP-D25 device along with a diagram of the full FSPS and BN ring set-up is shown in Figure 3.5.

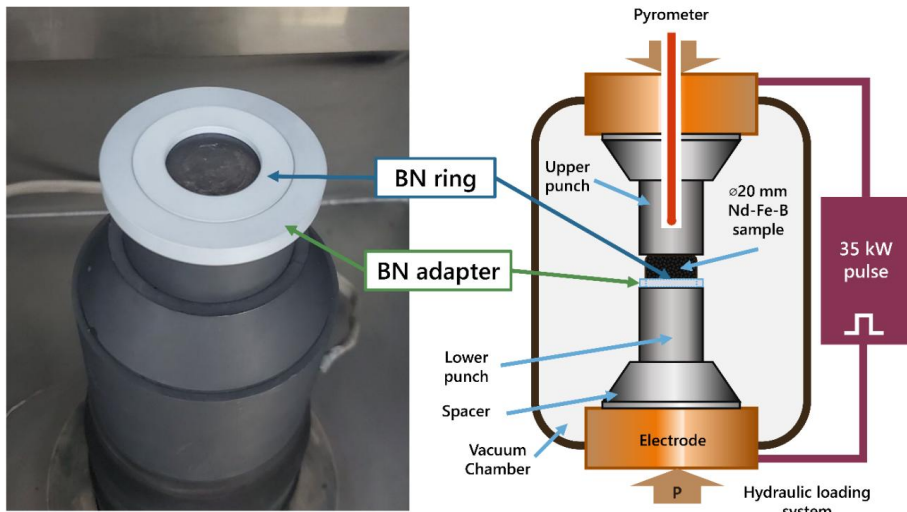


Figure 3.5 – Photo and diagram FSPS set-up including boron nitride ring and adapter

Parameters for FSPS experiments were kept the same as in Section 3.2.4, except that the pre-sintering parameters were changed from PRE1 to PRE2 (see Table 3.3) to follow the findings of Maccari *et al.* [87], which stated that increased dwell time during the pre-sintering stage could mitigate excessive

grain growth in the deformation stage. This aspect was especially important to maintain when anisotropic recyclate powder would be introduced into the experiments, as encouraging further growth in the anisotropic grains would detract from a more optimal magnetic behavior. Powder batches also differed between the FSPS experiments of Section 3.2.4, with an increased focus on generating samples made from 100 wt% scrap material as opposed to mixes of recyclate and commercial MQU-F. Several predominant experimental series were conducted using this setup. Firstly, pre-sintered MQU-F pellets were deformed under the constriction of 25-, 27-, 28-, 29-, and 30-mm diameter BN rings (series name BN1). Next, pre-sintered MQU-F pellets were deformed with larger rings of diameters 31-, 32-, and 33-mm (series name BN2). Finally, two recyclate powder batches, MRV1 and MRV2 (see Table 3.1), were pre-sintered and deformed using the 31-, 32-, and 33-mm diameter rings (series name BN3 and BN4, respectively). The rings and adapter had a height of 2.5 mm, leading to a limit to how much the Nd-Fe-B pellet could deform in the Z-direction. All FSPS experiments performed with a BN ring are listed in Table 3.6.

Table 3.6 – Summary of the FSPS experiments performed with BN ring constriction

BN Ring Flash SPS deformation

Series Name	Powder Used (see Table 3.1)	Pre-Sintering (see Table 3.3)	Flash SPS Processing (see Table 3.4)	BN ring diameters (mm)
BN1	MQU-F	PRE2	FSPS2	25, 26, 27, 28, 29, 30
BN2	MQU-F	PRE2	FSPS2	31, 32, 33
BN3	MRV1	PRE2	FSPS2	31, 32, 33
BN4	MRV2	PRE2	FSPS2	31, 32, 33

3.2.6 Spark Plasma Texturing

In tandem with the FSPS experiments using a BN ring, SPT experiments were performed as a means to generate clean, crack-free edges in the Nd-Fe-B samples. SPT experiments were done using titanium-zirconium-molybdenum alloy (TZM) dies and punches (Plansee, Reutte, Austria), as these could withstand much higher pressures than graphite tools. A diagram of the SPT set-up is shown in Figure 3.6. A pre-sintered or hot-compacted \varnothing 20 mm Nd-Fe-B sample was placed in the center of the TZM die. The TZM die used was either 30 or 40 mm in diameter.

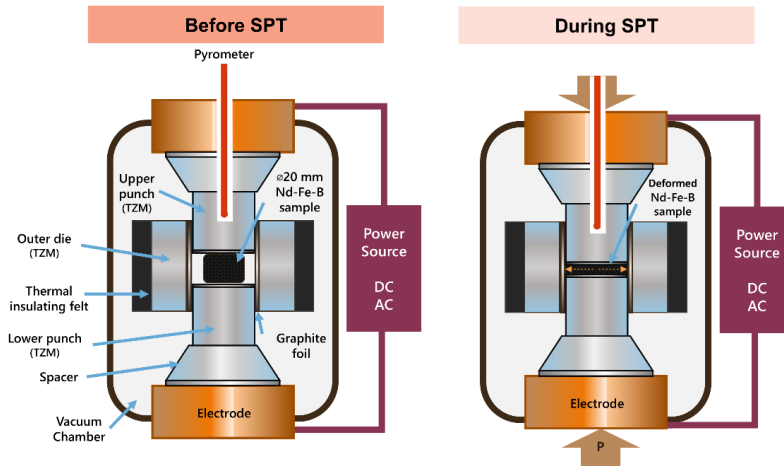


Figure 3.6 – Diagram showing the set-up before SPT and the effect on the sample during SPT

SPT1: SPT of pre-sintered and hot deformed compacts, \varnothing 20 mm to \varnothing 30 mm

In the first SPT experimental series, (referred to as “SPT1”), deformation under varied pressure and temperature was examined. Within the series, \varnothing 20 mm samples pre-sintered at 500 °C (PRE2, see Table 3.3) or hot-compacted at 725 °C (HC1, see Table 3.3) were placed in a \varnothing 30 mm FAST/SPS tool, which was lined with a 0.38 mm thick graphite foil (type SIGRAFLEX, SGL Carbon GmbH, Germany). The respective tool with the sample was mounted in the hybrid FAST/SPS device (H-HP-D25 SD/FL/MoSi, FCT Systeme GmbH, Germany) and the pre-load of 10 kN (= 32 MPa for a \varnothing 20 mm sample) was applied. This SPT cycle had several distinct phases:

1. The applied force was the minimum allowed by the HP-D25 device, 10 kN. Then, temperature was increased at a rate of 100 K/min.
2. When the temperature reached 600 °C, force was increased to 16 kN (50 MPa on a \varnothing 20 mm sample). This was meant to deform the sample from \varnothing 20 mm to \varnothing 30 mm.
3. Temperature continued to increase at a rate of 100 K/min to the desired maximum temperature (700-750 °C).
4. After achieving maximum temperature, the maximum deformation load was applied, which varied between 100 and 300 MPa on a \varnothing 30 mm sample. This load was applied over a 60 second period. Calculations of pressure were based on a \varnothing 30 mm sample rather than a \varnothing 20 mm sample, as the sample was already expected to expand to \varnothing 30 mm in Step 2.

5. After maximum force was reached, force was released. The current running through the tool was switched off, and the tool was allowed to cool.

A specific focus of this experimental series was to investigate if high pressure supports the formation of pronounced microstructural texture, even in a semi-dense compact. These deformations were directly compared to the deformation of dense compacts.

QD: SPT with a deformation speed focus, \varnothing 20 mm to \varnothing 30 mm

Based on suggestions from WILO SE, an experimental series was performed with a focus on the speed of deformation during the SPT process. Stated by Croat *et al.*, an optimal deformation speed was roughly 0.1 mm/s, with the entire deformation cycle occurring under less than 45 seconds [115]. This experimental series is referred to as quick deformation (shortened to “QD”) in this work. The steps of the deformation were as follows:

1. A starting force of 10 kN was applied to the \varnothing 20 mm pre-sintered compact. Temperature was increased to 600 °C at a rate of 100 K/min.
2. Once temperature reached 600 °C, force was increased to 16 kN (50 MPa on \varnothing 20 mm sample) in order to deform it to the edge of the \varnothing 30 mm die.
3. Simultaneous to the application of pressure, temperature continues to increase to 700-800 °C at a rate of 300 K/min. 16 kN is still applied.
4. Once the target temperature of 700-800 °C was achieved, the maximum pressure of 155 MPa was applied over a duration of 10 seconds.
5. After the 10 seconds to reach maximum pressure, pressure is released. The power pulse is switched off and the sample is allowed to cool.

SPT2 and SPT3: Scale-up of SPT, \varnothing 20 mm to \varnothing 40 mm deformation

To develop samples with a higher degree of deformation, a wider die was used to deform \varnothing 20 mm pre-forms. This higher diameter also had the potential to produce samples wide enough to cut a block magnet from, which is as a demonstrator part in a WILO SE water pump. A diagram of how a desired bar magnet is cut from an SPT deformed magnet, along with its desired proportions and dimensional tolerances, is shown in Figure 3.7.

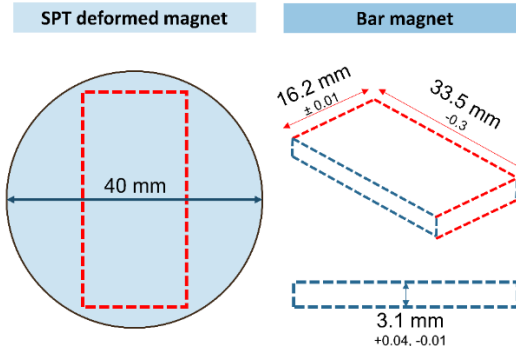


Figure 3.7 – Diagram showing a \varnothing 40 mm SPT deformed magnet and the dimensions of the desired bar magnet to be prepared by grinding and electro discharge machining

Several experimental series were performed in the \varnothing 40 mm TZM for optimization purposes. The first focused on the length of time to apply maximum force and is referred in this work as “SPT2”. The steps of a cycle in this series were as follows:

1. A starting force of 10 kN was applied to the \varnothing 20 mm pre-sintered compact. Temperature was increased to 800 °C at a rate of 100 K/min.
2. Once the target temperature of 800 °C was achieved, the maximum force of 126 kN (100 MPa on \varnothing 40 mm) was applied over a duration of between 30-240 seconds.
3. After maximum pressure is achieved, pressure is released. The power pulse is switched off and the sample is allowed to cool.

These trials were also repeated for larger pre-forms of 30 g. Deformation of larger pre-forms was done to generate samples with a final, post-deformation height of 3.5 mm. This series is referred to as “SPT3”. The purpose of these trials was to investigate the slower application of pressure, in opposition to the QD trials. It was also intended to avoid the high heating rate of 300 K/min of QD by going directly to 800 °C with a heating rate of 100 K/min.

SPT4: SPT of hot-compacted recyclate, \varnothing 20 mm to \varnothing 40 mm deformation

While the increase to a \varnothing 40 mm die improved the lateral expansion of the magnets during deformation, an improvement in height was necessary for the final bar magnet to be cut. Therefore, magnet pre-forms were generated with 30 g of material rather than the standard 15 g used for small-scale experiments. With the increase in height came the increase of collapse during deformation through SPT. With this in

mind, increased densification through higher temperature pre-compaction was explored as a solution, using hot-compaction temperatures of 600 and 700 °C. While this was done at the risk of inducing grain growth, starting from a denser pre-form would ideally lead to an easier and more complete deformation process. These larger scale trials were performed using the pre-compaction parameters labeled as “PRE3”, “HC2”, and “HC3” in Table 3.3.

This deformation series focused on slight adjustments to the “SPT3” trials, such as additional dwell time at maximum pressure and temperature. To mitigate any excess grain growth, as the hot compacts were already exposed to temperatures above 600 °C, it was decided to apply the maximum pressure under the shortest tested time period from the SPT2 series. Maximum pressure was therefore applied over 30 seconds. The full deformation cycle of this new series, “SPT4”, is as follows:

1. A starting force of 10 kN was applied to the Ø 20 mm pre-compact. Temperature was increased to 800 °C at a rate of 100 K/min.
2. Once the target temperature of 800 °C was achieved, the maximum force of 126 kN (100 MPa on Ø 40 mm) was applied over a duration of 30 seconds.
3. Maximum pressure and temperature were subsequently held for an additional 10 seconds.
4. After the dwell period, the power pulse is switched off and the sample is allowed to cool.

Summary of SPT experiments

For a better overview, a summary of the SPT experimental parameters and their code designations can be seen in Table 3.7. Further specifications, designating specific SPT series by their powder type or FAST/SPS compaction, can be seen in Table 3.8.

Table 3.7 – Phases of all SPT experiments with their respective changes in temperature and applied force

Name	Phase 1	Phase 2	Phase 3	Phase 4	Phase 5
SPT1	F: 10 kN T: increased to 600 °C Rate: 100 K/min	@ T = 600° C: F increased to 16 kN	F: 16 kN T: increased to 700-750 °C Rate: 100 K/min	@ T = 700-750° C, P increased to 100-300 MPa (F to 71 to 212 kN). Load applied over 60 sec.	Force released. Cooling.

QD	F: 10 kN T: increased to 600 °C Rate: 100 K/min	@ T = 600° C: F increased to 16 kN	F: 16 kN T: increased to 700-800 °C Rate: 300 K/min	@T = 700-800 C, P increased to 155 MPa (F to 110 kN). Load applied over 10 sec to achieve deformation speed of 0.1 mm/s	Force released. Cooling.
	F: 10 kN T: increased to 800 °C Rate: 100 K/min	@ T = 800 °C: F increased to 126 kN over duration of 30-240 seconds	Force released. Cooling.		
SPT2					
SPT3	F: 10 kN T: increased to 800 °C Rate: 100 K/min	@ T = 800 °C: F increased to 126 kN over duration of 30 seconds	Force released. Cooling.		
SPT4	F: 10 kN T: increased to 800 °C Rate: 100 K/min	@ T = 800 °C: F increased to 126 kN over duration of 30 seconds	Maximum T and P held for 10 seconds	Force released. Cooling.	

Table 3.8 – Powder selection, pre-sintering parameters, and TZM tool diameters for SPT experimental series

Series Name	Powders Used (see Table 3.1)	Pre-Sintering (see Table 3.3)	SPT parameters (see Table 3.7)	TZM Tool diameter (mm)
SPT1-HC1	MQU-F	HC1	SPT1	30
SPT1-PRE2	MQU-F	PRE2	SPT1	30
QD-MQUF	MQU-F	PRE2	QD	30
QD-MRV1	MRV1	PRE2	QD	30

QD-MRV2	MRV2	PRE2	QD	30
SPT2	MRV1	PRE2	SPT2	40
SPT3	MRV1	PRE3	SPT3	40
SPT4-PRE3	LCM2	PRE3	SPT4	40
SPT4-25-PRE3	25 wt% LCM2, 75 wt% MQU-F	PRE3	SPT4	40
SPT4-HC2	LCM2	HC2	SPT4	40
SPT4-25-HC2	25 wt% LCM2, 75 wt% MQU-F	HC2	SPT4	40
SPT4-HC3	LCM2	HC3	SPT4	40
SPT4-25-HC3	25 wt% LCM2, 75 wt% MQU-F	HC3	SPT4	40

3.2.7 Demonstrator Magnets

After completion of the SPT and FSPS experiments, a specific parameter set was chosen based on the best performance of the 100 wt% recycled magnets. While mixing commercial magnet powder almost universally improved magnetic performance, the unique capability of forming 100 wt% recycled magnets using ECAS processes was of specific interest in this project. Generation of these magnets was performed using the parameters listed in Table 3.9. Minor adjustments had to be made to the pre-compaction and SPT steps, which included:

- DEMO magnets were made from 35 g of LCM2, rather than 30 g. This would allow for taller samples after spark plasma texturing, with more flexibility for smoothing the magnet faces after deformation. LCM2 was chosen as the DEMO recyclate due to high availability.
- Pre-compaction “HC2” was performed in a Ø 20 mm TZM die rather than a graphite die. This change was made as the compacts would almost always crack the graphite dies upon extraction.
- Pre-compaction “HC2” was moved from the FCT HP D5 FAST/SPS device to the FCT HP D25 FAST/SPS device. This was due to the TZM punches being too tall for the HP D5.

Table 3.9 - Powder selection, hot-compaction parameters, and TZM tool diameters for demonstrator 100 wt% recycled magnets

<i>Pre-sintering</i>		<i>Spark Plasma Texturing</i>		
Series Name	Powders used	Hot-compaction (see Table 3.3)	Parameters (see Table 3.7)	TZM tool diameter (mm)
DEMO	100% LCM2 (35 g)	HC2 (in HP D25 device)	SPT4	40

After the DEMO sample was hot-deformed via SPT, the initial plan was to manually grind the faces using an ATM Saphir 550 programmable grinding machine and 80 grit SiC paper. However, due to the hardness of Nd-Fe-B, the consumption rate of 80 grit sandpaper became unsustainable. DEMO samples were therefore shipped to RUB for height reduction to 3.1 mm via cup grinder and cutting via electro discharge machining into bars of 33.5 x 16.2 mm at WILO. Four cut DEMO magnets were then tested in a rotor designed for a Stratos MAXO 40/0.5-4 Circulating Pump (WILO SE, Dortmund, Germany). The electromotive force (EMF) was measured at a rotational speed of 4000 RPM. This was compared with a rotor rotating at the same speed containing standard hot-deformed Nd-Fe-B magnets. This measurement was performed by clamping a stator to the pump setup and driving the rotor. A torque measurement shaft was connected to the rotor, and the induced voltage within the stator winding was measured. Measurements from the stator are transmitted to a 3-channel storage oscilloscope.

3.3 PM T15 Steel Swarf Recycling

The aim of the PM T15 steel recycling portion was to establish a potential direct recycling route for swarf contaminated with grinding medium that could not otherwise be removed. FAST/SPS would be used to generate a cutting disk from the PM T15 swarf as a demonstrator part. A general overview of the experimental process with the PM T15 swarf can be seen in Figure 3.8.

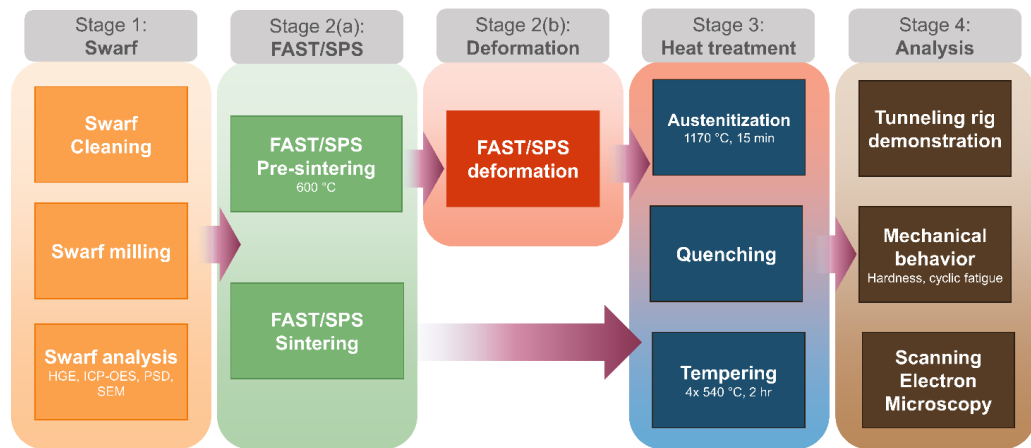


Figure 3.8 - Steps in the processing of PM T15 grinding swarf in this work

3.3.1 Thermodynamic Equilibrium Calculations

In order to accurately predict phase transition and phase volumes during sintering and heat treatment, thermodynamic equilibrium calculations were performed using data from compositional analysis of PM T15 powders. These included equilibrium phase diagrams and phase volume diagrams. Thermodynamic calculations were performed by colleagues at RUB using Thermo-Calc (TC) version 2024a software (Thermocalc software AB, Sweden) [156]. Based on the alloy chemistry, Thermo-Calc is capable of calculating thermophysical properties, phase-based properties, equilibrium and non-equilibrium solidification, homogenization, transformation kinetics, martensite transformations, and precipitation hardening. Calculations were performed using the database TCFE10, considering the chemical compositions obtained via compositional analysis. Some elements, such as B, N, O, and Al, were neglected, as Al₂O₃ particles are considered to be nonreactive. The considered phases were ferrite, austenite, MC, M₆C, M₇C₃, M₂₃C₆, cementite, and liquid. The resulting thermodynamic equilibrium calculations were then utilized to develop sintering parameters, optimize heat treatments, and predict if or when a liquid phase would form during processing.

3.3.2 Cleaning and Milling

Cleaning of the PM T15 swarf from its oil-based lubricant was done with acetone. On a lab scale, batches were repeatedly washed with acetone up to 7 times until CGHE analysis of the powder gave a C-content measurement that was as close as possible to PM T15 norm. Lab-scale oil removal was performed by RUB. For larger batches of powder, a combination of centrifugal oil removal was applied using a modified centrifuge with a sieving basket. The centrifugation was followed by acetone washing in a blender. PM T15 swarf was washed with acetone 6 times in bursts of 1 minute to achieve optimal oil removal. Larger scale oil removal was performed by ANTS.

Some sintering experiments were performed with PM T15 swarf without further processing steps. However, further experimental optimization required the powder to be smaller, more morphologically uniform, and as free from grinding contaminants as possible. Initial milling experiments were run at RUB, with the PM T15 swarf was subjected to ball-milling for 15 minutes at a speed of 350 RPM using WC milling balls of mixed sizes. A scaled-up milling process was developed by ANTS using a disc swing mill (Siebtechnik, Germany), seen in Figure 3.9, that milled the swarf for 180 seconds. A disk swing mill operates by swinging a dish-shaped grinding container with a disk that moves in a circle at high speeds.

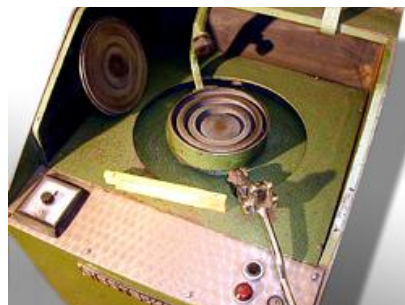


Figure 3.9 – Disk swing mill used by ANTS RWTH Aachen for milling PM T15 swarf

As PM T15 in differing states was used in different experiments, Table 3.10 gives a brief overview of the powder types used and how they are differentiated in sample names.

Table 3.10 – Overview of PM T15 powders used in this work

Abbreviation	Processing Steps	Material	Applied in Sec.
PS	Acetone washing	Cleaned PM T15 swarf	3.3.3
PSM	Centrifugation, acetone washing, milling	Milled PM T15 swarf	3.3.4

3.3.3 FAST/SPS Sintering of PM T15

Initial FAST/SPS trials were performed using PM T15 powder in its original tendril-shaped morphology. The idea behind the direct sintering of this swarf was to minimize the number of steps from swarf creation to swarf re-use as possible. Elimination or avoidance of additional steps also helps to reduce the amount of energy and resources needed for the direct recycling of the swarf. The morphology of the swarf led to a low tap density and difficulties filling the graphite tools for FAST/SPS.

Single-Stage FAST/SPS

5 g of un-milled swarf material was pre-compacted to 400 MPa in a hydraulic press to 20 mm diameter. The pellets were then placed inside a graphite die (SGL Carbon, SIGRAFINE R7710) with an inner diameter of 20 mm. For tool preservation and improvement of sample contact, a graphite foil with thickness 0.38 mm (SGL Carbon, SIGRAFLEX) was inserted. FAST/SPS was performed in an HP-D5 device (FCT Systeme GmbH, Rauenstein, Germany), and all experiments were performed under vacuum. The swarf was heated to a maximum temperature, ranging from 600-1050 °C, with a heating rate of 100 K min⁻¹. Temperature measurements were performed via thermocouple. A constant pressure of 50 MPa (16 kN) was applied throughout the procedure. The set-up for these experiments is similar to that of the Nd-Fe-B pre-sintering in Section 3.2.3, where the FCT HP-D5 device and a diagram of the experimental set-up can be seen in Figure 3.3. An overview of the sintering trials for this portion is listed in Table 3.11

Table 3.11 – Single stage FAST/SPS parameters for PM T15 pellets

FAST/SPS parameters – PM T15

Parameter set name	Powder Mass (g)	Dwell time (sec.)	Temperature (°C)	Force (kN)/Pressure (MPa)	Diameter (mm)	Heating rate (K/min)
PS1	5	30	600-1050	16/50	20	100

FAST/SPS pre-compaction and deformation

To further increase density in the FAST/SPS PM T15 samples, a two-step FAST/SPS process was carried out involving a pre-sintering and a deformation stage, similar to the SPT deformation of Nd-Fe-B described in Section 3.2.6. Unlike SPT, this FAST/SPS deformation was performed only with the goal of densifying the samples, not with inducing a specific texture into the microstructure. This process was also chosen to generate taller samples than from the single-stage FAST/SPS process.

In this experimental series, 17.5 g of PM T15 swarf was gradually added into a 20 mm graphite die lined with graphite foil, and incrementally, the swarf was pressed multiple times with a hand press to 50 MPa. These incremental pressings helped to ensure the amount of powder would fit into the die. Pre-

compaction of the swarf was then performed through a FAST/SPS cycle in the FCT HP-D5 device. Temperature was increased to 600 °C with a heating rate of 100 K/min under a pressure of 50 MPa. The samples dwelled at the maximum temperature for 30 seconds before pressure was released and cooling took place. The samples were removed, cleaned from the graphite foil with a knife, and then transferred to a 30 mm diameter TZM die for deforming. This TZM die was also lined with 0.38 mm graphite foil along the inner diameter and the faces of the punches. Deformation was performed again in the FCT HP-D5 with a maximum temperature of 950 °C and pressures of 50, 100, and 150 MPa on a 20 mm diameter face. Maximum pressure was held for 10 seconds before pressure was released and cooling began. An overview of these parameters can be seen in Table 3.12.

Table 3.12 – Pre-compaction and deformation parameters for two-stage FAST/SPS sintering of PM T15

FAST/SPS pre-compaction parameters – PM T15						
Parameter set name	Powder Mass (g)	Dwell time (sec.)	Temperature (°C)	Force (kN)/ Pressure (MPa)	Diameter (mm)	Heating rate (K/min)
PS2	17.5	30	600	16/50	20	100
FAST/SPS deformation parameters – PM T15						
Parameter set name	Starting Diameter (mm)	Dwell Time (sec.)	Temperature (°C)	Pressure (MPa)	Diameter (mm)	Heating rate (K/min)
PS2-D	20	10	950	50, 100, 150	30	100

After deformation, samples were sent to RUB to be heat treated. The samples were heat treated with the parameters used for standard PM T15, which included the following steps:

- Austenitization at 1220 °C for 20 minutes to partially solve the carbides in the matrix and homogenize the elemental distribution
- Quenching in oil
- Triple tempering in 550 °C for 2 hours each cycle. Material was cooled to room temperature in air between temperings. This is done for the controlled re-precipitation of the carbides.

Vickers hardness measurements were taken of the samples as-deformed, after quenching, and after quenching and tempering. Hardness measurements were performed at RUB. For more details, see Section 3.4.3.

Mitigating reaction with graphite

In the initial experimental series, it also became suspect that the protective graphite foil was reacting with the steel surface during sintering. Therefore, all future graphite foils that were to be in contact with steel swarf were sprayed with boron nitride (BN) spray as a protective coating. The sprays used were EKamold TG (3M Technical Ceramics, Germany) and Dr. Fritsch Boron Nitride Spray (Dr. Fritsch GmbH, Germany). Measurement of carbide concentration at sample surfaces was done via GD-OES by project partners at RUB. An example of how the BN coating appeared is seen in Figure 3.10.

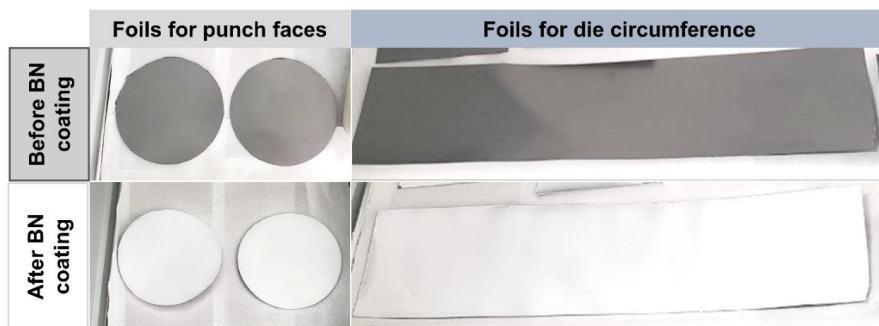


Figure 3.10 – Photos of graphite foils before and after coating with BN

3.3.4 FAST/SPS of Milled PM T15 and Scale-Up

Milled PM T15 swarf was later provided to alleviate issues regarding filling the FAST/SPS dies with the low tap density non-milled swarf. Choosing to mill the swarf also was thought to assist in improving the final density of the sintered samples. As larger samples could not be generated through pre-compaction and deformation, like the smaller scale trials in Section 3.3.3, focus had to be shifted in getting as dense a sample as possible in a single-stage FAST/SPS cycle. Deformation, especially at pressures like 150 MPa, could not be realized with graphite tools and the force limitations of the Dr. Fritsch DSP515 (Dr. Fritsch GmbH, Fellbach, Germany). Alternative parameters were developed on the small-scale FCT HP D5 to eventually transfer to the Dr. Fritsch DSP515.

Small-scale FAST/SPS sintering optimization

To develop a standard FAST/SPS sintering parameter set for the PM T15 recyclate, changes to dwell time, pressure, and temperature were explored, with justifications for each series. Limiting dwell time could possibly limit lip formation and minimize the time spent at maximum temperature for energy savings. Lowering the pressure could potentially mitigate the amount of material that is forced into the gap between the punches and the die, which would reduce the formation of a lip at the sample edge.

Attempts at a higher sintering temperature of 1050 °C could improve sinter density, and reaction with the graphite foil would be minimized with the use of boron nitride spray shielding the steel swarf from direct contact with graphite. This series of optimization experiments is referred to in this work as “PSMOpt”. All the experiments performed are listed in Table 3.13.

Table 3.13 – PSMOpt experiments with variations in dwell time, pressure, and temperature

Lower dwell time <i>Decrease time for lip to form</i>		Decrease Pressure <i>Decrease force pushing material out of punches</i>	Increase Temp, Decreased Pressure <i>Encourage densification without high pressure</i>
Single Stage FAST/SPS		Single Stage FAST/SPS	Single Stage FAST/SPS
Powder wt.	5 g	Powder wt.	5 g
Foil	Graphite + BN Spray	Foil	Graphite + BN Spray
Diameter	20 mm	Diameter	20 mm
Max. Pressure	50 MPa	Max. Pressure	10, 25, 50 MPa
Max. Temperature	950 °C	Max. Temperature	950 °C
Heating Rate	100 K/min	Heating Rate	100 K/min
Dwell time	1 min, 3 min, 5 min	Dwell time	5 min

Dr. Fritsch DSP515 Ø 100 mm and Ø 120 mm sample sintering

With the completion of parameter optimization on the small-scale, larger scale sintering was initiated with the Dr. Fritsch DSP515 device. Due to the limited availability of cleaned and milled PM T15, referred to as PSM, an alternative steel swarf was used to confirm the functionality of the chosen sintering parameters. This steel, AISI D2, was provided by BUW for a previous project [83], and sintering of D2 was used as a proof-of-concept for the later sintering of PSM. Sintering experiments were performed in Ø 100 mm and Ø 120 mm graphite dies, starting with Ø 100 mm to test the parameter validity before moving up to Ø 120 mm. The FAST/SPS device and die set-up are shown in Figure 3.11.

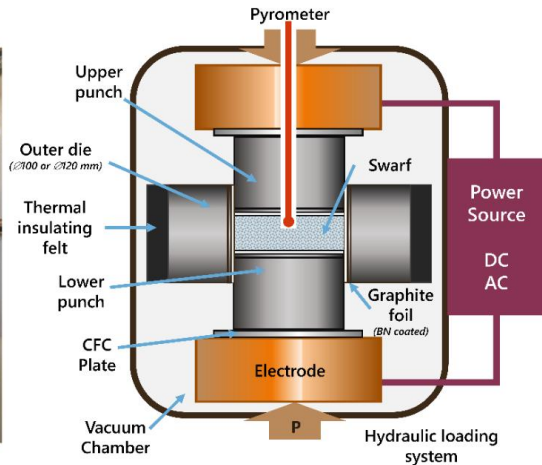


Figure 3.11 – Photo of the Dr. Fritsch DSP515 device and diagram of the set-up of a filled die in the device

The inner diameter of a \varnothing 100 mm graphite die was lined with 0.38 mm thickness graphite foil that had been thoroughly coated with BN spray. Two \varnothing 100 mm graphite sheets were also cut and sprayed with BN spray. These sheets would rest on the \varnothing 100 mm graphite punches with the BN side facing the steel swarf. After one punch and its graphite foil was situated at one opening of the die, 150 g of D2 powder was placed inside. Smoothing of the pile of swarf was performed by a custom-made leveling device. After the powder had been filled into the die, the top graphite foil and top punch was placed on top of the swarf from the opposite die opening. The filled die was then installed into the Dr. Fritsch DSP515 device, and the swarf was pre-pressed with 250 kN. Afterwards, the die was removed from the device, and the punches were independently pulled from the die cavity. Excess swarf that had escaped onto the punch faces was cleaned off before the punches were re-installed. The outer diameter of the graphite die was then secured by an insulating graphite felt, and carbon fiber composite (CFC) plates were placed on both punches. The die set-up was then installed back into the Dr. Fritsch DSP515. Vacuum was pulled, and the FAST/SPS sintering cycle was started. A force of 392 kN was applied, corresponding to 50 MPa of pressure, which was maintained through the experiment. A maximum temperature of 950 °C was reached at a heating rate of 100 K/min. The sample dwelled at maximum temperature and pressure for 5 minutes before cooling. After cooling, the sample was hammered out of the die with a rubber mallet or pressed out with a hydraulic press. Table 3.14 summarizes these experiments.

Table 3.14 - FAST/SPS parameters for the sintering of D2 in a \varnothing 100 mm die

FAST/SPS of D2 - \varnothing 100 mm

Parameter set name	Powder Mass (g)	Dwell time (sec.)	Temperature (°C)	Force (kN)/Pressure (MPa)	Diameter (mm)	Heating rate (K/min)
D2-100	150	300	950	16/50	100	100

Similar parameters were used for the scaling up of diameter from \varnothing 100 mm to \varnothing 120 mm. However, several key changes needed to be implemented for successful scale-up. The tolerance of the inner diameter of the \varnothing 120 mm did not leave enough of a gap for a 0.38 mm graphite foil. Therefore, the inner diameter graphite foil was replaced with a foil of 0.25 mm thickness. Full BN coating of the inner foil caused too much friction upon insertion of the upper and lower punches, making them difficult to remove after pre-pressing. Ethanol was used to wipe away the upper and lower 5 cm of BN coating on the graphite foil to allow for smoother insertion and removal of the punches. Extra punch-face foil was stacked in between the graphite punches and the BN-coated graphite foil. This created a barrier between any loose swarf and the graphite punch faces, mitigating the chance of a short-circuit hot-spot occurring during the FAST/SPS process. To generate a sample of at least 3 mm in height, the mass of swarf was increased from 150 g to 250-275 g. The force applied during sintering also had to be adjusted relative to a \varnothing 120 mm face. As the maximum force the Dr. Fritsch DSP515 is able to apply is 555 kN, the total pressure was chosen to be lowered to 45 MPa, corresponding to 508 kN, as to keep some distance from the machine's maximum. Parameters were tested with the D2 swarf before transitioning to the PM T15 PSM swarf. Dwell times of 1 minute and 5 minutes were implemented to see its effect on densification.

Table 3.15 - FAST/SPS parameters for the sintering of steel swarf in a \varnothing 120 mm die

FAST/SPS of D2 and PM T15 swarf - \varnothing 120 mm

Parameter set name	Powder Mass (g)	Dwell time (sec.)	Temperature (°C)	Force (kN)/Pressure (MPa)	Diameter (mm)	Heating rate (K/min)
D2-120	250	60, 300	950	508/45	120	100
PSM-120	250-275	60, 300	950	508/45	120	100

3.3.5 Heat treatment and Shaping

After FAST/SPS processing, \varnothing 120 mm samples were austenitized at 1170 °C for 10 min in an Ar atmosphere, which was subsequently followed by oil quenching. The austenitization temperature of 1170 °C was modified from the standard PM T15 austenitization temperature of 1220 °C due to the

slightly higher C-content of the swarf. Afterwards, the samples were tempered at 540 °C for 2 hours in a convection furnace. The tempering cycle was repeated four times. To achieve the shape of the final cutting disk, a Ø 80 mm hole had to be cut from the center of the sintered PM T15 disk. A diagram of the final measurements of this disk is seen in Figure 3.12. This would allow for installation into the RUB tunneling rig for testing [157]. Removal of the inner diameter of the disk was achieved by water cutting at RUB.

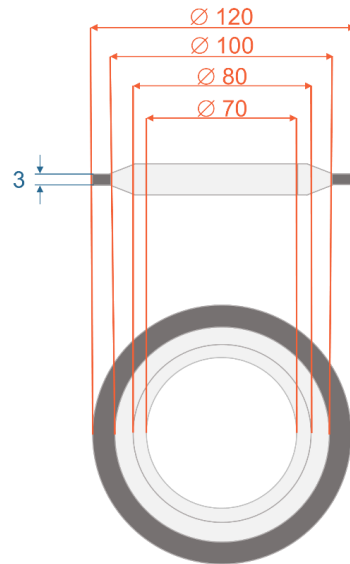


Figure 3.12 – Diagram of a PM T15 cutting disk (dark grey) in its adapter for the mock tunneling device (light grey). All dimensional values are given in mm.

3.3.6 Demonstrator Part

After shaping and heat treatment, disks sintered from PM T15 swarf were installed into a mock-tunneling rig developed by Ruhr-Universitaet Bochum, as seen in Figure 3.13 [157]. A counterpart of cylindrical sandstone from Anröchte, Germany was used as model material representing a tunneling surface. The disks were rotated counter to the cylinder. A static load of 2500 N was applied to the disks with occasional bumps of up to 5000 N during the test run. The tests were run for 20 minutes. After completion of the tests, the weight of the excavated material and the weight loss of the disk were measured. These tests were made in comparison with a pristine PM T15 cutting disk formed from HIP gas-atomized powder. Excavation mass from the sandstone cylinder and the mass loss from the respective disks were compared.

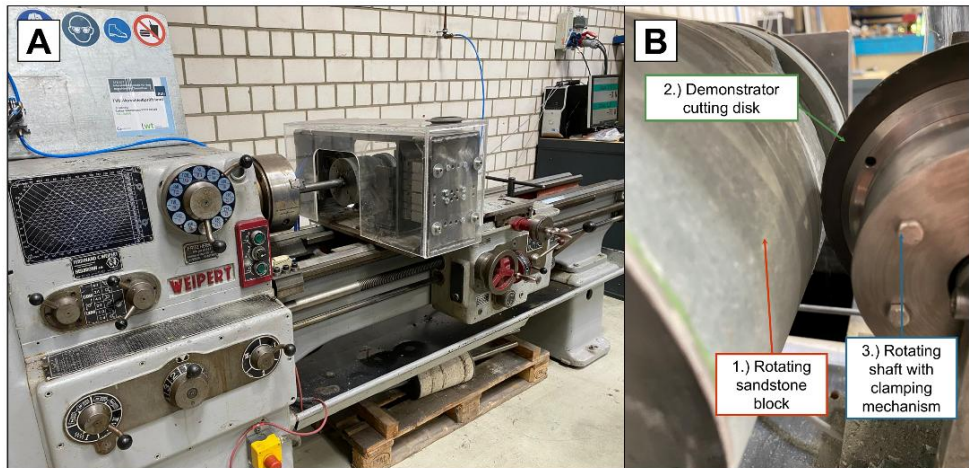


Figure 3.13 – A. Photo of the mock tunneling rig at RUB and B. example set-up of the tunneling experiment with a demonstrator cutting disk

3.4 Sample Characterization Methods and Process Evaluation

3.4.1 Microstructure and Compositional Analysis Post-Sinter

Electron microscopy, primarily scanning electron microscopy (SEM), was used for a variety of purposes in this work. In powder analysis, SEM helped in the characterization of the morphology and shape of both Nd-Fe-B and PM T15 powders. In the case of the Nd-Fe-B powders, images could be captured displaying the isotropic or anisotropic shape of the grains within the powder particles and the presence of alignment. After samples were processed by FAST/SPS, their microstructure gave key insights into the particular performance of the sample. In Nd-Fe-B samples, SEM could show whether FAST/SPS induced texture, anisotropy, or grain growth. In PM T15 samples, SEM displayed carbide formation, shape, and distribution, along with the presence of oxides, visual hints for the dissolution of SiC, and the integration of Al_2O_3 particles into the steel matrix. For all samples, SEM was key for examining the densification of the sample.

In a scanning electron microscope, an incident beam, also known as an electron probe, is accelerated between a cathode and anode and then focused by electron lenses onto a sample. The beam is scanned horizontally across a sample, and, depending on how electrons within the sample interact with the beam, different signals are generated. These signals are collected by various detectors and translated into an image that can be viewed by the user from a computer screen.

The primary SEM detectors used for this work were for secondary-electrons (SE) and back-scattered electrons (BSE). These electrons emitted by the sample after being hit with the incident beam give insight into different characteristics of the sample [158]:

- SE are weakly bound outer shell electrons that are generated within a small depth ($< 2 \text{ nm}$) below the sample surface. The SE signal detected by an SEM is generated from SE that escape from the sample surface into the vacuum, and the image developed from this signal is meant to display topographical contrast.
- BSE are electrons that have been ejected from the solid, scattering beyond a 90-degree angle. They can be distinguished from SE from their kinetic energies. They originate from deeper within the sample than SE, and the image developed from their signal displays “material contrast” due to differences in atomic numbers of near-surface regions of the sample.

Because of the multiple phases that exist within both the Nd-Fe-B and PM T15 samples, BSE was the primary SEM mode used for sample analysis. BSE helped in the identification of the Nd-rich grain boundary phase of Nd-Fe-B, which highlighted the individual grains of $\text{Nd}_2\text{Fe}_{14}\text{B}$. In PM T15, BSE highlighted the different carbides and grinding contaminants in the steel matrix.

Prior to SEM analysis, samples were prepared via metallography. Grinding and polishing were performed on the ATM Saphir 550 programmable grinding machine. Grinding of both PM T15 and Nd-Fe-B samples followed the same procedure, with grinding starting from 240 grit SiC paper followed by 400, 800, and 1200 grade grit paper. After grinding, samples were polished with 6, 3, and 1 μm diamond pastes and cleaned with a water-free 50 nm silica suspension.

A number of SEM devices were used in this work, based on availability or resolution for different microstructures. For Nd-Fe-B powder, PM T15 powder, and some sintered Nd-Fe-B samples, a Zeiss Gemini 450 (Carl Zeiss AG, Germany) using an acceleration voltage of 8 kV and working distance of 8.5 mm was used. A classical Everhardt-Thornley detector was used to image the morphology, and an InLens – SE (secondary electron) detector was used for the microstructures. When samples were sent for analysis by TU Darmstadt, SEM was conducted with a FEG-SEM JEOL JSM-7600 (JEOL, Japan) operated in secondary electron mode with a working distance of 8 mm and an acceleration voltage of 15.0 kV.

For PM T15 samples, SEM analysis was done with a Coxem EM-30N (Kosdaq Company, Korea) at an acceleration voltage of 10 kV or 15 kV and working distance of 15 mm. SEM images of PM T15 provided by RUB were captured via MIRA3 Tescan SEM (Tescan Group, Czech Republic) using an acceleration voltage of 15 kV and a working distance of roughly 15 mm.

A method of determining chemical composition during SEM was through energy dispersive X-ray analysis (EDX). In this method, inner-shell electrons are scattered inelastically by the incident beam, leaving an electron vacancy. This vacancy is short-lived, as an upper shell electron moves to fill this space, which subsequently emits a photon. The energy of this photon depends on the atomic number of the atom involved and the quantum numbers involved in the electron transition. This energy results in an X-ray emission spectrum that is specific to a single element, with each element able to produce at least one characteristic peak. Some elements display several peaks. The generation of a spectrum is performed through a dispersive device that can distinguish photons based on their energy or their wavelength [159]. EDX is performed through photon distinction through their energy. EDX of Nd-Fe-B samples in this work was performed with an Oxford Instruments X-Max 80mm² detector (Oxford Instruments, United Kingdom) at TU Darmstadt.

To determine depth profiles of certain compositions, glow discharge optical emission spectrometry (GD-OES) was performed by project partners at RUB. GD-OES allows for in-depth determination of major and trace elements using a pulsed radio frequency plasma source. It can measure down into a sample more than 150 μm of depth. The plasma emitted performs two tasks: it sputters a set diameter of the sample and excites the sputtered atoms. When the sputtered atoms are excited by the plasma, an optical spectrometer and an interferometer, which measures crater depth, can perform a quantitative elemental analysis with nanometric depth resolution. The spectrometer detects the photons emitted by

the de-excitation of the atoms in the plasma, and the energy of the photons are characteristic of the material. With information from both the spectrometer and the interferometer, an elemental depth profile of a sample can be made [160].

3.4.2 Nd-Fe-B: Magnetic Characterization

For large Nd-Fe-B samples, magnetic characterization was performed with Permagraph C-300 system (MAGNET-PHYSIK Dr. Steingroever GmbH, Köln, Germany) after previous magnetization in a pulsed field. Within a Permagraph device is an electromagnet that magnetizes and demagnetizes the magnet specimen to cycle it through its hysteresis loop. Both the magnetic field strength emitted by the device, H , and the polarization of the sample, J , are measured simultaneously through specialized measuring coils. An integrator processes the signal output of the coils. As the second quadrant of the hysteresis loop, the demagnetization curve, contains most of the vital information for characterizing a magnet, measurement is often stopped after H_{cJ} is reached. Magnetic measurements via Permagraph were performed by WILO SE.

Due to the size and shape of the deformed Nd-Fe-B samples, different portions of the samples were cut for Permagraph measurement. Cuts were done by electrical discharge machining. For the FSPS samples deformed without a die, the center was cut for measurement, as the edges were too cracked and mechanically unstable for measurement. For the FSPS samples deformed with a BN die, both edge and center samples were taken separately to see the influence of the die on the different parts of the sample. Depending on the size and stability of the sample, getting both cuts was not always possible. For the SPT1 samples, a semi-circular cut was made that contained portions from both the edge and the center of the sample. This cut would show a general bulk behavior of the sample. As samples became larger, different cuts became necessary. SPT2 and SPT3 samples had large cuts taken from the sample center. SPT4 samples had smaller cuts taken that included a mix of more central and more edge portions of the sample. The other half of the SPT4 samples were sent back for SEM analysis. Examples of cuts can be seen in Figure 3.14. It is important to keep in mind where these cuts are taken with regards to the magnetic performance. Cuts located more at the edge of the sample often show different performance to those at the sample center. While the hope is to make the magnetic behavior homogeneous across the bulk, this is not always possible.

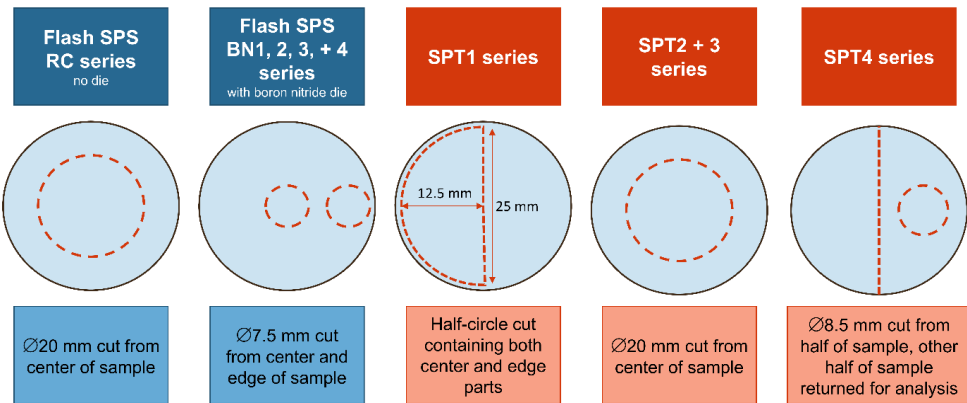


Figure 3.14 – Cuts of Nd-Fe-B samples for Permagraph measurement

For small Nd-Fe-B samples (>1 mm thick) and magnetic powders, magnetic behavior was measured using a vibrating sample magnetometer (VSM) module in a physical property measurement system type VSM-PPMS14 (Quantum Design, USA) at TU Darmstadt. A diagram of a VSM set-up can be seen in Figure 3.15. VSM is a technique used to measure the magnetic moment of a sample. To do so, the sample is vibrated perpendicularly to a magnetizing field. Through the vibration, and using Faraday's law of magnetic induction, information on the entire sample's magnetic moment can be obtained. The sample is placed on the end of a sample holder, typically a quartz rod. This holder is then placed between electromagnet poles oriented horizontal to each other. The sample is situated in an optimal XYZ position based on the magnetic minimum between the two electromagnet poles in the X direction and the maximum in the Y and Z directions. During the measurement process, the sample is subjected to a vibration at a fixed frequency. The change in the magnetic flux due to the vibration causes an AC voltage, which is induced in the pickup coils situated near to the electromagnetic poles. This change in magnetic flux, and thus the corresponding voltage, is proportional to the magnetic moment of the sample. The voltage induced by the magnetic flux is fed through an amplifier in order to obtain the information on the sample's magnetic moment. The measurements collected over time and through a set range of applied magnetic field strength builds a magnetization curve, from which, H_{cI} , B_r , M_s , and $(BH)_{max}$ can be determined or calculated [161].

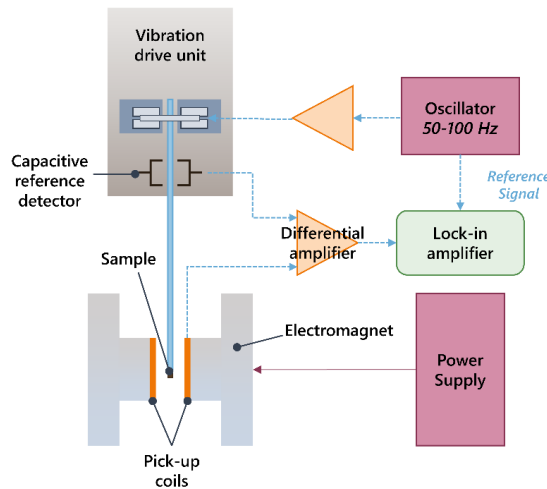


Figure 3.15- Diagram displaying the working components of a VSM along with the signal transmission.
Adapted from [162]

3.4.3 PM T15: Hardness

Vickers hardness tests were performed on all PM T15 samples. Vickers hardness is performed by indenting a sample with a pyramid-shaped indenter with opposite faces angled 136° from one another. Vickers hardness tests operate on a principle known as the law of proportional resistance, meaning that test force and indentation surface are proportional to each other. Hardness is defined with the following relationship in Equation (3.2):

$$HV = \frac{0.102 * F}{A} \quad (3.2)$$

Where F represents test force, and A represents the surface of the remaining indentation, calculated from the mean value, d , of the two diagonals of the indentation, d_1 and d_2 . Figure 3.16 describes the determination of d_1 and d_2 from the indentation. Equation (3.3) shows the calculation of d , while Equation (3.4) shows the calculation of A . Equation (3.5) describes the simplified HV equation in terms of d [163].

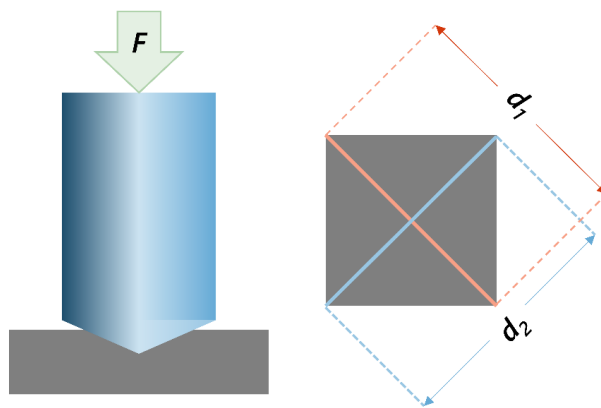


Figure 3.16 – Diagram showing the application of force by the indenter and the resulting diagonals formed in the sample. Adapted from [163]

$$d = \frac{d_1 + d_2}{2} \quad (3.3)$$

$$A = \frac{d^2}{2 * \sin 68^\circ} = \frac{d^2}{1.854} \quad (3.4)$$

$$HV = \frac{0.102 * 1.854 * F}{d^2} = \frac{0.1891 * F}{d^2} \quad (3.5)$$

In all hardness tests of PM T15 samples, HV30 testing was used. This corresponds to an applied force of 30 kgf (294.2 N) per indentation. 5 indentations were made across each sample. A KB30 S hardness testing device (KB-Prüftechnik, Germany) was used for all hardness testing. Hardness testing was performed by RUB.

3.4.4 Other Physical Properties

Density of cylindrical samples was calculated via geometric density, dividing the mass of the sample by its measured volume. Volume was calculated using an average of four height measurements and four diameter measurements taken randomly across the sample. Whenever a sample was non-cylindrical, Archimedes density measurements were taken in water or ethanol. For Nd-Fe-B samples, relative density was calculated in comparison to a standard Nd-Fe-B density of 7.55 g*cm^{-3} . For PM T15 swarf samples, a direct comparison could not accurately be made with pure PM T15, as every sample always

contained an unknown volume of grinding contaminants. Therefore, density measurements of the PM T15 samples are not relative, but actual. Most Nd-Fe-B samples have their density measured by the Archimedes method, due to their uneven faces and edges. These density measurements often correspond to the sample cuts made for Permagraph measurements and not the entire bulk.

For Nd-Fe-B samples, a useful measurement was the percentage change in height before and after the deformation stage. This has been previously described as the degree of deformation, and it is calculated using Equation (2.11). The degree of deformation is only valid when applied to samples that are dense or near-dense prior to deformation. However, it was also used to track changes in height in pre-sintered forms that had lower densities (roughly 70%). In these cases, its validity as a physical indicator for good magnetic performance is questionable, and it is rather a tool to track the effects of different temperature and pressure parameters on the deformation of semi-dense pre-forms.

3.4.5 Energy Consumption Measurements

Energy consumption of the various devices was measured by a PEL 103 power and energy logger (Chauvin Arnoux Metrix, France). The logger is installed onto a device with sensors at the electrical inputs of the chosen device. It conducts a polyphase measurement of electrical current and voltage during the device's on-time and operation cycles. It then outputs a log file with the collected data, along with power and energy consumption calculated. Energy consumption measurements were performed during chosen FAST/SPS cycles on both the H-HP-D25 device and the Dr. Fritsch DSP515 device themselves, along with their cooling systems, which are separate. These measurements could then be used to benchmark energy consumption to other processing methods, such as hot pressing or remelting.

4 Results and Discussion: Nd-Fe-B

4.1 Analysis of the Powders

The state of the recyclate powders gives an insight into why and how hot-deformed magnets behave the way they do. The initial microstructure, morphology, and oxygen content were all significant indicators. This section describes the key pieces of information gleaned from powder analysis. For full analytical breakdown of the powders, see Appendix A.

Influence of particle size and oxygen content on magnetic performance

Oxygen measurements of general crushed Nd-Fe-B powder from hot-deformed magnets showed an increase in oxygen with a decrease in particle size. Recyclate crushed Nd-Fe-B powder was received by ANTS in varying particle size fractions, which were analyzed via CGHE. This general overview is given by the black dashed line in Figure 4.1. Powders that were used for FSPS and FAST/SPS experiments are indicated with colored stars, and the oxygen content of the commercial MQU-F is displayed with a grey dashed line. All powders follow the trend of larger particle size leading to lower oxygen content. Though powders like RC1, RC2, LCM1, and LCM2 all have the same upper limit of particle size, both RC1 and LCM1 contain particles $<100\text{ }\mu\text{m}$. The inclusion of these smaller fractions leads to an increase of oxygen, as the greater surface area of the smaller particles allows for greater oxygen uptake. High oxygen content directly affects the magnetic performance of Nd-Fe-B magnets, as excessive oxidation negatively influences the Nd-rich phase necessary to decouple $\text{Nd}_2\text{Fe}_{14}\text{B}$ grains due to loss of Nd to oxides [81], [164]. As all recyclate powders have oxygen content higher than MQU-F, negative effects to the magnetic performance due to excess oxygen was expected in all magnets made from recycled powder. Though this was not the sole contributor to detriments to magnetic performance, it was a contributor nonetheless.

Even prior to sintering, the influence of oxygen content can be seen in the magnetic behavior of the powders. Figure 4.2A displays PSD data for select Nd-Fe-B recyclate powders, while Figure 4.2B displays the $(BH)_{\max}$ of select powders, measured via VSM, relative to their oxygen content. All powders analyzed are anisotropic, except for MQU-F, which is isotropic. Its isotropic nature explains its low $(BH)_{\max}$, as no texture has been induced in its melt-spun state. All other powders are recyclate powders generated from crushed hot-deformed Nd-Fe-B magnets. Most striking is the difference between the powders RC2 and RC1. These powders are almost identical, except that RC2 has had all powder $<125\text{ }\mu\text{m}$ sieved out, as displayed in Figure 4.2A. The removal of this powder fraction led to an increase in $(BH)_{\max}$ and an oxygen content closer to RC3, which has a powder size in the range of 500-1000 μm . This analysis showed that the inclusion of any powder fraction $<125\text{ }\mu\text{m}$ would likely detract from the final magnetic performance of any magnets produced. RC1 and LCM1 have very similar PSD

profiles, which was done intentionally in order to compare Nd-Fe-B in a crushed in a controlled lab environment to Nd-Fe-B crushed in an industrial environment, respectively.

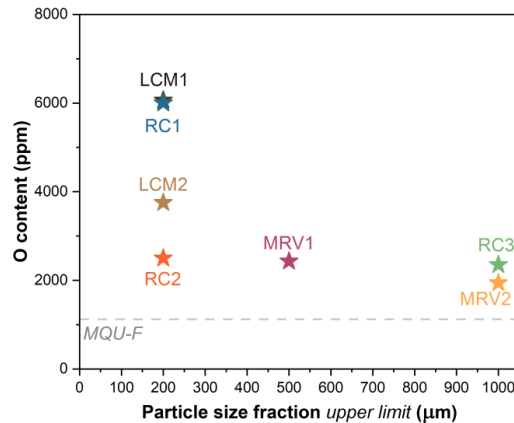


Figure 4.1 – Oxygen content of Nd-Fe-B powders analyzed by CGHE

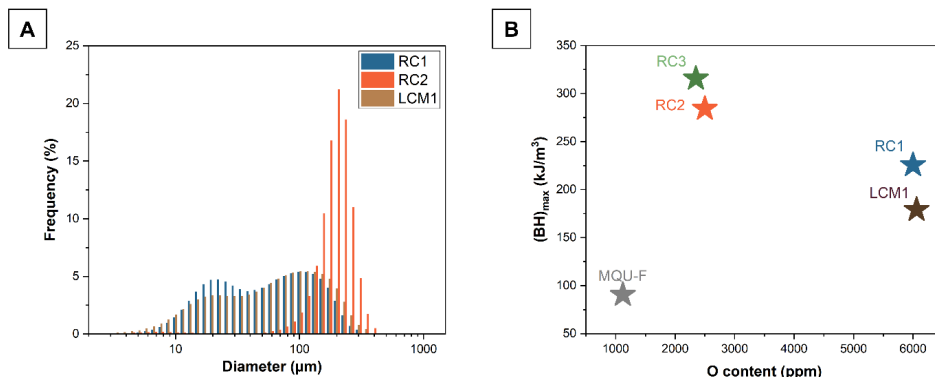


Figure 4.2 – A. PSD of select Nd-Fe-B recyclate powders and B. $(BH)_{\max}$ and oxygen content of select Nd-Fe-B powders

Morphology and microstructure

The shape and microstructure of the powders were expected to have a large influence on the final behavior of the sintered magnets. SEM images of selected powders can be seen in Figure 4.3. MQU-F, the commercial starting powder, is isotropic with grains of <100 nm and is therefore expected to experience grain growth and texturing during the hot-deformation process. All recyclate powders,

however, contain a textured microstructure with anisotropic grains, with thin grains of roughly 200-500 nm in width. A major goal of the use of ECAS in magnet recycling is to maintain this microstructure in the recycled magnets without causing excessive grain growth. Another goal is to apply uniaxial pressure in such a way that the anisotropic grains can rotate and align their c-axes to generate a newly reorganized texture with the c-axes parallel to the pressing direction. This depends partially on the packing of the particles in the pre-form. For instance, the morphology of MQU-F pristine powder is plate-like, with thin sheets of roughly 10 μm thickness. When filled into a die, these sheets can stack upon one another in a dense manner. All of the recyclate powders, though, have greater variations in thicknesses, sharp and blocky angles, and rough surfaces that can generate pores when compressed together in a pre-form. The powder shapes dictate some aspects of densification, and poor densification ultimately leads to a lower B_r .

What is also of note from the SEM analysis is the size variation between the recyclate material. RC3 is unusually large for powder metallurgical processing, with its particle size in the range of 500-1000 μm . This was an intentional choice, as a key advantage of FAST/SPS processing is its ability to use unconventionally sized and shaped powders.

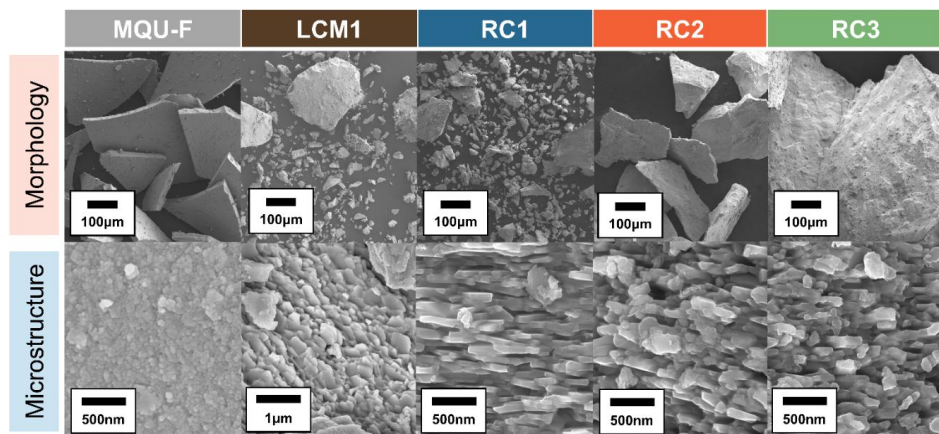


Figure 4.3- Morphology and microstructure of commercial MQU-F and select recyclate powders

4.2 Magnetic Performance and Microstructure of Flash SPS (FSPS) Samples

FSPS samples involves all samples deformed using FSPS, including the samples restricted by a BN die. This section summarizes key magnetic performance and microstructure developments during these experiments. For comprehensive data regarding deformation degree, density, and magnetic performance, see Appendix B. As mentioned in the “Neodymium magnet grades” portion of Section

2.3.4, the goal is to achieve a simultaneous B_r of 1.2-1.3 T and an H_{cJ} of 1300-1400 kA/m in these magnets.

4.2.1 Magnetic Performance of FSPS Samples from Mixed Recyclate and Commercial Powders

The results in this chapter were utilized for a publication in Advanced Energy and Sustainability [165]. Figure 4.5 displays the magnetic performance of the FSPS samples from the RC series (see Table 3.5). In this series, recyclates LCM1, RC1, RC2, and RC3 were mixed with varying amounts of pristine MQU-F powder.

The 100 wt% MQU-F sample, MQU-F-100, had the highest values across all magnetic properties ($H_{cJ} = 1587$ kA m⁻¹, $B_r = 1.13$ T, $(BH)_{max} = 243$ kJ m⁻³). This is close to and in agreement with the results of Mishra *et al.* for the same parameters ($H_{cJ} = 1483$ kA m⁻¹, $B_r = 1.18$ T, $(BH)_{max} = 264$ kJ m⁻³) with likely some variation in density causing the differences in B_r [23]. The sample made from 100 wt% LCM1 ($H_{cJ} = 724$ kA m⁻¹, $B_r = 1.1$ T, $(BH)_{max} = 171$ kJ m⁻³) displays behavior similar to the sample made from Mishra *et al.* with the same Flash SPS parameters ($H_{cJ} = 809$ kA m⁻¹, $B_r = 1.1$ T, $(BH)_{max} = 189$ kJ m⁻³). Similar B_r values are seen across decreasing wt% of LCM1 powder, with a maximum of 1.11 -1.12 T at 5-15 wt% LCM1. H_{cJ} of magnets containing LCM1 hover around 1500 kA m⁻¹ until the amount of LCM1 surpasses 20 wt%. The peak of H_{cJ} ($H_{cJ} = 1549$ kA m⁻¹) occurs at 10 wt% LCM1, while peak $(BH)_{max}$ (231 kJ m⁻³) for the LCM1 mixes is at 15 wt% LCM1. Between 10 and 15 wt% may be the point at which enough recycled material - which has already been deformed and therefore already has grain anisotropy and alignment - contributes positively to the magnetic performance of the sample. From there, H_{cJ} decreases rather linearly with increased amounts of LCM1. This is likely due to contributions from the high oxygen content of LCM1, the already out-of-spec behavior of LCM1, or the contribution of misaligned LCM1 particles that were frozen into place during pre-sintering.

The FSPS sample made from 100 wt% RC1, which is a recyclate powder that was mixed to be similar to LCM1, had a lower B_r than LCM1 at 100 wt% ($B_r = 0.96$ T). Furthermore, it had the lowest H_{cJ} and $(BH)_{max}$ of all 100 wt% recycled samples. Similar to LCM1, H_{cJ} values consistently decreased with increasing wt% of RC1. This could be due to the higher amount of small recyclate particles in RC1 when compared to LCM1, seen in Figure 4.2A. The additional oxygen, or possibly oxidized Nd, could be harming the magnetic performance.

Mixes of RC2, similar to LCM1, maintain consistent B_r values, even when approaching 100 wt % recycled material. 100 wt% RC2 is the only fully recyclate sample to have a B_r above 1.1 T. H_{cJ} values of RC2 mixes surpass 1400 kA m⁻¹, even at 20 wt% RC2, as opposed to RC1, which sees a larger dip in H_{cJ} at 20 wt%. The removal of the fine powder fraction, when comparing RC2 to RC1, clearly has a positive effect on the magnetic performance.

In terms of magnetic performance, samples made from a mix of RC3 outperformed all other samples in B_r , with samples of up to 20 wt% RC3 reaching nearly 1.15 T. However, remanence decreases abruptly beyond 50 wt% RC3, likely due to the drop in density [101]. Much like the samples produced by Mishra *et al.*, the deformed samples after Flash SPS tended to have ragged, cracked edges and a more homogeneous center. This effect was also much more pronounced with the 100 wt% RC3 sample, as can be seen in Figure 4.4. The edges of this sample were mechanically unstable and would crumble to the touch. Likewise, the sample with the lowest density was the sample made from 100 wt% RC3. This is likely due to the fact that this sample consisted entirely of large particles that had already been subjected to hot deformation and were already fully dense, therefore more resistant to a second deformation. The high uniaxial pressure may have also caused breaking in the particles, filling gaps in the pre-form rather than deforming. The particle size range of 500-1000 μm also did not permit for small particles to fill in all of the gaps created by the use of larger particles. Shifting the particle size range to include smaller particles, as those in the 200-500 μm range, may improve the density.

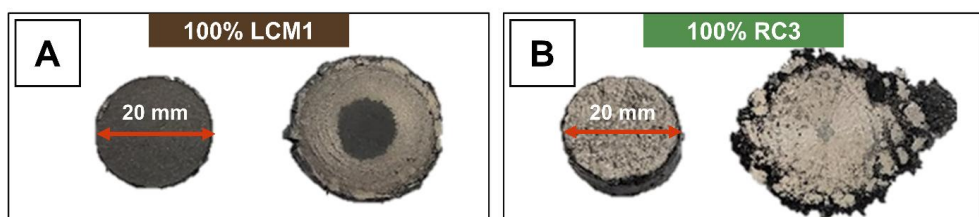


Figure 4.4 – A. Pre-sintered and FSPS deformed pellet from 100% LCM1 and B. Pre-sintered and FSPS deformed pellet from 100% RC3

When comparing the results of all magnetic properties, the highest wt% mix of scrap with the best performance was 50 wt% RC3 ($H_{cJ} = 1247 \text{ kA m}^{-1}$, $B_r = 1.12 \text{ T}$, $(BH)_{max} = 234 \text{ kJ m}^{-3}$). However, the large particle size of the scrap material leads to high brittleness after deformation. This sort of brittleness may not be optimal for net-shaping of recycled magnets. 100 wt% RC2 had the best magnetic performance of all 100 wt% recycled magnets ($H_{cJ} = 776 \text{ kA m}^{-1}$, $B_r = 1.13 \text{ T}$, $(BH)_{max} = 219 \text{ kJ m}^{-3}$), showing viability for the FSPS technique in generating magnets from 100 wt% recycled material. Adjustments were necessary to improve the coercivity and mechanical stability of the sample edges, however.

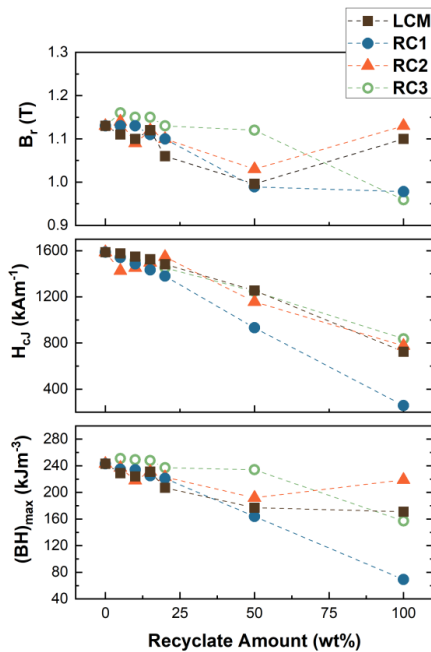


Figure 4.5 – Magnetic performance of FSFS samples made from mixed MQU-F and recyclate Nd-Fe-B powders with varying amounts of recyclate powder

4.2.2 Microstructure of Samples Made from Mixed Recyclate and Commercial Powders

Figure 4.6 shows several SEM images for FAST/SPS pre-sintered and FSFS deformed samples made from 100 wt% commercial and scrap material. In comparison, Figure 4.7 provides SEM images of samples with 15 wt% of recyclates LCM1 and RC3, samples referred to as LCM1-8515 and RC3-8515. Arrows in the upper right corner of each image show the direction of the applied uniaxial force in both the FAST/SPS pre-sintering and Flash SPS deformation stages.

The pre-sintered stage shows a large porosity within the samples, which was initially thought to be a key feature that allows for the direct production of new magnets via 100 wt% scrap material through FSFS deformation. In the industrial scale hot deformation process, samples must be nearly completely densified by hot pressing prior to hot deformation. Because this hot compaction occurs at a higher temperature than the pre-sintering stage used in this work, it was thought that the hot compaction would initiate excessive grain growth in forms made from anisotropic recyclate. However, the low density in the pre-form, could be responsible for Nd-rich phase segregation. This can be seen somewhat in the FSFS deformation image in Figure 4.6C, with the FSFS deformation of RC3 leading to many bright regions of Nd-rich phase in areas where pores used to be. This is likely due to the Nd-rich phase

liquifying during FSPS deformation and being squeezed into gaps left by the low pre-form density due to a combination of deformation and capillary action. In further experiments, Nd-rich phase segregation was associated with negative effects to the magnetic behavior. This may be part of the reason why the $(BH)_{\max}$ of 100% RC3 is lower than that of 100% RC2, despite the fact that the RC3 powder had a higher starting $(BH)_{\max}$ than RC2.

As can be seen in Figure 4.7, in the pre-sintered stage for samples containing any amount of recycled material, the particles of recyclate are clearly distinct from the MQU-F flakes. Recyclate particles are highlighted with green dashes and labeled. MQU-F can be seen wrapping around the abnormal shapes of the recycled particles, with some flakes cracking or breaking from conforming to the shapes of the recycled particles. Excess cracking and wide variations in particle size create more powder particle contact points, and a higher number of contact points is expected to lead to more hot spots during FSPS [23]. The higher heat generation at the contact points may lead to the easier melting of the Nd-rich during the deformation process in these regions. Localized heating at cracks occurs due to the change of direction of the electric current at the tips of the crack, causing heat concentrations at the crack tips [166], [167]. As mentioned before, bright Nd-rich segregations can be seen in the deformed 100 wt% LCM1 and 100 wt% RC3 samples, more frequently than in the 100% MQU-F sample. This could be due to a coarsening of already existing Nd-rich grain boundaries, which formed from the previous deformation of the recyclate particles. When combined with high heat, which is generated from a higher number of cracks and particle interfaces, a segregation of the Nd-rich liquid phase could occur [81], [168]. Formation of an especially thick Nd-rich region is often associated with contaminants, such as oxygen, on the particle surface and Nd surface segregation at interfaces [72]. In an ideal case, the Nd-rich phase would be surrounding the $\text{Nd}_2\text{Fe}_{14}\text{B}$ grains in a thin and dense layer, decreasing the magnetic coupling and improving the coercivity. The combination of localized liquification early in the FSPS process and squeezing of the Nd-rich phase into gaps may be affecting coercivity.

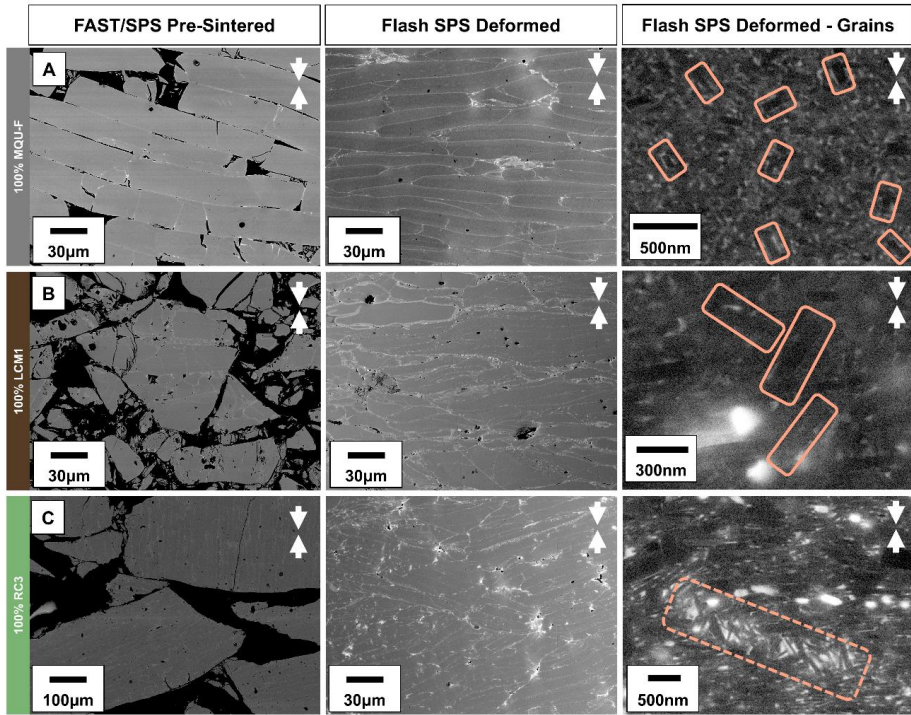


Figure 4.6 – SEM images showing the FAST/SPS pre-sintered morphology, FSPS deformed morphology, and FSPS grains in samples made from A. 100% MQU-F, B. 100% LCM1, and C. 100% RC3. Significantly misaligned grains are highlighted in solid orange, with regions of misalignment highlighted in dashed orange. Contrast has been digitally enhanced for improved clarity.

Coarsening of the nanocrystalline grains is another reason for the drop of H_{cJ} . This effect occurs in all samples during the deformation stage, but the most notable version of this effect occurs at interfaces and within what is suspected to be previously recycled particles. In Figure 4.7, SEM analysis shows the integration of recycled particles into the matrix is relatively homogeneous. Recyclate particles, highlighted in the pre-sintered stage with a green outline, cannot be differentiated easily in the matrix after FSPS deformation anymore.

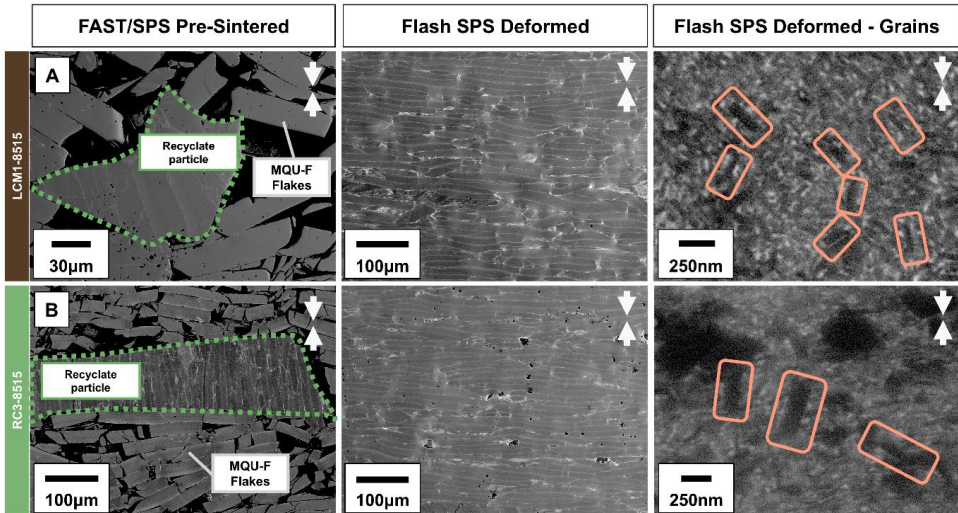


Figure 4.7 - SEM images showing the FAST/SPS pre-sintered morphology, FSPS deformed morphology, and FSPS grains in samples made from A. LCM1-8515 and B. RC3-8515. Recyclates are highlighted in green, while misaligned grains are highlighted in orange. Contrast has been digitally enhanced for improved clarity.

The deformation stage with Flash SPS is seen to promote anisotropic grain growth and texture in the samples. In Figure 4.6A, the final stage MQU-F-100 sample appears to have rectangular grains of <500 nm, even though they are not very well aligned. Instances of unaligned grains or regions of unaligned grains are highlighted by orange rectangles in the SEM images. In Figure 4.7B, RC3-8515 has instances of blocky, square shaped grains. Though differentiation between where recycled powder ends and commercial powder begins is not quite possible in the SEM images post-FSPS, it can be inferred that the larger grains mainly originate from the isotropic growth of grains in the formerly hot-deformed recyclate powder. This inference is made because the 100 wt% MQU-F sample did not display similar grain growth patterns.

Unlike Mishra *et al.*, texturing of Nd-Fe-B was not performed successfully at the nanocrystalline level. Ideally, the grains would have elongated morphology and stacked in a brick-wall-like structure perpendicular to the applied force. However, this was not observed. In Figure 4.6C, the case of the 100 wt% RC3 sample, some alignment can be seen. This alignment likely came from the initial hot deformation of the magnet, as the alignment is not perpendicular to the pressing direction and is isolated to the observed particle. This lack of texture is part of what drives the low B_r observed in nearly all samples. Improvement to texturing would lead to an improvement in B_r and consequently lead to an increase in the energy product. Exposing the magnet powder to a strong magnetic field for alignment

of the scrap particles prior to sintering, a technology standard in the production of sintered magnets [101], may be one way to improve the texture. In this work, this technique was not explored.

The relatively high B_r seen in RC3 samples is expected to be due to the large particles creating islands of alignment within the bulk of the magnet sample. In contrast, these islands may also be counterproductive to B_r , as the particles are randomly oriented in the bulk in the current state of development. A schematic of how this affects the overall magnetic behavior can be seen in Figure 4.8. In this schematic, two extreme scenarios are shown regarding how the alignment of an anisotropic particle can affect magnetic performance. In Scenario A, the anisotropic particle falls into the die and is pre-sintered having favorable alignment, and the c-axes of its grains are already parallel to the pressing direction. In Scenario B, the anisotropic particle falls into the die and is pre-sintered with unfavorable alignment, and the c-axes of its grains are perpendicular to the pressing direction. This scenario assumes that the deformation cannot effectively rotate the grains, and the unfavorable alignment is frozen in the magnet bulk. This misalignment detracts from the overall magnet behavior of the bulk.

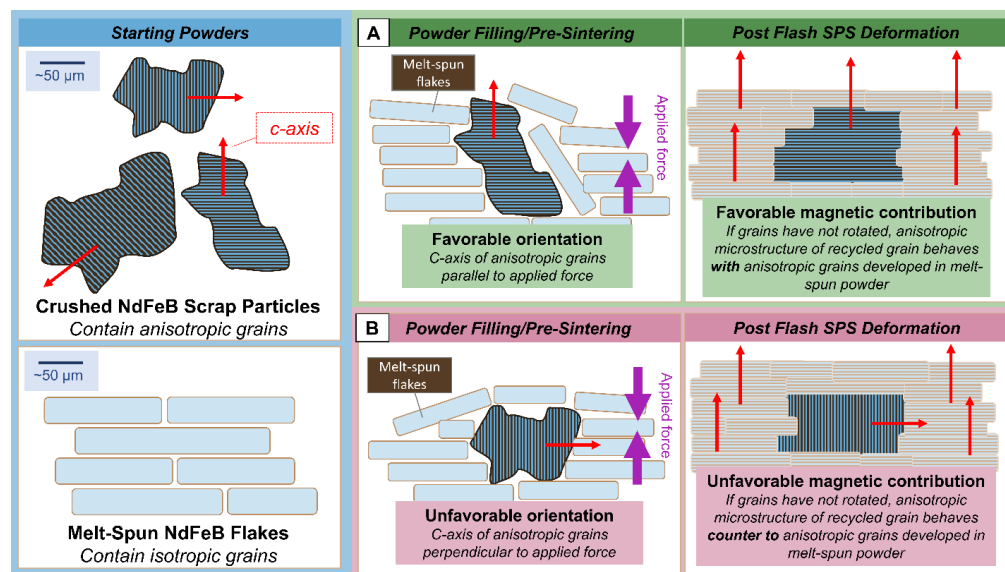


Figure 4.8 – Schematic showing two scenarios of anisotropic particles deforming into the Nd-Fe-B matrix without grain rotation, with (Scenario A) favorably oriented grains and (Scenario B) unfavorably oriented grains

An example of this can be seen in Figure 4.7B, in the FAST/SPS pre-sintered column. A large RC3 particle (outlined in green) shows particle texture from its first hot deformation. Though this is not a view of the granular structure, it can be assumed that, due to the nature of the hot-deformation process,

the orientation of the grains is similar to that of the particles. These particles are columnar, with their long, lateral sides parallel to the pressing direction. Unless the pressing force during deformation is large enough to promote full 90° rotation of the grains within the particles and to force the c-axis perpendicular to the pressing direction, the magnet will not achieve the highest possible remanence [70].

4.2.3 Analysis of MQU-F Samples Deformed with Boron Nitride Dies (25-30 mm)

With the conclusion of producing FSPS magnets without a die, the introduction of the BN dies was thought to assist in cleaner, smoother edges during FSPS sintering. In Figure 4.9, the results are seen to be mixed. The use of a 30- or 29-mm die, in the case of MQU-F starting pellets, does lead to somewhat cleaner edges. Further constriction by smaller dies, though, led to cracked edges. Smaller diameter dies also did not allow the pellet to experience the maximum degree of deformation, causing their final heights to be taller than the counterparts deformed with larger dies.

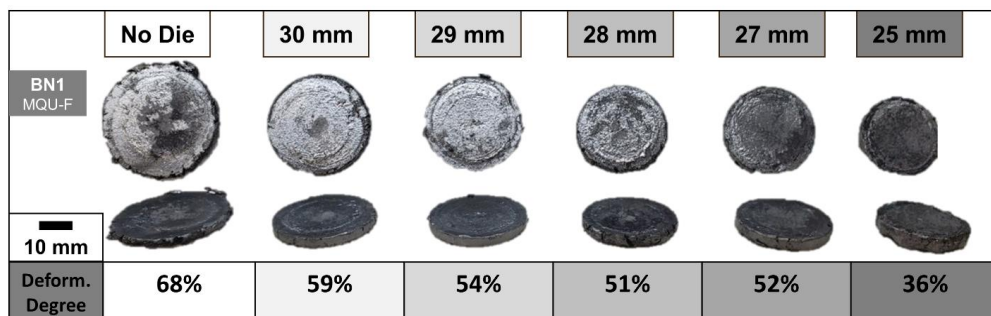


Figure 4.9 – Photo of the BN1 series of FSPS deformed MQU-F pellets, showing their tops and edges from no die to 25 mm die restriction, with deformation degree listed below each respective sample. Further information in Appendix B.

Though it was intended to extract both an edge and center sample from each pellet for magnetic measurements, with the cuts seen in Figure 3.14, the fragility of some of the samples led to only edge or only center measurements to be taken. The exception was the 30 mm sample, which was large and stable enough to have both points measured. Based on the suboptimal magnetic performance, seen in Figure 4.10, experiments were not repeated to obtain both center and edge measurements. The sample with no die, BN1-nodie, outperformed nearly all other samples in remanence and coercivity. A notable exception is the edge of the 28 mm sample, BN1-28, which displayed a high remanence yet a low coercivity ($B_r = 1.28$, $H_{cJ} = 696$). Though the high remanence did lead to the sample having a high $(BH)_{max}$, the low coercivity leads it to still be out-of-spec. High remanence from this edge may be due to the edges of the magnets having the greatest opportunity to flow, while the center remains stationary.

The effect is also seen in the magnet deformed without a die, with the edge having higher B_r . Freedom for the material to flow could lead to better grain rotation, and therefore better texturing. Another interesting aspect from these experiments is the similarity between the 30 mm sample's edge and center values. While the addition of the die did not improve the magnetic performance, it did, in this case, improve homogeneity of the magnetic behavior across the sample, when compared to the sample deformed with no die.

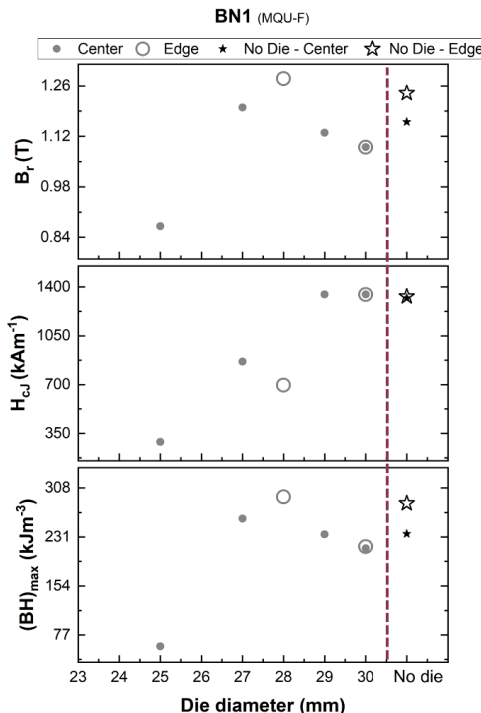


Figure 4.10 – Magnetic performance of FSPS samples deformed with 25-30 mm diameter BN dies in comparison to a sample deformed without a die

Though the magnetic behavior of BN1-30 appears to be homogeneous from the magnetic analysis, SEM analysis does show an influence of the die wall on the morphology and microstructure of the sample. In Figure 4.11, an image taken at the very edge of the sample shows the MQU-F platelets bending due to the resistance of the BN die. Orange dotted lines are used to indicate different regions of bend, with blue arrows used to indicate the normal direction to the platelets. In the upper left corner of the image, some platelets are seen to be completely parallel to the pressing direction. From roughly 1 mm into the sample, the bending begins to occur, with the normal gradually becoming more and more parallel to the

pressing direction closer to the edge. While the grain size appears to be within range, as seen in the grain level magnification, there is also bend towards the edge, as the grain texture tends to follow the behavior of the MQU-F platelets. There are also larger grains in some platelets and larger grains at contact points between platelets. Bands of larger grains within the MQU-F platelets could be due to the higher heating at the contact points between platelets, leading to more liquified Nd-rich phase, in turn facilitating more mass transfer. The larger grains could also be due to the melt-spinning of the MQU-F flakes. When flakes are melt-spun, the portion of the flake in contact with the metallic wheel cools faster than the portion in contact with the atmosphere. The wheel-facing part of the flake will therefore cool faster and develop smaller grains, while the atmosphere-facing part will cool slower, causing larger grains to form [169]. The majority of the grains appear to be of desired texture and size, though, confirming that the FSPS with the BN die does produce anisotropic grains from the isotropic MQU-F powder. Detriment to the texturing only comes from the edge region of the magnet experiencing friction from the die wall.

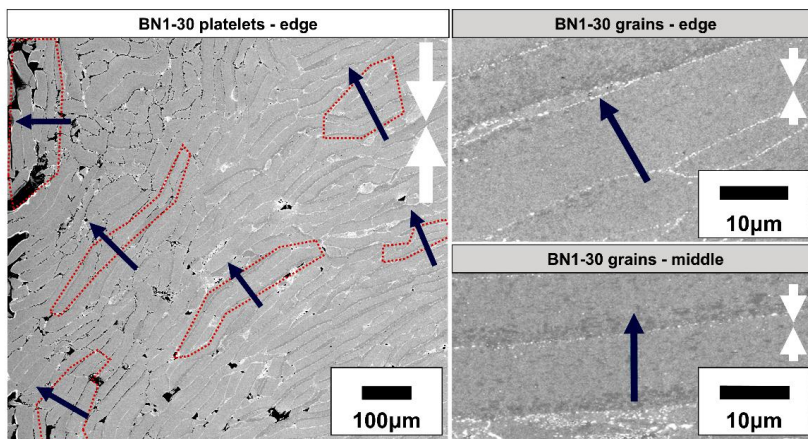


Figure 4.11 – SEM images of BN1-30, from the magnification of individual MQU-F platelets and grain magnification. Orange shapes are shown to track the bending of platelets against the friction of the die, while blue arrows indicate the normal of the platelets and/or grains. Contrast has been digitally enhanced for improved clarity.

With the idea now that improved flow would likely increase the B_r , it was decided to increase the diameters of the BN dies to allow for more movement during the deformation process. This was expected to increase the degree of deformation as well. A larger die diameter may also decrease the bending region of the MQU-F platelets, as the sample would make contact with the BN die later in the deformation process than with the smaller dies, and therefore experience the friction of the die wall later in the deformation.

4.2.4 Analysis of Samples made from Recyclate or Commercial Powders Deformed with Boron Nitride Dies (31-33 mm)

After receiving larger dies, experiments were performed with deforming recycled Nd-Fe-B powder alongside the commercial MQU-F powder. Figure 4.12 displays photos of the edges of the different sample series, BN2 (MQU-F), BN3 (MRV1), and BN4 (MRV2), deformed with 31-33 mm dies. In the BN2 series, the size and number of cracks seems to increase with increasing die diameter. This is counter to the BN3 series, where the restriction in almost all cases appears to improve the integrity of the sample edges. BN4 had a mixed appearance of cracks and high integrity, but this may be related to the fact that the BN4 series often cracked the BN dies during deformation. The expansion of the BN4 samples was so great during deformation that die destruction was almost inevitable when these samples were deformed. This expansion was likely due to the low densities of the starting pellets, as the large powder size allowed for many gaps to be formed during the pre-sintering phase. Instead of flowing like a pellet made from finer powder, likely the collapse of powder particles falling into gaps was more sudden and, therefore, expansion became more rapid. The pressure on the BN die, especially if it was inhomogeneous, likely led to the breakage.

10 mm	No Die	33 mm	32 mm	31 mm
BN2 MQU-F				
Deform. Degree	68%	65%	65%	65%
BN3 MRV1				
Deform. Degree	79%	63%	64%	63%
BN4 MRV2				
Deform. Degree	72%	65%	63%	56%

Figure 4.12 - Photos of the BN2, BN3, and BN4 series of FSPS deformed MQU-F and recyclate pellets, showing their edges from samples deformed with 31-, 32-, and 33-mm BN dies and no die. Further information in Appendix B.

In this experimental series, it was deemed more important to know the general magnetic behavior across both the edge and center of the samples simultaneously. Therefore, samples were cut in half for measurement rather than having portions taken from their edge and center. With evidence obtained already that the edge is likely to have better B_r , the priority instead became knowing whether the whole magnet could have viable performance. Figure 4.13 displays the performance of the whole magnets with both edge and center considered in the magnetic measurements.

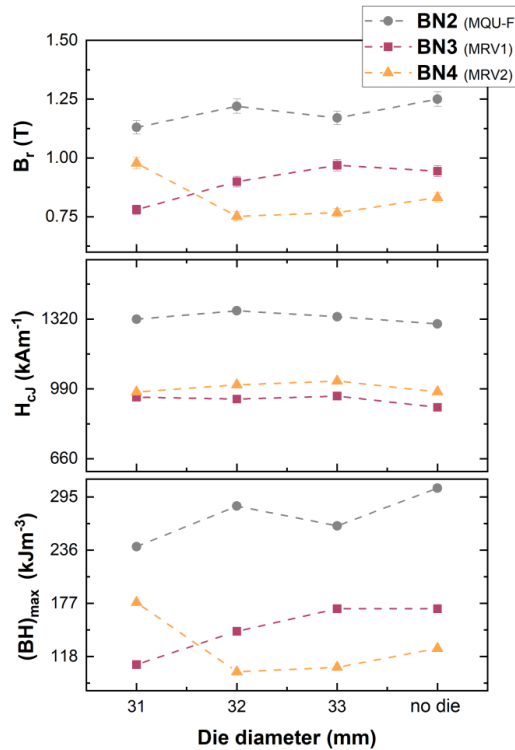


Figure 4.13 - Magnetic performance of FSFS samples from the BN2, BN3, and BN4 series

BN2, made from the commercial MQU-F, outperformed both recyclate series BN3 and BN4 across all diameters. This was to be expected, as many challenges needed to be overcome for either the BN3 or BN4 series to achieve optimal performance, such as unified grain texturing, mitigated grain growth, greater improvement in density, and otherwise. For both BN3 and BN4, it appears that decreased restriction by increasing the die diameter led to small increases in B_r , with a complete lack of die leading to a slightly lower H_{cJ} . What is most notable, though, is BN4-31, the MRV2 sample deformed in a 32 mm BN die. This powder, which is unusually large for powder metallurgy processes (500-1000 μm), certainly led to a lower starting density in the pre-sintered pellet, as mentioned before. The rapid expansion of the pellets made from this powder was likely what caused the breakage of many BN dies. Interestingly, BN4-31 saw an increase in B_r ($B_r = 0.98 \text{ T}$) greater than any of its counterparts. Likely, the restriction of the 31 mm die helped to increase the density more than the other dies. As increased density has a direct relationship to increased remanence, this positive effect of densification was seen in the magnetic performance. Unfortunately, this B_r value, along with all B_r values of samples made from recycled material, falls below the desired value of at least 1.2 T. Coercivity of all 100% recycled magnets also does not surpass $H_{cJ} > 1300 \text{ kA/m}$. The sample BN2-32, a sample made from MQU-F and

constricted by a 32 mm die, does show that some benefit exists at this level of restriction, with a higher B_r ($B_r = 1.22$ T) seen when compared to BN2-31 ($B_r = 1.13$ T) and BN2-33 ($B_r = 1.17$ T). It even has an H_{cJ} value within target range ($H_{cJ} = 1359$ kA/m). Still, it is outperformed by BN1-nodie (data re-used here from the BN1 series), with total lack of restriction allowing for better flow and degree of deformation ($B_r = 1.24$ T, $H_{cJ} = 1331$ kA/m). This sample can achieve the target magnetic performance, but it contains no recycled material.

4.3 Magnetic Performance and Microstructure of Spark Plasma Texturing (SPT) Samples

With the conclusion of FSPS investigations, the focus was then shifted to a different form of deformation, SPT. With more fine control during the deformation process, it was thought that a more viable sample made from 100% recycled material could be obtained through this technique as opposed to FSPS. For comprehensive data regarding deformation degree, density, and magnetic performance, see Appendix C.

4.3.1 SPT Comparison Between Hot-Compacted and Pre-Sintered Pellets from Commercial Powder

For this experimental series, SPT was performed using the “SPT1” parameters listed in Table 3.7. In this series, MQU-F powder was either hot compacted using the FAST/SPS pre-processing parameters “HC1” or pre-sintered with “PRE2”, with details of these parameter sets listed in Table 3.3. HC1 samples prior to deformation have a starting relative density of ~95%, while PRE2 have a density closer to ~70%. Figure 4.14 displays the magnetic performance of SPT1-PRE2 and SPT1-HC1, with their variations in deformation temperature and pressure. The samples deformed at the lower temperature of 700 °C are indicated with dashed lines, while the samples pre-sintered with the PRE2 parameters are shown in grey. SPT1-PRE2 samples were only deformed at 700 °C, as there were issues with the pre-sintered form shattering during the initial application of uniaxial pressure by the FCT HP-D25 device. Therefore, only one series of SPT1-PRE2 samples were deformed using the SPT1 parameter set.

In the case of deformation of the hot-compacted forms, SPT1-HC1, deformation at 750 °C rather than 700 °C shows an increase of B_r across all deformation pressures. SPT1-HC1-P10T75, the sample deformed under 100 MPa and 750 °C, shows the greatest magnetic performance of the SPT1 series ($B_r = 1.17$, $H_{cJ} = 1407$, $(BH)_{max} = 258$ kJ/m³). Several of the other samples, however, do not trail far behind, at least in terms of $(BH)_{max}$. The pre-sintered sample SPT1-PRE2-P20T70 ($B_r = 1.15$, $H_{cJ} = 1502$, $(BH)_{max} = 243$ kJ/m³) only differs slightly in B_r but exceeds H_{cJ} when compared to SPT1-HC1-P10T75. This is likely explained for two reasons. Firstly, SPT1-HC1-P10T75, since it is hot-compacted at a high temperature before deformation, could have experienced some grain growth during the hot-compaction stage. This grain growth was then amplified during deformation. While this is not wholly detrimental, and the magnetic behavior is still close to desired, the influence of the grain growth is seen in the drop in coercivity. This potential grain growth is further amplified as the pressure is increased to 200 and 300 MPa, with H_{cJ} continuing to drop for all hot-compacted samples but remaining quite stable for pre-sintered samples. Secondly, the density of the hot-compacted samples prior to deformation was considerably higher than that of the pre-sintered forms. As the pre-sintered forms had to close many pores before the start of deformation, their lower density certainly detracts from the B_r , which has a

direct relationship with the sample density. The higher number of gaps in the PRE2 samples, relative to HC1, are presumed to be the main cause for the pellets breaking when a high load is applied.

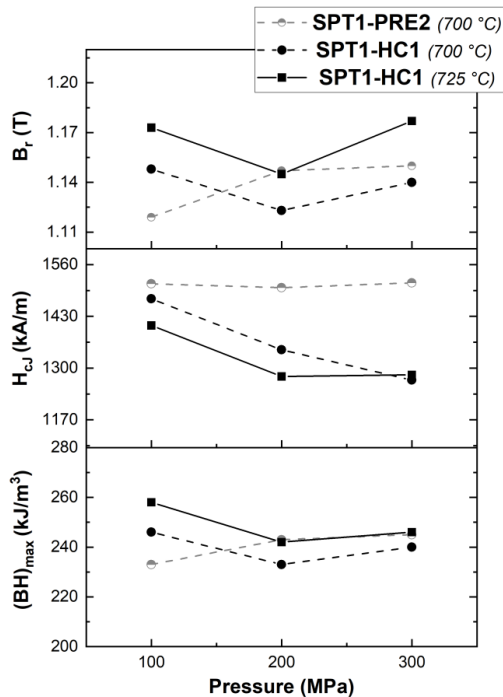


Figure 4.14 - Magnetic performance of SPT samples from the SPT1-HC and SPT1-PRE2 series. Hot deformation temperature is given in parentheses.

SEM analysis of SPT1-HC1 samples deformed at 750 °C confirms the growth of grains with increasing pressure, as seen in Figure 4.15. These images show that the excessive grain growth begins at, at least, 100 MPa and becomes more frequent during the 200 and 300 MPa deformation, especially at the contact points between former MQU-F platelets. At 300 MPa, bright regions of Nd-rich phase also seem to segregate more than at other compaction pressures. This can possibly be attributed to the Nd-rich phase becoming liquid and being squeezed forcefully into the limited gaps in the near-dense compact. Some Nd-rich phase in Figure 4.15C also appears somewhat raised. This could be due to the Nd oxidizing when in contact with the air prior to SEM analysis, creating small, raised islands of neodymium oxides. Though both the 100 MPa and 200 MPa samples have bright Nd-rich segregated areas as well, neither seem to have an Nd concentration high enough for these islands to form. This segregation is quite detrimental to the magnetic performance, as it draws Nd away from the grain boundary phase that magnetically isolates the individual grains.

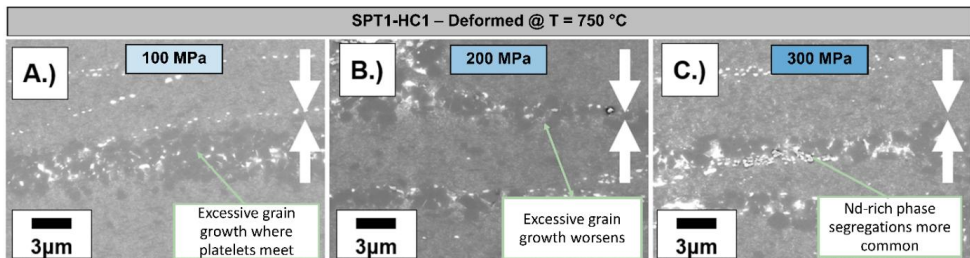


Figure 4.15 – SEM images of SPT1-HC1 samples deformed at 750 °C across the applied pressures of A. 100, B. 200, and C. 300 MPa

From this work, it was determined that the application of pressure above 100 MPa likely contributed more detriments than benefits to the microstructure, at least in the case of samples hot compacted at such a high temperature of 725 °C and beyond. The idea of hot compacting pre-forms was put aside for the time being, as it appeared that the risk of excessive grain growth would only be worse with recycled anisotropic material.

4.3.2 Quick Deformation SPT

With advice from WILO SE and references to deformation speed in literature, stating that 0.1 mm/s would be optimal [115], focus shifted to prioritizing the deformation speed during SPT. Several trials were run to determine which parameters were needed to achieve a quick deformation (QD) speed of 0.1 mm/s, primarily in the final stage of deformation. A graph displaying the results trials can be seen in Appendix D. A graph is also included that compares the QD speeds to deformation speeds of other SPT experiments. In short, it was determined that the application of 150 MPa over a brief period of 10 seconds would lead to the target deformation speed of 0.1 mm/s. This appeared to work over a variety of temperatures, which led to experiments of quick deformation being performed at 700, 750, and 800 °C. The parameters for this SPT series are labeled as “QD” and further clarified in Table 3.7. With these parameters, deformation speeds of roughly 0.1 mm/s were achieved in the final stage of deformation, and exact speed values for each sample are listed in Appendix C.

Figure 4.16 shows the stark difference in magnetic performance between the MQU-F and recycle samples. No sample made from 100% recycled material could reach a B_r of even 1 T, with H_{cJ} values being similarly low. Thus the highest achieved $(BH)_{max}$ by the recycled samples was only 111 kJ/m³, achieved by QD-MRV1-P15T80, which was deformed at a maximum temperature of 800 °C. While the performance of the recycled samples is considerably poorer than the FSPS samples of Sections 4.2.1 and 4.2.4, the behavior of these samples show a somewhat inverted relationship with the behavior of the QD-MQUF samples. Both B_r and H_{cJ} improve for the recycled samples with increasing temperatures, while a higher temperature hinders H_{cJ} in QD-MQUF.

While previous experiments focused on tuning the parameters for MQU-F, these experiments show that parameter optimization should be directly made for recycled material, especially if the goal is to generate a magnet from 100% recycled material. Several aspects differ between MQU-F and recycled magnet powder, such as powder morphology, packing of the powder, particle surface contact, grain anisotropy or isotropy, and grain size. The sintering at a higher temperature may have been more favorable for QD-MRV1 and QD-MRV2 because the packing of their irregular powder particles needed higher temperatures for better densification. Once QD-MQUF platelets could overcome the minimal gaps between one another, excess energy from the higher temperature sintering likely led to excessive grain growth. Croat also states that thermomechanical grain alignment begins at 800 °C, understandably meaning the temperature is favorable for particles that already have anisotropy to realign themselves [115].

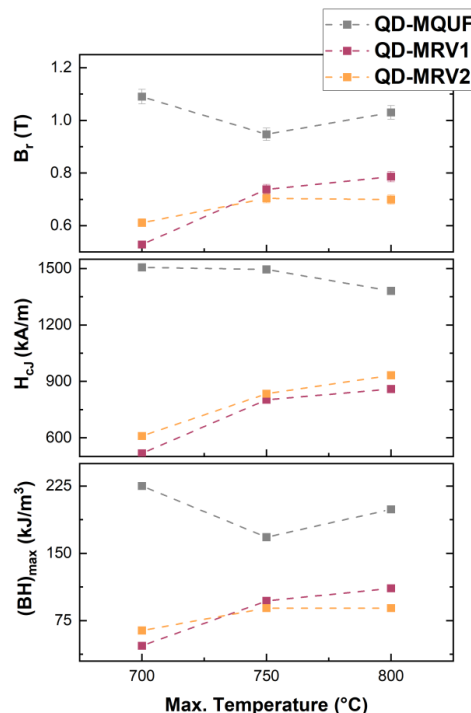


Figure 4.16 - Magnetic performance of SPT samples from the QD series

SEM analysis of these samples displays some of the reasons for the poor magnetic performance. Figure 4.17 shows issues with the magnet samples on both a particle and a granular scale. In Figure 4.17A, large, dark grey portions of the image correspond to the expected excessive grain growth, which happened primarily at particle interfaces. However, on the granular scale, dark pores are also visible. It

is possible that the MQU-F platelets could fully fuse and densify in the Z-direction, with the application of uniaxial pressure in this direction. With full platelet contact achieved in this direction, grains then began to grow. This can be inferred by how the platelets tend to have excess growth in contact with platelets above and below but less so with platelets to the right and left. These gaps in the XY-plane were then flooded with the liquid-phase Nd-rich grain boundary phase, as all experiments were performed above its melting point. The amount of liquid phase appears to have not been enough to push out all of the air and fill the gaps, as evidenced by dark pores surrounding the top of the Nd-rich segregation in Figure 4.17A. The recyclate powders of MRV1 and MRV2 experienced similar issues, with the quick deformation not allowing enough time for the sample to fully densify. QD-MRV2-P15T80, seen in Figure 4.17C, especially displays pores prevalent in the XY-space between particles. In this image, Nd-rich segregations appear much more irregular than those of QD-MRV1-P15T80 or QD-MQUF-P15T80. Both samples also exhibit examples of this Nd-rich pattern, with this pattern being isolated to several specific particles in the matrix. While pores seem to be the most obvious “sink” for the liquified Nd-rich phase, particles with more isotropic grain morphology that may not be tightly packed together could also behave as a trap for the Nd-rich phase. It is possible that, prior to deformation, these regions had already been disturbed by the pre-sintering process to have unshapely grains causing an open pore network. Regardless, any Nd-rich phase segregation that is separate from the grain boundary layer draws Nd away from its role as a magnetic isolator for individual grains and instead places it as an obstacle to optimal magnetization. Deforming a magnet too quickly appears to exacerbate this issue.

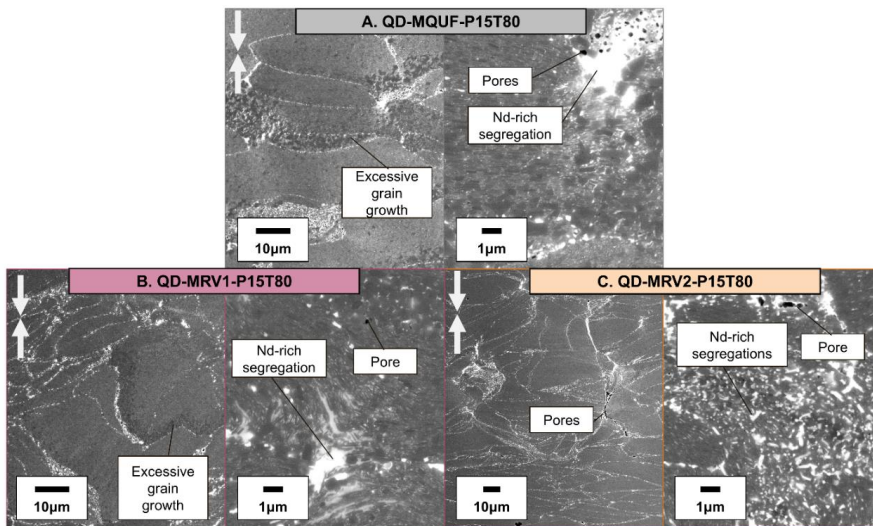


Figure 4.17 – BSE SEM images of QD samples deformed under 150 MPa, 800 °C consisting of 100% A. MQU-F, B. MRV1, and C. MRV2. Arrows indicate pressing direction

4.3.3 Gradual Pressure Application SPT and Scale-Up

Further discussions with WILO SE suggested that the application of pressure needed to be more gradual as opposed to tailored specifically to the deformation speed of 0.1 mm/s. As the influence of gradual pressure application had not yet been explored, several time periods were selected. The FCT HP D25 device would elevate the force from its baseline applied force of 10 kN up to 126 kN, which translates to 100 MPa on a Ø 40 mm sample. The effect of the pressure application duration would be measured with samples deformed over 30, 120, and 240 seconds. Initially, only 15 g pre-forms were deformed with these parameters, in the series referred to as “SPT2”. To see the feasibility of deforming a larger sample, a 30 g sample was also deformed, referred to as “SPT3”. As a control, a 15 g sample was deformed under the baseline pressure of 10 kN. The parameters for these SPT experiments are labeled as “SPT2” and “SPT3” and further clarified in Table 3.7. All samples in these trials were made from 100 wt% recycled material, MRV1, as the previous QD trials showed that optimization of MQU-F deformation parameters would not always translate directly to the recycled material. Therefore, focus was narrowed on generating samples that either wholly consisted of or partially contained recycled material.

Figure 4.18 shows the magnetic performance of all the SPT2 and SPT3 deformed samples. SPT2 trials had a slight improvement in B_r with an increase in pressure application from 30 to 120 seconds. This unfortunately came with a simultaneous decrease in coercivity. The longer duration of 240 seconds negatively affected both coercivity and remanence. Likely the slowing of the process allowed for a longer exposure to the high temperature of 800 °C, driving the Nd-rich liquid phase to transfer more mass into grain growth. Unlike in the QD series, all SPT2 samples were able to achieve $B_r > 1$ T. Considering that B_r is strongly related to density, improved densification is primarily responsible for this [101]. The decreased speed of the process likely allowed for more time for the particles to become more malleable through the partial or full melting of the Nd-rich grain boundary phase. With the slow application of pressure, particles could deform into the remaining gaps of the pre-form and greatly improve density. This deformation of the particles into the gaps would also prevent the sudden squeezing of the Nd-rich liquid phase into available gaps, avoiding pronounced Nd-rich phase segregation.

The results change when the pre-form is increased to 30 g, such as the case with SPT3. Only one pressure application experiment was performed with a 30 g MRV1 sample pre-sintered at 500 °C. This is due to the pre-form being unable to withstand the applied pressure. As the FAST/SPS device would increase its uniaxial pressure from 10 kN upwards, the pre-form would collapse, essentially crumbling back into powder. The FCT HP D25 would register this collapse as a tool breakage and immediately cease the FAST/SPS cycle, with a graph displaying this abrupt end shown in Figure A 3 (Appendix D). While the low density was sufficient for the smaller 15 g samples to withstand the applied pressure, the

pores present in the 30 g pre-form likely caused greater weakness with its increased height. The ratio between the surface area and the pre-form height may have also caused the collapse, as choosing to not scale the face area with the height detracted from its structural stability. The reality of this collapse is reflected in how similar the SPT3 trial is to the 10 kN trial, in terms of magnetic performance. Neither of these samples really experienced a “deformation,” in the sense that their particles were forcibly distorted laterally. Rather, they both experienced more of a compaction, as the Nd-rich grain boundary still was liquid, and a uniaxial force of some sort was still applied. Both samples expanded laterally and experienced a height reduction. The 10 kN trial shows that the application of higher-than-baseline force is necessary to improve magnetic performance. The SPT3 trial shows that, even when the higher-than-baseline force is applied, the pre-form needs to have the stability to resist it enough to experience deformation.

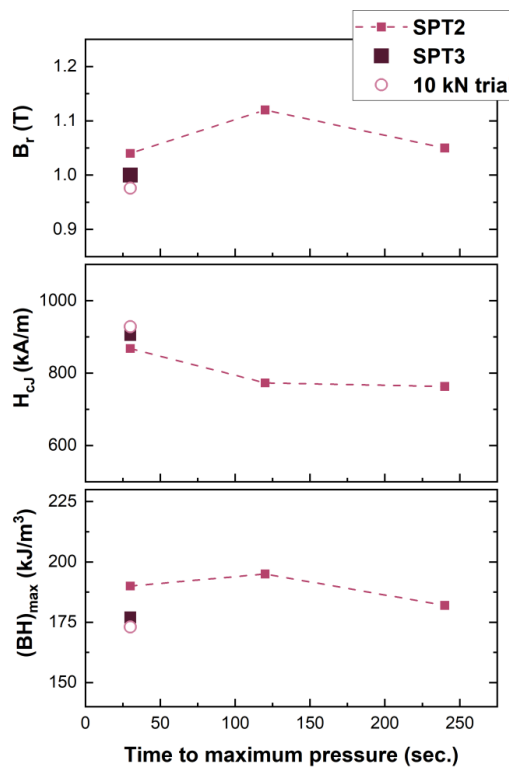


Figure 4.18 - Magnetic performance of SPT samples from the SPT2 and SPT3 series, relative to a control sample deformed under the default 10 kN of force

4.3.4 SPT of Recyclate Hot Compacts

With the observation of 30 g pre-forms collapsing under the force of deformation, an increase of pre-form density seemed to be key to proper deformation. Both 100 wt% and 25 wt% LCM2 samples were prepared and hot-compacted at temperatures of 600 and 700 °C. Samples hot compacted at 600 °C were roughly 88% dense, while samples hot compacted at 700 °C were closer to 95% dense. Figure 4.19 displays SEM images of the LCM2 pre-forms prior to deformation via SPT. The large gaps in the sample pre-sintered at 500 °C explain the poor structural integrity of these samples when exposed to the pressure of SPT. The sample hot-compacted at 600 °C contains much fewer large gaps between particles, generating a network more suitable to resist the applied deformation force. Samples hot compacted at 700 °C appear to be near fully dense. While this is the best case when considering structural stability and force resistance, it is clear by SEM analysis that this temperature is already generating some Nd-rich phase segregation. This pre-compaction temperature induces a liquid Nd-rich phase, as it surpasses the phase's melting temperature of 660 °C. If densification of the compact is not achieved prior to the liquid phase forming, then the Nd-rich phase has an opportunity to squeeze into remaining pores that have not been closed through total powder compaction. Inducing a liquid phase also increases the likelihood of grain growth, as the presence of a liquid phase suggests increased mass transfer. The sample hot-compacted at 600 °C also appears to have some of this prominent Nd-rich segregation, as some portions of the sample were likely achieving temperatures high enough to melt the Nd-rich phase. The frequency of these segregations was smaller than that of the sample hot-compacted at 700 °C, but it suggests that the ideal hot-compaction temperature lies somewhere between 500 and 600 °C. Optimization beyond the scope of this work could determine a temperature at which the particle network is stable enough to undergo SPT while liquefying the Nd-rich phase as little as possible.

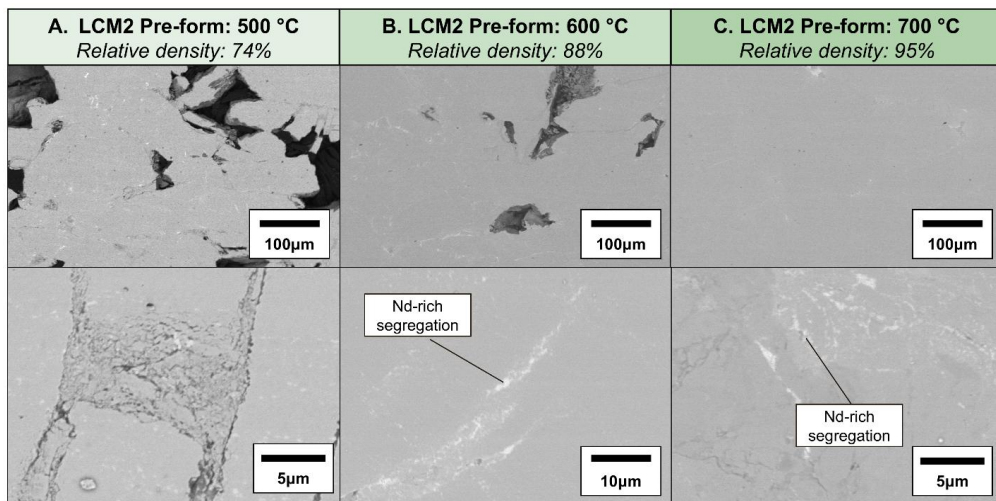


Figure 4.19 – SEM images of two different magnifications of LCM2 pre-forms sintered at A. 500, B. 600, and C. 700 °C

Figure 4.20 displays the magnetic performance of the SPT4 series samples. LCM2 pre-forms pre-sintered at 500 °C had the same issue as with MRV1 pre-forms deformed under load, in that their poor density did not allow the forms to properly resist the deformation force in the SPT step. This is reflected in the considerably low B_r values of both 100 wt% LCM2 and 25 wt% LCM2 samples. The sample deformed which contained 25 wt% did manage to reach a remanence value of 1 T, but this did not differ much from the sample made from 100 wt% LCM2. H_{cJ} values for both 500 °C pre-forms are also decidedly similar, suggesting no significant deformation occurred and that the magnets were primarily just densified. Clear improvements were seen in the deformed samples that were hot compacted at 600 or 700 °C prior to deformation. In the case of 600 °C hot compaction, the B_r for the fully recycled samples reached 1.11 T and further improved to 1.24 T with the 700 °C hot compaction. While the remanence for the sample hot compacted at 700 °C approaches the target value of 1.3 T, the coercivity unfortunately shows a decline across pre-form temperature increases, with the best balance of coercivity and remanence for 100 wt% recycled magnets occurring with the hot-compaction temperature of 600 °C. This is reflected in the hysteresis curves shown in Figure 4.21A, with the SPT4-HC2 sample displaying a squarer curve than the other two samples.

The mixing of 25 wt% LCM2 with 75 wt% MQU-F generates stronger magnets than those with LCM2 alone. Across all pre-form temperatures, the mixed recyclate and commercial samples outperform the 100 wt% recycled samples. Of note is the sample hot-compacted at 600 °C, which achieved a $(BH)_{max}$ of 313 kJ/m³, the highest of all magnet samples produced between both Flash SPS and SPT trials. With its H_{cJ} of 1060 kA/m and B_r of 1.28 T, these values would qualify it as

somewhere between an N40 and N42 grade magnet [121]. While not quite at the target performance, within the timeframe of this work, this magnet composition shows the greatest potential for use as a demonstrator magnet containing any amount of recycled material. When 75 wt% commercial material is mixed with the recyclate, the influence of the hot compaction temperature is less visible on the squareness of the curves, as seen in Figure 4.21B. This implies that a higher volume percentage of recycled material leads to a greater sensitive to hot compaction parameters.

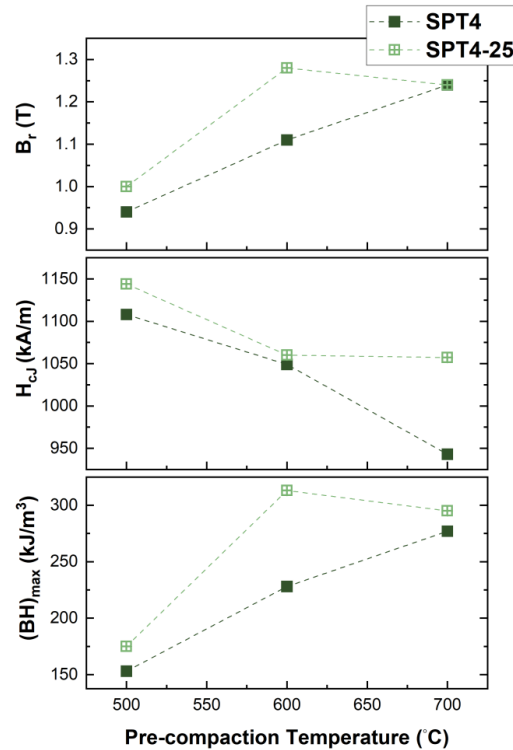


Figure 4.20 - Magnetic performance of SPT samples from the SPT4 series, consisting either of 100 wt% LCM2 (SPT4) or 25 wt% LCM2, 75 wt% MQU-F (SPT4-25)

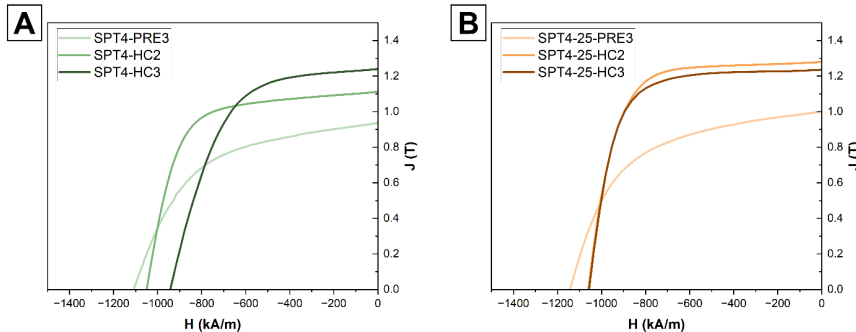


Figure 4.21 – 2nd quadrant J-H magnetic hysteresis curves of A. SPT4 and B. SPT4-25 samples

Ultimately, the goal is to demonstrate the possibility of generating a new magnet from 100 wt% recycled material. Therefore, the 100 wt% LCM2 magnets hot compacted at 600 °C, SPT4-HC2, stands out to be the representative of choice for demonstrator magnets. These demonstrators would then be used in a WILO water pump motor, testing their ability to power a pump. Figure 4.22 displays the microstructure of an SPT4-HC2 magnet. In the sample center, the presence of singular pores indicates that full densification was still not achieved. Regardless, particles in the center have a higher likelihood of c-axis alignment to the pressing direction. This achievement can likely be attributed to the higher starting density of the pre-form. With the higher density, the influence of the applied pressure and the resistance of surrounding particles successfully forced the Nd₂Fe₁₄B grains into the desired alignment. This did come at the expense of some grain growth, especially at contact points between particles. This alignment was also not consistent throughout the entire sample body. At the sample edge, the friction of the die wall once again caused an upward bend in the microstructure, with the deformation causing platelets to climb to a near perpendicular alignment with the uniaxial pressing force. Grain alignment, in most cases, mirrors the behavior of the former particles. In some cases, though, the particles develop large isotropic grains rather than misaligned grains. The sample edge also has a higher frequency of pores than the sample center. The relevance of these findings relies heavily on whether the entire sample volume would be used in a bar magnet. Further investigation is necessary to determine how deep within the sample volume this bending effect is observed. If an Nd-Fe-B disk is SPT deformed with the intention of cutting out bar magnets, then the less desirable edges can be removed. What is most valuable from this microstructure analysis, though, is the confirmation that SPT can cause thermomechanical grain realignment in recycled hot-deformed powder without leading to all grains becoming oversized.

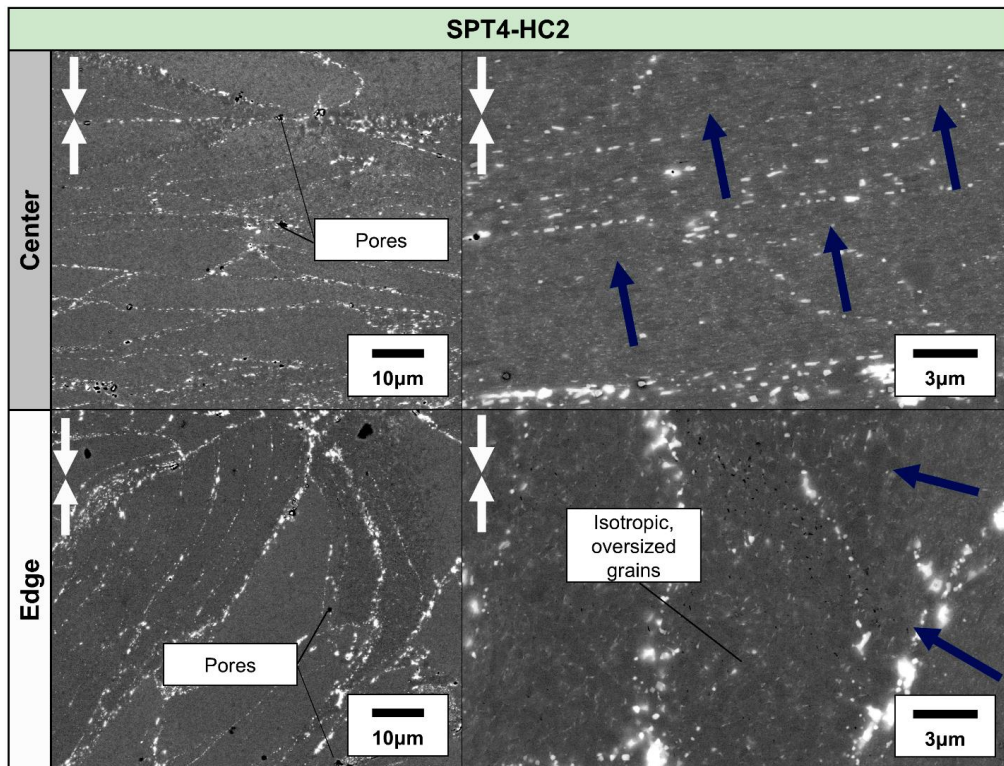


Figure 4.22 – SEM images of the center and edge of the SPT4-HC2 sample, at magnifications to see the sample platelets and grains. Blue arrows represent the alignment of the c-axis in the particles. Contrast has been digitally enhanced for improved clarity.

While this combination of hot compaction and SPT deformation did successfully generate 100 wt% recycled magnets, some processing issues still remain. Firstly, as the hot compact is quite tall (> 10 mm), initial extraction from the graphite die is challenging. The tall cylindrical side of the compact creates a lot of friction relative to the die wall, and cracking of the graphite die has been observed nearly during 80% of all sample extractions. Though a graphite sheet is in place, which would be expected to lubricate the process somewhat, an alternative may need to be considered. Perhaps a wider die opening and thicker graphite sheet, such as 0.5 mm thickness, would be necessary to accommodate for both the expansion of the compact during sintering and the successful extraction. Alternatively, a die with an insert designed to be ejected together with the sample could ease extraction. Secondly, the arrangement of the hot compact in the TZM die used for deformation could be improved. During this work, the compacts were placed inside the die at the approximate center. Placing the compacts as exactly as possible in the center would help in accurate force application. Other experiments by project partners

have included a graphite foil with a cut-out specifically to center the sample [170]. This could be added in future works to further improve the process.

4.3.5 Modifications for a Demonstrator Magnet

With satisfying results from the SPT4 experiments, 6 demonstrator magnets were produced using the specifications described in Table 3.9. While only 4 magnets are necessary for the pump motor, two additional magnets were formed as back-up. As stated, the frequent destruction of the graphite dies during the extraction of hot compacts prompted the use of a TZM die as an alternative. Regardless of the die being graphite or TZM, the expansion of the hot compacts did not occur uniformly along the height of the sample, as seen in Figure 4.23A. The width of the top and bottom of the sample would be wider than the sample middle, with widths often reaching 21 mm. This bowing likely contributed to the graphite dies cracking, as the thicker portions of the sample would create great resistance against the die wall. This bowing effect may be due to Nd-rich liquid phase forming at the interface with the graphite punches. Due to the high Fe-content of the Nd-Fe-B sample, some graphite may have been reacting with or diffusing into the compact during the FAST/SPS cycle. This influence by carbon may have increased the electrical resistance at the sample faces. With increased electrical resistance comes greater Joule heating, and the sample faces may have experienced higher temperatures than the sample center. This would have allowed more of the Nd-rich phase to liquify and make the upper and lower portions of the sample more malleable than the center. Though the circumference of the sample was also in contact graphite, the uniaxial application of electrical current and pressure likely encouraged greater interaction between Fe and C at the planar sample faces rather than along its cylindrical wall. Bowing could also be due to density gradients within the sample, caused by the friction of the wall. Areas with lower density would experience a higher sintering shrinkage, causing inhomogeneity in the sample shape.

Due to the height of the TZM punches, hot compaction was moved from the HP D5, which could not handle the increased height, to the FCT HP D25, shown in Figure 4.23B. This allowed for both the hot compaction and SPT to be performed within the same device. FCT HP D25 tracking of various cycle parameters are graphed in Figure A 4 of Appendix D.

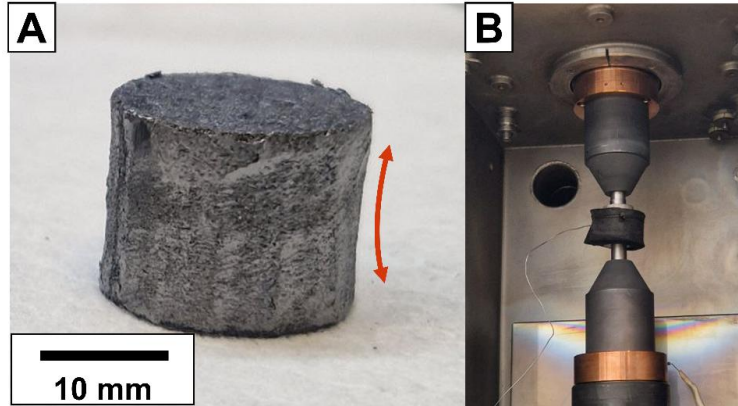


Figure 4.23 – A. DEMO pre-form roughly 15 mm in height showing bowing from sample top to bottom, indicated with an orange arrow, and B. FAST/SPS set-up in the FCT HP D25 device using a TZM die for HC2 hot compaction

The DEMO samples predictably had the same rough and wavy faces upon extraction as all previous SPT samples, as shown in Figure 4.24A. With the extra 16% mass increase from the SPT4 series to DEMO, the average height of the DEMO samples after hot deformation was measured to be roughly 4.3 mm. This allowed for 1.2 mm of tolerance during the smoothing of the sample faces. As shown in Figure 3.7, the target height for a demonstrator magnet was 3.1 mm $+0.04/-0.01$. Initially it was planned that the DEMO samples would be ground down to this height using wet-grinding on an ATM Saphir 550 device with 80 grit SiC sandpaper. However, the hardness of Nd-Fe-B at room temperature can exceed HV 600 [171]. With this hardness, the SiC sandpaper was often worn out after only 1-2 min of grinding. Each face of a sample could consume 10 sheets of 80 grit sandpaper to be worn down to a flat surface, as seen in Figure 4.24B. With several hours of exchanging paper, along with a mix of manual and machine-applied pressure, one DEMO magnet was ground to the target thickness, as seen in Figure 4.24C. Continued grinding using this method was deemed impractical, and the remainder of the DEMO magnets were sent to RUB to be ground to target thickness using a cup grinder, which could be successfully applied to achieve the desired thickness with reasonable effort.

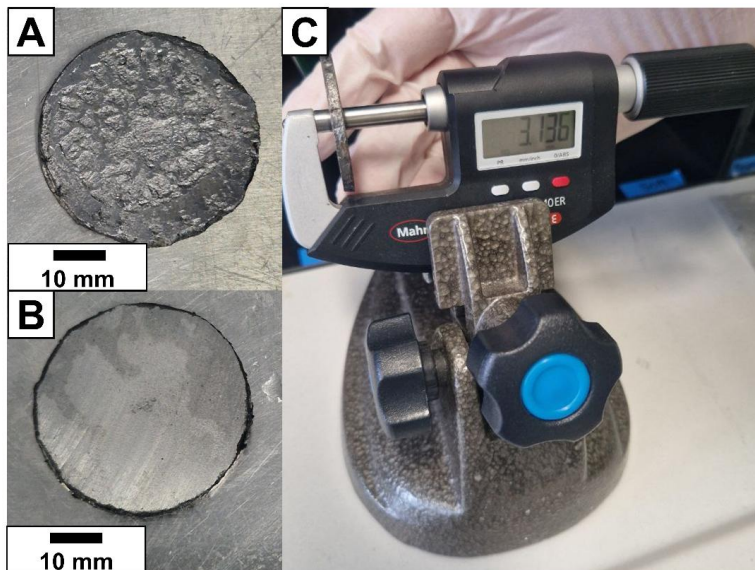


Figure 4.24 – A. DEMO sample before grinding, B. DEMO sample after grinding the face with multiple 80 grit sandpaper sheets, and C. a DEMO sample after grinding to target thickness

4.3.6 Operation of the Demonstrator Magnets in a Water Pump Motor

Figure 4.25A and B show the bar magnets extracted from the DEMO samples using electrical discharge machining by WILO SE, shaped to their target dimensions. Damage and cracking were observed in the bar magnets. SPT deformation likely caused this damage, either from incomplete deformation, damage upon extraction, or sample flaking due to internal cracking. Commonly, pieces of the DEMO magnets would break or flake from the surface during extraction. As seen in Figure 4.25B, a crack runs from the edge of the DEMO sample down towards the center. These cracks could be due to several reasons, including stresses during sample extraction from the TZM die or mechanically weakened regions in the bulk, such as through Nd-rich segregations. Nevertheless, the bar magnets were installed into a rotor, shown in Figure 4.25C, used for the Stratos MAXO 40/0.5-4 Circulating Pump by WILO SE. The set-up for EMF measurements is shown in Figure 4.25D.

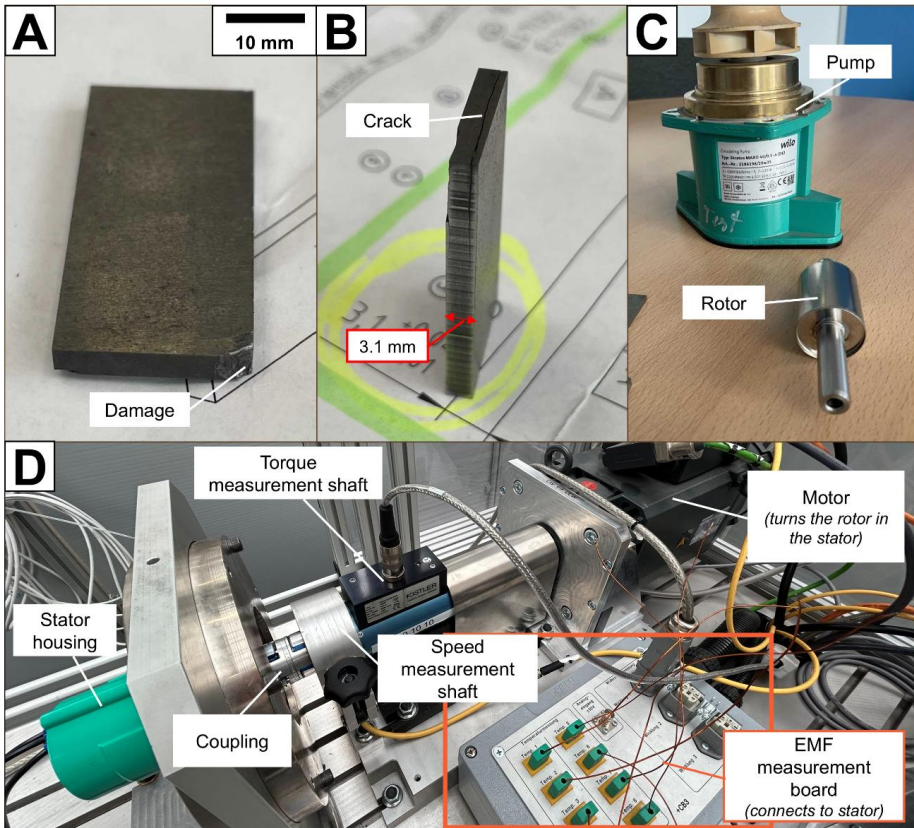


Figure 4.25 – Photos of A. a bar magnet after electrical discharge machining, showing damage in the corner from the deformation process, B. a side-view of the bar magnet with a visible crack down the magnet bulk, C. the rotor where the bar magnets were installed, along with the WILO SE circulating pump where the rotor was utilized, and D. the set-up of the EMF measurement. Photos, electrical discharge machining, and EMF tests provided by WILO SE.

EMF of the two tested rotors is listed in Table 4.1. When exposed to a rotational speed of 4000 RPM, the standard rotor delivered an EMF of 80.55 V. The rotor with the DEMO magnets produced an EMF of 76.51 V, roughly 5% lower than the standard rotor. This translates to a 5% lower torque, if the pump were in operation. Because the H_{cJ} of the DEMO magnets is lower than that of the standard WILO magnets, their behavior relative to temperature is also worse. When Nd-Fe-B magnets are exposed to higher temperatures, their demagnetization curve contracts, leading to decreases in H_{cJ} , B_r , and $(BH)_{max}$ [172]. As the H_{cJ} of DEMO (1060 kA/m) is considerably lower than the target values (1300-1400 kA/m), this would lead to a quicker decrease in magnetic performance with rising temperatures.

Table 4.1 – Comparison of the EMF of a standard WILO rotor to rotor with DEMO magnets installed at the same rotational speed

Rotor	Rotational Speed (rpm)	Electromotive force (V)
WILO standard	4000	80.55
4 DEMO magnets	4000	76.51

4.4 Process Energy Consumption

The collection of energy consumption measurements helps to contextualize the energy usage of ECAS processes for industrial purposes. Figure 4.26A displays the energy consumption measurements from the HP D5 device during an HC2 FAST/SPS cycle with a reduced dwell time. If an additional 30 seconds of dwell is considered, extrapolation of total energy consumption by the HP D5 device is likely 1300-1400 Wh, with its cooler consuming an additional 600-700 Wh. If the FSPS route would be taken to hot deform the magnet, the HP D25 device would consume roughly 2310 Wh with its cooler consuming an additional 1600 Wh. Using the HP D25 device for the SPT4 method of hot deformation, the energy consumption of the HP D25 would rise to roughly 2730 Wh with an additional 1610 Wh for the cooler.

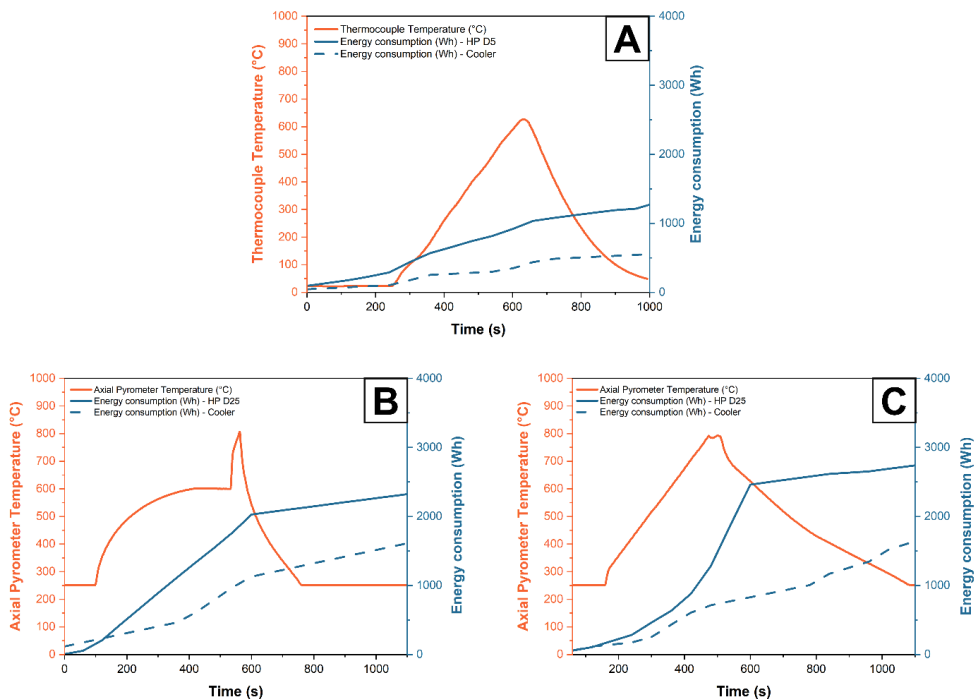


Figure 4.26 – Energy consumption of the A. FCT HP D5 device and its cooler over a FAST/SPS sintering cycle of HC2 with a 30 second dwell rather than 60 seconds, and the FCT HP D25 device and its cooler over a B. FSPS2 cycle and C. SPT4 cycle

Table 4.2 shows a summary of the energy consumption of the FAST/SPS hot compaction along with the two ECAS deformation routes of flash SPS and SPT. SPT requires an extra roughly 400 Wh when compared to FSPS. The highest achieved $(BH)_{max}$ for a 100 wt% recycled FSPS sample was with RC2-

0100, achieving a $(BH)_{max}$ 219 kJ/m³. The highest achieved $(BH)_{max}$ for a 100 wt% recycled SPT4 sample, SPT4-HC2, which used the hot compaction temperature of 600 °C, was 228 kJ/m³. As both processes require the similar types of FAST/SPS hot compaction, this energy was not included in comparative calculations. Normalizing for volume, the RC2-0100 could at maximum have a diameter of 20 mm and a height of 3.31 mm, leading to a volume of 1040 mm³, or roughly 1.04e-6 m³. Ideally, the SPT4 sample could have the desired volume of a bar magnet (L = 33.5 mm, W = 16.2 mm, H = 3.1 mm), or roughly 1680 mm³ (1.68e-6 m³). When the $(BH)_{max}$ values of the samples are multiplied by their volumes, RC2-0100 would have roughly 0.22 J of magnetic energy, while SPT4-HC2 would have 0.38 J. When considering the amount of external electrical energy, in Wh, needed to achieve this magnetic energy, the FSPS sample requires roughly 17 kWh/J and the SPT sample requires 11 kWh/J. In short, both processes require similar amounts of energy input for samples with magnetic strength at a similar order of magnitude. While at face value, the SPT process consumes more energy, it in turn produces a compact with a larger volume of mechanically stable magnetic material that also has a higher magnetic strength than its best performing FSPS counterpart.

Table 4.2 – Energy consumption values for FAST/SPS hot compaction and ECAS deformation techniques

Process	Energy consumption, device (Wh)	Energy consumption, cooler (Wh)	Total energy consumption (Wh)	Energy input per magnetic energy (kWh/J)
FAST/SPS hot compaction	1300-1400	600-700	1900-2100	-
Flash SPS deformation	2310	1600	3910	17
Spark plasma texturing	2730	1610	4340	11

It is important to note that FSPS of 30 g pre-forms hot-compacted at 600 °C were not produced within this work, due to time limitations. It is certainly possible that FSPS of these larger, more mechanically stable pre-forms could lead to similar $(BH)_{max}$ values than those of the SPT samples. It could also lead to FSPS samples with better end mechanical stability and more available magnetic volume to be shaped into a bar magnet. This could then lead to FSPS deformation having a lower overall electrical energy input per joule of magnetic energy. From an industrial application standpoint, this would have a variety of benefits and drawbacks. FSPS has a significantly shorter cooling time, as a large tool surrounding the magnet does not need to be cooled, nor is any insulation present trapping heat. FSPS is a quicker process to set up within a machine, as no graphite foil needs to be fit within a die. However, temperature

cannot be precisely controlled due to the FSPS process relying on the sudden release of electrical power flowing through the sample. Ultimately, the energy consumption of the two processes is not significantly different, but, at the moment, SPT would be the process that generates the most attractive magnetic behavior per input of electrical energy.

Ideally, this energy consumption would be most useful in direct comparison of ECAS processes to the established hot-pressing and hot-deformation process used for the manufacturing of anisotropic Nd-Fe-B magnets on an industrial level. Several inferences can be made when knowing the process parameters of each step. For instance, the FAST/SPS hot-compaction is performed at a maximum temperature of 600 °C, while commercial hot-pressing is performed with a die temperature roughly at 870 °C. FAST/SPS hot-compaction is performed under vacuum, while hot-pressing is performed in open air with an argon purge. Though the FAST/SPS hot compaction occurs at temperatures 200 °C lower than hot-pressing, the necessity for vacuum could push the energy consumption to be higher than hot-pressing. In exchange, it would also consume fewer gaseous resources. After hot-pressing, the magnet is immediately moved to be hot-deformed, while still retaining heat. In the ECAS processes, the FAST/SPS hot compact must be cooled to room temperature, cleaned of graphite, install into the SPT die, and re-heated to 800 °C. The hot deformation process, while occurring at a temperature of 870 °C, occurs in 30-45 seconds, again under an argon purge [115]. SPT once again must be performed under vacuum and has a full cycle time of roughly 15 minutes. While exact kWh values were not found in literature for the whole commercial hot deformation process, several factors indicate that the ECAS processes are likely more energy intensive. The factors include cycle run time, the use of vacuum instead of argon, and the necessity to cool to room temperature before heating to deformation temperature.

While the energy consumption comparison to commercial hot deformation can only be speculated, energy consumption values for sintered Nd-Fe-B magnets are more readily available. Though this comparison should not be considered one-to-one, it does put the ECAS energy consumption into perspective. The densification and microstructural control steps to compare could be isostatic pressing, sintering, and annealing, for instance. Based on technical specifications from equipment vendors, Zakotnik et al. estimates that, for 300 kg of material, isostatic pressing consumes 0.06 kWh/kg, sintering consumes 0.46 kWh/kg, and annealing consumes 0.08 kWh/kg. 300 kg is estimated to be the maximum capacity for the chosen sintering and annealing devices. Therefore, the total energy consumption for the densification and microstructural management of a sintered Nd-Fe-B magnet is roughly 0.6 kWh/kg. If the SPT process produces a single 1680 mm³ bar magnet of density 7.55 g/cm³, this magnet would weigh approximately 13 g. When compared to the 4340 Wh needed to deform the magnet via SPT, the energy consumption of SPT alone would be over 340 kWh/kg. With the hot compaction included, this energy consumption is further increased to nearly 500 kWh/kg. While it is not always practical to

compare industrial scale production to lab-scale trials, it is important to recognize that scale-up will also need to include several magnitudes of energy consumption reduction per kg of material to be industrially viable. It is also important to mention the energy savings from not having to mine new material. Mining metals for new magnets consumes between 30-33.4 kWh/kg, which could be counted as energy saved by the ECAS direct recycling [173].

4.5 Summary

In both FSPS and SPT, adding commercial MQU-F to any recyclate powder improves the magnetic behavior. The best performance of all Nd-Fe-B samples deformed via ECAS processes was a sample hot-deformed via SPT containing 25 wt% recycled LCM2 and 75 wt% MQU-F, achieving a $(BH)_{max}$ of 313 kJ/m³. In the mixed recycled FSPS samples of Section 4.2.1, samples could achieve target H_{cJ} (1300-1400 kA/m) with up to roughly 25 wt% recycled material. FSPS samples were not able to achieve the target B_r values of 1.3-1.4 T, however. The SPT sample, SPT4-25-HC2, the same sample that achieved the highest $(BH)_{max}$, was the closest to target B_r of any sample containing recycled material, at $B_r = 1.28$ T. It did not achieve target H_{cJ} , though ($H_{cJ} = 1060$ kA/m).

Though the highest magnetic performance was achieved with mixed samples, the primary goal was to demonstrate the capability of ECAS of consolidating magnets with 100 wt% recycled powder. Nearly all samples produced by FSPS failed to produce a $(BH)_{max}$ much higher than 170 kJ/m³. The one exception was the FSPS sample of RC2-0100, with a $(BH)_{max}$ of 219 kJ/m³. The powder of this sample was tailored specifically to not contain the particle size fraction <125 μ m, which contributed too much oxygen contamination to the process. This powder became the inspiration for LCM2, a powder of size 180-200 μ m which in turn produced the best performing 100 wt% recycled magnets. The 100 wt% recycled magnet with the best balance of B_r and H_{cJ} was SPT4-HC2 ($B_r = 1.11$ T, $H_{cJ} = 1049$ kA/m, $(BH)_{max} = 228$ kJ/m³). SPT4-HC2 was also designed with the intention of being a demonstrator magnet, reaching a final height >3.1 mm to be ground down to fit WILO specifications. The DEMO magnet series was then produced, based off SPT4 with some modifications, including 5 g more powder mass and hot-compaction in a TZM die. These magnets were generated with the intention of smoothing and shaping for use in a WILO water pump motor.

To produce these demonstrator magnets, several parts of the pre-forming and deformation process needed to be optimized. Firstly, while previous experiments succeeded in deforming pre-forms pre-sintered at 500 °C [23], [87], [165], [170], these samples did not have the desired dimensions for a usable bar magnet. When attempting to use SPT to deform taller 500 °C pre-sintered samples, these samples tended to collapse under the application of force. To withstand the deformation force, pre-forms were instead hot-compacted at 600 °C, which created a denser particle matrix prior to

deformation. This led to better densification during SPT deformation, leading to samples with both improved magnetic performance and the correct dimensions for cutting out the desired bar magnets.

The parameters of SPT were also explored and optimized. Large behavioral differences between 100 wt% MQU-F and 100 wt% recycled material under different processing parameters led to the focus of developing parameters specifically for recycled magnets. For example, the quick deformation performed in Section 4.3.2 led to some of the worst performing magnets over the whole experimental period. However, it made clear that the recyclate has a more positive response to a higher deformation temperature than MQU-F. This led to the decision to keep the SPT temperature at 800 °C when working with 100 wt% recycled samples. The choice of 100 MPa as a deformation pressure is also higher than the pressure deemed suitable for ECAS MQU-F deformation, as seen in other experiments [170]. The nature of the recycled particles, though, with their angular shapes and irregular stacking, likely necessitates more coercion to fully densify. The gradual application of pressure over a period of time, such as 30 seconds, also appears to have a positive influence on magnetic performance. While this period could risk excessive grain growth, the application of pressure too quickly can lead to a high frequency of Nd-rich phase segregation. A slower period of pressure application likely takes advantage of the increased sample malleability, due to some or all of the Nd-rich phase liquifying. The quick application of pressure risks forcing the liquid Nd-rich phase into pores, causing more pronounced phase segregation.

In brief, the best ECAS method for producing 100 wt% recycled magnets in this work was a combination of hot-compaction at 600 °C followed by SPT deformation at 800 °C, with a maximum pressure of 100 MPa applied over a 30 second period. This produced magnets with a $(BH)_{\max} > 200$ kJ/m³ and dimensions large enough to extract bar magnets from for demonstration of operation in the rotor of a WILO water pump. The DEMO magnets were able to produce 95% of the EMF of standard WILO magnets at a rotational speed of 4000 RPM.

5 Results and Discussion: PM T15 High-Speed Steel

5.1 Analysis of the Swarf

Table 5.1 gives a compositional overview of the swarf when compared to reference material – a sample produced via HIP of gas atomized PM T15 powder – and nominal composition of PM T15 from literature. The reference sample was densified at a temperature of 1150 °C under a pressure of 100 MPa in an Ar atmosphere for 3 hours. The appearance of Al in the swarf and the higher O-content relative to the reference is due to the presence of Al_2O_3 grinding medium contaminants. Higher oxygen could also be due to oxidation, due to the small particle size of some fractions of the swarf and exposure to liquids, such as grinding lubricant and acetone, that may have contained dissolved oxygen. Oxygen content did increase slightly between un-milled and milled powder, meaning that some oxygen may have been introduced during milling. The other difference of note is the higher C-content in the swarf when compared to the reference. Though it is only roughly 0.1 wt% higher than the nominal range, this shift ultimately changes key properties such as the solidus temperature. This excess carbon likely comes from residual lubricant oil and binder from the grinding wheels. Figure 5.1 displays a phase diagram calculated specifically for the PM T15 swarf with the increase C-content considered. Marked in a red dashed line is the C-content of the swarf. As mentioned in Section 2.4.2, austenitization of HSS is typically performed at temperatures between 1290-1330 °C. Specifically, PM T15 is austenitized at 1220 °C [131]. However, due to the high C-content of the swarf, this temperature is roughly at solidus, where a liquid phase will begin to form and therefore cannot be used for austenitization of the parts made from PM T15 swarf. Lower austenitization temperatures can be used, but this leads to incomplete carbide dissolution. As carbon content increases with higher austenitization temperatures, the final martensite will also contain more carbon. With less carbon in martensite, the final hardness will suffer. There can also be residual ferrite if the austenitization is performed at too low over a temperature, which will also affect the steel's hardness.

Table 5.1- Compositional analysis in wt% of the PS (as delivered) and PSM (milled) swarf, in comparison to nominal literature values and a reference sample. In the reference and PSM, heavy elements were measured using XRF. In PS, heavy elements were measured via ICP-OES. *C, N, and O measured via CGHE

Sample name (see Table 3.10)	Sample Type	C*	Mn	Si	Cr	Mo	V	W	Co	Al	N*	B	O*
Nominal ([31])	-	1.5-1.6	0.15-0.40	0.15-0.40	3.75-5.00	max 1.00	4.50-5.25	11.75-13.00	4.75-5.25	-	-	-	-
Reference	HIP sample	1.59 ± 0.01	0.33 ± 0.00	0.50 ± 0.14	4.32 ± 0.05	0.48 ± 0.03	4.74 ± 0.06	12.09 ± 0.02	4.91 ± 0.11	<0.001	0.09 ± 0.01	-	0.01 ± 0.00
PS	swarf	1.75 ± 0.1	0.31 ± 0.01	0.38 ± 0.02	4.79 ± 0.07	0.42 ± 0.01	5.16 ± 0.11	13.7 ± 0.5	5.18 ± 0.10	0.01 ± 0.00	0.11 ± 0.01	0.02 ± 0.00	0.39 ± 0.01
PSM	milled swarf	1.70 ± 0.1	0.33 ± 0.01	0.39 ± 0.01	4.91 ± 0.06	0.51 ± 0.01	5.09 ± 0.03	12.38 ± 0.06	5.07 ± 0.03	0.04 ± 0.02	0.12 ± 0.02	0.02 ± 0.01b	0.44 ± 0.03

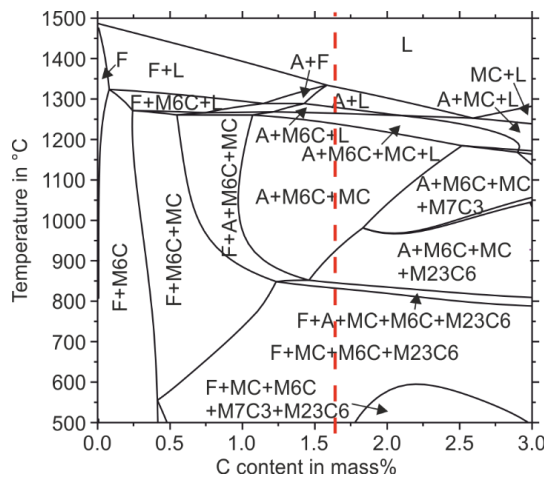


Figure 5.1 – Phase diagram displaying steel phases and carbides at various C-contents and temperatures, calculated for the PM T15 swarf via ThermoCalc by colleagues at RUB. C-content of the swarf is marked with a red dashed line.

Another challenging characteristic of the initial swarf, labeled as PS, was its poor apparent and tap density. While initial studies were performed with PS, the decision was ultimately made to add a milling step to further process the swarf, with milled swarf labeled as “PSM”. Table 5.2 shows the significant difference in apparent and tap density of the powders due to the additional milling step. The reason for the poor density of PS is primarily its morphology, as the swarf was tendril-like and spring-like in shape, trapping air and resisting compression. This can be seen in Figure 5.2A and Figure 5.3A. Figure 5.2A

especially highlights the interlocking behavior of the PM T15 tendrils, creating agglomerates that can easily trap lubricant and grinding particles. Introducing milling as a processing step helped to homogenize the swarf morphology and allow for an easier to handle powder. Figure 5.2B and Figure 5.3B show the more flake-like, flat, and less tangled swarf after milling. The behavior of the swarf after milling also allowed for the possibility of effective magnetic separation, if needed. Previously, the agglomerates of un-milled swarf would keep contaminants trapped during magnetic separation. Now, the flakes of milled PM T15 could escape from one another and be sorted from grinding medium. Though this was considered as an additional processing step, magnetic separation was not realized within the scope of this work, and most swarf handled still contained grinding medium. A large grinding particle, likely Al_2O_3 , can be seen underneath milled PM T15 swarf in Figure 5.2C.

Table 5.2 – Densities and particle size distribution data of un-milled (PS) and milled (PSM) PM T15 swarf

Sample name (see Table 3.10)	Apparent density (g/cm ³)	Tap density (g/cm ³)	d_{10} (μm)	d_{50} (μm)	d_{90} (μm)
PS	0.3	0.4	16.4	71.0	186.6
PSM	2.2	2.5	11.5	40.6	108.7

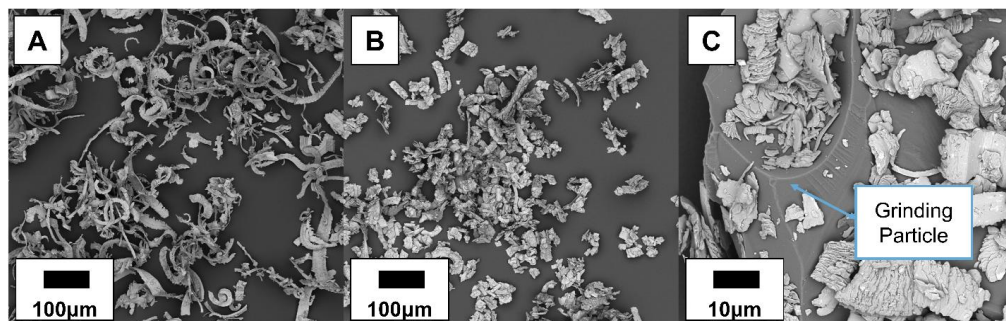


Figure 5.2 – SEM images of A. PS swarf, B. PSM swarf, and C. PSM swarf surrounding a large grinding particle

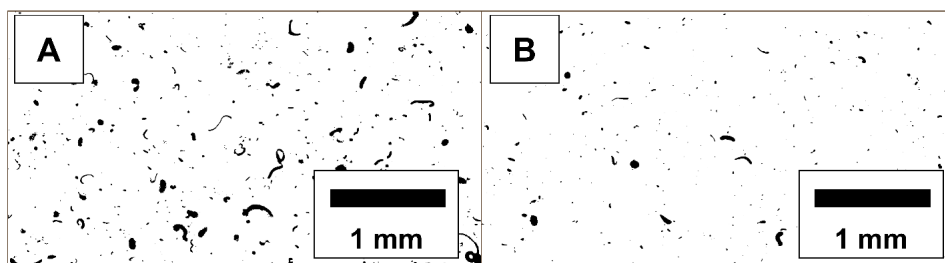


Figure 5.3 – Random QicPic frames of A. PS swarf and B. PSM swarf

5.2 Analysis of Samples from Un-Milled Swarm

Prior to the introduction of a milling step, PS was used in initial FAST/SPS trials. It was thought that the FAST/SPS process could handle the un-milled material, but several adaptations had to be made to generate a dense sample.

5.2.1 Single-Stage FAST/SPS

As shown in Figure 5.1, the initial solidus temperature of the swarm was determined to be at 1222 °C. Sintering experiments were designed to not reach this temperature, with the highest experimental temperature input being 1050 °C. This temperature was the starting temperature for FAST/SPS trials. However, samples sintered at this temperature had difficult issues with extraction. A tall lip formed at the edge of the sample from material seeping in between the graphite punches and the die. This material mechanically sealed the sample onto the graphite punch, and attempts to remove this sample ended up breaking the sample and the graphite punch, as seen in Figure 5.4.

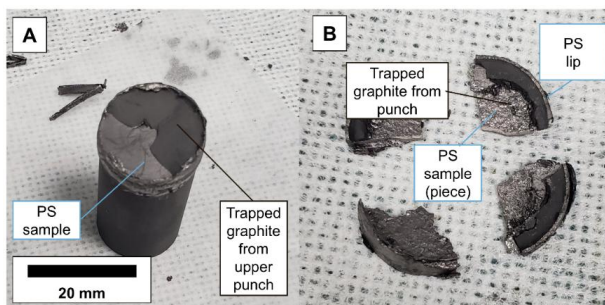


Figure 5.4 – A. PS sample stuck onto graphite punch and B. PS sample removed from punch, but broken and trapping residual graphite. (FAST/SPS parameters: 100 K/min to 1050 °C, 50 MPa pressure, dwell for 5 minutes)

Several ideas were proposed as to why this lip was forming. One suggestion was that the multiple phase changes occurring between 800-900 °C were affecting the ductility of the swarm. In Figure 5.5, for both PM T15 (nominal composition from Table 5.1 [131]) and PS, a transition between ferrite and austenite occurs at 800-900 °C. M₂₃C₆ carbides are also dissolving, with full dissolution occurring for the swarm at roughly 990 °C. These transitions could be causing the swarm to become more ductile and allowing material to be squeezed between the gaps of the punches and die through plastic deformation. A second suggestion was that the interface of the PS with the graphite was leading to a reaction. The steel in direct contact with the pure carbon graphite was likely absorbing carbon during the heating process of FAST/SPS. This hypothesis was confirmed with SEM imaging, as Figure 5.6A shows a carbon layer roughly 1 μm thick on the outer portion of a sintered PS sample. Large carbides also congregate under

the carbon layer. This carbon gradient likely further affected the solidus at the steel interface, and it is possible that the high carbon content caused a liquid phase to form in some areas. According to Figure 5.1, though, this temperature would have to be above 1200 °C, even if the C-content is 3 wt% or above. FAST/SPS can generate hot spots, especially at contact points. Even if the occurrence of >1200 °C hot spots was inhomogeneous, any formation of a liquid could lubricate solid material into the crevice between the die and punch, leading to the tall lip during the sintering process.

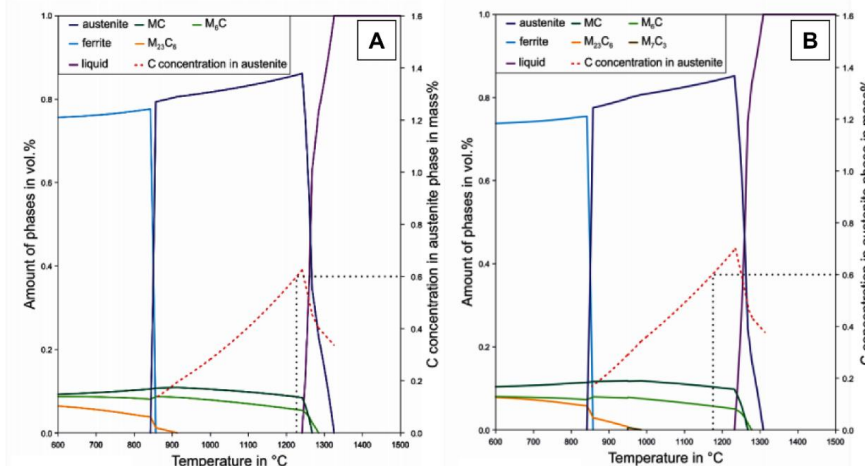


Figure 5.5 – Calculated volume content of stable phases for A. nominal PM T15 [131] and B. PS swarf. C-concentration in the austenite phase is denoted with a dotted red line. The targeted maximum C-concentration of 0.6 mass% is marked with a dotted grey line. From [174]

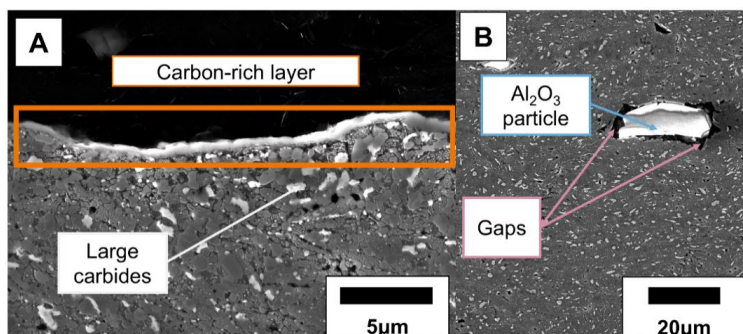


Figure 5.6 – SE SEM images of a PS sample sintered by FAST/SPS at 950 °C (pressure: 50 MPa, dwell time: 5 min), specifically focusing on A. the carbon-rich layer at the contact between PS and graphite and B. Formation of large gaps between an Al₂O₃ particle and the steel matrix

In order to mitigate this lip formation, and to successfully extract PS samples without breakage, the maximum FAST/SPS sintering temperature was lowered. A variety of temperatures were attempted, both to see the lower limit of achieving a stable part after FAST/SPS and to see and from which parameters a lip would stop forming. This experimental series is referred to as PS1, and the set maximum temperature was varied between 600 and 1050 °C, as listed in Table 3.11. Lip height was calculated through measuring sintered PS samples before and after the lip was removed through breaking and sanding. Figure 5.7 shows the effect of various sintering temperatures on the lip height and the density of the samples. All samples sintered below 1050 °C were able to be successfully extracted from the graphite die, even if the lip was nearly 1 mm in height. From below 800 °C, the lip drastically shrinks until it disappears at a sintering temperature of 700 °C. This lends some credibility to the idea that the phase transition between 800-900 °C was causing seepage from increased ductility, but likely this phenomenon was not the sole contributor to the lip. Though the lip vanishes at these lower temperatures, the density also suffers. While density only varies slightly between the broken 1050 °C sample and the successfully extracted 950 °C sample, SEM imaging shown in Figure 5.6B shows that this sintering process does not completely seal the grinding medium into the steel matrix. Gaps are visible between the Al_2O_3 particles and the rest of the matrix, which could lead to the hard phase easily breaking out. This experimental series suggested that single-stage FAST/SPS sintering of PS would not be practical, especially if scaled up.

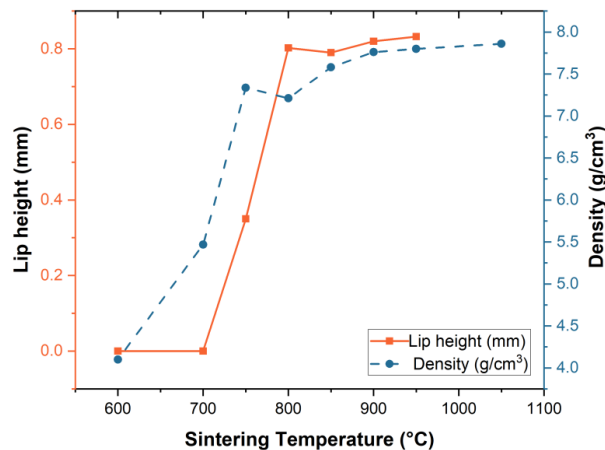


Figure 5.7 – Changes in density and lip height of PS samples sintered at varied FAST/SPS maximum temperatures (pressure: 50 MPa, dwell time: 5 min)

Regardless, an interesting feature of these experiments was the ability to generate a stable part at sintering temperatures as low as 600 °C. In conventional sintering, it is common for sintering temperature to be considered somewhere between 0.66 to 0.75 of melting temperature for pure metals [175]. The onset of a liquid phase for PS is 1222 °C, meaning sintering should begin somewhere between roughly 700-850 °C, going by this standard. The ability for the 600 °C sintered samples to hold their form may be attributed to a few reasons. Firstly, the pressure during FAST/SPS could trigger an interlocking of the particles at lower temperatures. Secondly, plastic deformation and the formation of hot spots at various interfaces within the samples, then led to a “pre-sintering”, not so unlike the pre-sintering of Nd-Fe-B forms in previous chapters. The observation of this pre-sintering led to the idea that, if full density could not be achieved with a single-stage FAST/SPS cycle, a multi-stage deformation could lead to a dense sample.

5.2.2 FAST/SPS Pre-sintering and Deformation

With the success of generating stable, semi-finished parts with a density of around 4.2 g/cm³ at FAST/SPS sintering temperatures as low as 600 °C, small-scale deformation attempts were performed on these pre-sintered compacts. These deformation experiments were performed with parameters listed in Table 3.12. Regardless of deformation pressure, measured geometric density post-deformation ranged around 7.1 g/cm³. Geometric density likely does not reflect very accurately on the real density in these cases, however. As seen in Figure 5.8, full deformation to the edge of the 30 mm TZM die only occurred with the application of 150 MPa. The samples deformed at lower pressures have a non-uniform circular shape, leading to irregular measurement of geometric density. Increase in deformation pressure also led to irregularities on the surfaces of the samples, creating divots that caused the sample height to vary across its face. For better visualization, densification was instead examined using SEM of cross-sections, as seen in Figure 5.9, to see if all pores in the metal matrix had been removed through the deformation process. While the sample deformed at 50 MPa already appeared to be near-dense, the sample deformed at 150 MPa improved in tightly conforming around Al₂O₃ contaminant particles. In these SEM images, pores are highlighted where the steel matrix failed to conform entirely to the shape of the grinding particle. Deformation at 150 MPa had minimized these pores relative to the lower pressure deformations.

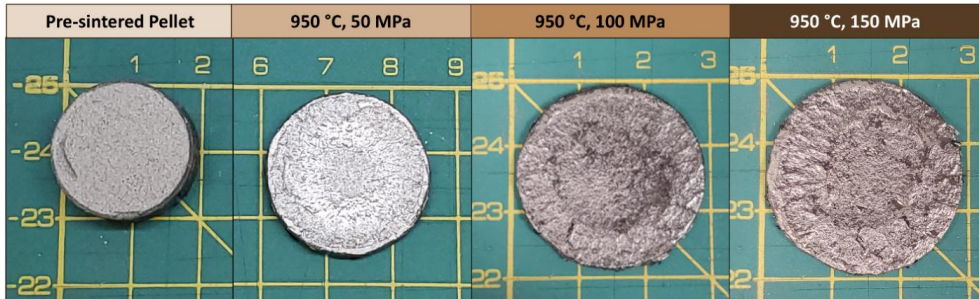


Figure 5.8 – Photos of pre-sintered PS from the PS2 pre-sintering parameters and samples treated with the PS2-D set of deformation parameters

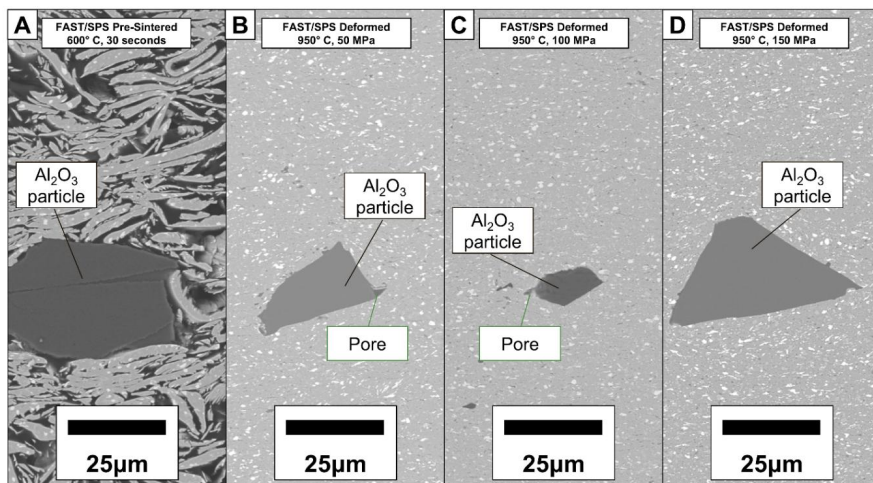


Figure 5.9 – BSE SEM images of A. PS2 pre-sintered form, and PS2-D samples deformed at 950 °C and B. 50 MPa, C. 100 MPa, and D. 150 MPa. Dark grey Al_2O_3 particles are found and highlighted in each sample.

The samples deformed at 150 MPa were large and stable enough for heat treatment and hardness measurements, performed by Felix Grosswendt of Ruhr-Universität Bochum. Hardness testing was done on the PSD-2 samples in their as-deformed state, after austenitization and quenching, and after austenitization, quenching and tempering. In these cases, austenitization was performed at 1220 °C. The transition away from using un-milled PS and towards milled PSM was beginning at this time, and deformed samples of PSM were also made at a deformation pressure of 150 MPa. These samples were also tested for hardness at the same stages as the PSD-2 samples. Results of the hardness tests are illustrated in Figure 5.10. First to note is that the samples made from milled swarf do not vary greatly from the samples made from un-milled swarf, with respect to hardness and microstructure. This is

beneficial information to recognize, as the milled swarf is much easier to handle when compared to the un-milled swarf. Evidence that the switch to milled swarf would not affect the end hardness was vital for the movement towards using milled swarf exclusively. Secondly, many of the samples approach the target value of 916 HV30 after quenching and tempering, but they do not achieve this value consistently. The large change in hardness between the as-deformed state and the quenched state is likely due to the carbon on the surface diffusing into the material. Prior to quenching, a hard carbide shell, like in Figure 5.11A, rested on the surface of the steel, influencing the hardness measurements. While this carbide shell may have given target hardness values for as-deformed samples, the inner bulk of the sample likely remained considerably below target hardness. If this carbide shell were to wear away, such as during tool usage, the weaker bulk would be exposed. A softer inner bulk would also impact the structural integrity of the tool.

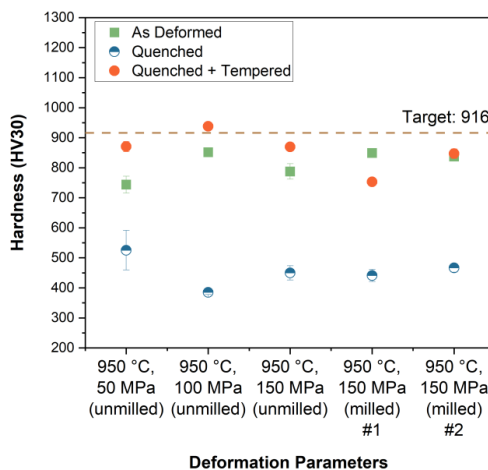


Figure 5.10 – Hardness testing of PSD-2 samples and deformed PSM samples in their as-deformed state, after quenching, and after quenching and tempering. For quenching and tempering parameters, see Section 3.3.3.

The issue of carbon diffusion from the graphite tools was also reflected in the evolution of the steel during heat treatment. Figure 5.11 shows a FAST/SPS deformed sample before and after heat treatment. Directly after FAST/SPS sintering, the carbide layer at the surface of the steel is visible, yet isolated to the surface of the steel. Subsequent heat treatment allows for these carbides to diffuse further into the steel matrix, affecting the concentration of carbon across the sample and leading to melt phases forming at lower temperatures than normal for PM T15 steel. Though densification had been achieved through FAST/SPS deformation, prevention of the carbide layer forming became the next problem to address.

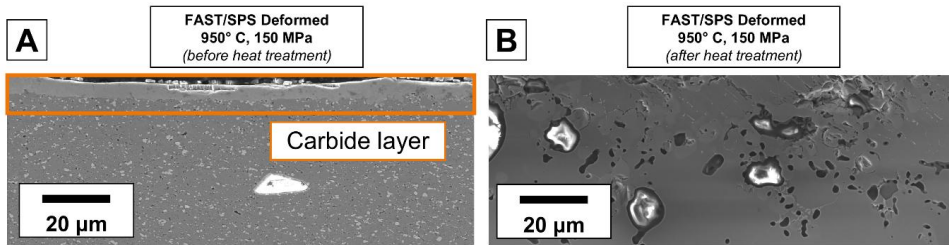


Figure 5.11 – SE SEM images of A. a PS2-D sample directly after FAST/SPS deformation and B. the same sample after austenitization at 1220 °C, quenching and tempering

From these experiments onwards, any graphite foil that was meant to be in contact with the steel swarf during the sintering process was coated with boron nitride (BN) spray. Prior to the graphite foil being placed into a die, it was sprayed 2-3 times evenly with BN, with several minutes between coatings to allow the layer to dry. This allowed for a barrier between the graphite and steel during the FAST/SPS cycle. EDX analysis showed that this barrier was successful, with a clearly visible boron-rich region at the surface of sintered PS2-D samples as indicated in Figure 5.12. The carbon analysis, seen in red, primarily reflects the epoxy the sample was embedded into. GD-OES measurements, performed by Felix Grosswendt at Ruhr-Universität Bochum, corroborate this occurrence. As seen in Figure 5.13, the addition of the BN barrier cut down the diffusion of carbon significantly when comparing the sample without (Figure 5.13A) and with (Figure 5.13B) coating. C-values remain higher than the nominal content (Table 5.1) at the immediate surface, so it is possible that irregularities or cracks in the BN barrier coating do not mitigate carbon diffusion entirely. Regardless, the influence of carbon diffusion was cut down enough to no longer form a carbide shell during sintering or melt phases at the sample surfaces during heat treatment. A slight diffusion of N, from the BN coating, also occurs as a side effect, but this is considered to be negligible for the chosen application.

While the deformation experiments proved successful with PS densification, even in its raw, un-milled state, this processing route would not be practical for scale-up. The large-scale FAST/SPS device, the Dr. Fritsch DSP515, would not be able to achieve 150 MPa of pressure on a Ø 120 mm form as its maximum applied force is roughly 550 kN. From these experiments, it became clear that FAST/SPS sintering of the PM T15 swarf within this project could only be performed with a BN coating on the graphite foils. However, large-scale FAST/SPS sintering had to return to single-stage FAST/SPS, which had to be further optimized in the following experiments.

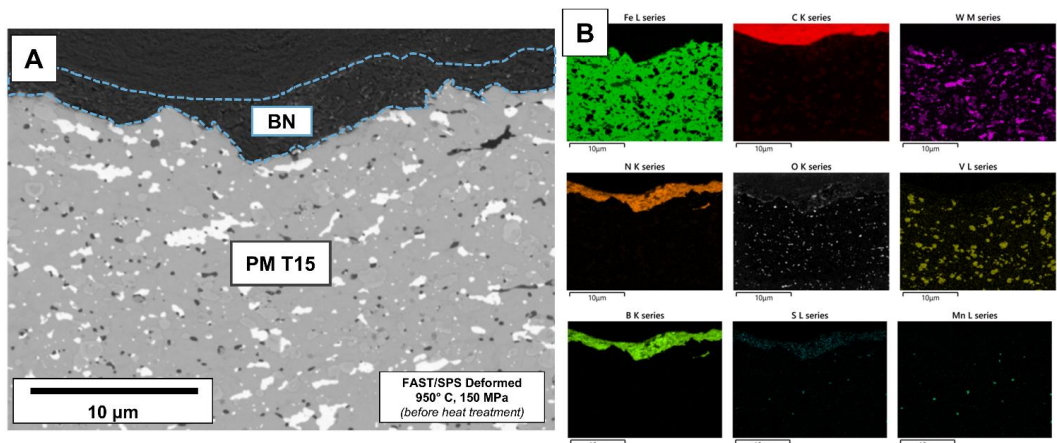


Figure 5.12 – A. SEM image of a PS2-D sample deformed at 950 °C under 150 MPa while in contact with BN-coated graphite, with a BN layer indicated by a dotted blue line, and B. EDX mapping of various elements, showing the distinct BN layer and isolation from carbon diffusion

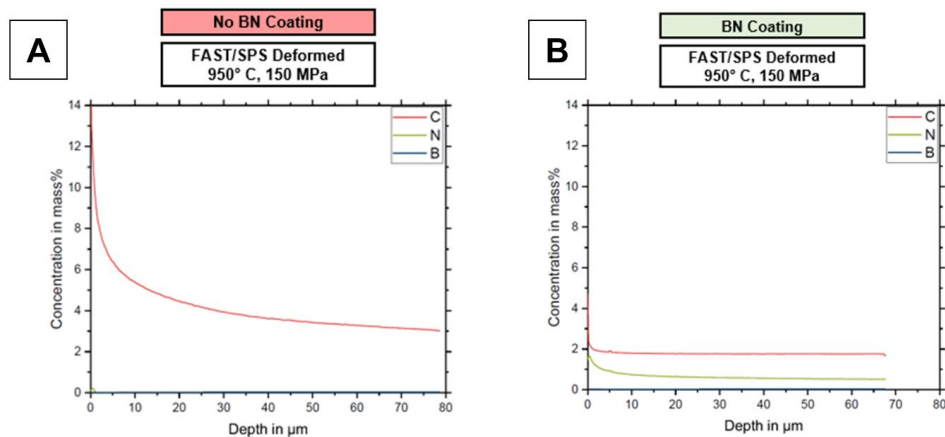


Figure 5.13 – GD-OES measurements of C, N, and B at the surface of PS samples deformed A. without a BN coating and B. with a BN coating

5.3 FAST/SPS Scale-Up to a Demonstrator Part

Preliminary FAST/SPS experiments in Section 5.2 helped in identifying the limits of PM T15 swarf sintering, including the possible formation of a melt phase and a large lip at temperatures above 1050 °C. Before starting scale-up, further minor adjustments were made in the sintering parameters on a Ø 20 mm sample, summarized in Table 3.13. These experiments led to several observations:

- Lowering the dwell time while maintaining the standard pressure and temperature (50 MPa and 950 °C) did not affect densification. Samples sintered with a dwell time of 1 minute had a density of roughly 7.73 g/cm³, and samples sintered with a dwell time of 5 minutes had a density of roughly 7.75 g/cm³. Average lip height did decrease from 1.5 mm (5 min dwell) to 0.8 mm (1 min dwell).
- Lowering the pressure to 10 MPa caused the sample to have a density of only 7.19 g/cm³. Samples sintered at 50 and 25 MPa of pressure did not differ greatly in density. Therefore, the sintering pressure should be kept at roughly 50 MPa, when possible.
- Sintering at 1050 °C again caused portions of the sample to melt, leading to molten leakage within the die. This was even with the use of the BN spray, showing that hotspots, carbon diffusion, or a combination of both were still causing some liquid phase to form. Therefore, it was decided to choose a constant sintering temperature of 950 °C in the following trials.

With these optimization trials completed, the sintering parameters for sintering large-scale PM T15 and D2 disks were established. As the density did not change significantly between samples sintered with a 1-minute and a 5-minute dwell time, it was decided to sinter initially with a 1-minute dwell to reduce energy consumption during the process.

5.3.1 Process Design and Troubleshooting

Sintering of large-scale disks started with a Ø 100 mm graphite form and using D2 steel rather than the less readily available milled PSM. The sintering of D2 was performed using the parameters listed in Table 3.14. These samples, referred to as “D2-100”, were initially sintered using the 5-minute dwell rather than the newly established 1-minute dwell. This longer dwell time helped to examine whether extended time in the FAST/SPS device would lead to the formation of a lip. No lip was formed during sintering, and extraction of the disk from the graphite die had no removal issues or tool breakage. An as-sintered D2-100 disk is pictured in Figure 5.14. Density of these samples ranged from roughly 5.6-5.9 g/cm³, with variations in the densities due to the different amounts of grinding waste sintered within each sample. This is considerably lower than the nominal density of D2 (7.7 g/cm³), indicating already

that the sintering parameters would not lead to a one-to-one scale-up. At the \varnothing 100 mm stage, the major issue that required troubleshooting was some unevenness in height at the sample edge. This occurred when graphite foil folded in from the circumference of the disk and was wedged against the steel powder, creating an indent. On observation of this issue, better care was taken on the insertion of the punches to prevent the circumference foil from breaking and folding in.



Figure 5.14 - \varnothing 100 mm D2-100 disk viewed from the side and from the face (FAST/SPS temperature: 950 °C, pressure: 50 MPa, dwell: 1 min)

With confirmation of favorable performance from the \varnothing 100 mm die, work transitioned to sintering the D2 steel in the \varnothing 120 mm graphite die, with the samples referred to as “D2-120”. Transition from the smaller to larger diameter was not one-to-one, however. With the post-sinter density of the D2 steel being on average 5.7 g/cm³, and with a target final height of 3 mm, 250 g of D2 was utilized for the \varnothing 120 mm disk. The tolerance of the \varnothing 120 mm punches and dies available at the institute could not handle the 0.38 cm thickness graphite foil, especially not after the addition of a BN coating. If punches could be inserted into the die with the coated foil, they often became so trapped that they could only be removed by hydraulic press. This would cause a variety of issues with sintering of the steel. Firstly, as punches could not be manually pressed down to be in direct contact with the swarf due to the friction of the BN coating, the swarf could shift and become unevenly distributed during transport to the FAST/SPS device. Uneven distribution of powder led to an uneven distribution of force, and, in this case, a higher pressure point in the swarf resulted in cracking and breaking of the graphite punches. Secondly, once the punches were successfully pressed in via pre-pressing, they could not be manually removed. This meant that other errors, such as loose swarf between the punches and folds in the graphite foil, could not be examined and addressed before sintering. Consequences of these issues are seen in Figure 5.15.

After consultation with Dr. Fritsch GmbH, the thickness of the circumference graphite foil was lowered from 0.38 mm to 0.25 mm in thickness. Several techniques were introduced to level out the swarf inside the die before lowering in the upper punch, such as smoothing with a specific smoothing tool, tapping, and running a paintbrush or espresso comb along the edge of the swarf to break up and remove swarf clinging up the inner wall of the die.

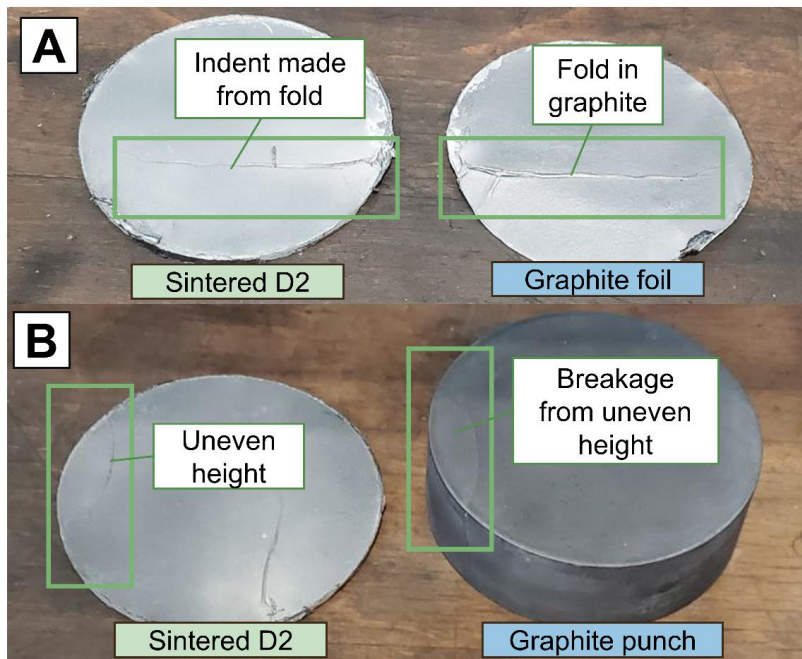


Figure 5.15 – D2-120 samples and their irregularities, including A. a crease made in the steel from a fold in the graphite and B. uneven height distribution leading to a broken graphite punch

With these new techniques established, milled PM T15 (PSM) was used for ongoing studies instead of D2. Though many issues had been addressed by replacing the thick foil with a thin one, and by leveling the swarf, new issues arose with the introduction of PSM. As PSM was smaller and not as agglomerated as the D2 swarf, it was much more mobile when poured into the die cavity. This caused it to escape through the crevices during pre-pressing and settle in between the graphite punch and the protective graphite foil. If swarf residuals were not thoroughly cleaned from the punch, they often reacted with the graphite punch, creating a region of lower electrical resistance for the next FAST/SPS cycle. The movement of more electricity through these zones during FAST/SPS then created hotspots in specific points of the next swarf disk, melting the swarf in these specific zones during the FAST/SPS cycle. These melted zones would then cool into raised points on the face of the sample, once again creating a pressure point that would break the graphite punches when pressure was applied. An example of this is

seen in Figure 5.16. The formation of a melt phase was confirmed via SEM cross-section, as seen in Figure 5.17. Red arrows indicate roughly the area that was the hottest, with the molten phase radiating into the bulk of the sample. This analysis showed that the hot spot was isolated to the side of the sample in contact with the faulty punch and did not fully dissipate through the thickness of the sample.

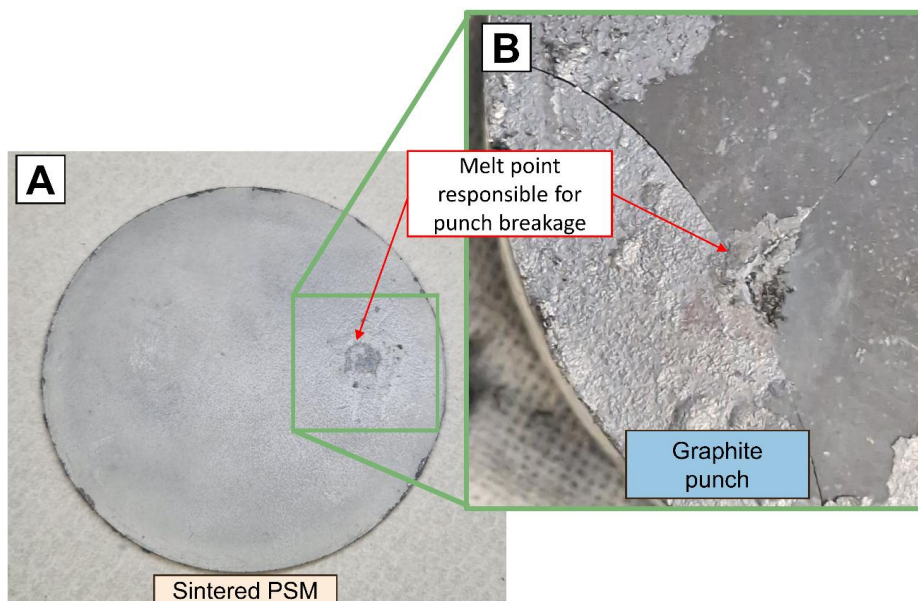


Figure 5.16 – Photos of A. a PSM-120 sintered disk, made of milled PM T15 swarf (PSM) with a raised portion on the sample face and B. a crack on its graphite punch corresponding to the raised region on the sample (FAST/SPS temperature: 950 °C, pressure: 50 MPa, dwell: 1 min)

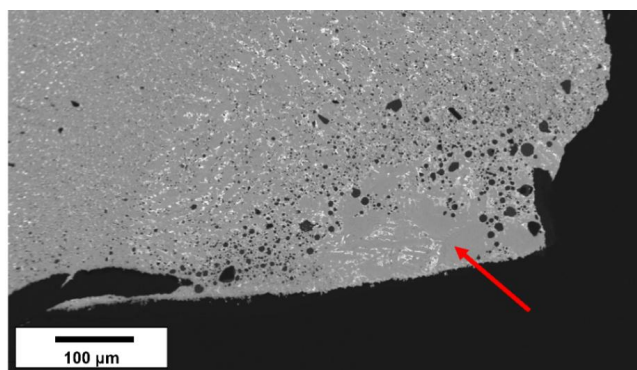


Figure 5.17 – BSE SEM analysis of the melted point on the PSM-120 sample, with the hotspot indicated roughly by a red arrow

Further improvements needed to be implemented with the nature of the PSM considered. The first improvement made was the removal of several centimeters of BN coating from the upper and lower portion of the circumference graphite foil. This created less resistance for the insertion and removal of the graphite punches, making it easier to take out the punches for thorough cleaning with ethanol after pre-pressing. The second improvement was to increase distance between the graphite punches and the swarf with the addition of more face foils. After the initial face foil with a BN coating was placed on top of the swarf, three additional foils of 0.38 mm thickness each were stacked on top, creating a barrier roughly 1.4 mm between the graphite punch and the swarf. If any swarf were to escape the die cavity and seep up the inner die wall, it was expected to be trapped within one of the layers of graphite foil and not react with the face of the graphite punch. An exploded-view diagram of the final \varnothing 120 mm FAST/SPS tool used for all subsequent steel sintering experiments is shown in Figure 5.18.

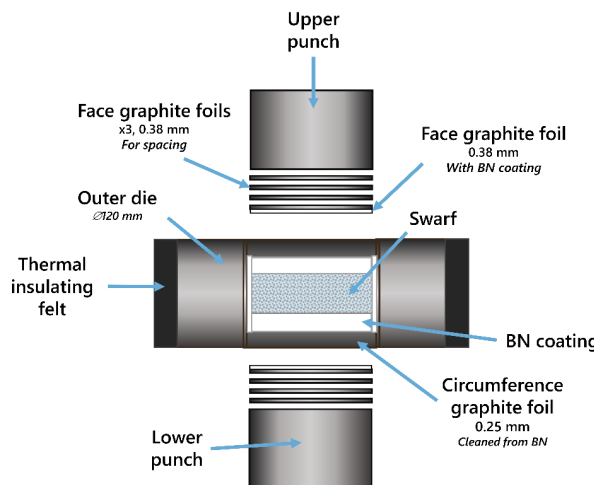


Figure 5.18 – Exploded-view diagram of the final \varnothing 120 mm die set-up for PSM-120 sintering

Based on \varnothing 20 mm sintering of PSM, it was initially planned for all PSM-120 samples to be sintered with a dwell time of 1 minute, as it was assumed that the density would not change for a shorter dwell time. Scale-up to \varnothing 120 mm, though, showed a stark difference in density between 1- and 5-minute dwell times. The densities for \varnothing 20 and \varnothing 120 mm samples sintered with differing dwell times are listed in Table 5.3. The 0.1 g/cm³ increase seen between PSM-120 and both \varnothing 20 mm samples could be attributed to a number of reasons, including a possible lower volume of grinding waste contamination or the leveling of the swarf leading to better force distribution during sintering. The difference between PSM-120 samples of 1- and 5-minute dwell, though, is more than likely due to the extended dwell period allowing for better pore closure and more time for mass transfer to occur. This evidence led to

the decision to sinter the demonstrator part with a dwell time of 5 minutes rather than 1 minute, even though this would increase the energy consumption during the FAST/SPS process. Nevertheless, the higher density would lead to easier and more efficient post-processing.

To allow for more tolerance for any small dents generated from folded foil, the mass of PSM powder used to sinter PSM-120 disks was increased from 250 g to 275 g. This increase did not have a noticeable effect on the final density. Height increased post-sinter from roughly 3.1 mm to 3.3 mm with the increase in mass. All PSM-120 samples designated for heat treatment and shaping were sintered with 275 g of PSM.

Table 5.3 – Comparison between PSM sintering diameters, dwell times, and final densities
(FAST/SPS temperature: 950 °C, pressure: 45 MPa)

Diameter (mm)	Dwell time (min.)	Density (g/cm ³)
20	1	7.73
20	5	7.75
120	1	7.85
120	5	8.05

Figure 5.19 displays photos of the PSM-120 disks directly after extraction from the Ø 120 mm die. The PM T15 surface is still coated with residual BN, making the disks appear a foggy white. This residual BN is removed via sandblasting prior to heat treatment. SEM images of different points within the disks are shown alongside of the photographs. While the density of both disks appears visually very similar, the PSM-120 disk sintered for 1 minute had a higher frequency of pores found during examination. In both samples, density across the cross-section appeared fairly consistent, with only a slight increase in pore appearance at the sample edges. Despite a thermal gradient likely forming during the FAST/SPS sintering process, no major microstructural inhomogeneities were observed.

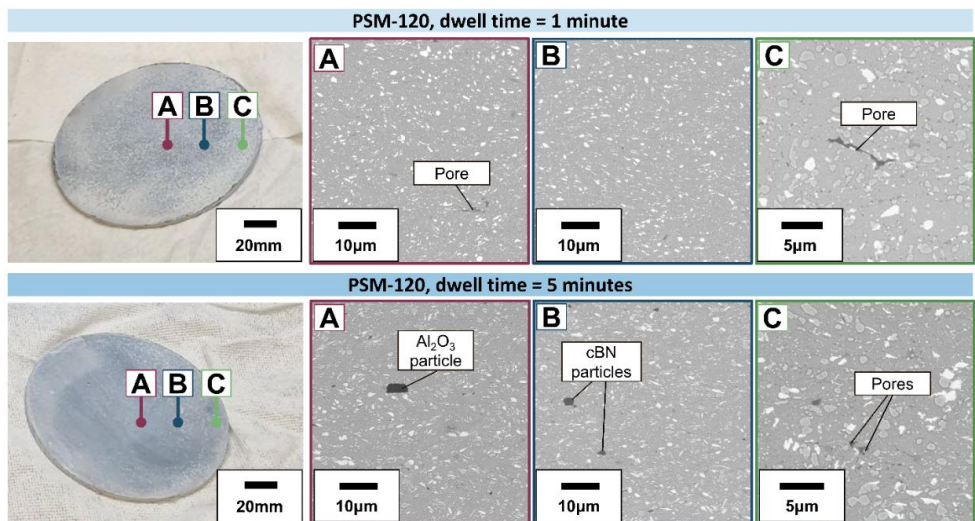


Figure 5.19 – Photos of PSM-120 disks sintered at dwell times of 1 minute (top) and 5 minutes (bottom), along with SEM images of the sample A. center B. off-center and C. edge, with grinding particles and pores labeled

5.3.2 Heat Treatment and Demonstrator Part

After FAST/SPS sintering, an inner hole of \varnothing 80 mm was cut from the center of the disk by water jet cutting at RUB. The inner portion of the disk was then used for a variety of static and cyclic mechanical tests, which have been performed and described in detail by Treppmann [174]. Heat treatment was performed on both the inner and outer portions of the disk following the steps described in Section 3.3.5, which, for convenience, are reiterated in Table 5.4. In the case of the PSM-120 disks, the austenitization temperature had to be lowered from a more typical temperature range of 1175-1225 °C [176]. As measured and described by Treppmann [174], this is due to the effect of the excess carbon content on the stable phases, shown previously in Figure 5.5. Increased carbon content affects the austenite stability and carbide formation. The adjustment in temperature helped to avoid excessive solute C from leading to excessive retained austenite (RA). The presence of RA would decrease the hardness of the final sample. As seen in Section 5.2.2, 1220 °C austenitization of \varnothing 20 mm samples led to poor microstructure. Therefore, it was decided to lower the austenitization temperature to 1170 °C for the PSM-120 disks.

Table 5.4 – Heat treatment stages and temperatures for standard PM T15 and PSM-120

Sample	Austenitization	Quenching	Tempering
Standard PM T15	1215 °C	Quenching in oil	540 °C for 2 hours (x4)
PSM-120 disks	1170 °C	Quenching in oil	540 °C for 2 hours (x4)

In the swarf, prior to sintering, excess C could be attributed to binder from the grinding wheels, residual lubricant oil, or other organic material the swarf is exposed to during processing. After FAST/SPS sintering, it is observed that the C-content of the Ø 120 mm disks stays relatively stable at roughly 1.7 wt%, which almost fulfills the standard for nominal PM T15. However, this slight increase in carbon does affect phase stability. While it is expected that organic material would be burnt off by the FAST/SPS process, the sintering duration may not have been long enough to allow gases from the burnt organics to escape. The duration may also have been so short as to not even burn some long-chain polymer binders that may have been present on the grinding wheels. It is also possible that some of the BN coating is scraped off by the swarf during sintering, exposing the graphite foil once again to the steel in some regions of the sample. Though the exact cause of the excess carbon is not specifically known, it regardless influences the behavior of the sintered steel.

As seen in Figure 5.5, reference PM T15 has a 0.6 mass% solute C at its austenitization temperature of 1215 °C. The PSM-120 sample, with its higher C-content, would have a 0.67 mass% solute C at this temperature. Solute C contents greater than 0.6 mass% promote excessive austenite retention after quenching. Therefore, it was deemed impractical to have the PSM-120 samples austenitized at the standard temperature of 1215 °C, and the austenitization temperature was chosen to instead be 1170 °C. At this temperature, solute C within the PSM-120 disks would be at the target 0.6 mass%. While this temperature is quite lower than optimal, it only sits 5 °C outside of the recommended austenitization temperature range for T15 [176].

Excess carbon not only influences the austenitization but also the solidus temperature. As seen in the small-scale FAST/SPS trials of Section 5.2.1, swarf in contact with carbon from the graphite tools behaved with greater ductility, with melt occurring in some cases, even at set maximum sintering temperatures of 1050 °C. While this behavior could be blamed on the inhomogeneity of Joule heating within the sample, it could also be due to the high carbon uptake influencing the steel. According to the ThermoCalc calculations, even the slight increase from 1.6 mass% C standard in PM T15 to the 1.7 mass% C in PSM-120 caused the solidus temperature of the PM T15 swarf to drop to 1222 °C. Attempting to austenitize the PSM-120 disks at the standard temperature of 1215 °C would cause partial

melting, leading to eutectic carbide networks [177]. These networks would subsequently decrease toughness, cause warpage, and distort the shape of the disk [178].

After austenitization, quenching and tempering, the hardness of the PSM-120 disk exhibited a hardness of 869 ± 23 HV30. This is approximately 9% lower than the hardness of the reference sample, which had a hardness of 955 ± 2 HV30 [174]. This discrepancy could be due to the PSM-120 disk not achieving 100% density or due to the greater presence of oxides in the recycled part. It is clear that the addition of the grinding material, such as Al_2O_3 , did not synergistically improve the hardness. Rather, Al_2O_3 inclusions led to local high stresses due to their sharp edges, which are expected to lead to crack formation at a lower cycle fatigue range when compared to the PM T15 reference [174], [179], [180]. Presence of the grinding material in the metal matrix also reduced the mean free matrix path length, leading to an increased acceleration of crack propagation [174]. Nevertheless, the PSM-120 disk showed similar compressive yield strength as the PM T15 reference. The master thesis of Michelle Treppmann of RUB contains further details, which are summarized in a recent publication (in submission).

5.3.3 Operation of the Demonstrator Part

Operation of the demonstrator was initiated by M. Treppmann and, afterwards, continued by F. Grosswendt of RUB. The heat-treated PSM-120 disk, with the inner diameter of 80 mm removed, was then installed into the mock-tunneling rig at Ruhr-Universität Bochum and exposed a static load of 2500 N, with bumps of up to 5000 N, against a sandstone pillar for 20 minutes. The resulting mass removal of the sandstone pillar is listed in Table 5.5. Over this 20-minute period, the PSM-120 disk was able to remove 424 g of sandstone. The PM T15 reference disk, made from HIP of gas atomized powder, removed 219 g. Though the PSM-120 disk was able to remove nearly double the amount of sandstone, this came at the expense of the edge of the disk degrading. Figure 5.20 shows the resulting chips of metal breaking away from the disk after only 5 min of testing cycle operation. This has both benefits and disadvantages. As a benefit, the disk behaves as if it is “self-sharpening.” As pieces of the edge break away, a thinner edge is put in contact with the sandstone pillar. This thinner edge leads to an increase in applied pressure to the sandstone, and an increased pressure helps in removing more material. This increased thinness can be seen in Figure 5.21B, where a light microscopy image of the PSM-120 disk edge is displayed.

The major disadvantage of the loss of mass is the subsequent loss of operating time. The PSM-120 disk can only operate so long before the majority of its mass breaks away, and no microstructural mechanism is put in place within the disk to halt the self-sharpening. The quick wearing away of the disk means that, in a realistic tunneling scenario, more disks would need to be on-hand for replacement, and frequent operational downtime would be needed for disk replacement.

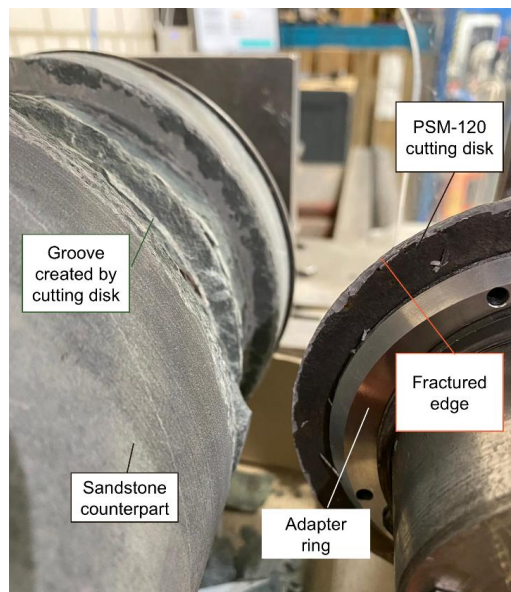


Figure 5.20 – PSM-120 disk displaying a fractured edge after 5 minutes of simulated tunneling against a sandstone counterpart. Photo by F. Grosswendt of RUB.

Table 5.5 – Amount of sandstone removed by each disk and how much mass of each disk was lost in the 20 min testing cycle

Disk type	Sandstone removed (g)	Disk mass loss (g)
PM T15 reference	219	0
Recycled PM T15	424	0.9

Part of the increased fracture frequency of the PSM-120 disk could be attributed to the angular corundum inclusions. However, as seen in Figure 5.21C, not all cracks form solely due to corundum inclusions. Weakness in the material could also be due to a high percentage of oxides formed from the PM T15 swarf itself. These oxides may have formed from oxidation of the swarf during any portion of pre-processing, such as the grinding process itself, milling, or acetone cleaning. Minimizing oxides in the steel swarf prior to sintering may be necessary to improve the behavior of recycled steel disks.

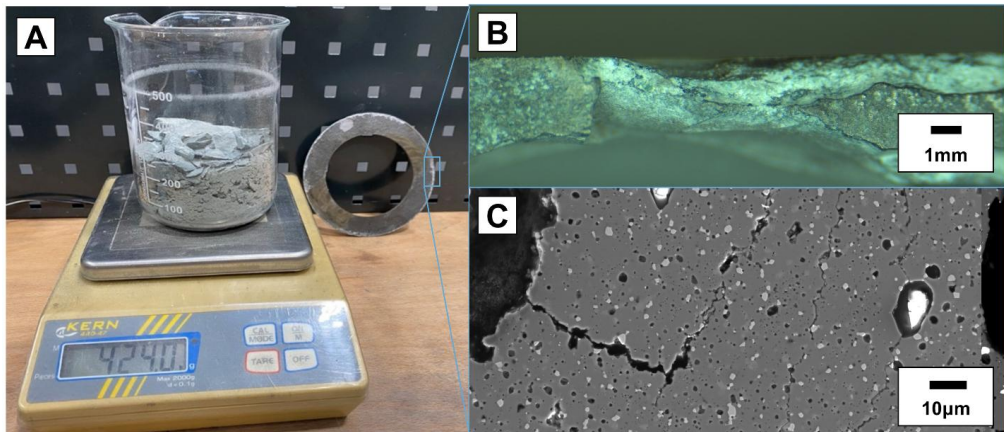


Figure 5.21 – A. Photo of a beaker holding the sandstone material removed by the PSM-120 disk, with the PSM-120 disk in the background after 20 minute tunneling test, B. light microscopy image of the PSM-120 edge after testing, and C. SEM image of the PSM-120 edge after testing, showing cracks. Experimental work by M. Treppmann with continuation and photos by F. Grosswendt, RUB.

5.4 Energy Consumption and Life Cycle Analysis

Similar to the Nd-Fe-B magnets, the production of these disks via FAST/SPS also has a high energy consumption per kg of material when compared to industrial processes for manufacturing cutting disks through powder metallurgy. Figure 5.22 displays the energy consumption of the Dr. Fritsch DSP515 device and its cooler over a PSM-120 cycle with a 1-minute dwell time. The FAST/SPS device and its cooler consume 8130 Wh and 4660 Wh respectively, totaling to roughly 12.9 kWh of energy consumed during the cycle. As the PSM-120 cycle has a dwell time of 5 minutes, extrapolation would further increase the energy consumed by 3300 Wh, leading to an energy consumption of roughly 16.3 kWh. With each recycled disk having a mass of 275 g, this leads to the energy consumption per unit mass being 59 kWh/kg. This value is roughly tenfold the estimated powder metallurgical energy consumption, which, according to literature, is 5.0 kWh/kg per “typical” PM part [181]. Sintering multiple disks at once by using a respective multiple tool design would be a promising measure to lower this value [182].

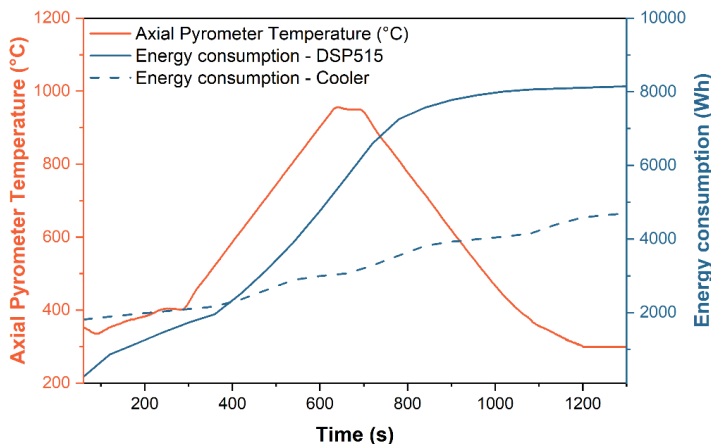


Figure 5.22 - Energy consumption of the Dr. Fritsch DSP515 device and its cooler over a PSM-120 FAST/SPS sintering cycle, 1 min dwell time

In tandem to the FAST/SPS production of the PM T15 steel swarf disks, life cycle analysis (LCA) was carried out by ANTS of RWTH Aachen. Using cradle-to-gate analysis and ReCiPe 2016 v1.03 (midpoint), production of a \varnothing 120 mm disk with a mass of 150 g through both the recycling route and traditional metal production were compared. The team used the OpenLCA 2.0.3 software and the EcoInvent v3.10 database for calculations. Literature-based information regarding material losses was utilized for the industrial route of casting and machining, while material losses on the lab-scale could be measured for the recycled disks. Their findings showed that the utilization of FAST/SPS as a

recycling route led to a much greater cumulative energy demand in comparison to the conventional route, alongside a much greater global warming potential and water consumption potential. The reason for this is attributed to the high energy consumption of FAST/SPS needed to process only one disk. Despite avoiding the re-melting of the steel material, sintering via FAST/SPS requires a high energy input for its quick heating rate, and, at the moment, only one disk can be produced with every FAST/SPS cycle. If the process could be scaled that the energy input could lead to multiple disks being produced, this issue could be mitigated. Better still, if the energy input for the FAST/SPS cycle came from 100% renewable sources, the two processes would be slightly more comparable. Upstream, the washing of the steel swarf with acetone is also a large contributor to the power and water consumption potential and global warming potential of the recycling route. Recycling the used acetone, or transitioning to a greener solvent, may help to lower these values [183].

5.5 Summary

Direct recycling of contaminated PM T15 swarf into a new cutting disk is possible by FAST/SPS processing. The morphology and contaminant content of the swarf does dictate the effectiveness of the FAST/SPS sintering, however. For one, the initial, tendril and spring-like morphology of the metallic flakes inhibits full densification and adds difficulty to the filling of FAST/SPS dies. Successful densification of the spring-shaped swarf was only possible through the use of two-step FAST/SPS pre-sintering and deformation. Once the swarf was milled to more manageable flakes, die filling and scale-up became more feasible.

Sintering of the PM T15 in graphite dies lined with graphite foil led to carbon diffusing into the steel. This affected the phase stability of the steel and changed its thermodynamic behavior. A combination of carbon diffusion and the thermal gradient or hot spots during FAST/SPS would even occasionally lead to a liquid phase forming, causing issues for sample extraction. These issues could be mitigated through the use of a BN spray separating the steel from the graphite. All scaled-up FAST/SPS experiments utilized this BN spray to prevent excessive carbon contamination.

The final FAST/SPS parameters used for the sintering of full-scale \varnothing 120 mm disks included a maximum temperature of 950 °C reached after a ramp of 100 K/min and held for 5 minutes. A pressure of 45 MPa was applied and held over this period. After cooling, the disk was heat-treated with a PM T15 heat treatment modified for the disk's increased carbon content. After shaping and testing on the RUB mock tunneling rig, the disk was able to remove more material from a sandstone cylinder than a reference disk made from HIP gas-atomized PM T15. This was due to a "self-sharpening" effect, as pieces from the recycled PM T15 disk would chip off from its edge, and the thin edge would exert more pressure on the sandstone. This can be viewed as both a benefit and a disadvantage. If the self-

sharpening could be controlled, the disk could be perceived as more attractive to use. If it cannot be controlled, the disk will eventually wear itself away and need to be frequently replaced. The propagation of cracks inside the disk, causing material to break off, is attributed to both the Al_2O_3 inclusions and high amount of oxides.

In short, while FAST/SPS is a successful process to generate disks from contaminated swarf, improving the quality of these disks lies primarily in improving the swarf itself. Reducing oxide contamination, removing any residual grinding medium, and milling the swarf to a manageable morphology would all assist in the ease and improved behavior of future disks.

6 Conclusion and Relevance to Industrial Application

Electric current assisted sintering (ECAS) processes are promising for the sintering of powders which are difficult to process by any other methods. This makes ECAS attractive for the direct recycling of metal swarf from end-of-life products or metallic waste from mechanical machining.

6.1 ECAS in Hot-Deformed Nd-Fe-B Recycling

Previous work on FSPS deformation of commercial MQU-F powder has shown the possibility of achieving or even surpassing the magnetic performance of hot-deformed magnets, with optimization leading to a $(BH)_{\max}$ of 350 kJ/m³ [87]. SPT of MQU-F has also been shown to achieve a $(BH)_{\max}$ of 353 kJ/m³, with some uncertainty as to the possibility of scale-up [170]. While the focus of this work was not to find an alternative to hot deformation for commercial magnets, findings did reiterate that a possibility exists for ECAS to generate hot-deformed magnets with competitive performance. Figure 6.1 displays the remanence and coercivity of all magnets generated from 100 wt% MQU-F in this work. Many FSPS samples approached the target values ($B_r \sim 1.3\text{-}1.4$ T, $H_{cJ} \sim 1300\text{-}1400$ kA/m) despite parameter optimization being specifically tailored to work for anisotropic scrap material. Further investigation of FSPS with a BN die could be viable for increased remanence in FSPS deformed MQU-F. This route was ultimately not pursued due to persistent die breakage from the deformation of pre-forms made from 100 wt% recycled material. However, potential still exists for optimizing FSPS within a specifically designed die for improved magnetic performance with commercial powder.

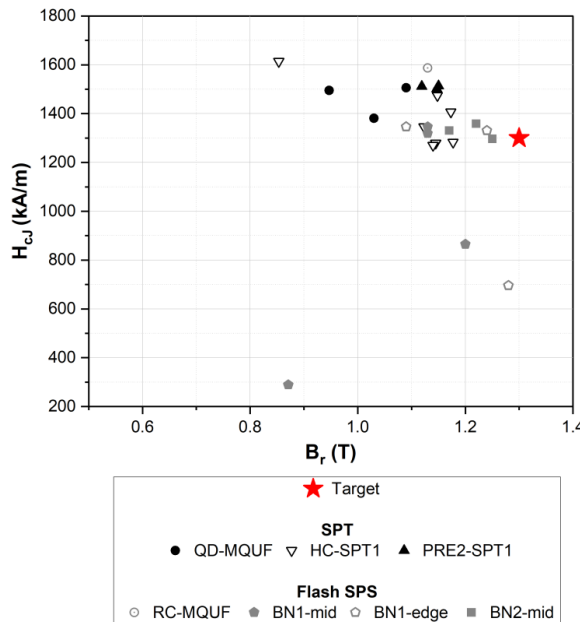


Figure 6.1 - Remanence and coercivity values for all samples generated with 100 wt% MQU-F powder in this work

The most industrially attractive aspect of this work is certainly the confirmation that ECAS processing can produce functioning magnets from 100 wt% recycled hot-deformed Nd-Fe-B scrap material. Figure 6.2 displays the magnetic performance of all samples made from 100 wt% recycled material in this work. The SPT4 series, in this case, is the closest to the target values of all samples. Further optimization to the hot-compacting and deformation could likely synergize and lead to performance closer to the target values. Scale-up has also been shown to be possible using SPT deformation, as magnetic performance was either equivalent or improved with the use of a larger deformation die. The possibility exists that a sample made from 100 wt% recycled material could be deformed to a much larger diameter, such as \varnothing 100 mm or greater. Afterwards, bar magnets of a desired size could be cut from the disk. This, however, depends largely on if the magnetic performance could be homogenous across a disk at such a wider scale. Further investigation in this direction would be necessary to make this production route attractive to industry.

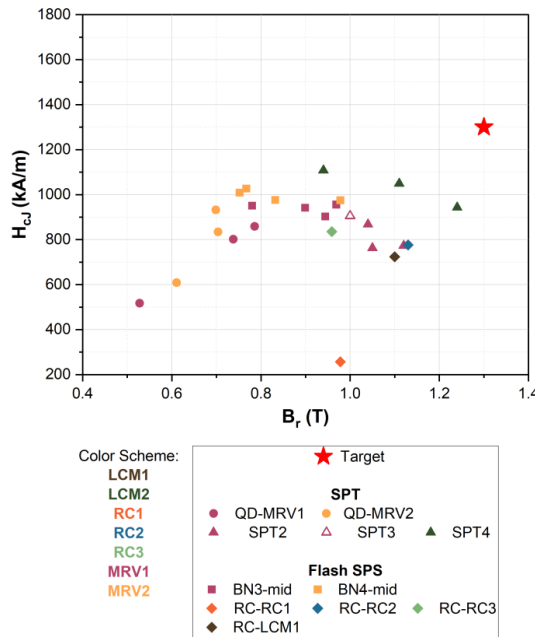


Figure 6.2 - Remanence and coercivity values for all samples generated with 100 wt% recyclate powder in this work

As a compromise, mixing recycled hot-deformed Nd-Fe-B scrap with commercial Nd-Fe-B melt-spun powder can improve the magnetic performance. If an industry is targeting only a certain wt% of material to be recycled, without sacrificing too much in terms of performance, this option is the most viable. Figure 6.3 displays the magnetic performance of all samples generated from mixed recycled and commercial material generated in this work. In the RC-series, shown as the half-filled diamonds in Figure 6.3, MQU-F was systematically varied in 95, 90, 85, 80, and 50 wt%. The cluster around 1.1 T contains the samples with >50 wt% MQU-F, while the outliers are the 50 wt% MQU-F samples. This indicates that increasing the amount of commercial Nd-Fe-B powder leads to more viable magnets with better performance. The FSPS samples appear to have a high coercivity and $B_r > 1$ T, but their mechanical stability may deem them unattractive for use. Using 75 wt% MQU-F for the SPT4-25 series brought samples closer to target than before. As with the 100 wt% recycled magnets, synergistic and simultaneous optimization of both the pre-forming and deformation steps could bring these values even closer to the industrial target.

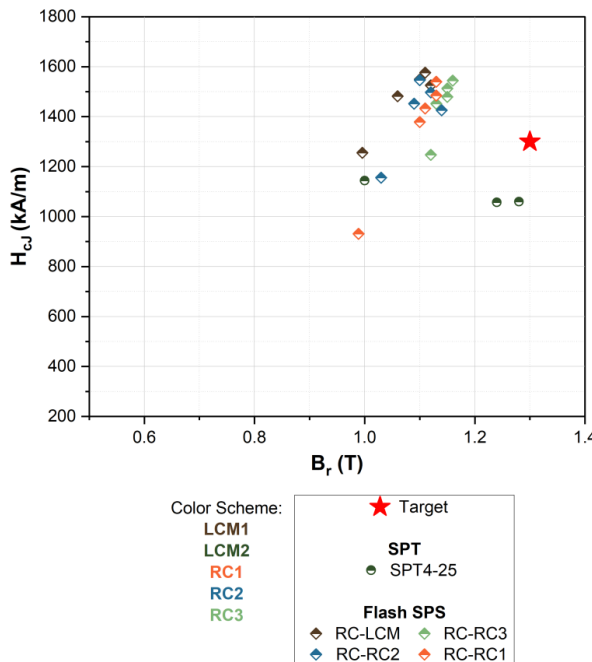


Figure 6.3 - Remanence and coercivity values for all samples generated with mixed recyclate and MQU-F powder in this work.

Figure 6.4 is given to directly compare the ECAS generated recycled samples to standard sintered Nd-Fe-B magnet grades. While the magnetic performance does not correspond with the target grades, the 100 wt% recycled magnets are still viable for use as N38 and N35 grade Nd-Fe-B magnets. Mixing in commercial material with the recycled material improves the performance enough to also include the N40 grade. If the recycled N35 grade magnet were to be used in a wind turbine, for example, it would be cheaper than any “H” grade magnet per MWh, but it would require more magnet mass than any higher-grade magnet. This increase in mass is due to N35’s lower energy density, $(BH)_{\max}$. Plus, it would be need be constantly kept below 80 °C, as magnetic performance is influenced by temperature [172], [184]. N35 magnets are typically used in consumer goods such as electronics, magnetic therapy products, magnetic toys, and magnetic closures [185]. Therefore, generating 100 wt% recycled hot-deformed magnets would also mean repurposing them entirely, requiring them to be used in a lower-temperature application due to both their lower strength and their risk of demagnetization at high temperatures.

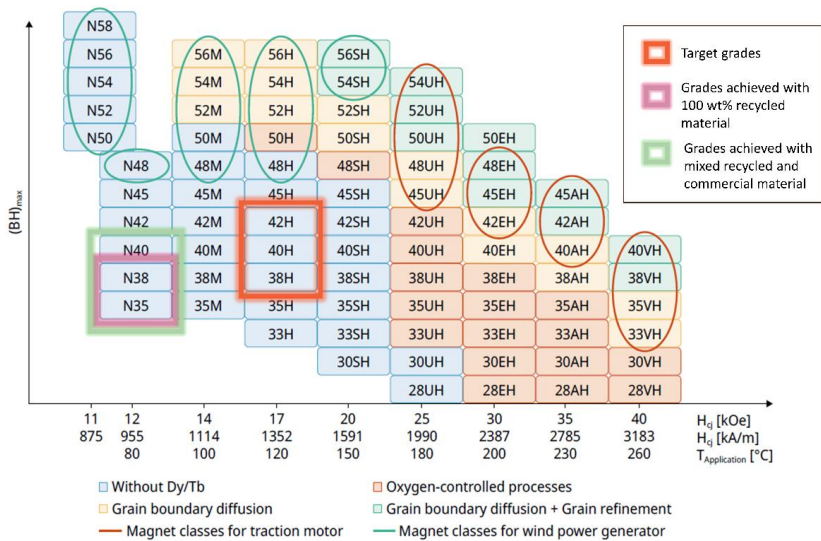


Figure 6.4 - Commercially available Nd-Fe-B magnet grades with details of typical magnetic parameters and operating temperatures. Target grades of this project and achieved grades are highlighted based on the legend to the right. Graph modified from [186], originally based on [120], [187].

Another important aspect for industry to be aware of is the particle size fraction of the Nd-Fe-B scrap they wish to reuse. As explained in Section 4.2.1, the results for mixed recyclate FSPS samples, sieving out the fine fraction of $<125\text{ }\mu\text{m}$ scrap led to increased magnetic performance. While this work did not explore a solution for this “dust” fraction, it could be of most use in leaching due to the high surface area-to-volume ratio of fine powder. For the moment, the oxygen content in this fraction is too high for direct recycling. Thankfully, this means that an industry would not need to put in a massive amount of energy to crush scrap magnets into a fine powder. It has been demonstrated in this work that FAST/SPS can handle relatively coarse powder, and that the best performing recycled magnets come from a particle size around $200\text{ }\mu\text{m}$. Ideally, the “dust” fraction would be low if crushing steps are optimized for generating roughly $200\text{--}500\text{ }\mu\text{m}$ particles. Still, if complete recycling is the goal, more work is needed to determine the fate of powder that is too small for direct recycling.

In Section 4.4, the energy consumption of the different ECAS deformation processes, FSPS and SPT, were compared. The conclusion was made that, considering the samples produced in this work, the SPT process would produce more magnetic strength per Wh of energy consumed. What was also discussed in this section, though, is the fact that not all FSPS possibilities have been exhausted, including the FSPS of 30 g hot-compacted pre-forms. The current limitation of FSPS lies primarily in the volume of

usable magnet material it can produce, as FSPS samples made from 100 wt% recycled Nd-Fe-B often had poor structural stability at the edges with a limited densified center. Optimization of FSPS could lead to a more attractive industrial application than SPT. This is due to a variety of reasons. Firstly, FSPS does not require expensive specialized TZM tools. In tandem to saving on tool costs, FSPS would not need the labor time dedicated to lining the TZM tools with graphite foil or cleaning a sample of its graphite foil after deformation. SPT often requires additional cooling after the programmed cycle is completed, with the die often idling for an additional 15-20 minutes inside the FAST/SPS device to reach room temperature. FSPS samples, in contrast, are near room temperature after a 10-minute programmed cooling period, as there is little thermal mass trapping excess heat after the flash. In short, FSPS is a faster, less labor intensive, and more cost effective ECAS deformation technique than SPT. Dedicating further research to FSPS as an Nd-Fe-B recycling technique may make ECAS more attractive to industry. Reduction of the energy consumption of either ECAS will be key for industrial interest as well. Currently, both ECAS options consume nearly 1000x more energy than that needed for sintered Nd-Fe-B [173]. Scaling the technology to produce larger magnets or multiple magnets at once will be necessary to make it industrially feasible.

6.2 PM T15 Steel Swarf Recycling via FAST/SPS

Regarding the swarf itself, several improvements could be made to ensure better mechanical behavior post-sinter. For example, the corundum shed from the grinding wheels was embedded into the PM T15 matrix as an inert. However, the angular shape of these grinding particles contributed to weaknesses in the steel. If a milling stage is included to reduce steel swarf into a manageable morphology, perhaps some aspect of the milling could be modified to also round the corundum particles. Eliminating the sharp angles of inert inclusions could increase the strength of the composite material. Contrastingly, it may be more effective to remove the hard inclusions entirely by improved magnetic separation. Further improvements would also have to be made to control the amount of further oxides within the steel. The FAST/SPS process takes place under a vacuum of roughly 0.4 mbar. Literature has shown that high Cr alloys begin to experience a direct carbothermal reduction starting at a temperature of 800 °C under vacuum [188]. This means that the metallic oxide reacts with carbon to form the pure metal and carbon monoxide. In the case of the PM T15 swarf, using the excess C-content remaining from lubricant or grinding wheel binder as a reducing agent may be at first perceived as a viable option. This way, the C-content is lowered, and excess oxides are reduced. In reality, solving these issues is much more complicated and requires control of other process aspects, such as precise atmosphere control. The admixing of graphite within an oxidized steel alloy powder is often suggested as a way to reduce the oxides present. Utilizing the carbothermal reaction as a reduction path for iron oxide is only kinetically

effective above 900 °C, at which point admixed graphite will have already dissolved into the steel matrix [189].

The FAST/SPS processing of these disks also has a high energy consumption when compared to standard powder metallurgical processes, as discussed in Section 5.4. To make this process more attractive would mean further work on scale-up, such as the production of multiple disks at once. It would also require the isolation of a specific waste stream of a specific metal grade. As waste streams often get mixed together in industry, there would also need to be investment in waste stream segregation during the production of PM T15 tools. This could mean downtime for different machining processes in order to completely clean them of one waste before a different material is machined. Alternatively, it could mean machine lines designated to one metal only. This could be perceived as limiting production capacity and as economically disadvantageous. Regardless, a massive predictor of the quality of a directly recycled tool lies in the quality of the swarf to begin with.

7 Outlook

In this work, ECAS processes succeeded in two key goals. Firstly, ECAS was utilized to make hot-deformed magnets with 100 wt% recycled hot-deformed Nd-Fe-B material with a $(BH)_{\max} > 200 \text{ kJ/m}^3$. SEM analysis showed that SPT deformation was able to thermomechanically align anisotropic grains close to a new, desired alignment. Secondly, ECAS, specifically FAST/SPS, could generate $\varnothing 120 \text{ mm}$ cutting disks made from contaminated PM T15 steel swarf. These disks were heat-treated and tested on a mock tunneling device by M. Treppmann and F. Grosswendt of RUB. This tunneling demonstration showed the disks had a “self-sharpening” effect that allowed them to remove more sandstone than a reference PM T15 disk.

As of writing, no other process exists to directly recycle hot-deformed Nd-Fe-B scrap into new magnets. SPT has shown the potential to align the Nd-Fe-B grains to their desired orientation without excessive grain growth. This would not be possible, however, without a near-dense pre-form. Its internal structure must be dense enough to withstand the application of the deformation without crumbling, yet not so densified as to have large grains forming. Hot compaction via FAST/SPS at $600 \text{ }^{\circ}\text{C}$ were the most successful candidates for deformation.

In terms of the ECAS Nd-Fe-B experiments, potential still lies in the FSPS of Nd-Fe-B. Due to time limitations, FSPS of Nd-Fe-B pre-forms hot compacted at $600 \text{ }^{\circ}\text{C}$ was not performed. The shorter cycle time of FSPS and less stringent tool requirements make this an attractive next step in experimentation with recycled Nd-Fe-B. This work has made it clear that scale-up of ECAS Nd-Fe-B deformation is highly dependent on the initial pre-form density. As this observation was made quite late in the experimental series, there is still potential for further optimization. Regardless, demonstrator magnets made from 100 wt% recycled material and deformed by SPT were tested in a WILO SE rotor and produced 95% of the EMF generated by a rotor containing commercial hot-deformed Nd-Fe-B magnets.

Another interesting possibility for continued Nd-Fe-B recycling via ECAS is scaling up the SPT process. Depending on device limitations and material availability, it could be possible to SPT deform recycled Nd-Fe-B magnets to a much larger diameter, such as $\varnothing 100 \text{ mm}$. From a disk of this size, many more bar magnets can be extracted. Alternatively, the SPT process can be modified to deform Nd-Fe-B pre-forms into a bar magnet directly. This would come with challenges specific to the geometry of a bar magnet die, how the pre-form expands to fill it properly, and how the electrical current and thermal gradient of the FAST/SPS process will behave with geometric elements like corners.

It is also possible to have a hybrid system for hot-compaction and deformation that combines ECAS with traditional hot-pressing. If hot-pressing a pre-form at $600 \text{ }^{\circ}\text{C}$ to the desired density is possible, this could eliminate the labor necessary for the preparation of a graphite die, the cleaning of the pre-form of

excess graphite, and the high energy cost of operating a FAST/SPS device. The further exploration of hot-deformed Nd-Fe-B recycling will be highly dependent on many factors, including material availability in the future, the ease of extracting Nd-Fe-B magnets from electrical waste, and the attractiveness of direct recycling in comparison to indirect recycling methods like leaching REEs. Future discussions about direct recycling Nd-Fe-B will also need to consider magnet coatings, any influence of corrosion on the magnet, and the mixing of different magnet scrap when handling electronic waste.

For the PM T15 experiments, improvements in the disks will likely come from improvements in the swarf itself, as previously discussed in this work. Besides swarf optimization, a next step of interest could be stacking and sintering multiple disks at once in a FAST/SPS device. This would make the process more industrially attractive, as it would decrease the amount of energy needed per kg of tool output. Alternative uses for the PM T15 disks could be explored, rather than using them in a tunneling device.

This work also adds to the body of research exploring metal matrix composites made via FAST/SPS. FAST/SPS processing of the PM T15 swarf did allow contaminants like Al_2O_3 to be suspended in a steel matrix. While the effect did not end up being synergistic, the composite was successfully formed. This opens up questions regarding what materials could be embedded in a metal matrix to enhance certain properties. Regardless of what those materials end up being, FAST/SPS has shown itself as a process capable of making new composites possible, which can be attractive from an upcycling perspective.

Acknowledgements

No achievement is ever accomplished in a vacuum. This work was made possible by a whole score of people helping me in all sorts of ways – in scientific ways, from assisting me with analysis to taking time to fill in the gaps of my knowledge, and in social ways, from cooking with me, hiking with me, or taking the time to chat in my office. The academic, mental, and emotional support I've received from everyone is really what carried me through this PhD. Though space is limited, I will do my best to honor as many people as I can here!

First and foremost, thank you to my doctoral and scientific supervisor at IMD-2, Prof. Martin Bram. He allowed me the space to explore the experimental work that seemed most relevant to this topic and gave me very valuable guidance when I felt stuck at dead ends. He always supported my desire to connect with other researchers, try out new ideas, and seek help from industry. Thanks to him, I had the privilege to present at conferences across the world and make a lasting network among the powder metallurgical community. His patience and diplomacy are traits to be admired. Thank you for three great years of supervision.

Thank you to the multitude of people at IMD-2 who made all of this work possible. A huge thank you goes especially to Ralf Steinert, who always had my back at the FAST/SPS, despite the many tools that got broken along the way. Thank you to Erhan Sucuoglu and the team at the IMD-2 Werkstatt who always fixed my tools. Thank you to Prof. Olivier Guillon, who supported me through work reports, gave helpful suggestions and encouragement, and directed me to new and fruitful opportunities. Thank you to Dr. Doris Sebold, who did excellent SEM analysis of my samples and always made time to discuss the analysis with me. Thank you to Nadine Wettengl for all of the ICP-OES and CNO analysis. Thank you to Andrea Hilgers for the PSD measurements. Thank you to all of the colleagues who trained me on lab devices! And a big thank you to the friends I made along the way: Cati, Yuning, Franziska, Denise, David, Kevin, Luca, Martin, Moritz, Christian, Laura, Maike, Johannes, and Artur, among others. Thank you to my FZJ friends outside IMD-2, especially Tine for all our adventures, and Thanh for getting help when I broke my leg on the train. Ouch!

So much support came from outside FZJ as well. A huge thank you to Martin Krengel at WILO SE, who performed all the Permagraph measurements. He ended up receiving many, many magnets in the mail from me and patiently took the time to measure them all. A big thank you as well to Dr. Fernando Maccari, previously of TU Darmstadt. His knowledge was so, so valuable in figuring out what was going on with my magnets, and he contributed a lot of time and effort to helping me understand what I'm looking for when SEM imaging Nd-Fe-B. Thank you to Prof. Oliver Gutfleisch and the rest of the Functional Materials group at TU Darmstadt as well for discussion and support! And thank you to Dr.

Iliya Radulov of Fraunhofer IWKS for collaborating with me on a paper – work that gave me great direction to the best results I was able to achieve from my magnets.

None of these experiments would be possible without the other GENESIS project team members. Thank you so much to Felix Grosswendt at RUB for excellent collaboration and back-and-forth. We were able to accomplish so much due to his great and timely communication, commitment to getting things right, and patience to keep me up to speed. He produced a lot of valuable parts of this thesis, including GD-OES analysis, ThermoCalc calculations, XRF, hardness testing, and SEM images. Thank you to Michelle Treppmann, who worked with Felix during her master thesis and provided some excellent analysis into the behavior of the steel disks. Thank you to Anna-Caroline Assmann at RWTH Aachen ANTS, who put in a lot of time crushing magnets and cleaning swarf for me to use in all my experiments. Thank you to Dr. Wiebke Hagedorn, who had great discussions with me about the LCA aspect of this work. Thank you to Prof. Sebastian Weber of RUB, my second supervisor, who supported me with feedback throughout this project. A big thank you to Jens Huber and Franco De Angelis at Dr. Frisch for all of their help with troubleshooting and training with the DSP515 device. Thank you to the industrial partners of the GENESIS project for contributing resources and thank you to the Bundesministerium für Wirtschaft und Energie (BMWE) for funding this project.

Thank you to my friends around the world who have gotten me to this point. Thank you Jenny and Rachelle for keeping up with me 3000 miles away. Thank you to my friends in family in France who have offered me a couple weeks of escape every year from my scientific work – Elise and Eric, Christine, Aina, Lydia and Max. Thank you to my NRW squad going through the Auslander struggle like me – Domenica, Randi, Bruna, Mari, and Dieter. Thank you to all my pen pals who have been patiently waiting for a response from me – I swear I'll have time to write now; I'm done with my thesis!

Thank you to my parents, Veronica and Laszlo, who have always supported my academic interests, even when they have taken me to another continent. I wouldn't be here without their tireless efforts through my entire life to help me reach my potential. Thank you for always seeing the best in me, even when I've been stubborn. Thank you to the rest of my family in the US, who have always been cheering me on from a distance.

And finally, thank you to Maik. Without him, I wouldn't be at FZJ in the first place. He has always worked his hardest for me, always been patient, accommodating, and loving. He always took on more responsibilities when I was sick or struggling, always tried his best for me, and always made things work, even while he was working on his own PhD at the same time. My words could not possibly capture the gratitude I have for him. Thank you Maik – I love you.

List of Figures

Figure 1.1 - Organization and distribution of tasks within the GENESIS Project.....	3
Figure 2.1 – Visual representation of the sintering process via coarsening and densification. Adapted from [60].....	6
Figure 2.2 – Schematic displaying the types of sintering mechanisms that lead to neck formation and grain coarsening (1-3) and shrinkage (4-6) using the three-particle model. The mechanisms are as follows: 1. Surface diffusion, 2. Lattice diffusion from the surface, 3. Evaporation and re-condensation, 4. Grain boundary diffusion, 5. Lattice diffusion from the grain boundary, and 6. Plastic flow through dislocations. Adapted from [62].....	8
Figure 2.3 –Schematic of an example of a FAST/SPS setup.....	14
Figure 2.4 - Schematic of an example of a Flash SPS setup.....	15
Figure 2.5 – Diagram showing visualizations of the categories of magnetic susceptibility with arrows representing magnetic polarization	18
Figure 2.6 - The origin of domains, with explanations on their effect on magnetic energy. Adapted from [87].....	20
Figure 2.7 – B - H and J - H/M - H curves showing their key points of extrinsic data and the difference between soft and hard magnetic behavior.....	23
Figure 2.8 – Crystallographic Nd-Fe-B unit cell [95].....	24
Figure 2.9 - Proposed mechanism for anisotropic grain development in hot-deformed Nd-Fe-B magnets. Adapted from [67]	27
Figure 2.10 - Typical heat treatment cycle of W-based high-speed steels. Adapted from [130].....	31
Figure 3.1 - Example QicPic analysis of a single PM T15 particle	34
Figure 3.2 – Steps in the processing of hot-deformed Nd-Fe-B recycled scrap in this work	36
Figure 3.3 – FCT HP-D5 FAST/SPS device and diagram of set-up for pre-sintering of Nd-Fe-B powder	40
Figure 3.4 – FCT H-HP-D 25 hybrid FAST/SPS device and diagram of FS/SPS set-up for Nd-Fe-B deformation.....	41
Figure 3.5 – Photo and diagram FS/SPS set-up including boron nitride ring and adapter.....	43
Figure 3.6 – Diagram showing the set-up before SPT and the effect on the sample during SPT	45

Figure 3.7 – Diagram showing a \varnothing 40 mm SPT deformed magnet and the dimensions of the desired bar magnet to be prepared by grinding and electro discharge machining.....	47
Figure 3.8 - Steps in the processing of PM T15 grinding swarf in this work	52
Figure 3.9 – Disk swing mill used by ANTS RWTH Aachen for milling PM T15 swarf.....	53
Figure 3.10 – Photos of graphite foils before and after coating with BN	56
Figure 3.11 – Photo of the Dr. Fritsch DSP515 device and diagram of the set-up of a filled die in the device	58
Figure 3.12 – Diagram of a PM T15 cutting disk (dark grey) in its adapter for the mock tunneling device (light grey). All dimensional values are given in mm.....	60
Figure 3.13 – A. Photo of the mock tunneling rig at RUB and B. example set-up of the tunneling experiment with a demonstrator cutting disk	61
Figure 3.14 – Cuts of Nd-Fe-B samples for Permagraph measurement	65
Figure 3.15- Diagram displaying the working components of a VSM along with the signal transmission. Adapted from [159].....	66
Figure 3.16 – Diagram showing the application of force by the indenter and the resulting diagonals formed in the sample. Adapted from [160].....	67
Figure 4.1 – Oxygen content of Nd-Fe-B powders analyzed by CHGE.....	70
Figure 4.2 – A. PSD of select Nd-Fe-B recyclate powders and B. $(BH)_{\max}$ and oxygen content of select Nd-Fe-B powders.....	70
Figure 4.3- Morphology and microstructure of commercial MQU-F and select recyclate powders	71
Figure 4.4 – A. Pre-sintered and FSPS deformed pellet from 100% LCM1 and B. Pre-sintered and FSPS deformed pellet from 100% RC3	73
Figure 4.5 – Magnetic performance of FSPS samples made from mixed MQU-F and recyclate Nd-Fe-B powders with varying amounts of recyclate powder	74
Figure 4.6 – SEM images showing the FAST/SPS pre-sintered morphology, FSPS deformed morphology, and FSPS grains in samples made from A. 100% MQU-F, B. 100% LCM1, and C. 100% RC3. Significantly misaligned grains are highlighted in solid orange, with regions of misalignment highlighted in dashed orange. Contrast has been digitally enhanced for improved clarity.....	76
Figure 4.7 - SEM images showing the FAST/SPS pre-sintered morphology, FSPS deformed morphology, and FSPS grains in samples made from A. LCM1-8515 and B. RC3-8515. Recyclates are	

highlighted in green, while misaligned grains are highlighted in orange. Contrast has been digitally enhanced for improved clarity	77
Figure 4.8 – Schematic showing two scenarios of anisotropic particles deforming into the Nd-Fe-B matrix without grain rotation, with (Scenario A) favorably oriented grains and (Scenario B) unfavorably oriented grains.....	78
Figure 4.9 – Photo of the BN1 series of FSPS deformed MQU-F pellets, showing their tops and edges from no die to 25 mm die restriction, with deformation degree listed below each respective sample. Further information in Appendix B.	79
Figure 4.10 – Magnetic performance of FSPS samples deformed with 25-30 mm diameter BN dies in comparison to a sample deformed without a die.....	80
Figure 4.11 – SEM images of BN1-30, from the magnification of individual MQU-F platelets and grain magnification. Orange shapes are shown to track the bending of platelets against the friction of the die, while blue arrows indicate the normal of the platelets and/or grains. Contrast has been digitally enhanced for improved clarity.	81
Figure 4.12 - Photos of the BN2, BN3, and BN4 series of FSPS deformed MQU-F and recyclate pellets, showing their edges from samples deformed with 31-, 32-, and 33-mm BN dies and no die. Further information in Appendix B.	82
Figure 4.13 - Magnetic performance of FSPS samples from the BN2, BN3, and BN4 series.....	83
Figure 4.14 - Magnetic performance of SPT samples from the SPT1-HC and SPT1-PRE2 series. Hot deformation temperature is given in parentheses.....	86
Figure 4.15 – SEM images of SPT1-HC1 samples deformed at 750 °C across the applied pressures of A. 100, B. 200, and C. 300 MPa	87
Figure 4.16 - Magnetic performance of SPT samples from the QD series	88
Figure 4.17 – BSE SEM images of QD samples deformed under 150 MPa, 800 °C consisting of 100% A. MQU-F, B. MRV1, and C. MRV2. Arrows indicate pressing direction.....	89
Figure 4.18 - Magnetic performance of SPT samples from the SPT2 and SPT3 series, relative to a control sample deformed under the default 10 kN of force	91
Figure 4.19 – SEM images of two different magnifications of LCM2 pre-forms sintered at A. 500, B. 600, and C. 700 °C.....	93
Figure 4.20 - Magnetic performance of SPT samples from the SPT4 series, consisting either of 100 wt% LCM2 (SPT4) or 25 wt% LCM2, 75 wt% MQU-F (SPT4-25)	94
Figure 4.21 – 2 nd quadrant J-H magnetic hysteresis curves of A. SPT4 and B. SPT4-25 samples.....	95

Figure 4.22 – SEM images of the center and edge of the SPT4-HC2 sample, at magnifications to see the sample platelets and grains. Blue arrows represent the alignment of the c-axis in the particles. Contrast has been digitally enhanced for improved clarity.....	96
Figure 4.23 – A. DEMO pre-form roughly 15 mm in height showing bowing from sample top to bottom, indicated with an orange arrow, and B. FAST/SPS set-up in the FCT HP D25 device using a TZM die for HC2 hot compaction.....	98
Figure 4.24 – A. DEMO sample before grinding, B. DEMO sample after grinding the face with multiple 80 grit sandpaper sheets, and C. a DEMO sample after grinding to target thickness	99
Figure 4.25 – Photos of A. a bar magnet after electrical discharge machining, showing damage in the corner from the deformation process, B. a side-view of the bar magnet with a visible crack down the magnet bulk, C. the rotor where the bar magnets were installed, along with the WILO SE circulating pump where the rotor was utilized, and D. the set-up of the EMF measurement. Photos, electrical discharge machining, and EMF tests provided by WILO SE	100
Figure 4.26 – Energy consumption of the A. FCT HP D5 device and its cooler over a FAST/SPS sintering cycle of HC2 with a 30 second dwell rather than 60 seconds, and the FCT HP D25 device and its cooler over a B. FSPS2 cycle and C. SPT4 cycle	102
Figure 5.1 – Phase diagram displaying the present iron and carbide contents at various C contents and temperatures, calculated for the PM T15 swarf via ThermoCalc by colleagues at RUB. C-content of the swarf is marked with a red dashed line	108
Figure 5.2 – SEM images of A. PS swarf, B. PSM swarf, and C. PSM swarf surrounding a large grinding particle	109
Figure 5.3 – Random QicPic frames of A. PS swarf and B. PSM swarf	109
Figure 5.4 – A. PS sample stuck onto graphite punch and B. PS sample removed from punch, but broken and trapping residual graphite. (FAST/SPS parameters: 100 K/min to 1050 °C, 50 MPa pressure, dwell for 5 minutes).....	110
Figure 5.5 – Calculated volume content of stable phases for A. nominal PM T15 [128] and B. PS swarf. C-concentration in the austenite phase is denoted with a dotted red line. The targeted maximum C-concentration of 0.6 mass% is marked with a dotted grey line. From [171]	111
Figure 5.6 – SE SEM images of a PS sample sintered by FAST/SPS at 950 °C (pressure: 50 MPa, dwell time: 5 min), specifically focusing on A. the carbon-rich layer at the contact between PS and graphite and B. Formation of large gaps between an Al ₂ O ₃ particle and the steel matrix	111
Figure 5.7 – Changes in density and lip height of PS samples sintered at varied FAST/SPS maximum temperatures (pressure: 50 MPa, dwell time: 5 min)	112

Figure 5.8 – Photos of pre-sintered PS from the PS2 pre-sintering parameters and samples treated with the PS2-D set of deformation parameters	114
Figure 5.9 – BSE SEM images of A. PS2 pre-sintered form, and PS2-D samples deformed at 950 °C and B. 50 MPa, C. 100 MPa, and D. 150 MPa. Dark grey Al ₂ O ₃ particles are found and highlighted in each sample.....	114
Figure 5.10 – Hardness testing of PSD-2 samples and deformed PSM samples in their as-deformed state, after quenching, and after quenching and tempering. For quenching and tempering parameters, see Section 3.3.3.	115
Figure 5.11 – SE SEM images of A. a PS2-D sample directly after FAST/SPS deformation and B. the same sample after austenitization at 1220 °C, quenching and tempering.....	116
Figure 5.12 – A. SEM image of a PS2-D sample deformed at 950 °C under 150 MPa while in contact with BN-coated graphite, with a BN layer indicated by a dotted blue line, and B. EDX mapping of various elements, showing the distinct BN layer and isolation from carbon diffusion	117
Figure 5.13 – GD-OES measurements of C, N, and B at the surface of PS samples deformed A. without a BN coating and B. with a BN coating.....	117
Figure 5.14 - Ø 100 mm D2-100 disk viewed from the side and from the face (FAST/SPS temperature: 950 °C, pressure: 50 MPa, dwell: 1 min).....	119
Figure 5.15 – D2-120 samples and their irregularities, including A. a crease made in the steel from a fold in the graphite and B. uneven height distribution leading to a broken graphite punch	120
Figure 5.16 – Photos of A. a PSM-120 sintered disk, made of milled PM T15 swarf (PSM) with a raised portion on the sample face and B. a crack on its graphite punch corresponding to the raised region on the sample (FAST/SPS temperature: 950 °C, pressure: 50 MPa, dwell: 1 min).....	121
Figure 5.17 – BSE SEM analysis of the melted point on the PSM-120 sample, with the hotspot indicated roughly by a red arrow	121
Figure 5.18 – Exploded-view diagram of the final Ø 120 mm die set-up for PSM-120 sintering	122
Figure 5.19 – Photos of PSM-120 disks sintered at dwell times of 1 minute (top) and 5 minutes (bottom), along with SEM images of the sample A. center B. off-center and C. edge, with grinding particles and pores labeled	124
Figure 5.20 – PSM-120 disk displaying a fractured edge after 5 minutes of simulated tunneling against a sandstone counterpart.....	127
Figure 5.21 – A. Photo of a beaker holding the sandstone material removed by the PSM-120 disk, with the PSM-120 disk in the background after 20 minute tunneling test, B. light microscopy image of the	

PSM-120 edge after testing, and C. SEM image of the PSM-120 edge after testing, showing cracks	128
Figure 5.22 - Energy consumption of the Dr. Fritsch DSP515 device and its cooler over a PSM-120 FAST/SPS sintering cycle, 1 min dwell time	129
Figure 6.1 - Remanence and coercivity values for all samples generated with 100 wt% MQU-F powder in this work	133
Figure 6.2 - Remanence and coercivity values for all samples generated with 100 wt% recyclate powder in this work	134
Figure 6.3 - Remanence and coercivity values for all samples generated with mixed recyclate and MQU-F powder in this work.	135
Figure 6.4 - Commercially available Nd-Fe-B magnet grades with details of typical magnetic parameters and operating temperatures. Target grades of this project and achieved grades are highlighted based on the legend to the right. Graph modified from [183], originally based on [117], [184].....	136

List of Tables

Table 2.1 - Material transport mechanisms during sintering, specifically in polycrystalline solids, with numbers corresponding to the illustrated mechanisms in Figure 2.2 [62].	8
Table 2.2 – Performance of neodymium magnets in the industry specified range. Data from [118] ...	26
Table 2.3 – Compositional limits of T15 steel (wt%) [128]	29
Table 3.1 - Overview of unmixed Nd-Fe-B powders used in this work, with different particle sizes achieved by sieving.....	37
Table 3.2 - Overview of mixed commercial and recycle Nd-Fe-B powders used in this work	38
Table 3.3 – Table of parameters used for Nd-Fe-B sample pre-sintering and hot compaction	41
Table 3.4 – Flash SPS processing parameters used in this work	42
Table 3.5 – Summary of parameters for the FSPS series “RC”	42
Table 3.6 – Summary of the FSPS experiments performed with BN ring constriction	44
Table 3.7 – Phases of all SPT experiments with their respective changes in temperature and applied force	48
Table 3.8 – Powder selection, pre-sintering parameters, and TZM tool diameters for SPT experimental series	49
Table 3.9 - Powder selection, hot-compaction parameters, and TZM tool diameters for demonstrator 100 wt% recycled magnets	50
Table 3.10 – Overview of PM T15 powders used in this work	53
Table 3.11 – Single stage FAST/SPS parameters for PM T15 pellets.....	54
Table 3.12 – Pre-compaction and deformation parameters for two-stage FAST/SPS sintering of PM T15	55
Table 3.13 – PSMOpt experiments with variations in dwell time, pressure, and temperature	57
Table 3.14 - FAST/SPS parameters for the sintering of D2 in a \varnothing 100 mm die	59
Table 3.15 - FAST/SPS parameters for the sintering of steel swarf in a \varnothing 120 mm die	59
Table 4.1 – Comparison of the EMF of a standard WILO rotor to rotor with DEMO magnets installed at the same rotational speed	101
Table 4.2 – Energy consumption values for FAST/SPS hot compaction and ECAS deformation techniques	103
Table 5.1- Compositional analysis in wt% of the PS (as delivered) and PSM (milled) swarf, in comparison to nominal literature values and a reference sample. In the reference and PSM, heavy elements were measured using XRF. In PS, heavy elements were measured via ICP-OES. *C, N, and O measured via CGHE.....	108
Table 5.2 – Densities and particle size distribution data of un-milled (PS) and milled (PSM) PM T15 swarf.....	109

Table 5.3 – Comparison between PSM sintering diameters, dwell times, and final densities (FAST/SPS temperature: 950 °C, pressure: 45 MPa)	123
Table 5.4 – Heat treatment stages and temperatures for standard PM T15 and PSM-120	125
Table 5.5 – Amount of sandstone removed by each disk and how much mass of each disk was lost in the 20 min testing cycle	127

Bibliography

- [1] O. Gutfleisch, M. A. Willard, E. Brück, C. H. Chen, S. G. Sankar, and J. P. Liu, “Magnetic Materials and Devices for the 21st Century: Stronger, Lighter, and More Energy Efficient,” *Adv. Mater.*, vol. 23, no. 7, Dec. 2010.
- [2] Y. Matsuura, “Recent development of Nd–Fe–B sintered magnets and their applications,” *J. Magn. Magn. Mater.*, vol. 303, no. 2, pp. 344–347, Aug. 2006, doi: 10.1016/j.jmmm.2006.01.171.
- [3] S. Sugimoto, “Current status and recent topics of rare-earth permanent magnets,” *J. Phys. Appl. Phys.*, vol. 44, 2011.
- [4] E. Alonso, A. M. Sherman, T. J. Wallington, M. P. Everson, F. R. Field, R. Roth, and R. E. Kirchain, “Evaluating Rare Earth Element Availability: A Case with Revolutionary Demand from Clean Technologies,” *Environ. Sci. Technol.*, vol. 46, no. 6, pp. 3406–3414, Mar. 2012, doi: 10.1021/es203518d.
- [5] H. Kara, A. Chapman, T. Crichton, P. Willis, and N. Morley, “Lanthanide Resources and Alternatives,” Oakdene Hollins Research and Consulting, Aylesbury, United Kingdom, DFT-01 205 issue2.doc, May 2010.
- [6] V. Balaram, “Rare earth elements: A review of applications, occurrence, exploration, analysis, recycling, and environmental impact,” *Geosci. Front.*, vol. 10, no. 4, pp. 1285–1303, July 2019, doi: 10.1016/j.gsf.2018.12.005.
- [7] Y. Bian, S. Guo, L. Jiang, J. Liu, K. Tang, and W. Ding, “Recovery of Rare Earth Elements from NdFeB Magnet by VIM-HMS Method,” *ACS Sustain. Chem. Eng.*, vol. 4, no. 3, pp. 810–818, Mar. 2016, doi: 10.1021/acssuschemeng.5b00852.
- [8] Z. Hua, J. Wang, L. Wang, Z. Zhao, X. Li, Y. Xiao, and Y. Yang, “Selective Extraction of Rare Earth Elements from NdFeB Scrap by Molten Chlorides,” *ACS Sustain. Chem. Eng.*, vol. 2, no. 11, pp. 2536–2543, Nov. 2014, doi: 10.1021/sc5004456.
- [9] J. A. Bogart, B. E. Cole, M. A. Boreen, C. A. Lippincott, B. C. Manor, P. J. Carroll, and E. J. Schelter, “Accomplishing simple, solubility-based separations of rare earth elements with complexes bearing size-sensitive molecular apertures,” *Proc. Natl. Acad. Sci.*, vol. 113, no. 52, pp. 14887–14892, Dec. 2016, doi: 10.1073/pnas.1612628113.
- [10] I. Makarova, E. Soboleva, M. Osipenko, I. Kurilo, M. Laatikainen, and E. Repo, “Electrochemical leaching of rare-earth elements from spent NdFeB magnets,” *Hydrometallurgy*, vol. 192, p. 105264, Mar. 2020, doi: 10.1016/j.hydromet.2020.105264.
- [11] J. A. Bogart, C. A. Lippincott, P. J. Carroll, and E. J. Schelter, “An Operationally Simple Method for Separating the Rare-Earth Elements Neodymium and Dysprosium,” *Angew. Chem. Int. Ed.*, vol. 54, no. 28, pp. 8222–8225, 2015, doi: 10.1002/anie.201501659.
- [12] H. Fang, B. E. Cole, Y. Qiao, J. A. Bogart, T. Cheisson, B. C. Manor, P. J. Carroll, and E. J. Schelter, “Electro-kinetic Separation of Rare Earth Elements Using a Redox-Active Ligand,” *Angew. Chem.*, vol. 129, no. 43, pp. 13635–13639, 2017, doi: 10.1002/ange.201706894.
- [13] S. Ramanath, T. C. Ramaraj, and M. C. Shaw, “What Grinding Swarf Reveals,” *CIRP Ann.*, vol. 36, no. 1, pp. 245–247, Jan. 1987, doi: 10.1016/S0007-8506(07)62596-7.
- [14] J. Kopac and P. Krajnik, “High-performance grinding—A review,” *J. Mater. Process. Technol.*, vol. 175, no. 1, pp. 278–284, June 2006, doi: 10.1016/j.jmatprotec.2005.04.010.
- [15] C.-M. Lee, Y.-H. Choi, J.-H. Ha, and W.-S. Woo, “Eco-friendly technology for recycling of cutting fluids and metal chips: A review,” *Int. J. Precis. Eng. Manuf.-Green Technol.*, vol. 4, no. 4, pp. 457–468, Oct. 2017, doi: 10.1007/s40684-017-0051-9.
- [16] J. Ni, Y. Yang, and C. Wu, “Assessment of water-based fluids with additives in grinding disc cutting process,” *J. Clean. Prod.*, vol. 212, pp. 593–601, Mar. 2019, doi: 10.1016/j.jclepro.2018.12.066.
- [17] H. Fu, M. A. Matthews, and L. S. Warner, “Recycling steel from grinding swarf,” *Waste Manag.*, vol. 18, no. 5, pp. 321–329, Aug. 1998, doi: 10.1016/S0956-053X(98)00042-7.
- [18] O. Guillon, J. Gonzalez-Julian, B. Dargatz, T. Kessel, G. Schierning, J. Räthel, and M. Herrmann, “Field-Assisted Sintering Technology/Spark Plasma Sintering: Mechanisms,

Materials, and Technology Developments,” *Adv. Eng. Mater.*, vol. 16, no. 7, pp. 830–849, 2014, doi: 10.1002/adem.201300409.

[19] M. Bram, A. M. Laptev, T. P. Mishra, K. Nur, M. Kindelmann, M. Ihrig, J. G. Pereira da Silva, R. Steinert, H. P. Buchkremer, A. Litnovsky, F. Klein, J. Gonzalez-Julian, and O. Guillon, “Application of Electric Current-Assisted Sintering Techniques for the Processing of Advanced Materials,” *Adv. Eng. Mater.*, vol. 22, no. 6, p. 2000051, 2020, doi: 10.1002/adem.202000051.

[20] J. G. Noudem, D. Kenfaui, D. Chateigner, and M. Gomina, “Toward the enhancement of thermoelectric properties of lamellar Ca₃Co₄O₉ by edge-free spark plasma texturing,” *Scr. Mater.*, vol. 66, no. 5, pp. 258–260, Mar. 2012, doi: 10.1016/j.scriptamat.2011.11.004.

[21] N. S. Weston, B. Thomas, and M. Jackson, “Processing metal powders via field assisted sintering technology (FAST): a critical review,” *Mater. Sci. Technol.*, vol. 35, no. 11, pp. 1306–1328, July 2019, doi: 10.1080/02670836.2019.1620538.

[22] M. R. Mphahlele, E. A. Olevsky, and P. A. Olubambi, “Chapter 12 - Spark plasma sintering of near net shape titanium aluminide: A review,” in *Spark Plasma Sintering*, G. Cao, C. Estournès, J. Garay, and R. Orrù, Eds., Elsevier, 2019, pp. 281–299. doi: 10.1016/B978-0-12-817744-0-00012-X.

[23] T. Prasad Mishra, L. Leich, M. Krengel, S. Weber, A. Röttger, and M. Bram, “NdFeB Magnets with Well-Pronounced Anisotropic Magnetic Properties Made by Electric Current-Assisted Sintering,” *Adv. Eng. Mater.*, vol. 25, no. 1, p. 2201027, 2023, doi: 10.1002/adem.202201027.

[24] M. E. B. Seiffert and C. Loch, “Systemic thinking in environmental management: support for sustainable development,” *J. Clean. Prod.*, vol. 13, no. 12, pp. 1197–1202, Oct. 2005, doi: 10.1016/j.jclepro.2004.07.004.

[25] J. Markard, R. Raven, and B. Truffer, “Sustainability transitions: An emerging field of research and its prospects,” *Res. Policy*, vol. 41, no. 6, pp. 955–967, July 2012, doi: 10.1016/j.respol.2012.02.013.

[26] J. Rockström, W. Steffen, K. Noone, Å. Persson, F. S. I. Chapin, E. Lambin, T. Lenton, M. Scheffer, C. Folke, H. J. Schellnhuber, B. Nykvist, C. de Wit, T. Hughes, S. van der Leeuw, H. Rodhe, S. Sörlin, P. Snyder, R. Costanza, U. Svedin, M. Falkenmark, L. Karlberg, R. Corell, V. Fabry, J. Hansen, B. Walker, D. Liverman, K. Richardson, P. Crutzen, and J. Foley, “Planetary Boundaries: Exploring the Safe Operating Space for Humanity,” *Ecol. Soc.*, vol. 14, no. 2, Nov. 2009, doi: 10.5751/ES-03180-140232.

[27] M. Geissdoerfer, P. Savaget, N. M. P. Bocken, and E. J. Hultink, “The Circular Economy – A new sustainability paradigm?,” *J. Clean. Prod.*, vol. 143, pp. 757–768, Feb. 2017, doi: 10.1016/j.jclepro.2016.12.048.

[28] G. Gaustad, M. Krystofik, M. Bustamante, and K. Badami, “Circular economy strategies for mitigating critical material supply issues,” *Resour. Conserv. Recycl.*, vol. 135, pp. 24–33, Aug. 2018, doi: 10.1016/j.resconrec.2017.08.002.

[29] P. Johnston, M. Everard, D. Santillo, and K.-H. Robèrt, “Reclaiming the definition of sustainability,” *Environ. Sci. Pollut. Res. Int.*, vol. 14, no. 1, pp. 60–66, Jan. 2007, doi: 10.1065/espr2007.01.375.

[30] J. Ehrenfeld, “The Roots of Sustainability,” *MIT Sloan Management Review*, vol. 46, no. 2, 2005.

[31] A. J. McMichael, C. D. Butler, and C. Folke, “New Visions for Addressing Sustainability,” *Science*, vol. 302, no. 5652, pp. 1919–1920, Dec. 2003, doi: 10.1126/science.1090001.

[32] W. McDonough and M. Braungart, *Cradle to Cradle: Remaking the Way We Make Things*. Farrar, Straus and Giroux, 2010.

[33] N. M. P. Bocken, I. de Pauw, C. Bakker, and B. van der Grinten, “Product design and business model strategies for a circular economy,” *J. Ind. Prod. Eng.*, vol. 33, no. 5, pp. 308–320, July 2016, doi: 10.1080/21681015.2016.1172124.

[34] D. Achilias, *Material Recycling: Trends and Perspectives*. BoD – Books on Demand, 2012.

[35] J. Hopewell, R. Dvorak, and E. Kosior, “Plastics recycling: challenges and opportunities,” *Philos. Trans. R. Soc. B Biol. Sci.*, vol. 364, no. 1526, pp. 2115–2126, July 2009, doi: 10.1098/rstb.2008.0311.

[36] B. K. Reck and T. E. Graedel, “Challenges in Metal Recycling,” *Science*, vol. 337, no. 6095, pp. 690–695, Aug. 2012, doi: 10.1126/science.1217501.

[37] B. Tansel, “From electronic consumer products to e-wastes: Global outlook, waste quantities, recycling challenges,” *Environ. Int.*, vol. 98, pp. 35–45, Jan. 2017, doi: 10.1016/j.envint.2016.10.002.

[38] “Direct Recycling of Materials - ReCell Center.” <https://recellcenter.org/research/direct-recycling-of-materials/> (accessed Aug. 15, 2024).

[39] L. Li, J. B. Dunn, X. X. Zhang, L. Gaines, R. J. Chen, F. Wu, and K. Amine, “Recovery of metals from spent lithium-ion batteries with organic acids as leaching reagents and environmental assessment,” *J. Power Sources*, vol. 233, pp. 180–189, July 2013, doi: 10.1016/j.jpowsour.2012.12.089.

[40] R. K. Mishra, E. G. Brewer, and R. W. Lee, “Grain growth and alignment in hot deformed Nd-Fe-B magnets,” *J. Appl. Phys.*, vol. 63, no. 8, pp. 3528–3530, Apr. 1988, doi: 10.1063/1.340731.

[41] I. Bakas, C. Fischer, A. Harding, S. Haselsteiner, D. McKinnon, J. Kosmol, L. Milius, A. Plepys, N. Tojo, H. Wilts, and D. Wittmer, “Present and potential future recycling of critical metals in WEEE,” Copenhagen Resource Institute, Copenhagen, Nov. 2014.

[42] Y. Yang, A. Walton, R. Sheridan, K. Güth, R. Gauß, O. Gutfleisch, M. Buchert, B.-M. Steenari, T. Van Gerven, P. T. Jones, and K. Binnemans, “REE Recovery from End-of-Life NdFeB Permanent Magnet Scrap: A Critical Review,” *J. Sustain. Metall.*, vol. 3, no. 1, pp. 122–149, Mar. 2017, doi: 10.1007/s40831-016-0090-4.

[43] M. Schönfeldt, O. Diehl, E. Brouwer, K. Opelt, J. Gassmann, and O. Gutfleisch, “Recycling of rare earth permanent magnets for advanced electric drives - Overcoming the criticality and supply risk,” 2018, Accessed: Aug. 28, 2023. [Online]. Available: <https://publica.fraunhofer.de/handle/publica/412543>

[44] M. Schönfeldt, U. Rohrmann, P. Schreyer, M. Hasan, K. Opelt, J. Gassmann, A. Weidenkaff, and O. Gutfleisch, “Magnetic and structural properties of multiple recycled and sustainable sintered Nd-Fe-B magnets,” *J. Alloys Compd.*, vol. 939, p. 168709, Apr. 2023, doi: 10.1016/j.jallcom.2023.168709.

[45] O. Diehl, M. Schönfeldt, E. Brouwer, A. Dirks, K. Rachut, J. Gassmann, K. Güth, A. Buckow, R. Gauß, R. Stauber, and O. Gutfleisch, “Towards an Alloy Recycling of Nd–Fe–B Permanent Magnets in a Circular Economy,” *J. Sustain. Metall.*, vol. 4, no. 2, pp. 163–175, June 2018, doi: 10.1007/s40831-018-0171-7.

[46] A. Ikram, M. Awais, R. Sheridan, A. Walton, S. Kobe, F. Pušavec, and K. Žužek Rožman, “Spark Plasma Sintering as an Effective Texturing Tool for Reprocessing Recycled HDDR Nd-Fe-B Magnets with Lossless Coercivity,” *Metals*, vol. 10, no. 3, Art. no. 3, Mar. 2020, doi: 10.3390/met10030418.

[47] L. Leich, A. Röttger, M. Krengel, and W. Theisen, “Recycling of NdFeB Magnets by Electrodischarge Sintering—Microstructure, Magnetic, and Mechanical Properties,” *J. Sustain. Metall.*, vol. 5, no. 1, pp. 107–117, Mar. 2019, doi: 10.1007/s40831-018-0204-2.

[48] J. M. Allwood, M. F. Ashby, T. G. Gutowski, and E. Worrell, “Material efficiency: A white paper,” *Resour. Conserv. Recycl.*, vol. 55, no. 3, pp. 362–381, Jan. 2011, doi: 10.1016/j.resconrec.2010.11.002.

[49] W. Hagedorn, S. Jäger, L. Wieczorek, P. Kronenberg, K. Greiff, S. Weber, and A. Roettger, “More than recycling – The potential of the circular economy shown by a case study of the metal working industry,” *J. Clean. Prod.*, vol. 377, p. 134439, Dec. 2022, doi: 10.1016/j.jclepro.2022.134439.

[50] I. P. Flint, A. Cabrera Serrenho, R. C. Lupton, and J. M. Allwood, “Material Flow Analysis with Multiple Material Characteristics to Assess the Potential for Flat Steel Prompt Scrap Prevention and Diversion without Remelting,” *Environ. Sci. Technol.*, vol. 54, no. 4, pp. 2459–2466, Feb. 2020, doi: 10.1021/acs.est.9b03955.

[51] K. E. Daehn, A. Cabrera Serrenho, and J. M. Allwood, “How Will Copper Contamination Constrain Future Global Steel Recycling?,” *Environ. Sci. Technol.*, vol. 51, no. 11, pp. 6599–6606, June 2017, doi: 10.1021/acs.est.7b00997.

[52] M. Haupt, C. Vadenbo, C. Zeltner, and S. Hellweg, “Influence of Input-Scrap Quality on the Environmental Impact of Secondary Steel Production,” *J. Ind. Ecol.*, vol. 21, no. 2, pp. 391–401, 2017, doi: 10.1111/jiec.12439.

[53] M. Xylia, S. Silveira, J. Duerinck, and F. Meinke-Hubeny, “Weighing regional scrap availability in global pathways for steel production processes,” *Energy Effic.*, vol. 11, no. 5, pp. 1135–1159, June 2018, doi: 10.1007/s12053-017-9583-7.

[54] T. A. Branca, V. Colla, D. Algermissen, H. Granbom, U. Martini, A. Morillon, R. Pietruck, and S. Rosendahl, “Reuse and Recycling of By-Products in the Steel Sector: Recent Achievements Paving the Way to Circular Economy and Industrial Symbiosis in Europe,” *Metals*, vol. 10, no. 3, Art. no. 3, Mar. 2020, doi: 10.3390/met10030345.

[55] D. Schubert, C. Reschke, H. Biedermann, and R. Deike, “Verfahren zur Entlösung von kühlschmierstoffbehafteten Metallspänen und -schlämmen,” 2019, pp. 581–591.

[56] M. Grosso, A. Motta, and L. Rigamonti, “Efficiency of energy recovery from waste incineration, in the light of the new Waste Framework Directive,” *Waste Manag.*, vol. 30, no. 7, pp. 1238–1243, July 2010, doi: 10.1016/j.wasman.2010.02.036.

[57] H. Fu and M. A. Matthews, “Comparison between supercritical carbon dioxide extraction and aqueous surfactant washing of an oily machining waste,” *J. Hazard. Mater.*, vol. 67, no. 2, pp. 197–213, June 1999, doi: 10.1016/S0304-3894(99)00037-0.

[58] H. Fu and M. A. Matthews, “Separation processes for recovering alloy steels from grinding sludge: Supercritical carbon dioxide extraction and aqueous cleaning,” *Sep. Sci. Technol.*, vol. 34, no. 6–7, pp. 1411–1427, 1999, doi: 10.1080/0149639908951100.

[59] A. H. Tkaczyk, A. Bartl, A. Amato, V. Lapkovskis, and M. Petranikova, “Sustainability evaluation of essential critical raw materials: cobalt, niobium, tungsten and rare earth elements,” *J. Phys. Appl. Phys.*, vol. 51, no. 20, p. 203001, Apr. 2018, doi: 10.1088/1361-6463/aaba99.

[60] S. Kang, *Sintering: Densification, Grain Growth, and Microstructure*. Elsevier, 2005.

[61] M. E. Fine, “Introduction to Chemical and Structural Defects in Crystalline Solids,” in *The Chemical Structure of Solids*, N. B. Hannay, Ed., New York, NY: Springer US, 1973, pp. 283–333. doi: 10.1007/978-1-4684-2661-8_5.

[62] M. N. Rahaman, *Sintering of Ceramics*. Boca Raton: CRC Press, 2013. doi: 10.1201/b15869.

[63] M. Kindelmann, “Field assisted sintering of yttria ceramics for plasma etching applications,” Forschungszentrum Jülich GmbH Zentralbibliothek, Verlag, 2021. Accessed: Aug. 20, 2024. [Online]. Available: <https://juser.fz-juelich.de/record/897474>

[64] D. L. Johnson, “Ultra-Rapid Sintering,” in *Materials Science Research: Volume 16 Sintering and Heterogeneous Catalysis*, G. C. Kuczynski, A. E. Miller, and G. A. Sargent, Eds., Boston, MA: Springer US, 1984, pp. 243–252. doi: 10.1007/978-1-4613-2761-5_17.

[65] E. Olevsky and D. Dudina, *Field-Assisted Sintering: Science and Applications*, 1st ed. Springer Charm, 2018.

[66] J. Trapp, A. Semenov, O. Eberhardt, M. Nöthe, T. Wallmersperger, and B. Kieback, “Fundamental principles of spark plasma sintering of metals: Part II – about the existence or non-existence of the ‘spark plasma effect,’” *Powder Metall.*, vol. 63, no. 5, pp. 312–328, Dec. 2020, doi: 10.1080/00325899.2020.1829349.

[67] R. L. Coble, “Sintering Crystalline Solids. I. Intermediate and Final State Diffusion Models,” *J. Appl. Phys.*, vol. 32, no. 5, pp. 787–792, May 1961, doi: 10.1063/1.1736107.

[68] R. E. Smallman and R. J. Bishop, “Chapter 4 - Defects in solids,” in *Modern Physical Metallurgy and Materials Engineering (Sixth Edition)*, R. E. Smallman and R. J. Bishop, Eds., Oxford: Butterworth-Heinemann, 1999, pp. 84–124. doi: 10.1016/B978-075064564-5/50004-5.

[69] R. M. German, “Chapter Ten - Sintering With External Pressure,” in *Sintering: from Empirical Observations to Scientific Principles*, R. M. German, Ed., Boston: Butterworth-Heinemann, 2014, pp. 305–354. doi: 10.1016/B978-0-12-401682-8.00010-0.

[70] K. Hioki, “High performance hot-deformed Nd-Fe-B magnets (Review),” *Sci. Technol. Adv. Mater.*, vol. 22, no. 1, pp. 72–84, Dec. 2021, doi: 10.1080/14686996.2020.1868049.

[71] D. Lee, J. S. Hilton, S. Liu, Y. Zhang, G. C. Hadjipanayis, and C. H. Chen, “Hot-pressed and hot-deformed nanocomposite (Nd,Pr,Dy)/sub 2/Fe/sub 14/B//spl alpha/-Fe-based magnets,” *IEEE Trans. Magn.*, vol. 39, no. 5, pp. 2947–2949, Sept. 2003, doi: 10.1109/TMAG.2003.815755.

[72] R. K. Mishra, “Microstructure of hot-pressed and die-upset NdFeB magnets,” *J. Appl. Phys.*, vol. 62, no. 3, pp. 967–971, Aug. 1987, doi: 10.1063/1.339709.

[73] R. K. Mishra, T.-Y. Chu, and L. K. Rabenberg, “The development of the microstructure of die-upset Nd-Fe-B magnets,” *J. Magn. Magn. Mater.*, vol. 84, no. 1, pp. 88–94, Feb. 1990, doi: 10.1016/0304-8853(90)90168-P.

[74] G. Sutradhar, A. K. Jha, and S. Kumar, “Production of sinter-forged components,” *J. Mater. Process. Technol.*, vol. 41, no. 2, pp. 143–169, Feb. 1994, doi: 10.1016/0924-0136(94)90058-2.

[75] A. Fais, “A faster FAST: Electro-Sinter-Forging,” *Met. Powder Rep.*, vol. 73, no. 2, pp. 80–86, Mar. 2018, doi: 10.1016/j.mprp.2017.06.001.

[76] H. V. Atkinson and S. Davies, “Fundamental aspects of hot isostatic pressing: An overview,” *Metall. Mater. Trans. A*, vol. 31, no. 12, pp. 2981–3000, Dec. 2000, doi: 10.1007/s11661-000-0078-2.

[77] M. H. Bocanegra-Bernal, “Hot Isostatic Pressing (HIP) technology and its applications to metals and ceramics,” *J. Mater. Sci.*, vol. 39, no. 21, pp. 6399–6420, Nov. 2004, doi: 10.1023/B:JMSC.0000044878.11441.90.

[78] R. M. German, P. Suri, and S. J. Park, “Review: liquid phase sintering,” *J. Mater. Sci.*, vol. 44, no. 1, pp. 1–39, Jan. 2009, doi: 10.1007/s10853-008-3008-0.

[79] R. German, *Liquid Phase Sintering*. New York, NY: Springer, 1985.

[80] M. G. Taylor, B. E. Davies, and I. R. Harris, “A comparative study of the sintering behaviour of NdFeB and PrFeB for permanent magnet applications,” *J. Magn. Magn. Mater.*, vol. 242–245, pp. 1375–1377, Apr. 2002, doi: 10.1016/S0304-8853(01)01237-9.

[81] B. E. Davies, R. S. Mottram, and I. R. Harris, “Recent developments in the sintering of NdFeB,” *Mater. Chem. Phys.*, vol. 67, no. 1, pp. 272–281, Jan. 2001, doi: 10.1016/S0254-0584(00)00450-8.

[82] J. Hankel, S. Jäger, and S. Weber, “Development of a recycling strategy for grinding sludge using supersolidus liquid phase sintering,” *J. Clean. Prod.*, vol. 263, p. 121501, Aug. 2020, doi: 10.1016/j.jclepro.2020.121501.

[83] S. Jäger and S. Weber, “Upcycling strategy of grinding swarf by supersolidus liquid phase sintering,” *Procedia CIRP*, vol. 90, pp. 546–551, 2020, doi: 10.1016/j.procir.2020.01.079.

[84] S. Grasso, Y. Sakka, and G. Maizza, “Electric current activated/assisted sintering (ECAS): a review of patents 1906–2008,” *Sci. Technol. Adv. Mater.*, vol. 10, no. 5, p. 053001, Nov. 2009, doi: 10.1088/1468-6996/10/5/053001.

[85] W. Ji, B. Parker, S. Falco, J. Y. Zhang, Z. Y. Fu, and R. I. Todd, “Ultra-fast firing: Effect of heating rate on sintering of 3YSZ, with and without an electric field,” *J. Eur. Ceram. Soc.*, vol. 37, no. 6, pp. 2547–2551, June 2017, doi: 10.1016/j.jeurceramsoc.2017.01.033.

[86] S. Grasso, T. Saunders, H. Porwal, O. Cedillos-Barraza, D. D. Jayaseelan, W. E. Lee, and M. J. Reece, “Flash Spark Plasma Sintering (FSPS) of Pure 2,” *J. Am. Ceram. Soc.*, vol. 97, no. 8, pp. 2405–2408, 2014, doi: 10.1111/jace.13109.

[87] F. Maccari, T. P. Mishra, M. Keszler, T. Braun, E. Adabifiroozjaei, I. Radulov, T. Jiang, E. Bruder, O. Guillou, L. Molina-Luna, M. Bram, and O. Gutfleisch, “Nanocrystalline Nd–Fe–B Anisotropic Magnets by Flash Spark Plasma Sintering,” *Adv. Eng. Mater.*, vol. 25, no. 18, p. 2300252, 2023, doi: 10.1002/adem.202300252.

[88] W. D. Callister and D. G. Rethwisch, *Fundamentals of Material Science and Engineering*, 5th ed. Wiley, 2015.

[89] J. M. D. Coey, Ed., “Magnetostatics,” in *Magnetism and Magnetic Materials*, Cambridge: Cambridge University Press, 2010, pp. 24–61. doi: 10.1017/CBO9780511845000.003.

[90] C. Kittel, “Chapter 12: Ferromagnetism and Antiferromagnetism,” in *Introduction to solid state physics*, 8. ed., [Repr.]. Hoboken, NJ: Wiley, 2005.

[91] R. O’Handley, *Modern Magnetic Materials*. John Wiley & Sons, 2000.

[92] B. D. Cullity and C. D. Graham, *Introduction to Magnetic Materials*. Wiley, 2009.

[93] F. Jimenez-Villacorta and L. Lewis, “Advanced Permanent Magnetic Materials,” in *Nanomagnetism*, 2014, p. 30.

[94] J. M. D. Coey, Ed., “Ferromagnetism and exchange,” in *Magnetism and Magnetic Materials*, Cambridge: Cambridge University Press, 2010, pp. 128–194. doi: 10.1017/CBO9780511845000.006.

[95] L. Néel, “Théorie du trainage magnétique des ferromagnétiques en grains fins avec application aux terres cuites,” *Ann. Géophysique*, vol. 5, pp. 99–136, 1949.

[96] R. F. Butler and S. K. Banerjee, “Theoretical single-domain grain size range in magnetite and titanomagnetite,” *J. Geophys. Res. 1896–1977*, vol. 80, no. 29, pp. 4049–4058, 1975, doi: 10.1029/JB080i029p04049.

[97] D. Jiles, *Introduction to Magnetism and Magnetic Materials*. Chapman & Hall, 1991.

[98] J. F. Herbst, J. J. Croat, and F. E. Pinkerton, “Relationships between crystal structure and magnetic properties in Nd2Fe14B,” *Phys. Rev. B*, vol. 29, no. 7, Apr. 1984.

[99] J. J. Croat, J. F. Herbst, R. W. Lee, and F. E. Pinkerton, “High-energy product Nd-Fe-B permanent magnets,” *Appl. Phys. Lett.*, vol. 44, no. 1, pp. 148–149, Jan. 1984, doi: 10.1063/1.94584.

[100] I. Dirba, A. Aravindhan, M. Muneeb, and O. Gutfleisch, “Grain size and coercivity tuning in Nd2Fe14B-based magnets prepared by high pressure hydrogen milling,” *J. Magn. Magn. Mater.*, vol. 582, p. 171018, Sept. 2023, doi: 10.1016/j.jmmm.2023.171018.

[101] D. Brown, B.-M. Ma, and Z. Chen, “Developments in the processing and properties of NdFeb-type permanent magnets,” *J. Magn. Magn. Mater.*, vol. 248, no. 3, pp. 432–440, Aug. 2002, doi: 10.1016/S0304-8853(02)00334-7.

[102] J. F. Herbst and J. J. Croat, “Neodymium-iron-boron permanent magnets,” *J. Magn. Magn. Mater.*, vol. 100, no. 1, pp. 57–78, Nov. 1991, doi: 10.1016/0304-8853(91)90812-O.

[103] M. Endoh, M. Tokunaga, E. B. Boltich, and W. E. Wallace, “Magnetic properties of Ga-added die-upset Nd-Fe-B magnets,” *IEEE Trans. Magn.*, vol. 25, no. 5, pp. 4114–4116, Sept. 1989, doi: 10.1109/20.42539.

[104] Y. Nozawa, K. Iwasaki, S. Tanigawa, M. Tokunaga, and H. Harada, “Nd-Fe-B die-upset and anisotropic bonded magnets (invited),” *J. Appl. Phys.*, vol. 64, no. 10, pp. 5285–5289, Nov. 1988, doi: 10.1063/1.342394.

[105] R. Islam, K. Vero, and J. P. Borah, “Historical overview and recent advances in permanent magnet materials,” *Mater. Today Commun.*, vol. 41, p. 110538, Dec. 2024, doi: 10.1016/j.mtcomm.2024.110538.

[106] R. Nakayama and T. Takeshita, “Nd-Fe-B anisotropic magnet powders produced by the HDDR process,” *J. Alloys Compd.*, vol. 193, no. 1, pp. 259–261, Mar. 1993, doi: 10.1016/0925-8388(93)90364-S.

[107] R. Nakayama, T. Takeshita, M. Itakura, N. Kuwano, and K. Oki, “Magnetic properties and microstructures of the Nd-Fe-B magnet powder produced by hydrogen treatment,” *J. Appl. Phys.*, vol. 70, no. 7, pp. 3770–3774, Oct. 1991, doi: 10.1063/1.349232.

[108] P. J. McGuiness, X. J. Zhang, X. J. Yin, and I. R. Harris, “Hydrogenation, disproportionation and desorption (HDD): An effective processing route for Nd₂Fe₁₄B-type magnets,” *J. Common Met.*, vol. 158, no. 2, pp. 359–365, Mar. 1990, doi: 10.1016/0022-5088(90)90071-Q.

[109] I. R. Harris and P. J. McGuiness, “Hydrogen: its use in the processing of NdFeB-type magnets,” *J. Common Met.*, vol. 172–174, pp. 1273–1284, Jan. 1991, doi: 10.1016/S0022-5088(06)80037-8.

[110] J. M. D. Coey and K. O’Donnell, “New bonded magnet materials (invited),” *J. Appl. Phys.*, vol. 81, no. 8, pp. 4810–4815, Apr. 1997, doi: 10.1063/1.365470.

[111] R. Nakayama, T. Takeshita, M. Itakura, N. Kuwano, and K. Oki, “Microstructures and crystallographic orientation of crystalline grains in anisotropic Nd-Fe-Co-B-(Ga or Zr) magnet powders produced by the hydrogenation-decomposition-desorption-recombination process,” *J. Appl. Phys.*, vol. 76, no. 1, pp. 412–417, 1994, doi: 10.1063/1.357091.

- [112] M. Sagawa, S. Fujimura, N. Togawa, H. Yamamoto, and Y. Matsuura, “New material for permanent magnets on a base of Nd and Fe (invited),” *J. Appl. Phys.*, vol. 55, no. 6, pp. 2083–2087, Mar. 1984, doi: 10.1063/1.333572.
- [113] M. Sagawa and H. Nagata, “Novel processing technology for permanent magnets,” *IEEE Trans. Magn.*, vol. 29, no. 6, pp. 2747–2751, Nov. 1993, doi: 10.1109/20.280924.
- [114] S. Liang, X. Shao, Y. Que, B. Guo, H. Bao, G. Tang, X. Yan, J. Bao, L. Yang, L. Qin, K. Shu, D. Chen, and Z. Song, “Recent advances in mechanical properties of sintered NdFeB magnets,” *J. Alloys Compd.*, vol. 1003, p. 175689, Oct. 2024, doi: 10.1016/j.jallcom.2024.175689.
- [115] J. J. Croat, “6 - Hot-deformed NdFeB permanent magnets,” in *Rapidly Solidified Neodymium-Iron-boron Permanent Magnets*, J. J. Croat, Ed., in Woodhead Publishing Series in Electronic and Optical Materials. Woodhead Publishing, 2018, pp. 225–295. doi: 10.1016/B978-0-08-102225-2.00006-5.
- [116] B. B. Straumal, Yu. O. Kucheev, I. L. Yatskovskaya, I. V. Mogilnikova, G. Schütz, A. N. Nekrasov, and B. Baretzky, “Grain boundary wetting in the NdFeB-based hard magnetic alloys,” *J. Mater. Sci.*, vol. 47, no. 24, pp. 8352–8359, Dec. 2012, doi: 10.1007/s10853-012-6618-5.
- [117] Y. Matsuura, S. Hirosawa, H. Yamamoto, S. Fujimura, M. Sagawa, and K. Osamura, “Phase Diagram of the Nd-Fe-B Ternary System,” *Jpn. J. Appl. Phys.*, vol. 24, no. 8A, p. L635, Aug. 1985, doi: 10.1143/JJAP.24.L635.
- [118] W. Grünberger, D. Hinz, A. Kirchner, K.-H. Müller, and L. Schultz, “Hot deformation of nanocrystalline Nd-Fe-B alloys,” *J. Alloys Compd.*, vol. 257, no. 1, pp. 293–301, July 1997, doi: 10.1016/S0925-8388(97)00026-1.
- [119] K. Khlopkov, O. Gutfleisch, R. Schäfer, D. Hinz, K.-H. Müller, and L. Schultz, “Interaction domains in die-upset NdFeB magnets in dependence on the degree of deformation,” *J. Magn. Magn. Mater.*, vol. 272–276, pp. E1937–E1939, May 2004, doi: 10.1016/j.jmmm.2003.12.1102.
- [120] “Sintered neodymium iron boron permanent magnets (English Version).” 2018.
- [121] “Grades of Neodymium,” *e-Magnets UK*. <https://e-magnetsuk.com/introduction-to-neodymium-magnets/grades-of-neodymium/> (accessed Feb. 25, 2025).
- [122] K. Hirota, H. Nakamura, T. Minowa, and M. Honshima, “Coercivity Enhancement by Grain Boundary Diffusion Process to Nd-Fe-B Sintered Magnets,” in *2006 IEEE International Magnetics Conference (INTERMAG)*, May 2006, pp. 910–910. doi: 10.1109/INTMAG.2006.374941.
- [123] Y. Une and M. Sagawa, “Enhancement of Coercivity of Nd-Fe-B Sintered Magnets by Grain Size Reduction,” *J. Jpn. Inst. Met.*, vol. 76, pp. 12–16, Jan. 2012, doi: 10.2320/jinstmet.76.12.
- [124] H. Sepehri-Amin, T. Ohkubo, and K. Hono, “The mechanism of coercivity enhancement by the grain boundary diffusion process of Nd-Fe-B sintered magnets,” *Acta Mater.*, vol. 61, no. 6, pp. 1982–1990, Apr. 2013, doi: 10.1016/j.actamat.2012.12.018.
- [125] W. Gruenberger, “The solution-precipitation creep - a model for deformation and texturing mechanisms of nanocrystalline NdFeB alloys,” July 1998, Accessed: Jan. 09, 2025. [Online]. Available: <https://www.osti.gov/etdeweb/biblio/20053347>
- [126] W. B. Kamb, “Theory of Preferred Crystal Orientation Developed by Crystallization under Stress,” *J. Geol.*, vol. 67, no. 2, pp. 153–170, Mar. 1959, doi: 10.1086/626571.
- [127] P. Tenaud, A. Chamberod, and F. Vanoni, “Texture in Nd-Fe-B magnets analysed on the basis of the determination of Nd₂Fe₁₄B single crystals easy growth axis,” *Solid State Commun.*, vol. 63, no. 4, pp. 303–305, July 1987, doi: 10.1016/0038-1098(87)90913-6.
- [128] Ch. Kuhrt, L. Schultz, K. Schnitzke, S. Hock, and R. Behrensmeier, “High-temperature compressive plastic deformation of Nd₂Fe₁₄B single crystals,” *Appl. Phys. Lett.*, vol. 59, no. 12, pp. 1418–1420, Sept. 1991, doi: 10.1063/1.105325.
- [129] M. Liu, L. Zhang, B. Zhao, F. Chen, X. Xia, Y. Yu, H. Yamamoto, and K. Ito, “Orientation dependence of plastic deformation of sintered Nd-Fe-B magnets at high temperature,” *Acta Mater.*, vol. 244, p. 118559, Jan. 2023, doi: 10.1016/j.actamat.2022.118559.

[130] L. Leich, A. Röttger, W. Theisen, and M. Krengel, “Densification of nanocrystalline NdFeB magnets processed by electro-discharge sintering – Microstructure, magnetic, and mechanical properties,” *J. Magn. Magn. Mater.*, vol. 460, pp. 454–460, Aug. 2018, doi: 10.1016/j.jmmm.2018.04.035.

[131] G. A. Roberts, R. Kennedy, and G. Krauss, *Tool Steels, 5th Edition*. ASM International, 1998.

[132] R. Angers, B. Champagne, and R. Tremblay, “PM high speed steels enriched in C, V and Ti,” *Met. Powder Rep.*, vol. 45, no. 12, pp. 844–846, Dec. 1990, doi: 10.1016/0026-0657(90)90577-4.

[133] M. K. Banerjee, “Physical Metallurgy of Tool Steels,” in *Reference Module in Materials Science and Materials Engineering*, Elsevier, 2018. doi: 10.1016/B978-0-12-803581-8.09810-6.

[134] E. Bain, “The Nature of Martensite,” *Trans. AIME*, no. 70, pp. 25–46, Jan. 1924.

[135] L. C. F. Canale, J. Vatavuk, and G. E. Totten, “12.02 - Introduction to Steel Heat Treatment,” in *Comprehensive Materials Processing*, S. Hashmi, G. F. Batalha, C. J. Van Tyne, and B. Yilbas, Eds., Oxford: Elsevier, 2014, pp. 3–37. doi: 10.1016/B978-0-08-096532-1.01202-4.

[136] J. I. Chang, J. J. Lin, J. S. Huang, and Y. M. Chang, “Recycling oil and steel from grinding swarf,” *Resour. Conserv. Recycl.*, vol. 49, no. 2, pp. 191–201, Dec. 2006, doi: 10.1016/j.resconrec.2006.03.014.

[137] N. Araya, G. O. Neves, A. I. Ramos Filho, C. Aguilar, J. D. Biasoli de Mello, C. Binder, A. N. Klein, and G. Hammes, “Study of silicon carbide dissociation into Fe and Fe C matrixes produced by die pressing and sintering,” *Mater. Chem. Phys.*, vol. 253, p. 123442, Oct. 2020, doi: 10.1016/j.matchemphys.2020.123442.

[138] K. S. Kumar, A. Lawley, and M. J. Koczak, “Powder metallurgy T15 tool steel: Part I. Characterization of powder and hot isostatically pressed material,” *Metall. Trans. A*, vol. 22, no. 11, pp. 2733–2745, Nov. 1991, doi: 10.1007/BF02851368.

[139] A. Kasak and E. J. Dulis, “Powder-Metallurgy Tool Steels,” *Powder Metall.*, vol. 21, no. 2, pp. 114–123, Jan. 1978, doi: 10.1179/pom.1978.21.2.114.

[140] A. SINGH, M. K. SINHA, V. JAGOTA, and R. KUMAR, “Production, characterisation and utilisation of grinding swarf/feedstock for synthesis of metal matrix composite through powder metallurgy process: A short communication,” *Sādhanā*, vol. 47, no. 3, p. 160, Aug. 2022, doi: 10.1007/s12046-022-01923-1.

[141] F. Großwendt, V. Bürk, B. Kopanka, S. Jäger, S. Pollak, L. Leich, A. Röttger, M. Petermann, and S. Weber, “A novel powder-metallurgical eco-friendly recycling process for tool steel grinding sludge,” *J. Clean. Prod.*, vol. 392, p. 136329, Feb. 2023, doi: 10.1016/j.jclepro.2023.136329.

[142] N. S. Weston and M. Jackson, “FAST-forge of Titanium Alloy Swarf: A Solid-State Closed-Loop Recycling Approach for Aerospace Machining Waste,” *Metals*, vol. 10, no. 2, Art. no. 2, Feb. 2020, doi: 10.3390/met10020296.

[143] N. S. Weston and M. Jackson, “FAST-forge – A new cost-effective hybrid processing route for consolidating titanium powder into near net shape forged components,” *J. Mater. Process. Technol.*, vol. 243, pp. 335–346, May 2017, doi: 10.1016/j.jmatprotec.2016.12.013.

[144] J. Swithenbank, J. Beer, D. Taylor, D. Abbot, and G. McCreath, “A laser diagnostic technique for the measurement of droplet and particle size distribution,” presented at the AIAA 14th Aerospace Sciences Meetings, Washington, DC: American Institute of Aeronautics and Astronautics, Jan. 1976. doi: 10.2514/6.1976-69.

[145] A. Annapragada and A. Adjei, “An analysis of the fraunhofer diffraction method for particle size distribution analysis and its application to aerosolized sprays,” *Int. J. Pharm.*, vol. 127, no. 2, pp. 219–227, Feb. 1996, doi: 10.1016/0378-5173(95)04217-2.

[146] R. Xu and O. A. Di Guida, “Comparison of sizing small particles using different technologies,” *Powder Technol.*, vol. 132, no. 2, pp. 145–153, June 2003, doi: 10.1016/S0032-5910(03)00048-2.

[147] W. Witt, U. Köhler, and J. List, “Direct Imaging of Very Fast Particles Opens the Application of the Powerful (Dry) Dispersion for Size and Shape Characterization,” 2004.

- [148] W. Yu and B. C. Hancock, “Evaluation of dynamic image analysis for characterizing pharmaceutical excipient particles,” *Int. J. Pharm.*, vol. 361, no. 1, pp. 150–157, Sept. 2008, doi: 10.1016/j.ijpharm.2008.05.025.
- [149] “Particle Shape,” *Sympatec | Analysers for Particle Size and Shape*. <https://www.sympatec.com/en/particle-measurement/glossary/fundamentals-of-particle-characterisation/particle-shape> (accessed Jan. 17, 2025).
- [150] H. G. Merkus, *Particle Size Measurements: Fundamentals, Practice, Quality*. Springer Science & Business Media, 2009.
- [151] H. Wadell, “Volume, Shape, and Roundness of Quartz Particles,” *J. Geol.*, vol. 43, no. 3, pp. 250–280, Apr. 1935, doi: 10.1086/624298.
- [152] L. Klein, “Carrier Gas Hot Extraction: Non-Metals in Metals,” *RevierLabor*, Oct. 2021.
- [153] J. Olesik, “Elemental analysis using ICP-OES and ICP/MS: An Evaluation and Assessment of Remaining Problems,” *Anal. Chem.*, vol. 63, no. 1, p. 2, Jan. 1991.
- [154] G. L. Bosco, “Development and application of portable, hand-held X-ray fluorescence spectrometers,” *TrAC Trends Anal. Chem.*, vol. 45, pp. 121–134, Apr. 2013, doi: 10.1016/j.trac.2013.01.006.
- [155] L. Leich, A. Röttger, R. Kuchenbecker, and W. Theisen, “Electro-discharge sintering of nanocrystalline NdFeB magnets: process parameters, microstructure, and the resulting magnetic properties,” *J. Mater. Sci. Mater. Electron.*, vol. 31, no. 22, pp. 20431–20443, Nov. 2020, doi: 10.1007/s10854-020-04562-6.
- [156] J. O. Andersson, T. Helander, L. Höglund, P. F. Shi, and B. Sundman, “Thermo-Calc and DICTRA, Computational tools for materials science,” *Calphad*, vol. 26, pp. 273–312.
- [157] L. Brackmann, A. Röttger, M. Treppmann, and S. Weber, “The behavior of cutting discs for mechanized tunneling under cyclic loading conditions,” *Tunn. Undergr. Space Technol.*, vol. 137, p. 105151, July 2023, doi: 10.1016/j.tust.2023.105151.
- [158] R. F. Egerton, “The Scanning Electron Microscope,” in *Physical Principles of Electron Microscopy: An Introduction to TEM, SEM, and AEM*, R. F. Egerton, Ed., Cham: Springer International Publishing, 2016, pp. 121–147. doi: 10.1007/978-3-319-39877-8_5.
- [159] R. F. Egerton, “Analytical Electron Microscopy,” in *Physical Principles of Electron Microscopy: An Introduction to TEM, SEM, and AEM*, R. F. Egerton, Ed., Cham: Springer International Publishing, 2016, pp. 149–169. doi: 10.1007/978-3-319-39877-8_6.
- [160] P. Chapon, S. Gaiaschi, and K. Shimizu, “Glow Discharge Optical Emission Spectrometry,” in *Compendium of Surface and Interface Analysis*, The Surface Science Society of Japan, Ed., Singapore: Springer, 2018, pp. 219–228. doi: 10.1007/978-981-10-6156-1_37.
- [161] A. O. Adeyeye and G. Shimon, *Handbook of Surface Science*, vol. 5. 2015.
- [162] T. Thomson, *Metallic Films for Electronic, Optical, and Magnetic Applications*. 2014.
- [163] K. Herrmann, *Hardness Testing: Principles and Applications*. Materials Park, United States: ASM International, 2012. Accessed: Jan. 22, 2025. [Online]. Available: <http://ebookcentral.proquest.com/lib/fz/detail.action?docID=3002452>
- [164] P. Nothnagel, K.-H. Müller, D. Eckert, and A. Handstein, “The influence of particle size on the coercivity of sintered NdFeB magnets,” *J. Magn. Magn. Mater.*, vol. 101, no. 1, pp. 379–381, Oct. 1991, doi: 10.1016/0304-8853(91)90786-A.
- [165] M. Keszler, F. Grosswendt, A.-C. Assmann, M. Krengel, F. Maccari, O. Gutfleisch, D. Sebold, O. Guillon, S. Weber, and M. Bram, “Direct Recycling of Hot-Deformed Nd–Fe–B Magnet Scrap by Field-Assisted Sintering Technology,” *Adv. Energy Sustain. Res.*, vol. 5, no. 1, p. 2300184, 2024, doi: 10.1002/aesr.202300184.
- [166] J. Orellana, I. Moreno-Viloslada, R. K. Bose, F. Picchioni, M. E. Flores, and R. Araya-Hermosilla, “Self-Healing Polymer Nanocomposite Materials by Joule Effect,” *Polymers*, vol. 13, no. 4, Art. no. 4, Jan. 2021, doi: 10.3390/polym13040649.
- [167] T. J.-C. Liu, “Joule heating behaviors around through crack emanating from circular hole under electric load,” *Eng. Fract. Mech.*, vol. 123, pp. 2–20, June 2014, doi: 10.1016/j.engfracmech.2014.01.016.

[168] T. Sakagami and K. Ogura, “A New Flaw Inspection Technique Based on Infrared Thermal Images Under Joule Effect Heating,” *Trans. Jpn. Soc. Mech. Eng. Ser. A*, vol. 58, no. 555, pp. 2224–2231, 1992, doi: 10.1299/kikaia.58.2224.

[169] R. Chuanbing and S. Baogen, “Nanocrystalline and nanocomposite permanent magnets by melt spinning technique,” *Chin. Phys. B*, vol. 27, no. 11, 2018.

[170] M. Keszler, I. A. Radulov, F. Maccari, T. Mutuk, M. Krengel, O. Guillon, O. Gutfleisch, and M. Bram, “Field assisted sintering and spark plasma texturing of Nd–Fe–B magnets with anisotropic magnetic properties,” *Powder Metall.*, p. 00325899251331431, Apr. 2025, doi: 10.1177/00325899251331431.

[171] Y. Luo, N. Zhang, and C. D. Graham Jr., “Variation of hardness with temperature in sintered NdFeB magnets,” *J. Appl. Phys.*, vol. 61, no. 8, pp. 3442–3444, Apr. 1987, doi: 10.1063/1.338747.

[172] M.-D. Calin and E. Helerea, “Temperature influence on magnetic characteristics of NdFeB permanent magnets,” in *2011 7TH INTERNATIONAL SYMPOSIUM ON ADVANCED TOPICS IN ELECTRICAL ENGINEERING (ATEE)*, May 2011, pp. 1–6. Accessed: July 02, 2025. [Online]. Available: <https://ieeexplore.ieee.org/abstract/document/5952212>

[173] M. Zakotnik, C. O. Tudor, L. T. Peiró, P. Afiuny, R. Skomski, and G. P. Hatch, “Analysis of energy usage in Nd–Fe–B magnet to magnet recycling,” *Environ. Technol. Innov.*, vol. 5, pp. 117–126, Apr. 2016, doi: 10.1016/j.eti.2016.01.002.

[174] M. Treppmann, “Characterization of FAST-recycled High-Speed Tool Steel Grinding Chips,” Master Thesis, Ruhr-Universitaet Bochum, Bochum, 2024.

[175] P. S. Liu and G. F. Chen, “Chapter Two - Making Porous Metals,” in *Porous Materials*, P. S. Liu and G. F. Chen, Eds. Boston: Butterworth-Heinemann, 2014, pp. 21–112. doi: 10.1016/B978-0-12-407788-1.00002-2.

[176] K. S. Kumar, A. Lawley, and M. J. Koczak, “Powder metallurgy T15 tool steel: Part II. Microstructure and properties after heat treatment,” *Metall. Trans. A*, vol. 22, no. 11, pp. 2747–2759, Nov. 1991, doi: 10.1007/BF02851369.

[177] J. Lentz, A. Röttger, and W. Theisen, “Solidification and phase formation of alloys in the hypoeutectic region of the Fe–C–B system,” *Acta Mater.*, vol. 99, pp. 119–129, Oct. 2015, doi: 10.1016/j.actamat.2015.07.037.

[178] M. R. Ghomashchi and CM. Sellars, “Microstructural Changes in As-Cast M2 Grade High Speed Steel during Hot Forging,” *Metall. Trans. A*, vol. 24, no. 10, pp. 2171–2180, Oct. 1993, doi: 10.1007/BF02648591.

[179] L. Brackmann, D. Wingender, S. Weber, D. Balzani, and A. Röttger, “Influence of hard phase size and spacing on the fatigue crack propagation in tool steels—Numerical simulation and experimental validation,” *Fatigue Fract. Eng. Mater. Struct.*, vol. 46, no. 10, pp. 3872–3891, 2023, doi: 10.1111/ffe.14107.

[180] P. A. Thornton, “The influence of nonmetallic inclusions on the mechanical properties of steel: A review,” *J. Mater. Sci.*, vol. 6, no. 4, pp. 347–356, Apr. 1971, doi: 10.1007/PL00020378.

[181] V. Kruzhakov and V. Arnhold, “Energy consumption in powder metallurgical manufacturing,” *Powder Metall.*, vol. 55, no. 1, pp. 14–21, Feb. 2012, doi: 10.1179/174329012X13318077875722.

[182] A. M. Laptev, M. Bram, D. Garbiec, J. Räthel, A. van der Laan, Y. Beynet, J. Huber, M. Küster, M. Cologna, and O. Guillon, “Tooling in Spark Plasma Sintering Technology: Design, Optimization, and Application,” *Adv. Eng. Mater.*, vol. 26, no. 5, p. 2301391, 2024, doi: 10.1002/adem.202301391.

[183] K. Grieff, “Bewertung der Stoffkreisläufe (AP9),” presented at the GENESIS Projekttreffen, Bochum, Jan. 24, 2025.

[184] N. A. Bhuiyan and A. McDonald, “Optimization of Offshore Direct Drive Wind Turbine Generators With Consideration of Permanent Magnet Grade and Temperature,” *IEEE Trans. Energy Convers.*, vol. 34, no. 2, pp. 1105–1114, June 2019, doi: 10.1109/TEC.2018.2879442.

[185] W. Z. Magnetics, “Introduction of Neodymium Magnet Grades,” *Holding Magnets Manufacturer | WZ Magnetics*, Apr. 12, 2024. <https://www.wzmagnetics.com/introduction-of-neodymium-magnet-grades-from-weizhong-magnetics/> (accessed Apr. 11, 2025).

- [186] M. Schönfeldt, O. Diehl, and J. Gassmann, *Recycling of NdFeB magnets in Germany*, 45 S., vol. 60. Berlin: DERA Rohstoffinformationen, 2024.
- [187] A. Furgeri, “Sustainable Design for Recycling,” presented at the Webinar: Rare Earth Elements in Sustainable Circular Economy, Oct. 08, 2020. [Online]. Available: <https://www.youtube.com/watch?v=kBchLYebb2c>
- [188] D. Chasoglou, E. Hryha, and L. Nyborg, “Effect of Sintering Atmosphere on the Transformation of Surface Oxides during the Sintering of Chromium Alloyed Steel,” *Powder Metall. Prog.*, vol. 9(2009), no. 3, pp. 141–155, 2010.
- [189] E. Hryha, L. Nyborg, A. Malas, S. Wiberg, and S. Berg, “Carbon control in PM sintering: Industrial applications and experience,” *Powder Metall.*, vol. 56, no. 1, pp. 5–10, Feb. 2013, doi: 10.1179/0032589912Z.00000000085.

Appendix A Nd-Fe-B recyclate powder data

Particle size, O content, N content, and VSM measurements

Powder Name	Particle Size Range [μm]	O content [ppm]	N content [ppm]	H_{cJ} [kA m^{-1}]	B_r [T]	$(BH)_{max}$ [kJ m^{-3}]
MQU-F	<400	1120	100	1693	0.74	90.5
LCM1	<200	6060	1000	1312	1.06	179.0
LCM2	180-200	3750	550	n.a.	n.a.	n.a.
RC1	<200	6000	350	1097	1.22	225.6
RC2	200-125	2500	80	1140	1.28	284.3
RC3	500-1000	2350	230	1174	1.31	315.6
MRV1	180-500	2430	180	n.a.	n.a.	n.a.
MRV2	500-1000	1940	150	n.a.	n.a.	n.a.

ICP-OES analysis

Powder Name	Nd [wt%]	Fe [wt%]	B [wt%]	Ga [wt%]	Co [wt%]	Pr [wt%]
MQU-F	30.6	60.0	0.80	0.54	5.57	0.11
LCM1	30.0	59.0	0.81	0.55	5.28	0.13
LCM2	29.4	58.5	0.86	0.55	5.58	<0.07
RC1	29.1	60.9	0.70	0.42	5.81	0.17
RC2	30.2	63.1	0.75	0.45	6.00	0.20
RC3	31.0	62.8	0.85	0.57	5.74	0.25
MRV1	30.0	62.1	0.90	0.58	5.80	<0.07
MRV2	28.7	60.0	0.86	0.55	5.60	<0.07

Appendix B Comprehensive magnetic performance data (Flash SPS)

Flash SPS of mixed recyclate samples (RC series)

Starting Powder					Pre-Sintered State		Deformed State					
Sample Code	Melt-spun Material	Scrap Material	Particle size range (recyclate) (µm)	wt% recyclate	Sample height (mm)	Relative density (%)	Sample height (mm)	Deform. degree z-direction (%)	Relative density (%)	H_{cJ} (kA m ⁻¹)	B_r (T)	$(BH)_{max}$ (kJ m ⁻³)
MQU-F-100	MQU-F	none	N/A	0	7.4	80%	3.09	58%	96%	1587	1.13	243
LCM1-9505	MQU-F	LCM1	<200	5	7.55	78%	3.53	53%	97%	1576	1.11	229
LCM1-9010	MQU-F	LCM1	<200	10	7.92	75%	3.32	58%	96%	1549	1.10	224
LCM1-8515	MQU-F	LCM1	<200	15	8.04	73%	3.52	56%	96%	1525	1.12	231
LCM1-8020	MQU-F	LCM1	<200	20	7.82	75%	3.47	56%	94%	1482	1.06	207
LCM1-5050	MQU-F	LCM1	<200	50	8.15	72%	3.70	55%	97%	1255	1.00	177
LCM1-0100	MQU-F	LCM1	<200	100	8.4	70%	3.68	56%	95%	724	1.10	171
RC1-9505	MQU-F	RC1	<200	5	7.87	75%	3.33	58%	99%	1540	1.13	235
RC1-9010	MQU-F	RC1	<200	10	7.75	74%	3.34	57%	98%	1485	1.13	234
RC1-8515	MQU-F	RC1	<200	15	7.9	75%	3.39	57%	97%	1433	1.11	225
RC1-8020	MQU-F	RC1	<200	20	7.56	74%	3.39	55%	93%	1379	1.10	221
RC1-5050	MQU-F	RC1	<200	50	8.11	72%	3.31	59%	98%	931	0.99	164
RC1-0100	MQU-F	RC1	<200	100	8.95	65%	4.06	55%	96%	257	0.98	69
RC2-9505	MQU-F	RC2	125-200	5	7.74	75%	3.43	56%	96%	1426	1.14	237
RC2-9010	MQU-F	RC2	125-200	10	7.77	74%	3.47	55%	98%	1452	1.09	218
RC2-8515	MQU-F	RC2	125-200	15	7.66	75%	3.46	55%	97%	1497	1.12	231
RC2-8020	MQU-F	RC2	125-200	20	7.87	74%	3.49	56%	97%	1546	1.10	223
RC2-5050	MQU-F	RC2	125-200	50	8.1	72%	3.67	55%	98%	1156	1.03	192
RC2-0100	MQU-F	RC2	125-200	100	8.3	70%	3.31	60%	95%	776	1.13	219
RC3-9505	MQU-F	RC3	500-1000	5	7.61	77%	3.30	57%	95%	1544	1.16	251
RC3-9010	MQU-F	RC3	500-1000	10	7.88	74%	3.27	59%	92%	1513	1.15	249
RC3-8515	MQU-F	RC3	500-1000	15	7.66	77%	3.27	57%	93%	1479	1.15	248
RC3-8020	MQU-F	RC3	500-1000	20	7.65	77%	3.06	60%	98%	1452	1.13	237
RC3-5050	MQU-F	RC3	500-1000	50	7.85	73%	3.31	58%	95%	1247	1.12	234
RC3-0100	MQU-F	RC3	500-1000	100	8.34	71%	2.72	67%	89%	836	0.96	157

Boron nitride ring (BN) Series

BN1 Series			Pre-sintered state		Deformed State						
Sample Code	Powder	BN die, mm	Sample height (mm)	Relative density (%)	Sample height (mm)	Deform. degree z-direction (%)	Relative density (%)	Edge or center	H_{cJ} (kA m ⁻¹)	B_r (T)	$(BH)_{max}$ (kJ m ⁻³)
BN1-30	MQU-F	30	7.55	78%	3.08	59%	95%	Center	1346	1.09	213
BN1-30	MQU-F	30	7.55	78%	3.08	59%	92%	Edge	1346	1.09	216
BN1-29	MQU-F	29	7.16	84%	3.30	54%	93%	Center	1346	1.13	235
BN1-28	MQU-F	28	7.53	78%	3.67	51%	94%	Edge	696	1.28	294
BN1-27	MQU-F	27	7.96	74%	3.73	52%	94%	Center	865	1.20	260
BN1-25	MQU-F	25	7.31	79%	4.70	36%	92%	Center	289	0.87	59
BN1-nodie	MQU-F	none	7.78	75%	2.50	68%	88%	Center	1321	1.16	236
BN1-nodie	MQU-F	none	7.78	75%	2.50	68%	88%	Edge	1331	1.24	284
BN2 Series			Pre-sintered state		Deformed State						
Sample Code	Powder	BN die, mm	Sample height (mm)	Relative density (%)	Sample height (mm)	Deform. degree z-direction (%)	Relative density (%)	Edge or center	H_{cJ} (kA m ⁻¹)	B_r (T)	$(BH)_{max}$ (kJ m ⁻³)
BN2-31	MQU-F	31	7.82	75%	2.71	65%	93%	Edge + Center	1319	1.13	240
BN2-32	MQU-F	32	7.86	75%	2.76	65%	93%	Edge + Center	1359	1.22	285
BN2-33	MQU-F	33	7.83	75%	2.74	65%	93%	Edge + Center	1331	1.17	263
BN3 Series			Pre-sintered state		Deformed State						
Sample Code	Powder	BN die, mm	Sample height (mm)	Relative density (%)	Sample height (mm)	Deform. degree z-direction (%)	Relative density (%)	Edge or center	H_{cJ} (kA m ⁻¹)	B_r (T)	$(BH)_{max}$ (kJ m ⁻³)
BN3-31	MRV1	31	8.36	71%	3.08	63%	93%	Edge + Center	951	0.78	109
BN3-32	MRV1	32	8.36	72%	3.00	64%	85%	Edge + Center	942	0.899	146
BN3-33	MRV1	33	7.89	74%	2.96	63%	81%	Edge + Center	956	0.969	171
BN3-nodie	MRV1	none	8.19	76%	2.34	79%	94%	Edge + Center	903	0.944	171
BN4 Series			Pre-sintered state		Deformed State						
Sample Code	Powder	BN die, mm	Sample height (mm)	Relative density (%)	Sample height (mm)	Deform. degree z-direction (%)	Relative density (%)	Edge or center	H_{cJ} (kA m ⁻¹)	B_r (T)	$(BH)_{max}$ (kJ m ⁻³)
BN4-31	MRV2	31	7.05	84%	3.12	56%	89%	Edge + Center	975	0.978	178
BN4-32	MRV2	32	8.40	70%	3.11	63%	81%	Edge + Center	1009	0.752	101
BN4-33	MRV2	33	8.35	68%	2.92	65%	81%	Edge + Center	1027	0.767	106
BN4-nodie	MRV2	none	7.96	74%	2.25	72%	75%	Edge + Center	976	0.832	127

Appendix C Comprehensive magnetic performance data (SPT)

SPT1 series

SPT1-HC/PRE2 series		Pre-sintered state			Deformed state						
Sample Code	Powder	Pre-sinter Code	Sample height (mm)	Relative density (%)	Deform. code	Sample height (mm)	Deform. degree z-direction (%)	Relative density (%)	H_{cJ} (kA m ⁻¹)	B_r (T)	$(BH)_{max}$ (kJ m ⁻³)
SPT1-HC-P10T70	MQU-F	HC1	6.33	93%	SPT1	3.16	50%	96%	1474	1.15	246
SPT1-HC-P20T70	MQU-F	HC1	6.68	89%	SPT1	3.09	54%	97%	1346	1.12	233
SPT1-HC-P30T70	MQU-F	HC1	6.44	91%	SPT1	2.85	56%	96%	1270	1.14	240
SPT1-HC-P10T75	MQU-F	HC1	7.04	93%	SPT1	3.16	49%	98%	1407	1.17	258
SPT1-HC-P20T75	MQU-F	HC1	6.84	91%	SPT1	2.98	54%	96%	1279	1.15	242
SPT1-HC-P30T75	MQU-F	HC1	7.01	93%	SPT1	2.87	54%	98%	1283	1.18	246
SPT1-PS-P10T70	MQU-F	PRE2	7.57	77%	SPT1	3.15	58%	98%	1512	1.12	233
SPT1-PS-P20T70	MQU-F	PRE2	8.10	75%	SPT1	2.99	63%	98%	1502	1.15	243
SPT1-PS-P30T70	MQU-F	PRE2	8.56	74%	SPT1	2.95	66%	98%	1514	1.15	245

Quick deformation (QD) series

QD-MQUF series		Pre-sintered state				Deformed state								
Sample Code	Powder	Pre-sinter Code	Sample height (mm)	Relative density (%)	Deform. code	Sample height (mm)	Deform. Temp. (°C)	Deform. Press. (MPa)	Deform. Speed (mm/s)	Deform. degree z-direction (%)	Relative density (%)	H_{cJ} (kA m ⁻¹)	B_r (T)	$(BH)_{max}$ (kJ m ⁻³)
QD-MQUF-P15T70	MQU-F	PRE2	7.45	80%	QD	3.13	700	150	0.11	58%	96%	1506	1.09	225
QD-MQUF-P15T75	MQU-F	PRE2	7.60	77%	QD	3.16	750	150	0.12	58%	94%	1495	0.95	168
QD-MQUF-P15T80	MQU-F	PRE2	8.01	73%	QD	2.85	800	150	0.10	65%	97%	1381	1.03	199
QD-MRV1 series		Pre-sintered state				Deformed state								
Sample Code	Powder	Pre-sinter Code	Sample height (mm)	Relative density (%)	Deform. code	Sample height (mm)	Deform. Temp. (°C)	Deform. Press. (MPa)	Deform. Speed (mm/s)	Deform. degree z-direction (%)	Relative density (%)	H_{cJ} (kA m ⁻¹)	B_r (T)	$(BH)_{max}$ (kJ m ⁻³)
QD-MRV1-P15T70	MRV1	PRE2	8.10	73%	QD	3.16	700	150	0.14	61%	96%	517	0.53	47
QD-MRV1-P15T75	MRV1	PRE2	8.42	69%	QD	3.12	750	150	0.09	63%	92%	802	0.74	97
QD-MRV1-P15T80	MRV1	PRE2	8.08	72%	QD	3.12	800	150	0.10	61%	94%	859	0.79	111
QD-MRV2 series		Pre-sintered state				Deformed state								
Sample Code	Powder	Pre-sinter Code	Sample height (mm)	Relative density (%)	Deform. code	Sample height (mm)	Deform. Temp. (°C)	Deform. Press. (MPa)	Deform. Speed (mm/s)	Deform. degree z-direction (%)	Relative density (%)	H_{cJ} (kA m ⁻¹)	B_r (T)	$(BH)_{max}$ (kJ m ⁻³)
QD-MRV2-P15T70	MRV2	PRE2	7.23	81%	QD	3.18	700	150	0.13	56%	95%	609	0.61	64
QD-MRV2-P15T75	MRV2	PRE2	7.93	73%	QD	3.12	750	150	0.09	61%	93%	834	0.70	89
QD-MRV2-P15T80	MRV2	PRE2	8.30	70%	QD	3.14	800	150	0.09	62%	93%	932	0.70	89

SPT2 series

SPT2 Series		Pre-Sintered State			Deformed State									
Sample Code	Powder	Pre-sinter Code	Sample height (mm)	Relative density (%)	Deform. code	Sample height (mm)	Deformation temperature (°C)	Deformation Pressure (MPa)	Time to maximum pressure (seconds)	Deform. Degree z-direction (%)	Relative density (%)	H_{cJ} (kA m ⁻¹)	B_r (T)	$(BH)_{max}$ (kJ m ⁻³)
SPT2-30	MRV1	PRE2	8.32	73%	SPT2	2.195	800	100	30	83%	98%	868	1.04	190
SPT2-120	MRV1	PRE2	8.07	74%	SPT2	2.075	800	100	120	90%	96%	773	1.12	195
SPT2-240	MRV1	PRE2	8.04	73%	SPT2	2.09	800	100	240	92%	95%	763	1.05	182

Bibliography

SPT3 Experiment

SPT3 experiment		Pre-Sintered State			Deformed State									
Sample Code	Powder	Pre-sinter Code	Sample height (mm)	Rel. density (%)	Deform. code	Sample height (mm)	Deform. Temp. (°C)	Deformation Pressure (MPa)	Time to maximum pressure (seconds)	Deform. Degree z-direction (%)	Relative density (%)	H_{cJ} (kA m-1)	B_r (T)	$(BH)_{max}$ (kJ m-3)
SPT3	MRV1	PRE2	16,57	73%	SPT3	3.87	800	100	30	74%	97%	905	1,00	177
10 kN	MRV1	PRE2	7.35	75%	SPT3	2.71	800	100	30	76%	96%	928	0.98	173

SPT4 Series

SPT4 Series			Pre-Formed State					Deformed State						
Sample Code	Recyclate Powder (wt%)	Commercial Powder (wt%)	Pre-sinter Code	Pre-sinter temp. (°C)	Pre-sinter dwell time (sec.)	Sample height (mm)	Relative density (%)	Deform. code	Sample height (mm)	Deform. Degree z-direction (%)	Relative density (%)	H_{cJ} (kA m-1)	B_r (T)	$(BH)_{max}$ (kJ m-3)
SPT4-PRE3	LCM2 (100%)	n.a.	PRE2	500	120	16.35	74%	SPT4	3.77	77%	95%	1108	0.94	153
SPT4-HC2	LCM2 (100%)	n.a.	HC2	600	60	13.5	88%	SPT4	3.76	72%	97%	1049	1.11	228
SPT4-HC3	LCM2 (100%)	n.a.	HC3	700	60	12.86	95%	SPT4	3.68	71%	97%	943	1.24	277
SPT4-25-PRE3	LCM2 (25%)	MQU-F (75%)	PRE2	500	120	16.18	73%	SPT4	3.47	79%	95%	1144	1.00	175
SPT4-25-HC2	LCM2 (25%)	MQU-F (75%)	HC2	600	60	13.78	87%	SPT4	3.51	75%	96%	1060	1.28	313
SPT4-25-HC3	LCM2 (25%)	MQU-F (75%)	HC3	700	60	12.86	93%	SPT4	3.77	71%	95%	1057	1.24	295

Appendix D FAST/SPS and FSPS machine data

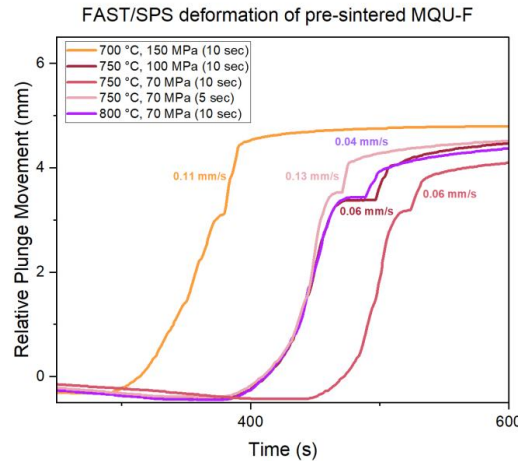


Figure A 1 - Trials for determining parameters for 0.1 mm/s (Section 4.3.2)

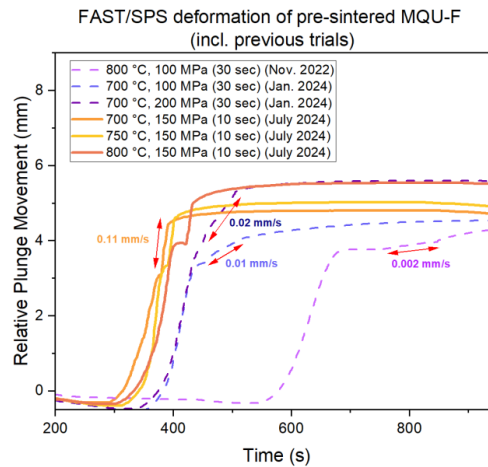


Figure A 2- Comparison of QD speeds to deformation speeds of other SPT trials (Section 4.3.2)

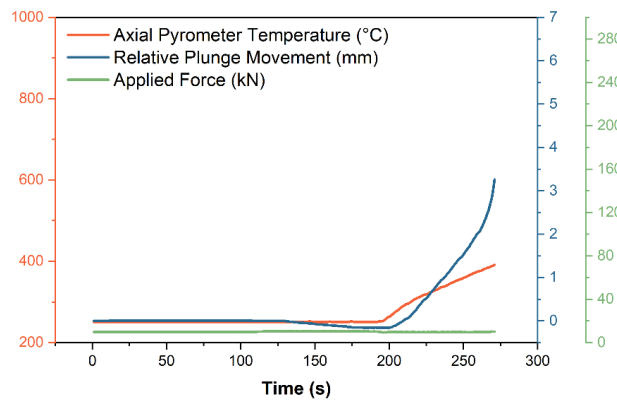


Figure A 3 – Attempted SPT3 deformation with a PRE2 pre-formed sample abruptly cut off due to sample collapse (Section 4.3.3)

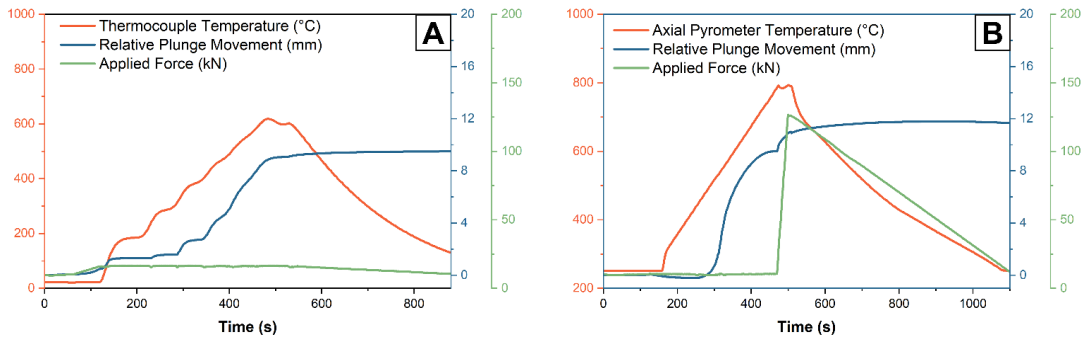


Figure A 4 – FCT HP D25 measurements of temperature, applied force, and plunge movement of the A. HC2 hot-compaction and B. SPT4 deformation of DEMO (Section 4.3.5)

List of Publications

Type	Citation	Authorship	Status
Journal	M. Keszler , F. Grosswendt, A.C. Assmann, M. Krengel, F. Maccari, O. Gutfleisch, D. Sebold, O. Guillon, S. Weber, M. Bram. (2023). Direct Recycling of Hot-Deformed Nd–Fe–B Magnet Scrap by Field-Assisted Sintering Technology. <i>Advanced Energy and Sustainability Research</i> , Vol. 5, Issue 1, pp. 2300184. DOI: 10.1002/aesr.202300184	First Author	Published
Journal	M. Keszler , I. Radulov, F. Maccari, T. Mutuk, M. Krengel, O. Guillon, O. Gutfleisch, M. Bram. (2024). Field assisted sintering and spark plasma texturing of Nd-Fe-B magnets with anisotropic magnetic properties. <i>Powder Metallurgy</i> . DOI: 10.1177/00325899251331431	First Author	Published
Conference Proceedings, Lecture	M. Keszler , T. P. Mishra, L. Leich, M. Krengel, T. Mutuk, O. Guillon, M. Bram. (2023). Field Assisted Sintering Techniques in Recycling NdFeB Magnets. In <i>Electric Field Enhanced Processing of Advanced Materials III: Complexities and Opportunities</i> , pp. 46. ECI Symposium Series. 2023, Tomar.	First Author	Published
Conference Proceedings, Lecture	M. Keszler , F. Grosswendt, S. Jaeger, A.C. Assmann, S. Weber, M. Bram (2023). Upcycling Of PM T15 Steel Swarf Via FAST/SPS Processing. In <i>Euro Powder Metallurgy 2023 Congress & Exhibition</i> . EPMA Publications. 2023, Lisbon. DOI: 10.59499/EP235761173	First Author	Published
Conference Proceedings, Lecture	M. Keszler , F. Grosswendt, A. C. Assmann, A. Roettger, S. Weber, O. Guillon, M. Bram. (2025). Direct Recycling of Tool Steel Swarf Using Field Assisted Sintering. In <i>Journal of the Japan Society of Powder and Powder Metallurgy</i> , Vol. 72(Supplement), pp. S211-S218. DOI: 10.2497/jjspm.14E-T16-02	First Author	Published
Conference Proceedings, Lecture	M. Keszler , F. Grosswendt, A. C. Assmann, M. Krengel, F. Maccari, O. Gutfleisch, D. Sebold, S. Weber, O. Guillon, M. Bram. (2025). Field Assisted Sintering in the Direct Recycling of Hot Deformed Nd-Fe-B Magnet Scrap. In <i>Journal of the Japan Society of Powder and Powder Metallurgy</i> Vol. 72(Supplement). DOI: 10.2497/jjspm.15E-SIS13-06	First Author	Published
Conference Proceedings, Poster	M. Keszler , F. Grosswendt, A.-C. Assmann, A. Roettger, S. Weber, O. Guillon, M. Bram. (2024). Densification and Austenitization of Recycled Tool Steel Swarf via Field Assisted Sintering. In <i>42. Hagener Symposium</i> . Deutsche Keramische Gesellschaft e.V. 2024, Hagen.	First Author	Published

Conference Proceedings,	M. Keszler , A.C. Assmann, F. Grosswendt, M. Krengel, F. Maccari, O. Gutfleisch, D. Sebold, S. Weber, O. Guillon, M. Bram. (2025) Utilizing field-assisted sintering in the direct recycling of hot-deformed Nd-Fe-B scrap . In <i>MaterialsWeek 2025</i> . DGM-Inventum GmbH. 2025, Frankfurt.	First Author	Published
Conference Proceedings,	M. Keszler , F. Grosswendt, A. C. Assmann, S. Weber, A. Roettger, O. Guillon, M. Bram. (2025) From Trash to Tool: Processing of D2 and PM T15 steel swarf into cutting disks using field assisted sintering . In <i>MaterialsWeek 2025</i> . DGM-Inventum GmbH. 2025, Frankfurt.	First Author	Published
Journal	F. Maccari, T. P. Mishra, M. Keszler , T. Braun, E. Adabifiroozjaci, I. A. Radulov, T. Jiang, E. Bruder, O. Guillon, L. Molina-Luna, M. Bram, O. Gutfleisch. (2023). Nanocrystalline Nd-Fe-B Anisotropic Magnets by Flash Spark Plasma Sintering . <i>Advanced Engineering Materials</i> , Vol. 25, Issue 18, pp. 2300252. DOI: 10.1002/adem.202300252	Contributing Author	Published
Conference Proceedings,	M. Bram, F. Maccari, M. Keszler , T.P. Mishra. (2023). Flash Spark Plasma Sintering Of Nd-Fe-B Magnets With Tailored Anisotropic Magnetic Properties . In <i>Euro Powder Metallurgy 2023 Congress & Exhibition</i> . EPMA Publications. 2023, Lisbon. DOI: 10.59499/EP235762561	Contributing Author	Published
Conference Proceedings,	M. Bram, M. Keszler , F. Grosswendt, S. Weber. (2024). Application of Field Assisted Sintering for the Recycling of Grinding Steel Swarf . In <i>Euro Powder Metallurgy 2024 Congress & Exhibition</i> . EPMA Publications. 2024, Malmö. DOI: 10.59499/EP246280685	Contributing Author	Published

Curriculum Vitae

Monica T. Keszler

m.keszler@fz-juelich.de | [monica-keszler](https://www.linkedin.com/in/monica-keszler/)

Cologne, North Rhine-Westphalia, 50825, Germany

OBJECTIVE

Motivated problem solver with specific interests in advancements in circular economy and recycling. Curious to apply new technologies to unsolved issues in the material supply chain. Performing good research and making it accessible, understandable, and clearly communicated are of high priority to me.

EXPERIENCE

- **Forschungszentrum Jülich, IMD-2** [⊕]
Doctoral Researcher
◦ Utilized field-assisted sintering techniques in the research of the direct recycling of hot-deformed Nd-Fe-B magnets
◦ Demonstrated direct recycling of D2 and PM Ti15 steel swarf into new tools through field-assisted sintering techniques
- **Institut de Chimie de la Matière Condensée de Bordeaux (ICMCB)** [⊕]
Material Science Intern - Master Thesis
◦ Investigated new recycling routes for Li-ion batteries via super-critical fluid separation
◦ Characterized sample surfaces and material compositions via X-ray diffraction (XRD), Fourier transform infrared spectroscopy (FTIR), inductively coupled plasma (ICP), scanning electron microscopy (SEM), and Raman spectroscopy
- **Technische Universität Darmstadt - Functional Materials Group** [⊕]
Advanced Research Lab Intern
◦ Optimized melt spinning parameters for magnetic nanocomposites
◦ Characterized melt spun samples through XRD, vibrating sample magnetometry (VSM), and SEM
- **Laboratoire de Chimie des Polymères Organiques (LCPO)** [⊕]
Organic Synthesis Intern
◦ Explored novel synthesis routes for poly(hydroxy)urethanes via less toxic precursors
◦ Characterized reaction kinetics and products via infrared (IR), nuclear magnetic resonance (NMR), and ultraviolet (UV) spectroscopy
- **Rogers Corporation** [⊕]
Resins Research and Development Co-op
◦ Parameterized specifications for successful and accurate printing of custom ceramic filled photopolymers
◦ Navigated and optimized 3D printer hardware and software for custom resin printing across multiple stereolithography (SLA) and digital light processing (DLP) platforms
- **Rogers Corporation** [⊕]
Functional Ceramics Research and Development Co-op
◦ Optimized parameters in magnetic material development for scale-up and further production
◦ Characterized electrical properties of films and coatings for use in electronics
◦ Assessed material characteristics through particle size analysis, SEM, and impedance analysis
- **Northeastern University** [⊕]
Engineering Education Researcher
◦ Illustrated comics as curriculum supplements in undergraduate chemical engineering courses
◦ Analyzed impact of comics as an educational tool based on classroom data
- **Roche Diabetes Care GmbH** [⊕]
Research Intern
◦ Analyzed polymer permeability for continuous blood glucose monitoring systems
◦ Implemented electrochemical testing for various hydrogels
◦ Tested improvements in handheld blood glucose monitoring systems
- **Ashland Specialty Ingredients** [⊕]
Process Engineering Co-op
◦ Optimized lab processes with wash and distillation units to limit by-product and maintain product purity for manufacturing
◦ Designed and executed experiments with glassware systems for scale-up of fragrances, hair care products, and monomer intermediates

EDUCATION

• Université de Bordeaux M.Sc. in Chemistry - AMIR - Double Degree ◦ Specialization in Advanced Materials: Innovative Recycling	Sept. 2019 - Sept. 2021 Bordeaux, France
• Technische Universität Darmstadt M.Sc. in Material Science - AMIR - Double Degree ◦ Specialization in Advanced Materials: Innovative Recycling	Oct. 2020 - Sept. 2021 Darmstadt, Germany
• Northeastern University B.S. in Chemical Engineering, Minor in Biochemical Engineering ◦ GPA: 3.67/4.0 ◦ Honors Program Graduate	Aug. 2014 - Dec. 2018 Boston, MA, USA

PEDAGOGICAL PUBLICATIONS

I = ILLUSTRATED

Regular contributor to the journal of Chemical Engineering Education from 2017. All contributions are listed below.

- [I.1] L. Landherr (w) and M. Keszler (p) (2017). **Drawn to Engineering: Humor in Exams.** *Chemical Engineering Education*, Vol. 51, Issue 3, pp. 126-127.
- [I.2] L. Landherr (w) and M. Keszler (p) (2017). **Drawn to Engineering: Presenting Audiences.** *Chemical Engineering Education*, Vol. 51, Issue 4, pp. 163-164.
- [I.3] L. Landherr (w) and M. Keszler (p) (2018). **Drawn to Engineering: Diversity Statement.** *Chemical Engineering Education*, Vol. 52, Issue 2, pp. 115-116.
- [I.4] L. Landherr (w) and M. Keszler (p) (2018). **Drawn to Engineering: Skeleton Notes.** *Chemical Engineering Education*, Vol. 52, Issue 3, pp. 221-222.
- [I.5] L. Landherr (w) and M. Keszler (p) (2018). **Drawn to Engineering: Exams Are Alive With The Sound of...Music?.** *Chemical Engineering Education*, Vol. 52, Issue 4, pp. 294-295.
- [I.6] L. Landherr (w) and M. Keszler (p) (2019). **Drawn to Engineering: Idea Theft.** *Chemical Engineering Education*, Vol. 53, Issue 1, pp. 63-64.
- [I.7] L. Landherr (w) and M. Keszler (p) (2019). **Drawn to Engineering: Evolving Your Teaching.** *Chemical Engineering Education*, Vol. 53, Issue 2, pp. 67. DOI: 10.18260/2-1-370.660-108007
- [I.8] L. Landherr (w) and M. Keszler (p) (2019). **Drawn to Engineering: Illumination.** *Chemical Engineering Education*, Vol. 53, Issue 3, pp. 145.
- [I.9] L. Landherr (w) and M. Keszler (p) (2019). **Drawn to Engineering: TA Doesn't Stand for Tomato Attack.** *Chemical Engineering Education*, Vol. 53, Issue 4, pp. 213-214.
- [I.10] L. Landherr (w) and M. Keszler (p) (2020). **Drawn to Engineering: Doing Our Best...Just Like Our Students.** *Chemical Engineering Education*, Vol. 54, Issue 4, pp. 175-176. DOI: 10.18260/2-1-370.660-123357
- [I.11] L. Landherr (w) and M. Keszler (p) (2021). **Drawn to Engineering: "Creating" Alternatives to Exams.** *Chemical Engineering Education*, Vol. 55, Issue 2, pp. 95-96. DOI: 10.18260/2-1-370.660-127943
- [I.12] L. Landherr (w) and M. Keszler (p) (2021). **Drawn to Engineering: The Future is Meow.** *Chemical Engineering Education*, Vol. 55, Issue 3, pp. 173-174. DOI: 10.18260/2-1-370.660-128875
- [I.13] L. Landherr (w) and M. Keszler (p) (2023). **Drawn to Engineering: Why Comics Anyway?.** *Chemical Engineering Education*, Vol. 57, Issue 2, pp. 77-78. DOI: 10.18260/2-1-370.660-132881
- [I.14] L. Landherr (w) and M. Keszler (p) (2024). **Drawn to Engineering: Brain Masonry.** *Chemical Engineering Education*, Vol. 58, Issue 1, pp. 61-62. DOI: 10.18260/2-1-370.660-134879

Frequent illustrator of comics encouraging K-12 students to become curious about chemical engineering, in collaboration with Northeastern University and the American Institute of Chemical Engineers (AIChE)

- [I.15] I. Hysi (w) and M. Keszler (p) (2023). **The Wide World of Chemical Engineering.** *AIChE Foundation - Doing A World Of Good Campaign*

SKILLS

- **Field Assisted Sintering Techniques:** FAST/SPS, Flash SPS, FAST deformation
- **Microscopy:** SEM, EDX, ImageJ analysis
- **Material processing and synthesis:** Melt spinning, SLA/DLP 3D printing, ceramics processing
- **Communication:** Public speaking, graphic design, illustration
- **Languages:** English (native), German (intermediate), French (intermediate)
- **Analytical software:** OriginLab
- **Graphic software:** Adobe Photoshop, Clip Studio Paint, Inkscape, Blender

Band / Volume 668

Effects of mucilage and extracellular polymeric substances on soil gas diffusion

A. Haupenthal (2025), v, 99 pp

ISBN: 978-3-95806-834-6

Band / Volume 669

Quantifying Recombination Losses and Charge Extraction in Halide Perovskite Solar Cells

L. Krückemeier (2025), vi, 286 pp

ISBN: 978-3-95806-835-3

Band / Volume 670

Investigation of Dynamic Material Changes During the Preparation of ZnPd Nanoparticles Supported on ZnO and their Catalytic Application in Methanol Steam Reforming on the Atomic Level

A. Meise (2025), xviii, 175 pp

ISBN: 978-3-95806-838-4

Band / Volume 671

Improving Energy Efficiency of Public Buildings by Influencing Occupant Behaviour using Dashboards and Gamification

E. Ubachukwu (2025), xxi, 191 pp

ISBN: 978-3-95806-840-7

Band / Volume 672

Exploring Plant Responses to Changing Environments: Integrating Phenotyping and Modeling Across Scales

F. M. Bauer (2025), xxix, 188 pp

ISBN: 978-3-95806-845-2

Band / Volume 673

A constitutive theory to represent non-idealities in contacting of SOC interconnect contacts

R. M. Pinto (2025), xii, 139 pp

ISBN: 978-3-95806-846-9

Band / Volume 674

Strontium titanate based materials for use as oxygen transport membranes in membrane reactors

Y. Tang (2025), XIV, 132 pp

ISBN: 978-3-95806-849-0

Band / Volume 675

Scaling Methods for the Production of Tungsten Fiber-Reinforced Composites via Chemical Vapor Deposition

A. Lau (2025), untersch. Pag.

ISBN: 978-3-95806-851-3

Band / Volume 676

Nanoscale analysis of high-temperature oxidation mechanisms of Cr₂AlC MAX phase and W-Cr-Y self-passivating tungsten alloy

A.J. S. Reuban (2025), ix, 142 pp

ISBN: 978-3-95806-855-1

Band / Volume 677

First principles simulations of high-entropy materials for energy storage

Y. Ting (2025), xviii, 169 pp

ISBN: 978-3-95806-858-2

Band / Volume 678

Deployment of Fuel Cell Vehicles in Road Transport and the Expansion of the Hydrogen Refueling Station Network

T. Grube, M. Sander (2025), iv, 61 pp

ISBN: 978-3-95806-859-9

Band / Volume 679

Entwicklung von nickelbasierten katalysatorbeschichteten Diaphragmen für die alkalische Wasserelektrolyse

C. B. Karacan (2025), 146 pp

ISBN: 978-3-95806-860-5

Band / Volume 680

Bewertung lokaler Eigenspannungsverteilungen bei der lokalen Bauteilreparatur durch Kaltgasspritzten

J.-C. Schmitt (2025), 154, xxvii pp

ISBN: 978-3-95806-861-2

Band / Volume 681

First principles study of the effect of substitution\doping on the performance of layered oxide cathode materials for secondary batteries

N. Yacoob (2025), iii, 126 pp

ISBN: 978-3-95806-864-3

Band / Volume 682

Field assisted sintering technology/spark plasma sintering in the direct recycling of hot-deformed Nd-Fe-B scrap and PM T15 steel swarf

M. T. M. Keszler (2025), viii, 173 pp

ISBN: 978-3-95806-866-7

Energie & Umwelt / Energy & Environment
Band / Volume 682
ISBN 978-3-95806-866-7

Mitglied der Helmholtz-Gemeinschaft